Synthesis, Structure and Physicochemical Properties of Some Metal-Organic Frameworks

A Thesis

Submitted for the Degree of

Doctor of Philosophy (Science)

By

Rakesh Debnath

Department of Chemistry

JADAVPUR UNIVERSITY

JADAVPUR, KOLKATA-700 032

INDIA

December, 2024

Dedicated

To

My Parents and My Sir

CERTIFICATE FROM THE SUPERVISOR

This is to certify that the thesis entitled "Synthesis, Structure and Physicochemical Properties of Some Metal-organic Frameworks" Submitted by Sri Rakesh Debnath who got his name registered on 22/08/2019 for the award of Ph. D. (Science) Degree of Jadavpur University, is absolutely based upon his own work under my supervision and that neither this thesis nor any part of it has been submitted for either any degree / diploma or any other academic award anywhere before.

Subrata nath Koner

(Signature of the Supervisor date with official seal)

DR. SUBRATA NATH KONER
Professor
Department of Chemistry
Jadavpur University
Kolkata – 700032, India

<u>Acknowledgement</u>

Finally, I am thanking full to my school sir, my guru respected Mr. Amit Basak, and Mr. Debashis Saha, for their continual support, encouragement and guidance in my education led to my accomplishments. Completion of this Ph.D. would have been difficult with out their encouragement.

Department of Chemistry,   (Rakesh Debnath)
Inorganic Chemistry Section,   (Senior research fellow)
Jadavpur University,
Kolkata-700032
India,
December, 2024

Table of Contents

CHAPTER 5: Cobalt(II) based bi-functional MOF as efficient tandem catalyst towards olefin oxidation followed by Knoevenagel condensation 137

List of Abbreviations

0D	Zero-dimensional
1D	One-dimensional
2D	Two-dimensional
ºC	Degree Centigrade
Å	Angstrom
3D	Three-dimensional
AAS	Atomic absorption spectroscopy
acac	Acetylacetonate
AIBN	2,2′-azo-bis-isobutyronitrile
BADA	Benzaldehyde dimethyl acetal
BASF	Baden Aniline and Soda Factory
BDC	1,4-benzenedicarboxylate
BET	Brunauer–Emmett–Teller
BOC	*tert*-butoxycarbonyl
bphdc	4,4′-biphenyldicarboxylate
bpydc	2,2′-bipyridine-5,5′-dicarboxylate
H_2ODA	2,2′-oxydiacetic acid
BTB	1,3,5-benzenetribenzoic acid
btc	Benzene-1,3,5-tricarboxylate
btec	1,2,4,5-benzenetetracarboxylate
CN	Coordination network
CSA	Control SBU approach
DMF	N,N-Dimethylformamide
DEF	N,N-Diethylformamide
DMSO	Dimethylsulfoxide
NMP	N-methyl-2-pyrrolidone
DMA	N,N-dimethylacetamide
DTA	Differential thermal analysis
EDX	Energy-dispersive X-ray
EPR	Electron paramagnetic resonance

EtOH	Ethanol
FOS	Functional Organic Site
FTIR	Fourier transform infrared
GC	Gas chromatography
H$_2$bdpb	1,4-bis[(3,5-dimethyl)pyrazol-4-yl]benzene
dpa	4,4′-dipyridylacetylene
H$_3$L	Pyrazole-3,5-dicarboxylic acid
HRMS	High resolution mass spectrometer
IR	Infrared
IRMOF	Isoreticular metal-organic framework
HKUST	Hong Kong University of Science and Technology
BUT	Butyric Metal Organic Frameworks
mcbdc	5-methoxycarbonyl-benzene-1,3-dicarboxylate
MeCN	Acetonitrile
MeOH	Methanol
MIL	Materials of Institute Lavoisier
MOF	Metal organic framework
MOM	Metal organic material
ndc	2,6-Naphthalenedicarboxylate
NHPI	N-hydroxyphthalimide
NMR	Nuclear magnetic resonance
NP	Nano particle
PBA	*p*-bromoacetophenone
PCP	Porous coordination polymer
pdc	Pyridine-2,5-dicarboxylate
PITA	2-pyridyl-imine terephthalate
POM	Polyoxometalate
POP	Porous organic polymer
PSM	Post-synthetic modification
PXRD	Powder X-ray diffraction
pyr	Pyrazine
pzdc	Pyrazole-3,5-dicarboxylate

SBU	Secondary building unit
PCU	Primitive cubic unit
SEM	Scanning electron microscopy
SH-SiO$_2$	Metal free mercaptopropyl-functionalized silica
SNT	Synthetic nanotube
TBHP	*tert*-butyl hydroperoxide
ted	Triethylenediamine
TEM	Transmission electron microscopy
TGA	Thermogravimetric analysis
THF	Tetrahydrofuran
TOF	Turn over frequency
TON	Turn over number
UV−Vis	Ultraviolet–visible
XRD	X-ray diffraction
IAST	Ideal Adsorbed Solution Theory
DABCO	1,4-diazabicyclooctane
TDC	Thiophene-2,5-dicarboxylate
H$_6$TATAT	5,5′,5′′-(1,3,5-triazine-2,4,6 triyl)tris(azanediyl)triisophthalate
H$_2$ODA	2,2′-oxydiacetic acid
TCBPA	tris(4′-carboxybiphenyl)amine
pypz	bis[3,5-dimethyl-4-(4′-pyridyl)pyrazol-1-yl
bpdc	4,4′-biphenyl dicarboxylic acid
bpydc	2,2′-bipyridine-5,5′-dicarboxylic acid
TEMPO	2,2,6,6-tetramethylpiperidine-N-oxyl
TPE	tetraphenylethene
H$_4$btca	1,2,4,5-benzene terta carboxylic acid
PCN	Porous coordination network
msitpa	5,5′,5′′-(methylsilanetriyl)triisophthalic acid
mdpy	4,4′-((9H-fluoren-9-ylidene)-methylene)dipyridine

Chapter 1

General introduction

and

Brief review

1.1 Introduction

Metal-organic framework (MOFs) or porous co-ordination polymers (PCP's) in recent years earned significant consideration in chemical science owing to their intriguing and customizable porosity, molecular topologies and diverse architecture lead to serving as beneficial materials for various fields. According to Yaghi et al., MOFs are of porous networked structures constructed by the coordination bonding of metal ions with organic linkers or bridging ligands. MOFs are constructed through linkage between coordinating metal centers or secondary-building units (SBUs) and organic linkers, resulting in open frameworks with persistent porosity, a stable framework, large surface area, and pore volume. The porosity can be attributed by lengthy organic linkers, generating huge storage space and multiple adsorption sites within MOF. Flexible and dynamic behavior of these crystalline materials towards the guest molecule and large internal surface area, make them more elegant compare to classical inorganic porous materials [1]. A variety of MOFs can be attributed by varying metal containing units and organic linkers [2], also the pore size and spatial cavity organization can be modified by carefully selecting metal centers and organic ligands, as well as altering their synthesis conditions. MOFs generally have large interior surface area (usually 500-7000 m^2/g), structural flexibility, adjustable porosity, changeable organic functionality, and physical/thermal stability, making them a viable alternative to traditional permeable materials such as activated carbons and zeolites [3]. Recent time, these new types of hybrid materials has drawn a lot of attention as functionalized materials also. Researchers are interested in designing and synthesizing materials that exhibit unique topological architectures for prospective uses in selective gas storage and separation, magnetism, photo-luminescence and sensing, heterogeneous catalysis, proton conduction, drug delivery and so on.

Photo-luminescent (PL) co-ordination polymers (PL-CPs) are being employed in a number of adaptive techniques for detecting and monitoring a wide range of analytes which are of great concerns for their harmful consequences in the environment and human health. Towards this end, PL-CPs are considered to be very promising because of their high sensitivity, selectivity, quick response and applicable in both solid and liquid phases [4]. MOFs, with their distinct features like large surface area, variable porosity, and customizable functional groups, are suitable materials for developing sensitive and selective fluorescence sensors.

Catalysis plays a significant role in the industrial synthesis of liquid fuels [5], bulk and specialty chemicals, pharmaceutical and agrochemicals etc. Over the last few decades, there has been significant advancement in the formulation of catalytic systems for both heterogeneous and homogeneous catalysis for organic transformation. Metal-organic frameworks (MOFs) are a new and versatile family of materials that have received tremendous attention for their application in the field of catalysis. MOF attributes some distinctive feature like highly tunable porosity, versatility of their frameworks that can be achieved by fine tuning synthetic procedure, robustness of the structure etc. that make them intriguing candidates for a wide range of catalytic applications, in the same way, as zeolite and aluminosilicate based heterogeneous catalysts are used. Among various catalytic reactions, tandem catalysis which allows multiple catalytic reactions to occur concurrently creates a lot of interest. Environment friendly method can be designed for producing complex compounds from low-cost, commercially available raw materials rather than conventional stepwise synthetic methods [6]. Efficient one-pot tandem reactions often require multifunctional catalysts that possess separate catalytically active regions for independent operation. In this field multifunctional MOFs with more than one active sites are exactly fulfilling the criteria required for tandem catalysis [7].

1.2 Metal-organic frameworks

Metal-organic frameworks (MOFs) or porous co-ordination polymers (PCPs) are representing a novel family of porous materials that exhibit unparalleled structural and chemical tenability. The complex host-guest chemistry, long-range order and synthetic adaptability of MOFs make them perfect platforms to explore designing of optimized functional materials for possible uses in numerous scientific and technological domains such as gas storage and separation, luminescent sensing, catalysis and many other applications. This is reflected in steady increase of number of high-quality publications, and citations, along with the ongoing growth of the field of studies reporting a variety of structures and, of course, growth of number of researcher's involvement. The following five advancements have contributed to an unparalleled upsurge in MOF research, namely, are (i) advances in cluster chemistry; (ii) maturation of organic synthesis pertinent to ligand preparation and post-synthetic modification; (iii) improvement in structure determination, particularly through X-ray crystallography and progress of hardware and software for characterization of sorption properties; (iv) interdisciplinary evolution of research on MOF and related fields and (v) the ever-expanding

potential in several applications. Because of their various uses in fields like molecular topologies and crystal engineering, MOFs are highly desirable and have been the subject of much research in luminescence and sensing [8-17], magnetism [18-20], drug delivery [21-22], gas storage and separation [23-26], catalysis [27-33] and proton conductance [34-36].
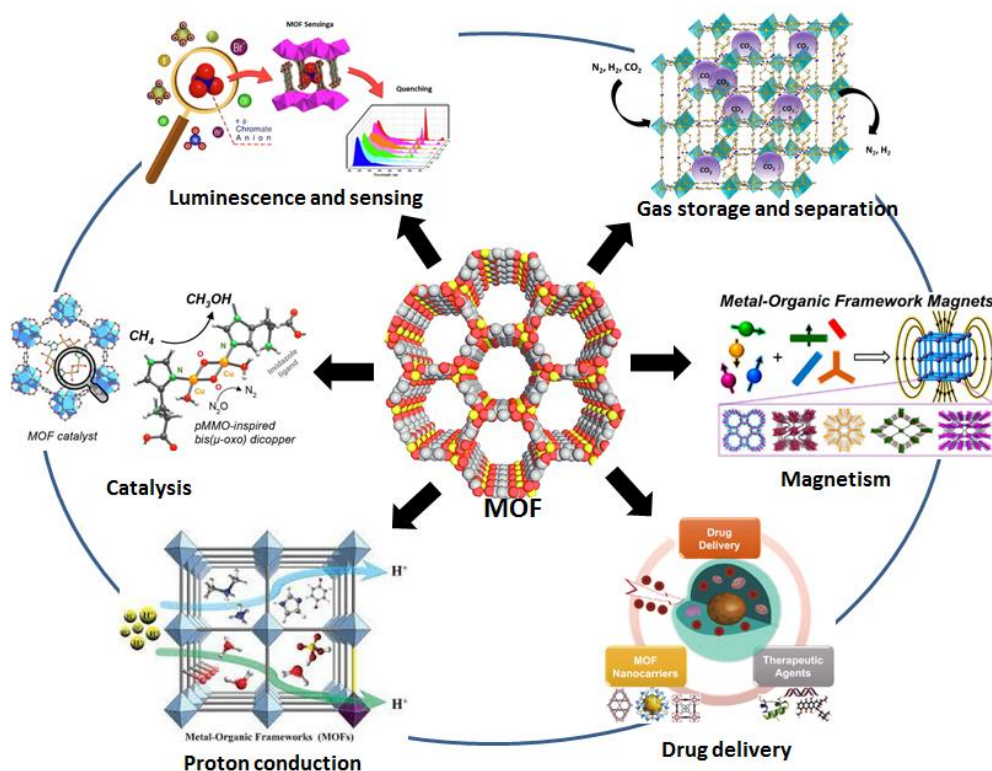
Scheme 1.1. Schematic representation of different application MOF

The phrase "coordination polymer" was initially utilized in a publication in 1916, although at that time there was no way to demonstrate infinite networks devoid of single-crystal X-ray crystallography [37]. The well-known Prussian blue compounds, which featured a three-dimensional coordination framework and were based on Fe-CN-Fe links, has been introduced later in 1936 [38]. However, research into materials with polymeric, occasionally porous architectures based on metal ions and organic bridge linkers did not significantly advance until the early 1990s [39]. Initial publications by Robson [40], Moore [41], Yaghi [42], and Zawarotko [43] contributed to the field of MOF, which currently witnessed of an exponential development as can be seen from growth of literature in this particular field. The first "MOF"

material named as MOF-5, was reported by research group of O. M. Yaghi [44]. The foundation of current advancement in metal-organic materials, or MOMs, is found in the seminal work of A. F. Wells, who established the straightforward and useful "node and spacer" theory of inorganic crystal formations. Inorganic crystal structures thus can be defined as metal ions (nodes) connected together through bonds (spacer or edge) [45].

1.2.1. Types and connectivity of MOF

MOF, all together, define the formation of extended structures constructed by metals and organic linkers. Coordination bonds and other weak chemical connections, such as van der Waals and hydrogen bonding interactions bind the metals and organic linkers that end up in MOFs. The metal ions designed as 'nodes' and the organic ligands as the 'linkers'. Depending upon the metal ion, variability of coordination numbers may be attained. Prediction of the network topology, even though not the determination of the cell parameters and the dimensionality of these compounds may be accomplished by the selection of metal ion and organic linker and also by more indirect circumstances such as selection of solvent and counter ions involved in the synthesis [46]. Additional components, for example counter ions, template molecules and surrounded non-bonding guest molecules can also take participate in arrangement, became a part of coordination polymer. Counter ions are required in a synthesis while using neutral ligands to afford the positive charge of the metal center is balanced. Counter anions for example ClO_4^-, BF_4^-, NO_3^-, $CF_3SO_3^-$, SiF_6^{2-} and PF_6^- etc. have been employed in this manner act as free guests, hydrogen-bond acceptors or coordination units [47]. Wealth of information has been gathered that showed minor adjustments to reaction parameters such as concentration, temperature, reaction time-duration, and pH have great impact on MOF synthesis and can reduce crystallinity or produce a coincidental result. Hence, the reaction conditions perform a dynamic role in determining the formation of final structure. As a result, the ultimate structure of the framework is dynamically determined by the reaction conditions. Solvent molecules can co-crystallize into the final structure and occupy the empty space as guest molecules. They do not only function as the reaction medium but may also influence the topology of the resulting framework, if porosity is achieved and the framework does not disintegrate upon desolvation. The guest solvent molecules may be removed after the structural

network has developed. Thus, the solvent may act as a template for the formation of porous phases [48].
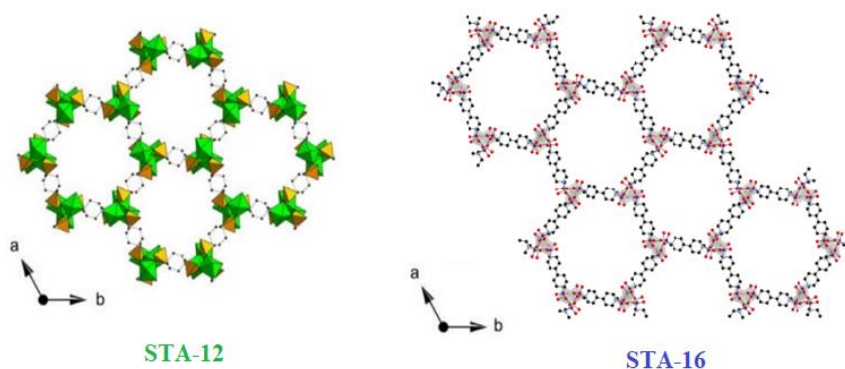
Figure 1.1. View of the hexagonal channels in the honeycomb like pore structure of metal bisphosphonates STA-12(Ni) (left) [49] and STA-16(Co) (right) [50]

As evidenced by the honeycomb-like structure of the isoreticular porous materials, it is conceivable to add functional groups to MOF compounds, alter the framework-forming metal cation, and adjust the pore size while maintaining the framework topology, for example, STA-12(Ni) [49] and STA-16(Co) [50] (Figure 1.1). The versatility implies that conventional materials might be restricted to a certain kind of interaction (for example, porous carbons can only be used in separations involving anhydrous components) whereas nature of the MOFs can be tuned. For example, by adding an amine group to an organic linker which is otherwise hydrophobic, might made a pore structure hydrophilic.

1.2.2 Secondary building unit (SBU)

In the context of metal-organic frameworks, "SBU" typically stands for "Secondary Building Unit". SBUs are the basic structural units that repeat and link together to form the framework structure of MOFs. In MOF, SBUs are often composed of metal ions or clusters coordinated to organic ligands. These SBUs can connect with each other through coordination bonds to form extended networks, resulting in the porous structures characteristic of the MOF.

The choice of SBUs and the design of their connectivity play a crucial role in determining the properties of MOFs, such as their pore size, surface area, and chemical reactivity. By carefully selecting and engineering SBUs, researchers can tailor the properties of MOFs for specific applications such as gas storage, catalysis and separation processes. In metal-organic frameworks, the formation of secondary building blocks (SBUs) is a crucial step in the synthesis process. Understanding and controlling the formation of SBU is essential for tailoring the properties of MOFs for various applications. SBUs are not supplied directly in a synthesis, however, these are formed in-situ under definite reaction conditions. Some common SBUs that are formed in MOFs are shown in Figure 1.2 [51]. Branched organic ligands, with above two coordinating functionalities, such as square tetrakis(4-carboxyphenyl)porphyrin (Figure 1.3a), tetrahedral adamantine-1,3,5,7-tetracarboxylic acid (Figure 1.3b), and trigonal 1,3,5-tris(4-carboxyphenyl)benzene (Figure 1.3c), are also recognized as SBU, nevertheless, they are formed before synthesis [52]. Because of this, it could be possible to predict the topology that will manifest in the final structure in certain circumstances. One may predict whether particular SBUs will be attached by particular metals and organic linkers during synthesis by using the index of SBUs that have been created for the synthesis of MOF.
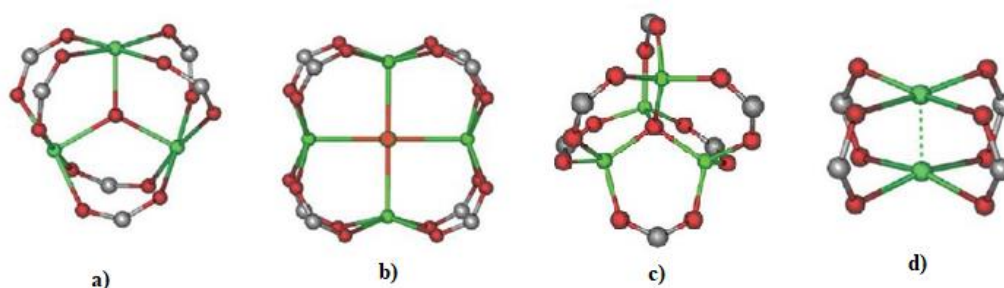
Figure 1.2. Structural representation of SBUs commonly occurs in the formation of metal-organic frameworks including (a) trigonal planar, (b) square planar, (c) tetrahedral and (d) tetragonal paddlewheel [51].

In order to manufacture MOF, the initial step involves selecting a discrete di-, tri-, or tetra-nuclear metal cluster to serve as a symmetrical module for polymerization utilizing a

multidentate linker. Depending on the shape of the SBU and linker, the metal clusters can function as SBUs and can be joined by linkers to create a network in a certain topology. A metal cluster serves as an inorganic SBU. Its shape is defined by atoms representing its points of extension to other SBUs. Those atoms define the underlying geometry of the SBU and geometry of the SBU is important to predict the overall topology of the network. For example, polymerization of paddle–wheel copper acetate (SBU) and multidentate linker 1,3,5,7-adamentanetetracarboxylate generate MOF-11. For the construction of MOF-11, the carboxylate carbon atoms of paddle-wheel copper acetate define its square geometry which is shown in Figure 1.2(d) [53].
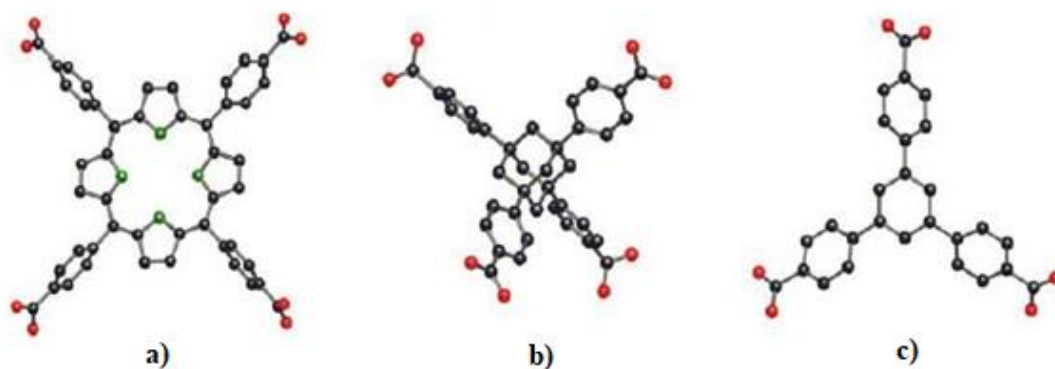
Figure 1.3. Some carboxylate SBUs which are pre-formed before synthesis of MOFs; (a) square tetrakis-(4-carboxyphenyl)porphyrin; (b) tetrahedral adamantine-1,3,5,7-tetracarboxylic acid and (c) trigonal 1,3,5-tris(4-carboxyphenyl)benzene [52]

There are several options available for organic linkers. Regular preference is given to ligands with stiff backbones because their rigidity facilitates the prediction of the structural network or geometry before synthesis begins, and because their rigidity, open-pore structure of the compound preserves long after the guest solvents have been removed. In essence, the linkers might be electrically neutral, cationic or anionic (Figure 1.4) [54]. The most commonly used neutral organic ligands are pyrazine and 4,4′-bipyridine (bpy) [55]. These linkers are very

effective for building pillar in three-dimensional networks [56]. Anionic linkers most frequently utilized, are carboxylate ligands [57]. Because of the ability to assemble metal ions into clusters, more stable frameworks may be produced. In contrary, cationic organic ligands have comparatively rarely been used because of their weaker affinity for cationic metal ions [58]. In the process of creating porous MOFs, such as longer bridging ligands, the organic linkers are also essential. While longer ligands provide vast holes that allow a second polymer network to interpenetrate the first formed network, this sort of ligand might cause certain issues inside a framework, such as interpenetration. This may lead to filling of voids in the frameworks; as a result, porosity is reduced or eliminated entirely. The size and form of the pores are known to be influenced by the topology of the framework, which is determined by the appropriate choice of metal ion and organic linker.
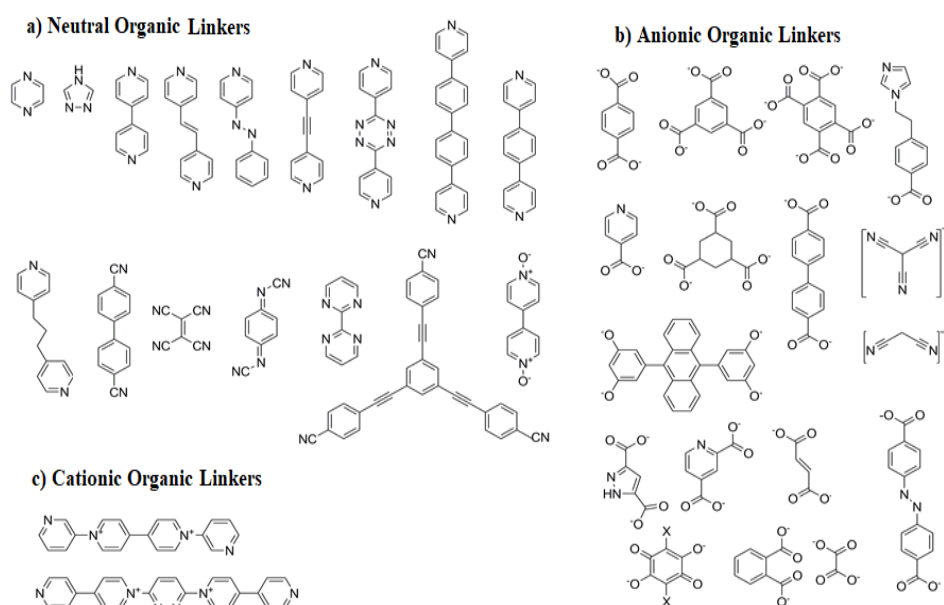
Figure 1.4. Examples of linkers used in MOFs [54]

A series of isoreticular material can be synthesize from the organic linkers containing same functional groups able to form different connectivity such as linear dicarboxylates (like benzene-1,4-dicarboxylate, biphenyl-4,4′-dicarboxylateetc). The isoreticular materials are topologically indistinguishable however the organic linking molecule is extended [52]. This is

represented by the MOF-5 [42] (also designated as IRMOF-1) and successively linked frameworks IRMOFs 2-16, where the identical $Zn_4O(COO)_6$ clusters afford the inorganic core, whereas the ligand between the carboxylate groups is diverse with maintenance of the cubic network of channels (Figure 1.5). Reticular synthesis is a tactic that makes use of SBUs that have already developed [57]. Reticular synthesis may also be used to build carboxylate MOFs using MOF-5 as a prototype in certain situations. These MOFs, which are made of the same net and topology as MOF-5, are known as isoreticular metal-organic frameworks (IRMOFs) (Figure 1.5). The organic ligands containing additional functional groups such as bromo (2), amino (3), n-propoxy (4), n-pentaoxy (5), cyclobutyl (6) and fused benzene functional groups (7), employed different functionality of the pendant groups in IRMOFs (1)-(7) and in length by substituting 1,4-benzenedicarboxylate producing IRMOFs 8-16, by 2,6-naphthalenedicarboxyalate (8), biphenyl-4,4′-dicarboxylate (10), pyrene-2,7-dicarboxylate (14) and terphenyl-4″-dicarboxylate (16) (Figure 1.5) [52, 59]. The same SBUs, namely $Zn_4O(COO)_6$ are present in both structures as in MOF-5; hence, the topology of the structures is the same despite variations in pore size and functionalities. Regarding adsorption and separation, the surface area of a porous framework compound is another crucial characteristic. The interaction between the guest molecules and the adsorbent surface is often significantly greater than the interaction between individual guests in most situations. There are several MOF compounds, which have incredibly high surface area, such as, MIL-101 which shows surface area of 4230 m^2/g [60], while MOF-177 shows 4500 m^2/g [52]. Not only did these materials have the largest surface areas among the MOF compounds that have been reported, they also had the maximum surface areas of all known porous materials. In contrast to other porous materials like amorphous carbons and silicas etc., the crystalline structure of MOFs allows for consistent pore systems across the material, facilitating improved repeatability and consistent sorption capabilities.
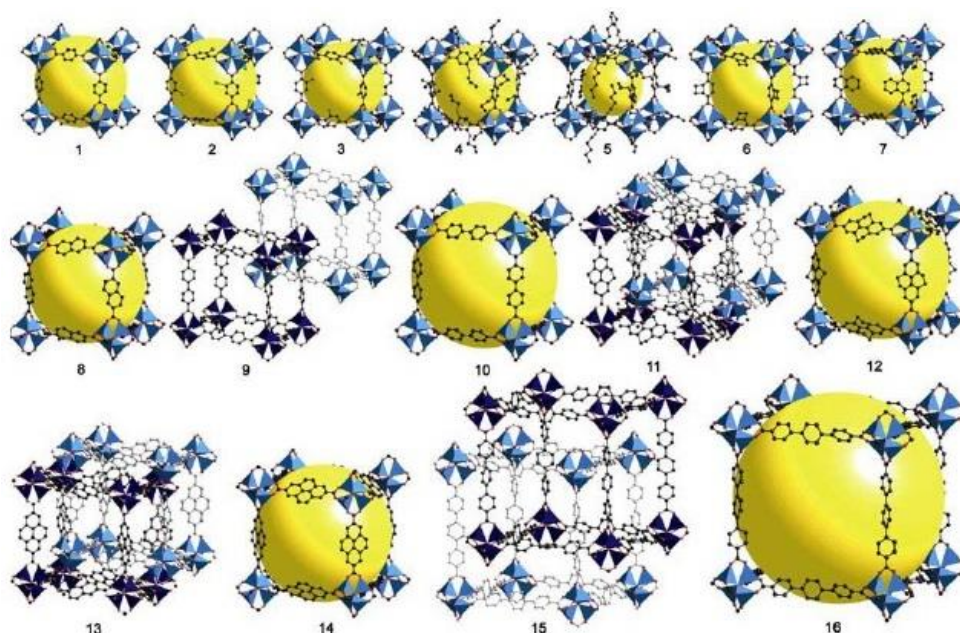
Figure 1.5. Structures of isoreticular MOFs (IRMOFs 1-16) using MOF-5 as the prototype [52]

The thermal stability of conventional materials is one area in which they still have benefits. Zeolites can, in some cases, be heated to temperatures in excess of 1000 °C in air without degradation [61] and that can allow for applications in the separation (or purification) of gases such as flue gas [62] or in high temperature catalysis [63]. Compared to zeolites, MOF materials typically have far less thermal stability but some examples of MOFs with strong metal-ligand bonds and stable organic components have shown thermal stability, in air, greater than 550 °C in case of porous variety [64] and over 600°C in high density non-porous variety of MOF [65].

1.3 Synthesis of MOF

As was previously mentioned, MOFs consist of two important parts: the organic ligands, also known as bridging linkers, and the metal ion. Formally, MOFs are synthesized by gently combining organic linkers with metal ions to form crystalline and porous structures. Several preparation techniques have been developed and used to prepare MOFs during the past few

decades. These are classified as conventional solvothermal methods, unconventional methods, and alternative methods. For example, diffusion-based crystallization, hydrothermal or solvothermal and ionothermal synthesis has been extensively used for MOF synthesis. Usually, MOFs are synthesized by using solvothermal or hydrothermal process [68], where the reactions are carried out in an organic solvent or in water, respectively, at high temperature under autogenous pressure. Though, these processes normally involve time-consuming reaction, from several hours up to several months, depending on the MOF of concern and the several factors such as solvent, temperature, concentrations of reactants etc. A microwave-aided method has been evolved in which synthesis of MOFs can be carried out in large scale in a few minutes or few hours [66]. This process can also control the size of crystal from near-millimeter to sub-micrometer by controlling the temperature and the concentration of reactants in solution.

There also exist quite of a few reports of synthesizing MOFs without the need for solvents; such attempts have been made to promote the expansion of environmentally benign processes [67]. The use of mechanical force in mechanochemical synthesis enables solvent-free interactions between metal oxides and organic linkers at ambient temperature. Furthermore, BASF has used the electrochemical production of MOFs on a commercial basis [68].

1.3.1 Microwave assisted method

Applications of microwave assisted methods for the quick synthesis of MOFs in hydrothermal settings are widespread. Tiny oxide and metal particles are created with the aid of the microwave technique [69]. Microwave is an electromagnetic radiation with frequency ranges between 300 and 300,000 MHz [70]. It comes from the interaction of electromagnetic waves with mobile solvent charges, such as polar solvent ions or molecules, and offers an effective means of heating. This method has been widely used to create metal oxides at the nano scale and it is also utilized in organic synthesis [70]. The temperature of the solution might be raised by microwaving for several hours in order to build metal nano sized crystals. This method involves filling a Teflon vessel with a substrate mixture and the required solvent. The vessel is then sealed and placed in the microwave for the desired time and temperature. Purpose of the microwave is to transform electromagnetic energy into thermal energy, which quickly warms the liquid mixture by interacting with solvent molecule's permanent dipole moment favoring their reorientation and alignment to an applied electric field or microwaves [71]. Polar molecules in a substrate mixture attempt to align themselves in an electromagnetic field and an

oscillating field, leading to permanent orientation changes. Molecules colliding at the right frequency will increase the temperature and kinetic energy of the system. It is specially an energy-efficient method of heating since the radiation interacts directly with the solution or reactant. The selection of the solvent and specific energy input should be taken into account [72]. In order to improve product purity for the specific synthesis of polymorphs, rapid crystallization and the creation of nanoscale products are the primary goals of microwave-assisted MOF synthesis [72].

1.3.2 Hydrothermal Synthesis of MOF

Zeolites are formed naturally in environments with natural high pressures (> 300 MPa) and temperatures (> 573 K), which resulted from burial metamorphism that occurred in the upper crust of the Earth. As a result, early attempts to produce synthetic zeolites were conducted under comparable circumstances. The subsequent shift in zeolite chemistry toward the alternative hydrothermal synthesis pathway proposed by Barrer and Milton did not occur until the 1950s [73]. The foundation of hydrothermal synthesis is the idea that precursors used to create microporous frameworks are insoluble at room temperature but readily soluble at temperatures and pressures between 100 and 260 °C [74]. The majority of MOFs described in the literature have been produced by solvothermal and hydrothermal synthetic techniques, often utilizing reaction bombs or closed Teflon lined stainless-steel autoclaves. The autoclave is designed as a thick-walled, sealed steel reaction tank with an inner wall coated with Teflon, allowing the reaction temperature to climb above the solvent's boiling point under high pressure. In these conditions, autogenous pressure is created, allowing the production of new products since the pressure inside the reaction vessel develops on its own without the need for external application. The pressure inside the vessel depends various factor such as temperature, quantity of the reactant as well as depend on the sealing of the vessel [75]. Under these circumstances, the viscosity of water reduces, improving the diffusion processes that facilitate crystal formation from the solution and allow the reactant's structural constituents to be retained in the final product [76]. This ''soft-chemistry'' method allows the formation of polymeric units via molecular building blocks [77]. Furthermore, the synthesis is changed to solvothermal synthesis by the use of different solvents in the reaction technique. Both solvothermal and hydrothermal synthesis techniques have been used to create new materials and advanced development of novel procedures for the synthesis of new functional materials with new geometries or crystal

formation [78]. Aprotic solvents include N,N-diethylformamide (DEF), N,N-dimethylfromamide (DMF), N-methyl-2-pyrrolidone (NMP), N,N-dimethylsulphoxide (DMSO), N,N-dimethylacetamide (DMA), acetonitrile, and toluene. Protic solvents are methanol, ethanol, and mixed solvents. As regards the synthesis of robust and stable MOF materials, hydrothermal techniques play a more crucial role than solution phase processes [79]. Although it is impossible to have time-to-time visual inspection of the growth of a crystal, given certain circumstances, the in-situ energy dispersive X-ray diffraction technique can provide insight into the mechanism of crystalline formation [80].

1.3.3. Mechanochemical Method

Mechanochemistry is the study of reactions between solids that are primarily initiated by mechanical energy. Without the use of a solvent, a mixture of a metal salt and an organic ligand is crushed in a ball mill or with a mortar and pestle. The ground mixture is then gently heated to remove any remaining volatile compounds and H_2O that may have generated as a bi-product in the reaction mixture. Compared to other approaches, the mechanochemical methodology is simpler to use for synthesis of MOFs. Chemical transformation occurs during mechanochemical synthesis when intramolecular bonds are mechanically broken [81]. Room temperature is the operating temperature of reaction, and organic solvents are avoided. A report on the first MOF synthesis using this method was published in 2006 [82]. Recently, this process is widely employed to create different types of MOFs.

1.3.4. Sonochemical method

Sonochemical synthesis of metal-organic frameworks is a relatively new and promising method for the fabrication of these porous materials. Sonochemistry involves the use of high-intensity ultrasound waves to induce chemical reactions in solutions [83]. When applied to MOF synthesis, ultrasound waves generate cavitation bubbles in the reaction mixture. These bubbles collapse violently upon reaching a critical size, generating localized hot spots with extremely high temperatures and pressures. This phenomenon facilitates rapid mixing, mass transfer, and nucleation, leading to accelerated crystal growth and the formation of MOFs. In 2008 sonication was used for the first time for the synthesis of MOFs [84].

1.3.5. Slow evaporation and diffusion method

The diffusion of layers method is a technique used in the synthesis of metal-organic frameworks (MOFs) to produce highly crystalline solids with well-defined structural motifs. In this method compatible solvents are used in which organic ligands and center metal ions are dissolved. Metal ions and organic ligands interact at the solvent interface to produce MOF crystals [85]. In slow evaporation method mixture of reagents is allowed to evaporate slowly to isolate crystalline MOF. Nucleation and growth process are facilitated by the formation of crystals at critical concentrations. To speed up the evaporation sometimes low boiling solvents are used [86, 87]. In the diffusion technique, the solvent layer is employed to separate the reagent solutions, or the physical barriers are controlled to allow for a gradual diffusion of the reagent solutions. After nucleation the solvent progressively permeates each layer, causing crystals to develop at the layer interface. Diffusion is especially used when the chemicals are not very soluble. Sometimes mixing of metal and ligand solutions at ambient temperature, MOFs are not generated. However, in some specific circumstances, the production of microcrystalline powder is obtained by mixing metal ions with ligand solution, which is not suitable for single crystal X-ray analysis. To address the problem of producing polycrystalline powder materials, a slow solvent diffusion method is favored. Often to achieve slow diffusion, the organic linker and the metal ion solution were separated by a buffer layer. To control diffusion sometimes gel is used. At the layer interface, where solvents are gradually transferred from one layer into neighboring layers, the desired crystal growth occurs [88]. Zheng *et al*. synthesized several copper and lanthanide containing framework compounds using diffusion method [89]. The diffusion method can be used for synthesizing sensitive MOFs under mild reaction conditions, but often prolonged synthesis process is a major disadvantage of this method.

1.4 Carboxylate based MOF

Several kinds of organic linkers have been strategically employed to build the MOFs. Organic carboxylates contribute to the formation of many functional property-based framework systems because of its numerous binding modes and they are also the most challenging candidate. The synthesis of several porous structures is the result of continued and targeted research into MOF systems [90]. The majority of MOFs have been created using the metal carboxylate strategy, which forms high symmetry structures by connecting divalent and trivalent metals with di- and tri- carboxylate linkers (Figure 1.6). While the carboxylate linkers

are not prone to self-condensation, the strong M-O-C links in the framework exhibit excellent thermal stabilities. There have been reports of different metal environments; in MOF-5, for instance, that contains four zinc atom clusters [44].
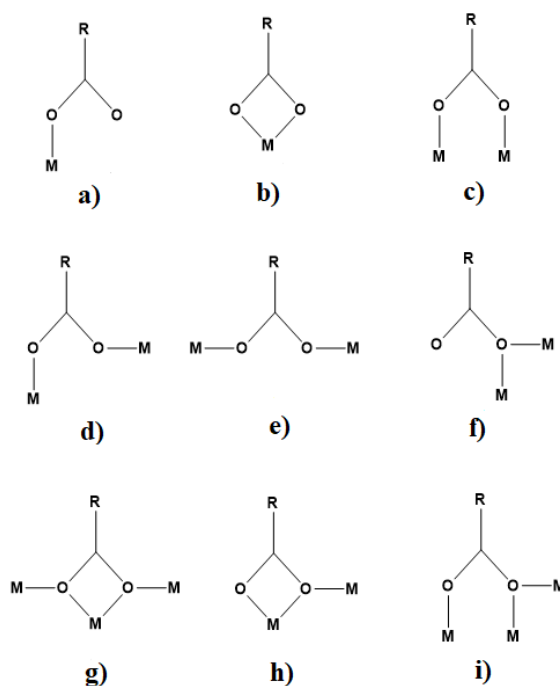
Figure 1.6. Coordination modes of carboxylate; (a) unidentate (b) chelating bidentate (c) *syn-syn* bridging (d) *syn-anti* bridging (e) *anti-anti* bridging (f) $\mu_{1,1}$-bridging (g) unidentate with $\mu_{1,1}$-bridging (h) chelation with $\mu_{1,1}$-bridging (i) chelation with $\mu_{1,2}$-bridging

Vanadium atoms chain in MIL-47 [91] and MIL-68 [92] and clusters of three chromium atoms connecting to the identical μ_3 oxygen atom are present in MIL-100 [93] and MIL-101 [94]. The structure MOF-5 was solved by O. M. Yaghi's research group in 1999; it is the first three-dimensional porous metal-organic framework structure that published in a scientific publication. The compound exhibits stability after removal of solvent molecules and shows permanent reversible nitrogen adsorption capacity at 77 K.

A whole family of related reticular MOF structures has been identified, as previously mentioned, having the primary structure that is comparable to MOF-5, however, by a variety of dissimilar dicarboxylate ligands (namely IRMOF-n series) [59]. It is possible to modify and tune the architecture and characteristics of the frameworks in a predictable way by employing different types of dicarboxylic acid linkers (Figure 1.7). Concurrent with the development of MOF-5, another intriguing porous carboxylate MOF compound, HKUST-1, was synthesized (abbreviated from Hong Kong University of Science and Technology) [95].
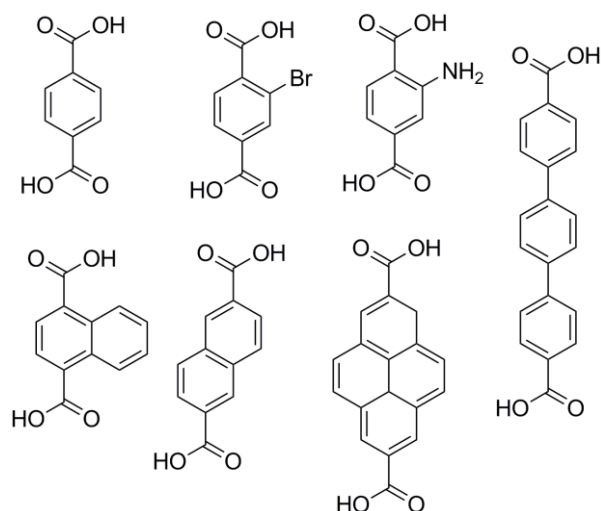
Figure 1.7. Examples of dicarboxylic acid linkers used in the IRMOF-n series of structures [52]

The MOF material was synthesized using copper nitrate salt and 1,3,5-benzenetricarboxylate (tri-mesic acid) linker. The structure comprises of di-nuclear copper units with a short Cu-Cu distance of 2.63 Ǻ. Viewed along the [100] plane, the structure encompasses 1-dimensional square shaped channels (diameter of ca. 10 Ǻ). These 1-dimensional channels are existing in all three crystallographic planes and the intersections create large hexagonal shaped channels (10 Ǻ in diameter). Water that has been physically adsorbed is occupying the channels, whereas water that has been chemically adsorbed is coordinated to the binuclear copper species. Thermal elimination of the metal-coordinated or chemically adsorbed water leaves the copper cations with empty coordination sites. These gaps or empty spaces serve as Lewis acids, promoting gas adsorption and catalysis. Bidentate capping ligands can be used to build

geometries that can be reliably terminated by the paddlewheel-based metal nodes that are frequently included in MOFs.

1.5 Application of MOF

Possible applications of MOF have been broadly covered the area gas storage and separation, heterogeneous catalysis, luminescence and sensing, drug delivery etc. [4-10]. Among this long list of potential applications, some selected and relevant topics will be discussed below.

1.5.1 Gas adsorption and separation studies

Metal–organic frameworks (MOFs) are organic-inorganic hybrid crystalline porous materials assembled by organic bridging linker and metal ions/cluster have been emerging at an accelerating rate due to existence of their high porosity and high pore volume, particularly for the gas adsorption studies. One of the oldest and most widespread uses for MOFs is gas adsorption and separation, for which many outstanding research studies have been published over the previous few decades. Owing to the multi-functionality and constantly growing needs, it makes sense to combine several methodologies in order to better explore the structure-performance link of MOFs. Gas adsorption and separation are one of the best applications which reflect the pores character of the MOF [96]. During this period with growing technology and science, air pollution i.e. harmful gas generated by industry like SO_2, NH_3 and CO is of great concern [97-100]. For this purpose, it is necessary to find an efficient adsorbent to remove this harmful gas and also look for the best materials to store fuel gases like H_2 and CH_4 [101]. In general, precise structural change makes it simpler to satisfy the demands of custom-made products. The function of pores as the primary site offers more opportunity for binding guest molecules. Certain specific strategies are implemented to control the pore environment guest molecules [102]. The binding force between the guest and the frameworks can be increased by adding functional groups to the skeleton or pores [103]. Incorporation of Lewis basic N-site increases the potential interaction between the guest and network and increase the gas storage capacity [104], in addition, a notable strategy is to produce open metal sites (OMS) by removing coordinated solvent molecules under negative pressure [105].

Gas adsorption and separation are also important procedures in industry. Therefore, it is worthy to explore for the materials with high adsorption capacity and separation efficiency.

Various traditional solid materials (e.g., zeolite, molecular sieve, and porous carbon) are available showing remarkable adsorption capacity but less efficient compared to MOF's [106] as it offers functionalized interface, designable structure, and atom-level control. In general, the adsorption and separation performance mainly evaluated by Q_{st} (adsorption capacity). This is a measure of enthalpy changes because of the adsorption process.

First microporous material was reported by Yaghi *et al*. in 1998 named as MOF-2, with formula $Zn(BDC)(H_2O)$ [BDC= 1,4-benzenedicarboxylate], [107]. The porosity of the reported compound was verified by surface area and pore volume measurement. The structure of MOF-2 composed of polynuclear metal cluster, $Zn_2(-COO)_4(H_2O)_2$ paddlewheel like secondary building units. A potential void space was filled with guest molecules, which can be eliminated under vacuum on heating to form the desolvated MOF-2, having formula $Zn(BDC)$. Structural integrity and porosity of the structure are sustained in presence of solvent molecules or guest molecules [108-110]. Gas adsorption studies revealed typical reversible type I gas sorption isotherms, as in zeolites, indicating that MOF-2 is permanently microporous, as demonstrated by nitrogen at 77K (Figure 1.8c) or carbon dioxide adsorption at 195K. However, the Langmuir surface areas for this specific MOF were calculated to be 270 and 310 m^2g^{-1} for N_2 and CO_2, respectively, which was smaller than conventional zeolite molecules. The finding of MOF-2 was a crucial point in progress of 3D structures of MOF materials, creating a plethora of opportunities of combination of SBUs with organic linkers.
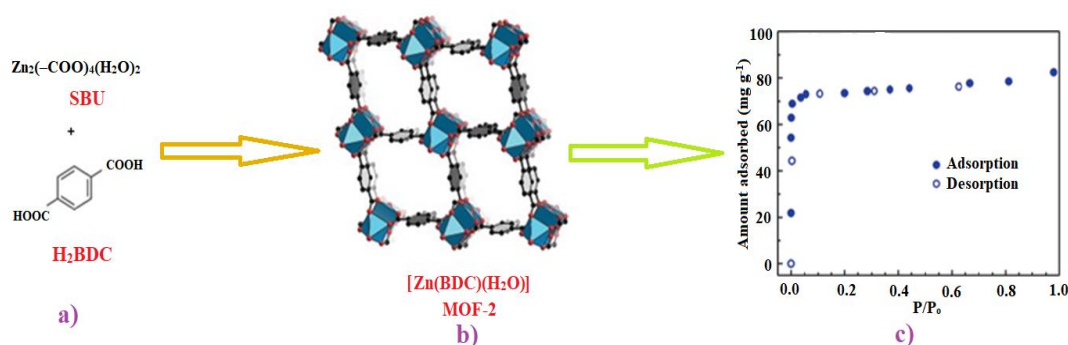
Figure 1.8. a) $Zn_2(-COO)_4(H_2O)_2$ secondary building units (SBUs) are linked through BDC linkers to form MOF-2; b) View of MOF-2 along the crystallographic [001] direction, the rectangular channels are clearly visible (hydrogen atoms are omitted for clarity). Color encryption: black, C atoms; red, O atoms; blue, Zn metal centered polyhedron; c) N_2 sorption isotherm of MOF-2 at 77 K [107]

In 1999, Yaghi *et al*. [44] further reported synthesis of a highly porous material, MOF-5 using octahedral basic zinc acetate building unit $Zn_4O(-COO)_6$ and BDC linkers (Figure 1.9). The name, MOF-5 coined in resemblance of the well-known zeolite -5. Because of the practical strain on frameworks, a primitive cubic (pcu) topology, which consists of single atom vertices connected by edges, exhibits little resistance to mechanical pressures. Conversely, the tetrahedral form of Zn_2O clusters are attached to rigid BDC linkers resulting in a 3D rigid structure having more thermodynamic stability [111, 112]. Excellent rigidity was gained through the activation process, even though mechanical forces leading the framework, which further showing unchanged in morphology up to 400 °C temperature under vacuum. MOF-5 was prepared by solvothermal treatment of zinc nitrate tetrahydrate and H_2BDC in a mixture of chlorobenzene and DMF solvents. The resulting framework contains voids space packed with DMF and chlorobenzene as guest molecules, which can be exchanged with chloroform and that may be eliminated under vacuum at room temperature. The desolvated MOF retained their structural integrity and framework stability.
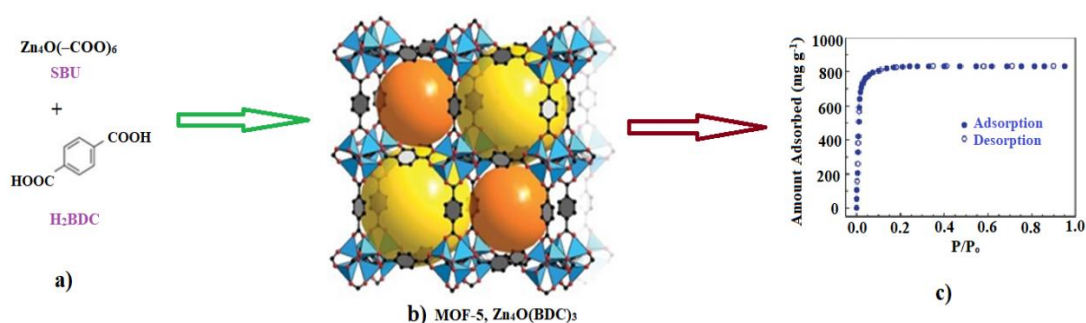
Figure 1.9. a) & b) Single-crystal-X-ray structure of MOF-5 built by $Zn_4O(-COO)_6$ SBUs, linked through BDC linkers (hydrogen atoms are omitted for clarity); Color encryption: black, C atoms; red, O atoms; light blue, Zn metal centered polyhedron; c) N_2 sorption isotherm of MOF-5 at 77 K [44]

Several MOFs are available showing remarkable adsorption capacities but very few of them show selective adsorption properties. Selectivity of MOF towards the adsorption depends on several factors. In several MOF molecular sieving effect is control the selectivity of adsorption. Kim *et al*. reported a manganese-based 3D MOF containing 1D channel, showing

selective H_2 adsorption over N_2 and Ar at 77 K and selectivity towards CO_2 adsorption over CH_4 at 195 K [113].

Zhou *et al.* recently reported an interpenetrated MOF, PCN-17 and has a porous structure made up of big cages connected by comparatively tiny openings [114]. However, it sustains its porosity at temperature as high as 480 °C. Pore (window) size of PCN-17 is reduced to around 3.5 Å, due to interpenetration and sulphate bridging, which causes H_2 and O_2 to be selectively adsorbed over N_2 and CO. As a result, this material may find use in the H_2 enrichment of N_2/H_2 exhaust as well as the separation of N_2, O_2 and H_2 from CO in fuel-cell applications (Figure 1.10).
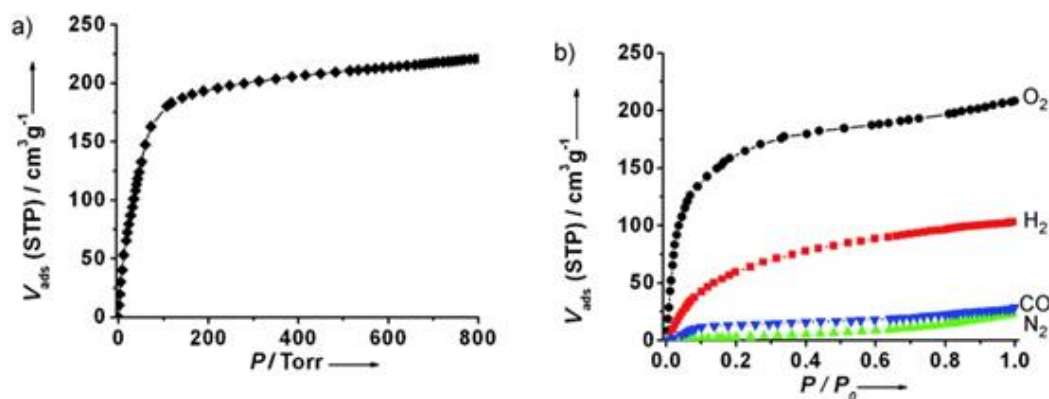
Figure 1.10. Gas-adsorption isotherms of the activated PCN-17; (a) CO_2 at 195 K; (b) H_2, O_2, N_2, and CO at 77 K (for H_2, P/P_0 represents a relative standard, STP standard temperature and pressure [114]

With the rapid rate of development all over world, it is of immense importance to find and create a clean, safe, and environmentally friendly energy source to fulfil the world's energy demand. The issue has become a major concern due to the depletion of oil supplies and the degradation of the natural environment due to use of fossil fuel [115]. Hence, an alter source is on demand, for which hydrogen energy is the one of the alternatives. Following are the reasons

why hydrogen energy seems to have the potential to develop into a future perfect energy source [115, 116]:

(i) The sole product of hydrogen combustion is water, which is clean and pollution-free.

(ii) Hydrogen energy belongs to renewable sources, and it can be regenerated by decomposing water through natural energy such as solar power and wind power.

(iii) Hydrogen energy has a high calorific value as per mass of H_2 (142 MJ/kg), which is equivalent to 3 kg of gasoline or 4.5 kg of coke. A smaller amount of hydrogen fuel is burned to give the same mileage as diesel or gasoline, reducing fossil fuel use.

Consequently, current research priorities are to develop a low-energy, stable, safe, and effective hydrogen storage technology [117].

Koner *et al*. reported a 2D layered alkaline earth metal based MOF compound, $\{[Mg_2(pzdc)_2(H_2O)_4]\cdot H_2O\}_n$ (pzdc = pyrazole-3,5-dicarboxylate). This MOF displayed significantly selective hydrogen (H_2) sorption (ca. 63 cc g^{-1}) over N_2 at 1 atm and 77K (Figure 1.11). Such a favored hydrogen uptake over nitrogen might be ascribed to the smaller inter layer separations which allows only H_2 molecules to enter into the layers, hindering the entry for the N_2 molecules wherein kinetic diameters of H_2 is around 2.89 Å, smaller than the kinetic diameters of N_2 which is 3.64 Å [118].
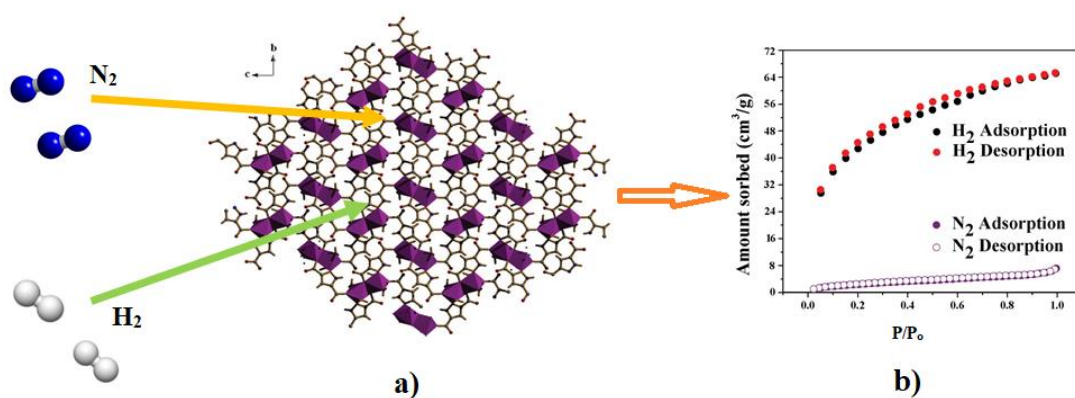
Figure 1.11. a) 2D network of compound $\{[Mg_2(pzdc)_2(H_2O)_4]\cdot H_2O\}_n$ propagated along the *bc* plane; b) H_2 and N_2 sorption isotherm at 77 K [118]

Bu *et al*. have reported a six-fold interpenetrated microporous Cd-based 3D MOF, which consists heterometallic tetranuclear cluster that affords two categories of 1D micro-channel along two opposite directions. Besides, the compound displayed highly selective gas sorption for H_2 in comparison to N_2. To eliminate guest solvent molecules compound was first immersed in pure methanol (CH_3OH) for 3 days, then filtrated and finally activation of methanol-exchanged MOF was undertaken at 120 °C under vacuum overnight. Gas sorption measurements showed that the activated MOF reveals very fascinating selective adsorption of H_2. The activated MOF adsorbed a significant quantity of H_2 (ca. 64 cc g^{-1}) compared to that of N_2 (ca. 15 cc g^{-1}). The MOF adsorped around 4.3 times higher amount of H_2 (64 cm^3/gm) than N_2 (15 cm^3/gm); showing its potential for selective separation of H_2 from a mixture of hydrogen and nitrogen. Such a favorable H_2 uptake over N_2 might be ascribed to effect of pore-size exclusivity; the micropores in activated MOF are conducive for permeation of H_2 but not for N_2. This might be due to their different kinetic diameters of 2.89 Å and 3.64 Å for H_2 and N_2, respectively. The MOF might find potential industrial application in hydrogen separation of the H_2/N_2 from industrial exhaust, for example, in synthesis of ammonia [119].

Colossal emission of anthropogenic carbon dioxide (CO_2) into the atmosphere has become a great environmental concern as it is the primary source of greenhouse gas causing climate change and significant ecological problems leading to global warming [122]. A variety of CO_2 capture systems, one of which is the CO_2 adsorption technique, have been developed to mitigate global warming. Along with trivial CCS methods, using of MOFs have been developing fast as new functional materials for the selective CO_2 adsorption for their vastly adjustable and ordered pore shape and size, greater surface areas with manageable pore surface properties, and high thermal stability [120-122].

Recently, Queen *et al*. reported a novel highly crystalline MOF, Cu-Sp5-EtOH which has a charged framework and it is likely to exhibit high selectivity of CO_2 over N_2. A new linker 1,3-bis(4-carboxyphenyl)-4,5-dihydro-1H-imidazol-3-ium tetrafluoroborate, has been synthesized first to construct a copper-based MOF, Cu-Sp5-EtOH. However, the pores of primary structure could not be opened because of strongly coordinated ethanol molecules. Hence, solvent exchange method was applied to replace EtOH with methanol to convert to Cu-Sp5-MeOH and further heating of solvent exchanged MOF under vacuum makes it easier to remove the solvent. Thereby small gas molecules like CO_2 easily get access into the desolvated

porous structure, Cu-Sp5. The porous MOF displayed exceptionally high selectivity of CO_2 over N_2 owing to the combination of framework charge and open-metal sites. The Ideal Adsorbed Solution Theory (IAST) based calculations were performed on single-component adsorption isotherms. The CO_2/N_2 selectivity of porous material, Cu-Sp5 exhibited a value of over 200 at pressures generally found in post-combustion flue gas (0.15 bar CO_2 / 0.85 bar N_2), showing the highest value reported till date [123].

Another compound [$Zn_2(TDC)_2DABCO$] (TDC = thiophene-2,5-dicarboxylate; DABCO = 1,4-diazabicyclooctane) displayed a significant carbon dioxide (CO_2) adsorption and CO_2/N_2 selectivity compared to the non-thiophene analogue [$Zn_2(BDC)_2DABCO$] (BDC = 1,4-benzenedicarboxylate). The maximum CO_2 uptake of [$Zn_2(TDC)_2DABCO$] is 67.4 cc g^{-1} at 298 K and 153 cc g^{-1} at 273 K and 1 bar pressure, whereas, in [$Zn_2(BDC)_2DABCO$], the corresponding sorption values were 46 cc g^{-1} at 298 K and 122 cc g^{-1} at 273 K, respectively (Figure 1.12). The isosteric heat of adsorption for CO_2 was low (23.65 kJ mol^{-1}), confirming superficial regeneration of the porous substance. Substitution of a phenyl group with thiophene substantially increases CO_2 adsorption as well as the CO_2/N_2 separation selectivity. The selected binding positions of adsorbed CO_2 in [$Zn_2(TDC)_2DABCO$] have been convincingly determined by in situ single crystal X-ray diffraction studies of CO_2-adsorbed [$Zn_2(TDC)_2DABCO$] [124].
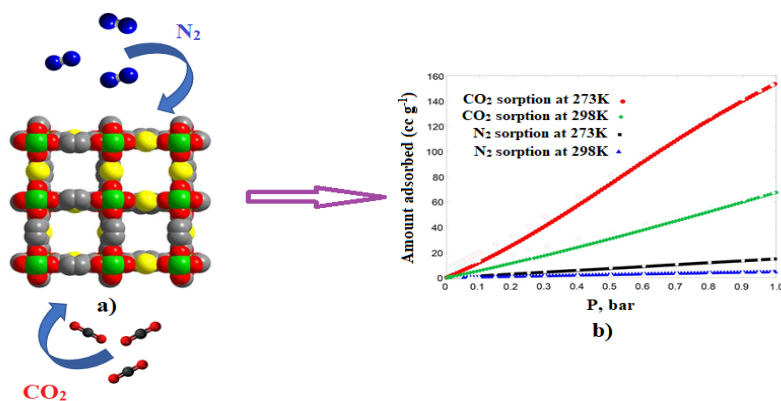
Figure 1.12. a) Van der Waals model of [$Zn_2(TDC)_2DABCO$] along the 4-fold axis; Color encryption: green, Zn metal centers; yellow, S atoms; red, O atoms; blue, N atoms; gray, C atoms (hydrogen atoms are omitted for clarity); b) CO_2 and N_2 sorption isotherms at 273K and 298K [124]

Owing to their low interior surface area, two-dimensional MOFs are believed to be unable to adsorb CO_2. But according to some recent research, 2D MOFs can hold CO_2 molecules [125, 126]. In a previous study of 2D layered MOF, $[Cu(BF_4)_2(bpy)_2]$ (bpy = 4,4′-bipyridine) displayed expansion/shrinkage structural conversion for CO_2 gated adsorption/desorption at 273 K temperature owing to of weak interlayer interactions [126]. Even a flexible 1D MOF $[Cu(BF_4)_2(bpp)_2]$ (bpp = 1,3-bis(4-pyridyl)propane) also showed expansion/ shrinkage structural conversion to adsorb gas molecules [127]. In both the cases there was no noticeable crystallographic void space.

1.5.2. Heterogeneous catalysis by MOF

As regards the numerous facets of application of MOF, organic reactions catalyzed by MOF are receiving increasing attention recently. Majority of MOFs are insoluble in nature, strengthen their applicability in heterogeneous catalysis field. In case of heterogeneous catalysis catalytic support is the critical component to enhance their efficiency [128]. Recent developments in the techniques for synthesizing MOF catalysts with desired structures enable us to precisely understand how the MOF supports facilitate catalytic efficacy. There are a significant number of well-designed MOF catalysts which by utilizing these support effects, outperform conventional catalysts, particularly in reactions occurring in relatively low temperature range (<300 °C). MOFs have been recently played a significant role as heterogeneous catalysts in Friedel-Crafts reactions [129-133], aldol condensation [134-136], Knoevenagel condensation [137-141], oxidation [142-145], cyanosilylation [146-148], various coupling reactions [149-156], carbon dioxide fixation [157,158] etc. However, catalytic applications of MOFs are limited due to their moisture sensitivity and stability.

1.5.2.1. MOF catalyzed condensation reaction

Koner *et al*. reported hydrothermal synthesis of a novel 3D alkaline-earth metal-based MOF compound, $[Ba(pdc)]_n$ (pdc = pyridine-2,5-dicarboxylate), catalyzes proficiently aldol condensation reactions of several aromatic aldehydes in presence of cyclohexanone and acetone in THF/triethylamine medium. $[Ba(pdc)]_n$ furnished notable yields (approx. 96%) under eco-friendly heterogeneous condition with 100% selectivity in a very short reaction time of 6 h. The catalyst was recycled up to five successive runs without noteworthy loss of catalytic activity [134]. The temperature of the catalytic reaction medium was maintained in the range 5-10 °C.

On increasing reaction temperature, condensation reaction occurred and benzylideneketone was formed from the β-aldol. The best result obtained in presence of THF (Tetrahydrofuran) medium. The decreasing order of efficiency of the catalyst followed by THF > THF-water > solvent-less medium. The catalytic reaction was not carried out in absence of triethylamine base. Further, the decreasing order of yield of the β-aldol followed by p- > o- > m-nitrobenzaldehyde.

Another example of MOF that catalyzed aldol condensation reaction in presence of toluene and small amount of concentrated H_2SO_4 under mild conditions to afford pyramidine-chalcones is $Cu_3(BTC)_2$ (BTC = benzene-1,3,5-tricarboxylate) as reported by Pathan *et al.* The catalyst exhibits a maximum isolated yield of 78%. The study also proved that absence of catalyst trace amount of conversion indicating the role of H_2SO_4 is just regulate the Lewis acidity of $Cu_3(BTC)_2$. Structural integrity of the catalyst is monitored by PXRD analysis [159].

One pot tandem synthesis is a very important catalytic process of organic synthesis due to its high efficiency, reduced production of waste that enables the quick conversion of more complex molecules from simple one and again with reduced of consumption energy. Multifunctional MOFs, in this field, are the promising candidates. Ramella *et al.* reported a Cu-based MOF named as Cu_3TATAT (H_6TATAT 5,5′,5″-(1,3,5-triazine-2,4,6 triyl)tris(azanediyl)triisophthalate) with free amine functionality [160]. It catalyzes one pot tandem reaction of alcohol oxidation followed by Knoevenagel condensation reaction efficiently without requirement of any added base. The benzylidenemalononitrile product was produced in high yield and selectivity from an inexpensive benzyl alcohol starting material under an oxygen atmosphere (Scheme 1.2). The role of the basic functionality was studied to demonstrate its role in the aerobic oxidation and Knoevenagel condensation reactions. Finally, the results demonstrated that recycled catalyst can be used more than five cycles while the yield was not considerably harmed.
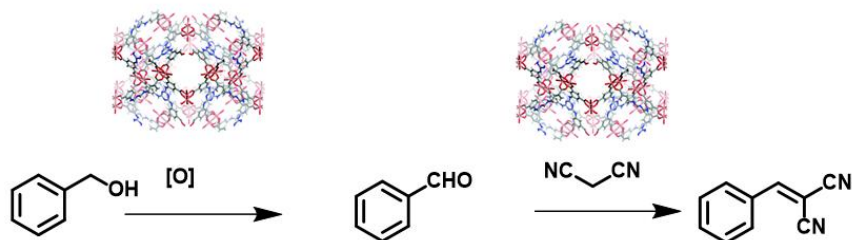
Scheme 1.2. One-pot reaction of oxidation-Knoevenagel condensation [160]

Likewise, PCN-124 displayed an exceptional catalytic efficacy in a tandem one-pot deacetalization-Knoevenagel condensation reaction as a supportive catalyst [161]. The catalytic reaction was performed with 0.5 mol% of PCN-124 as catalyst using 2 mmol substrate in DMSO-d_6 (d_6-Dimethyl sulphoxide) for 12 h. In this reaction, benzaldehyde dimethyl acetal was formed with ~100% conversion towards the formation of benzaldehyde which further reacted with malonitrile leading to formation of benzylidenemalononitrile with very high yield, ~100% in a tandem one-pot reaction (Scheme 1.3). The catalyst was used for four times and PXRD pattern of used catalyst did not demonstrate any structural change that proved the stability of MOF.
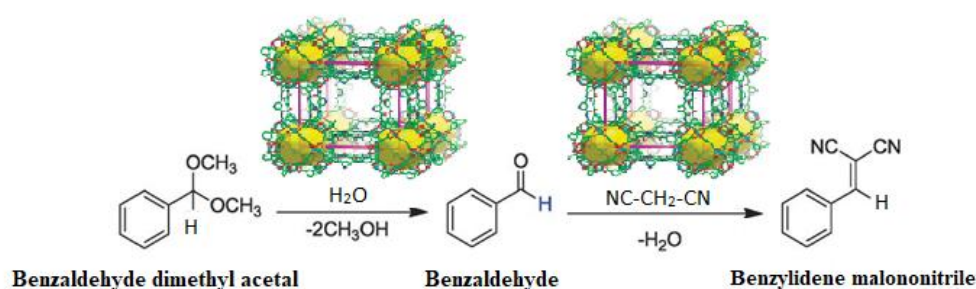
Scheme 1.3. One-pot reaction of deacetalization-Knoevenagel condensation [161]

1.5.2.2. MOF catalyzed oxidation reaction

Selective oxidation of organic molecules that produces value-added compounds by simple, easy, and sustainable processes using effective homogeneous and heterogeneous catalyst is of significant scientific interest which attracts ever-increasing attention. In liquid-phase oxidations, generally a soluble metal salt or complex is employed in combination with oxidants such as O_2 (or air), H_2O_2, or organic hydroperoxides (RO_2H). Mechanistic study of catalytic oxidation is suggested the oxidation activity is not only dependent on the active metal centres but is also closely related to the type of oxidants. It has been reported that MOFs perform well in molecular oxygen activation, and the reactions follow the free-radical-chain auto-oxidation mechanism [162].

Selective oxidation of unsaturated C=C in alkenes is an important organic transformation of industrial importance. In an early research work, N-hydroxyphthalimide (NHPI), usually used as an initiator to withdraw hydrogen from hydrocarbons, was incorporated into Fe(BTC) (1,3,5-benzenetricarboxylate [BTC]) to oxidize styrene into benzaldehyde, styrene oxide, and its derivatives under various reaction conditions. But due to relatively good stability of the olefin double bond, strong oxidants, such as tert-butyl hydroperoxide (TBHP) or H_2O_2, are generally utilized in the oxidation reaction of olefins [163].

Spodin *et al.* reported a novel metal-organic framework $\{[Cu_3Lu_2(ODA)_6(H_2O)_6]\cdot10H_2O\}_n$ (H_2ODA = 2,2'-oxydiacetic acid) which can effectively catalyzes oxidation of alkenes and benzylic hydrocarbons, using tert-butyl hydroperoxide (TBHP) as well as molecular oxygen (O_2) (Figure 1.13). Excellent conversions for cyclohexene (95%) and for cumene (91%) were obtained with O_2 under solvent-free condition in the absence of a co-catalyst [164].
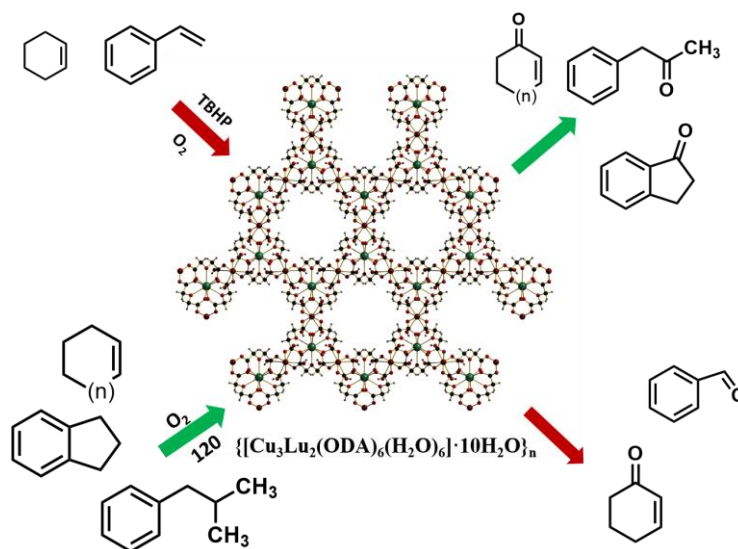
Figure 1.13. Schematic representation of Catalytic activity of
{[Cu₃Lu₂(ODA)₆(H₂O)₆]·10H₂O}ₙ towards olefin oxidation [164]

Jiang *et al*. reported a three-dimensional Cu-based MOF, [Cu(TCBPA)(DMA)] (TCBPA = tris(4′-carboxybiphenyl)amine; DMA = dimethylacetamide) showing catalytic activity in olefin epoxidation reactions [165a]. [Cu(TCBPA)(DMA)] was synthesized by a reaction between TCBPA and Cu(NO₃)₂·3H₂O under solvothermal condition. A DMA and H₂O mixture in 3:1 (v/v) ratio was used as solvent along with 15 drops of 3 M HCl solution. The crystal structure revealed the 3D framework of compound contains one dimensional channel (9.4 × 9.8 $Å^2$). After the removal of coordinated DMA and guest molecules (H₂O), 1D channels along to crystallographic *c*-axis clearly observed. Desolvated MOF was used in heterogeneous catalytic epoxidation reactions of olefins using TBHP which acts as an oxidant and the reaction carried out at 60 ℃ for 24 h (Figure 1.14). The observed results showed very high yield of epoxide products. Oxidation of cyclooctene and cis-stilbene, afforded 98% and 94% conversion, while epoxide yields are 91% and 82%, respectively. Notably, the reaction displayed excellent selectivity among non-terminal olefins.
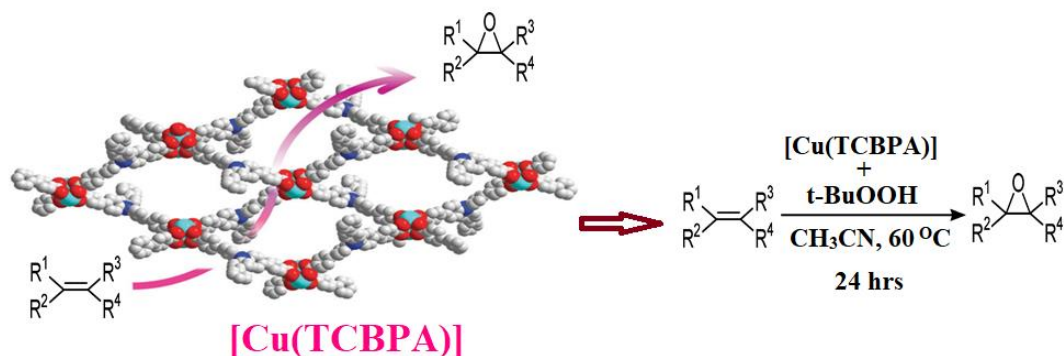
Figure 1.14. Space-filling view of compound [Cu(TCBPA)] (Cu atoms in turquoise) and its catalytic activity in olefins epoxidation reaction [165a]

Example of Cu(I)-based MOF, ({[Cu$_2$Br$_2$(pypz)]$_n$·nH$_2$O} (Cu-Br-MOF) [pypz = bis[3,5-dimethyl-4-(4′-pyridyl)pyrazol-1-yl] methane] has been investigated by Konar *et al*. [165b]. The structural analysis revealed pypz ligand which acts as a tritopic ligand linked through two Cu$_2$Br$_2$ dimeric units, establishing a 1D zig-zag chain, and those 1D chains further linked by a Cu$_2$Br$_2$ unit, finally formed a 2D structural framework parallel to the crystallographic *bc*-plane. The copper ions are four coordinated in a Cu$_2$Br$_2$ dimeric unit and having a tetrahedral geometry which demonstrated as an excellent heterogeneous catalyst for both aerobic homocoupling reactions and epoxidation of olefins (Figure 1.15). The aerobic homocoupling reaction requires only 3 mol% of catalyst and it did not involve any base or oxidant associated to other orthodox catalysts like Cu, Pd, Fe, and Au etc. for the conversion of arylboronic acids. The investigation of shape and size selectivity of the Cu(I)-based MOF catalyst in the homocoupling reaction has been also performed.
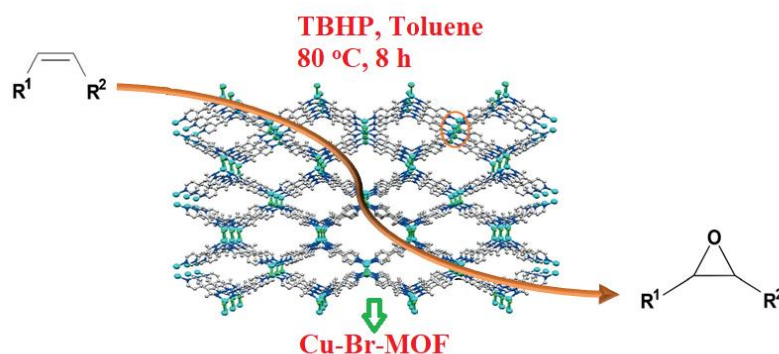
Figure 1.15. 2D framework of Cu-Br-MOF with rhomboid-shaped channels along the *a*-axis (Cu atoms in cyan) and olefins epoxidation catalyzed by Cu-Br-MOF [165b]

Han *et al*. recently reported a series of $PdCl_2$ moiety-decorated Y_6-MOFs adopting post-synthetic strategy were fabricated as applicable single-site catalysts for oxidation of styrene (Figure 1.16). Specifically, the functional organic linker, H_2bpydc (2,2′-bipyridine-5,5′-dicarboxylic acid), was first incorporated quantitatively into Y_6 clusters-based MOF, $[(CH_3)_2NH_2]_2[Y_6(\mu_3\text{-}OH)_8(bpdc)_6]$ (bpdc = 4,4′-biphenyl dicarboxylic acid) via post-synthetic ligand exchange [166]. The obtained Pd(II)-Y(bpydc)$_x$/(bpdc)$_{1-x}$ behave as highly efficient heterogeneous single-site catalysts for selective oxidative cleavage of styrene to benzaldehyde using O_2 as a oxidant under solvent-free and mild reaction conditions (1 atm and 80 °C). The selectivity of the oxidation reaction for benzaldehyde product can be altered by varying metal ligand ratio. High conversion of styrene and the selectivity for benzaldehyde can reach 88.7 % and 82.2 %, respectively using 0.024 mmol Pd(II) catalyst.
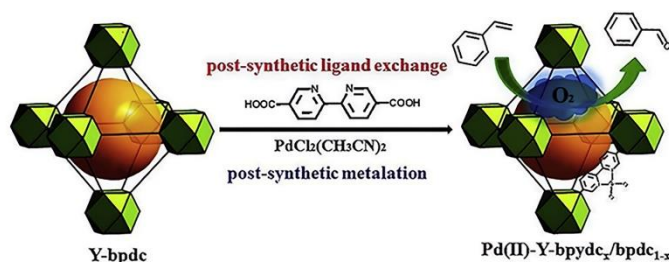
Figure. 1.16. Functional hexanuclear Y^{III}-cluster-based MOFs supported Pd(II) single-site catalysts for aerobic selective oxidation of styrene [166]

MOF based catalyst are also promising candidate for alcohol oxidations. This particular reaction is important for industrial application in pharmaceutical industry, agrochemical industry, specialty and fine chemical industry etc. Alcohols may be oxidized using a variety of ways, each with its own set of benefits depending on the target result and reaction circumstances. Metal-based reagents, organic peroxides, and molecular oxygen are all common oxidizing agents. Transition metal catalysts are widely used for alcohol oxidation due to easy accessibility, less hazardous nature, low cost and good catalytic efficacy. There are few examples available in the literature that showed Cu(II)/ TEMPO (TEMPO: 2,2,6,6-tetramethylpiperidine-N-oxyl) systems are catalytically active towards aerobic oxidation of primary alcohols in presence of base [167, 168].

In this context, Cu(II) based MOF named as Cu$_3$(BTC)$_2$ (BTC: 1,3,5-benzenetricarboxylate) reported by Garcia *et al*. is a good example [169]. It shows good oxidising activity towards benzyl alcohol oxidation to the corresponding benzaldehyde under low temperature and atmospheric pressure combined with TEMPO as a co catalyst. Due to the over oxidation the corresponding carboxylic acid is formed, which is the major deactivating agent for catalyst and it blocks the free active sites of Cu(II) centre. The highest yield of benzaldehyde (91%) is obtain combined with 2 equivalent TEMPO with catalyst (Scheme 1.4).
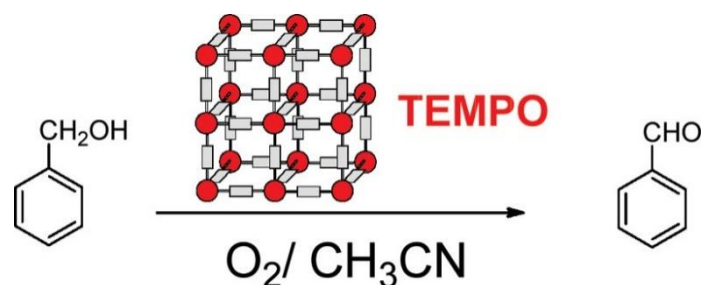
Scheme. 1.4. Aerobic oxidation of alcohols catalyzed by Cu₃(BTC)₂ (BTC: 1,3,5-benzenetricarboxylate) [169]

1.5.3. MOF for photoluminescence and sensing

MOFs that contains luminescent moiety are of importance in application of photoluminescence and sensing purpose. The optical characteristics of MOFs may be modified by adjusting the interactions between the various components from which they are built. MOFs are made of adaptable building blocks the fluorescence inside them can be originated from metal centres, ligands or the resulted moieties which constitute the compound [170]. In addition to the fluorescence produced by the MOFs sub-unit, certain photo-responsive elements can be added to MOFs to produce fluorescence to accomplish a range of functional uses [171]. The development of innovative dual emission for ratiometric sensors may be achieved by the mutual interaction and tuning of luminescence of the multiple fluorescent centers [172]. With the addition of several fluorescent units, luminescent MOF (LMOF) which provide quicker reaction times, can be used in a wide range of anticipated applications in the food sector with increased sensitivity, improved interference immunity, and the potential for remote monitoring. Compared with traditional sensing technologies, these materials afforded unique opportunities for metal ion sensing, detection of nitro explosive etc. By definition, luminescence is spontaneous emission of light (electromagnetic waves) by a substance not resulting from heat. In addition, it can be classified into two different classes typically, *viz.* fluorescence and phosphorescence. Different types of phenomena have been envisioned to perform vital role as the source of luminescence in LMOFs (Scheme 1.5) that encompass metal-based emission, ligand-based emission, emission owing to excimer or exciplex formation and guest attracted emission etc.

These processes exhibit most crucial roles and significant contributions to the emission property of LMOFs.

Organic linkers are usually the source of fluorescence in emissive MOFs. Ligand-centred luminescence is usually found in d^{10} metal such as Zn^{2+} and Cd^{2+} ions containing MOFs, since these ions having difficulty to undergo oxidation or reduction reactions because of their core structure of d-orbitals [173]. In MOF chemistry, organic linkers with prolonged electron conjugation have typically been used extensively for the development of chemical sensors. As a consequence of their emissive capabilities, the electronic transitions within the extended π-conjugated system may be predicted to yield the photo-fluorescence features. In fact, organic linkers serve as both the framework's skeletons and the main source of emissive characteristics of the systems.

For example, Wang *et al.* created two fluorescent MOFs, BUT-14 and BUT-15 [174], both are made of π-conjugated organic carboxylate ligands with Lewis basic sites. In this case the designed π-conjugated organic ligands provide efficient fluorescence, Lewis basic sites act as functional sites interact with metal ions, and the strong coordination bonds between the metal nodes and linkers endow high stability of the resulting MOFs. It was observed that, the resultant BUT-14 and BUT-15 showed similar emissions with the same excitations of corresponding acid ligands, indicating the fluorescence is mainly originated from the careful designing of π-conjugated organic ligands. Intense fluorescence of these LMOFs in aqueous medium endows the system an excellent selective detection ability towards Fe^{3+} in a water medium which can be achieved in terms of distinct fluorescent quenching mechanism. Besides, ligand-based luminescence, charge transfer methods [inter-ligand charge transfer (ILCT), metal-ligand charge transfer (MLCT), ligand-metal charge transfer (LMCT) etc.] relating aromatic organic linkers have also been reported and these types of luminescence in LMOFs have enormous potential to design sensory materials [175-177].

Lanthanide metals are major contributor in case of metal node-based luminescence property. Due to the Laporte forbidden f-f transitions in these types of lanthanides, weak emission profiles have been observed because of inefficient absorption. On complex formation with organic linkers, those organic molecules act as light absorber and consequently enhance emission intensity. This effect is known as "sensitization" or "antenna effect" [175-177].
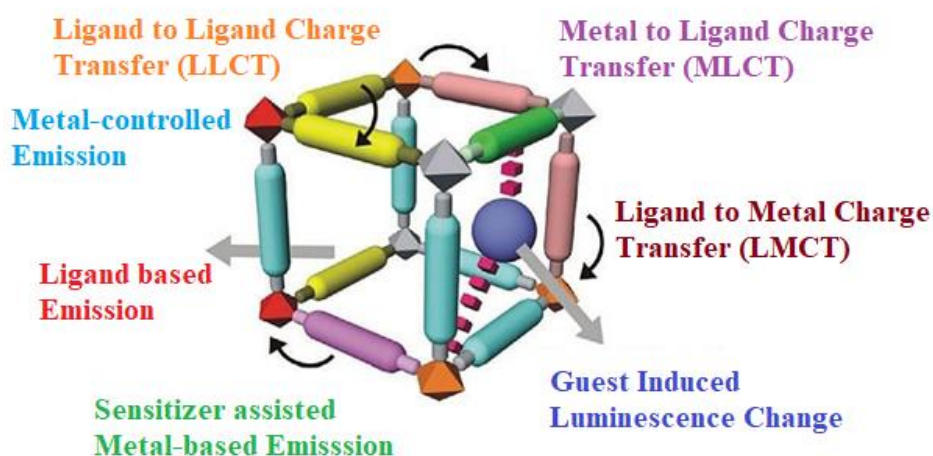
Scheme 1.5. Schematic representation of various types of processes in luminescent MOFs [176]

There are two basic types of luminescence, fluorescence and phosphorescence, which is shown by Jablonski diagram in Figure 1.17. Generally, fluorescence is fast process with nanosecond time period and phosphorescence is slow process with longer time period which may possibly last from microseconds to minutes or even hours. Luminescence in MOFs happens when electrons in the excited singlet state (S_1) come back to the ground state (S_0) by emission of photon. This luminescence property can either be quenched or intensified upon analyte absorption and is termed as "turn-off" or "turn-on" mechanism respectively. A large number of studies have compared for ligand-based fluorescence in variety of solvent medium. For instances a zinc based MOF, namely $[Zn_2(btca)(DMSO)_2]_n$ (H_4btca= 1,2,4,5-benzene terta carboxylic acid) has been synthesized solovothermally. The reported compound shows a solvent dependent fluorescence response with different intensity and emission maxima (Figure 1.18b). The compound exhibited emission maxima at 432 nm (λ_{em}), up on excitation at 300 nm in aqueous medium [178]. While the emission maxima (λ_{em}) is found to be different with varying solvent polarity. Maximum emission intensity is observed for H_2O (Figure 1.18a).
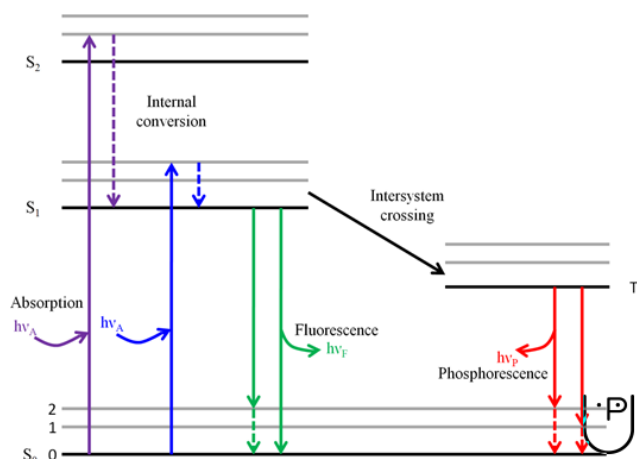
Figure 1.17. Brief representation of Jablonsky diagram
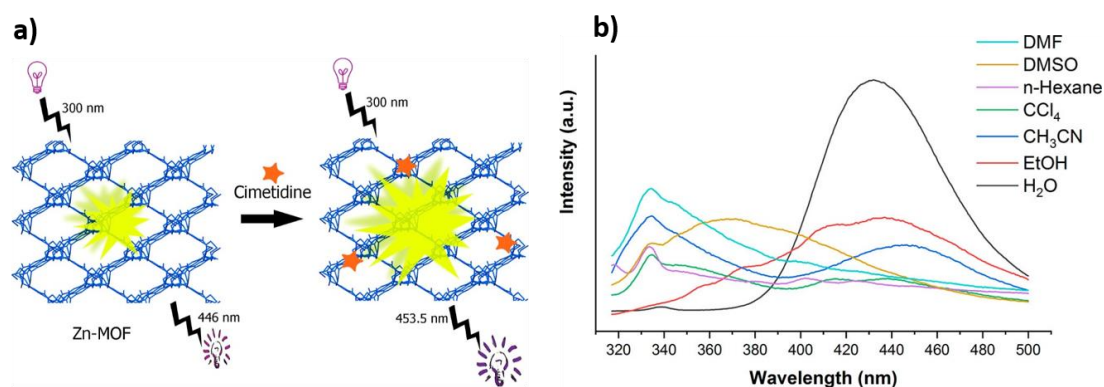
Figure 1.18. **(a) Schematic representation of fluorescence response of $[Zn_2(btca)(DMSO)_2]_n$** **(b) Comparison of fluorescence spectra of $[Zn_2(btca)(DMSO)_2]_n$ dispersed in various solvent media (λ_{ex}= 300 nm)[178]**

It is clear that MOF can detect the target analyte either by a fluorescence ''turn-on'' or ''turn-off'' process. In the ''turn-on'' method, a luminescence enhancement occurs in the MOF, whereas in the case of a ''turn-off'' event, the fluorescence intensity of the MOF declines. Remarkably, the former is superior for real-time sensing application. It is notable that MOFs based sensors are mostly works through "turn-off" phenomenon [179]. Additionally, the ''turn-off'' event can be caused by interfering analytes instead of the target analyte, which often leads to the wrong prediction and is the main obstacle for real-time application. The "turn-on"

procedure is highly desired in biological systems given that a dark background is necessary for luminescence increment. In the case of luminescence enhancement, the illumination occurs against a dark background and is easier to monitor than the quenching. Hence, it can be realized that "turn on" sensors have advantages over the "turn-off" sensors. Furthermore, "turn-on" sensing in biological systems is more desirable where enhancement of emission is easy to display in contrast to quenching [180]. MOFs have attracted enormous attention in past few years as "turn-on" probe towards sensing applications.

Zhao *et al*. synthesized a two-dimensional MOF based on the tetraphenylethene (TPE) core ligand, 4,4′-(2,2-diphenylethene-1,1-diyl)dibenzoicacid and Zn^{2+} metal ion (namely, NUS-1a, abbreviated from National University of Singapore) [181]. The porous MOF displayed a predictable aggregation-induced emission (AIE) features due to presence of rigid angular linkers in the structural network. The quantum yield of the parent material has been enhanced significantly upon treatment of various VOCs such as benzene, toluene, xylenes and mesitylene. The parent crystals when soaked with benzene exhibited the major red shift, however, in mesitylene it displayed blue shift. Further, the shift of peak in the photoluminescence spectra was consistent with turn-on response (Figure 1.16). This was attributed to the conformational variations initiated due to the interaction of the analytes with the phenyl rings of the MOF.

MOFs and their composites have demonstrated superior performance as fluorescence "turn-on" probes for the identification of various contaminants, as was previously noted. The high vapour pressure of volatile organic molecules, which include organic solvent molecules, poses a serious risk to human health [180]. There for detection of this molecule is also very important. In this regard, Zhang *et al*. performed an excellent study on the multi-colored ''turn-on'' detection of a variety of VOCs using a silver-chalcogenolate cluster-based MOF, Ag_{12}bpy [182]. Ag_{12}bpy showed a ''turn-off'' luminescence response in the presence of molecular oxygen, which was intercalated inside the pores of the MOF. Interestingly, in the presence of VOCs, a ''turn-on'' luminescence response was observed. The reason behind the ultra-fast ''turn-on'' luminescence response is the easy ingression of the VOCs in the microporous pores of the framework, while maintaining their structural integrity and also the high dipole moment of the reported metal-organic framework compound which maximized the host–guest interaction.
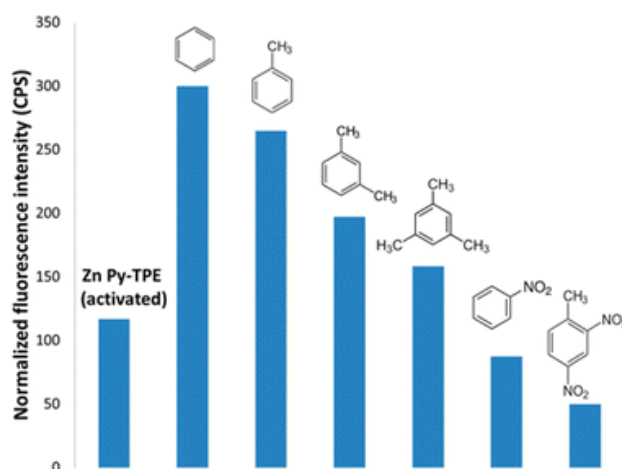
Figure 1.19. Emission intensity of Zn_2Cl_4Py-TPE in the presence of a variety of aromatic VOCs [183]

Lantham *et al*. showed the detection of electron rich aromatic VOCs through a ''turn-on'' process using a zinc-based MOF, $(Zn_2Cl_4Py$-TPE$)_4$-TCE) [183]. The molecule shows aggregation induced fluorescence (AIE) in the solid state due to blockage of the motion of the central phenyl ring of TPE unit which stops the intramolecular rotation and inhibit non radiative decay of the excited state occurs [184]. Based on this concept, luminescence property of the synthesized zinc MOF is explained. However, its fluorescence emission intensity was further enhanced in the presence of aromatic VOCs (Figure 1.19) together with the red shifting of its emission peak. The shifting in the emission peak and the ''turn-on'' luminescence response illustrate that the analytes gradually locked the rotation/vibration of the central phenyl ring, which led to an increase in the fluorescence intensity.

Tian *et al*. revealed solvothermal reaction of Cd^{2+} cations with a silicon-centered carboxylate linker (msitpa = $5,5',5''$-(methylsilanetriyl)triisophthalic acid) produced a novel metal-organic framework, $[Cd_3(msitpa)_4(H_2O)_5]\cdot DMA\cdot H_2O$ [185]. It is constructed by three $\{CdO_6\}$ clusters and organosilicone linkers to form a three-dimensional porous network. The MOF of steric organosilicone ligand is rare in the literature. Incidentally, it has displayed spontaneous formations of microtubular crystals, which is rarely reported previously. Additionally, the luminescence behavior of this MOF inspected in several organic solvents in disperse medium, exhibiting turn-on and turn-off luminescence responses for *n*-butanol and

acetone, respectively (Figure 1.20). Such solvent-mediated luminescence behaviors are of importance for the sensing of n-butanol and acetone solvent molecules. The interaction between open metal sites and guest solvent molecules played a major role in fluorescent sensing. In case of turn-on fluorescence effect, it is proposed that there is a weak interaction between hydroxyl and luminescent open metal sites of the activated MOF [185]. The pore captivity of the analyte in the molecular-sized channels of activated compound may enable the MOF to have strong interaction between n-butanol and host framework.
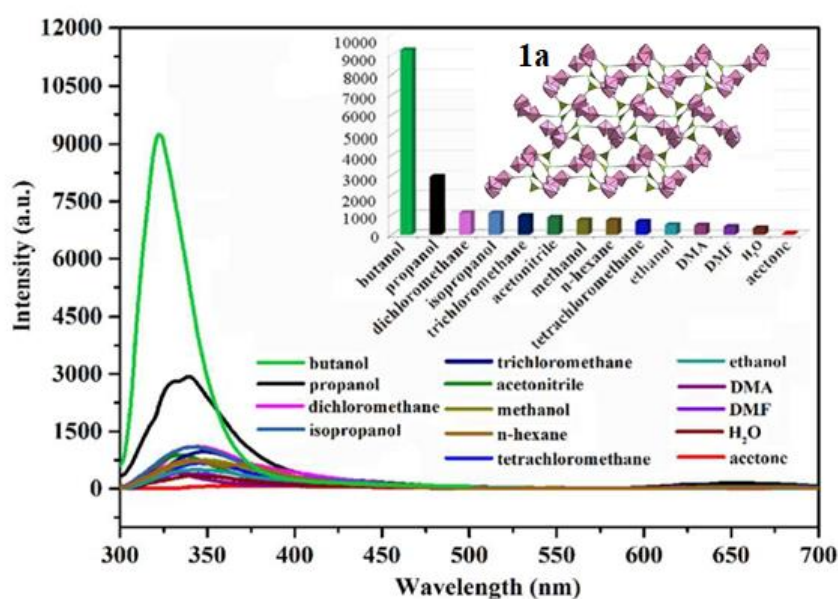
Figure 1.20. Luminescence spectra of activated MOF and the intensities (inset) including structure of activated MOF after interaction with various pure solvents (λ_{ex}= 280 nm) [185]

Of late, very selective and extremely sensitive luminescent MOFs have been created to identify a number of cationic species with high sensitivity. In real field studies, the MOFs can detect ions at significantly lower concentrations than the optimum concentration fixed by EPA and WHO, and in certain situations, the detection limit is quite low. The efficient host-guest interaction is the main reason behind the highly sensitive detection. Thus, it is possible to

control the selectivity and sensitivity by adding several functional moieties [186]. Guo *et al*. synthesized a cadmium-based highly stable MOF, $[Cd(3-NH_2-pba)_2]_4 \cdot 8DMF$, under solvothermal conditions for the selective and sensitive ''turn-on'' detection of silver metal ions [187]. The crystallographic investigation revealed that the framework is decorated with basic amine functional moieties. The emission spectrum of the MOF revealed the maximum emission at 470 nm (blue emission) upon excitation at 322 nm. This emission is due to the $\pi-\pi^*$ transition in the organic ligand (Figure 1.21). The luminescence intensity of the MOF was quenched in water, thus it acted as a water sensor in ethanol solvent. Interestingly, when this MOF was treated with several metal ions in water medium, its emission intensity at 479 nm considerably increased (almost 50 times) in the presence of silver metal ions. The interaction between the amino group and Ag^+ ion was confirmed by IR and XPS analysis.
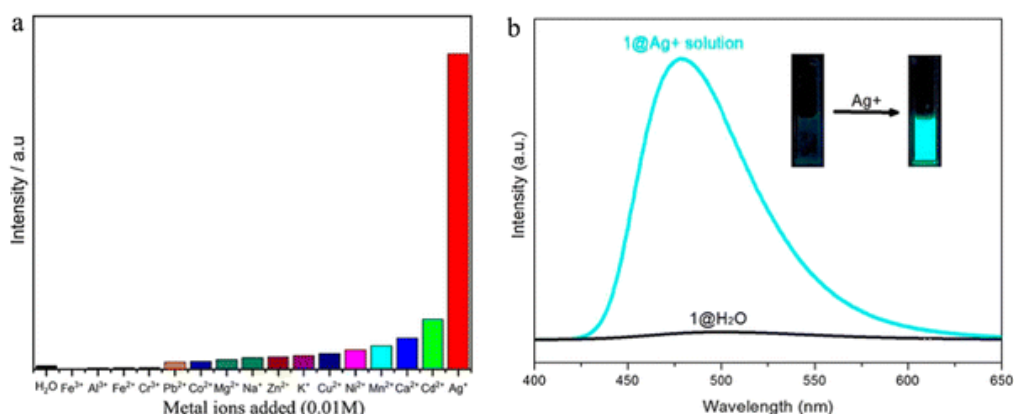
**Figure 1.21. (a) Fluorescence intensity of MOF in the presence of different metal ions in aqueous medium and (b) significant enhancement in the luminescent intensity of the MOF in the presence of silver metal ions (inset: colorimetric response of the MOF with silver ions) [187].**

Fe^{3+} ion is a very important element in living organisms, [188] but its excess leads to harmful health effects such cardiac arrest and Alzheimer's disease [189]. Hence, the detection and on-site monitoring of Fe^{3+}ions are critical. Zhang *et al*. used an AIE-active ligand (mdpy= 4,4′-((9H-fluoren-9-ylidene)-methylene)dipyridine) for the construction of a stable cadmium-based luminescent MOF, $[Cd(NDA)(mdpy)(H_2O)_2]_n$, (H_2NDA= 1,4-napthalenedicarboxylic acid) for the discriminating sensitive recognition of Fe^{3+} ions in water medium through the

fluorescence ''turn-on'' process [190]. The emission peak of the MOF appeared at 440 nm upon excitation at 324 nm. When the MOF was tested with a large number of metal ions (Figure 1.22), its emission intensity was considerably enhanced only in the presence of Fe^{3+} ions showing an LOD (LOD= Limit of detection) of 2.06×10^{-3} mM.
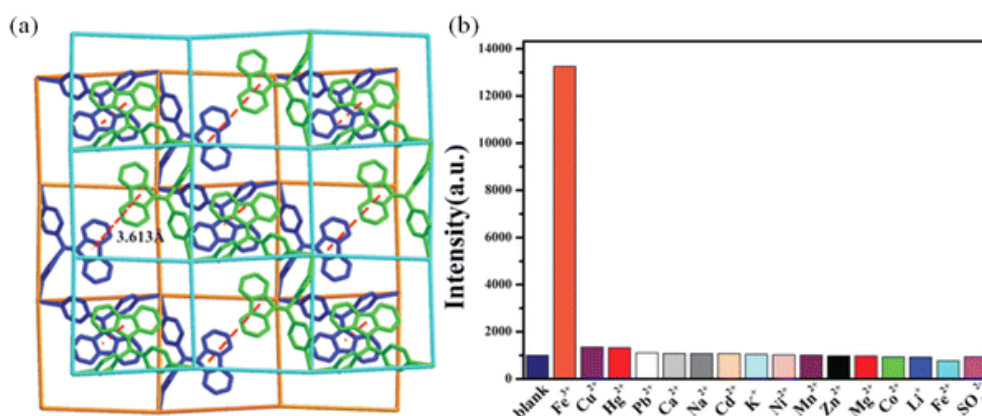
Figure 1.22. (a) Network of MOF showing $\pi \cdots \pi$ interaction between the parallel fluorene moiety and (b) selective turn-on detection of Fe^{3+} ions in aqueous medium [190]

Amongst different pollutants, nitroaromatics are one of the major hazardous pollutants due to their highly explosive nature [191] and they are poisonous to human health and aquatic life [192]. Nitrobenzene is most commonly used nitro explosive. Therefore, detection of nitro aromatics is of immense importance. Fu *et. al* synthesized a novel cadmium based 2D metal organic frame work, [Cd(1,4-ndc)(DMA)] (1,4-H_2ndc = 1,4-naphthalenedicarboxylic, DMA = N,N´dimethylacetamide) solvothermally [193]. The compound shows good sensing capacity towards nitro explosives with the limit of detection (LOD) 0.1 μM. The compound exhibits an emission peak 386 nm upon excitation at 330 nm (λ_{ex} = 330nm), which is comparable with the emission of 1,4-H_2ndc at 382 nm for π^*–n or π^*–π transition. In aqueous phase the compound shows different quenching efficiency compared with blank sample when treated with different explosives like 2-nitro-m-xylene (NX), 2-nitrophenol (2-NP), 2-nitrotoluene (2-NT), dinitrotoluene (DNT), (NB) and 2,4,6-trinitrophenol (TNP) and nitrobenzene. Among all the nitro explosives TNP has the highest quenching efficiency with a red shift of ~76 nm (Figure 1.23).
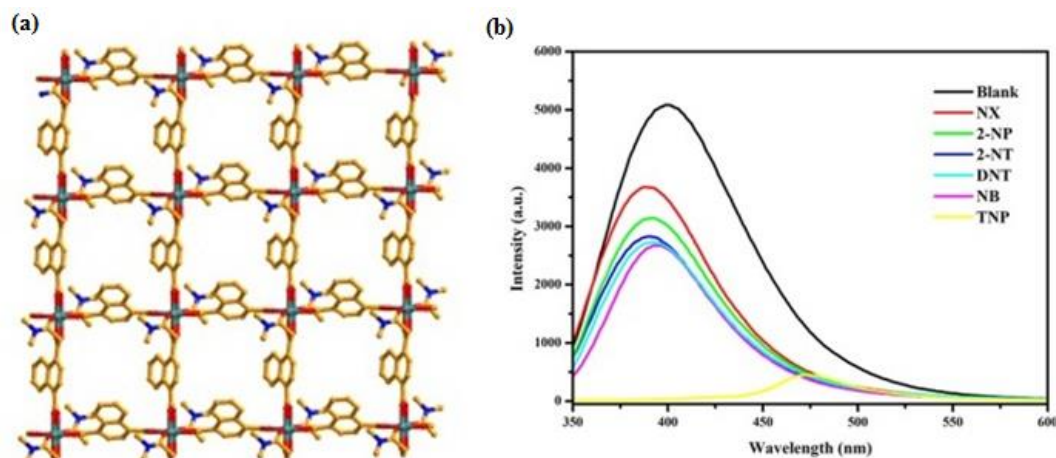
Figure 1.23. (a) 2D network of Cd-MOF; (b) The luminescent emission spectra of Cd-MOF with diverse nitro explosives in aqueous solution (λ_{ex} = 330 nm) [192].

1.6. Scope and objective of the present thesis

The properties of metal-organic frameworks demonstrate that they have potentiality in a large number of applications in fundamental and industrial perspective such as gas storage and separations, luminescence sensing and liquid phase heterogeneous catalysis etc. Due to the chemical versatility of MOFs, it is possible to design infinite number of structures by altering the building blocks and by using the perception of iso-reticularity. If all of these properties entirely used, the approach for the preparation of the active sites might be developed through adjustable fine-structure. Also, from literature survey, it is found that MOFs can be used as promising materials to perform efficient gas storage and separations, luminescent behaviors as well as potential catalysts in various organic reaction transformations, especially in epoxidation reaction. In this investigation effort was made to synthesis such microporous mixed-linker based MOFs for the study of gas sorption, especially selective CO_2 sorption also has been successfully shown in some cases. In addition, studies related to luminescence and heterogenous catalysis also undertaken using newly prepared MOFs. To complete the study following objectives were undertaken:

► To synthesize porous MOFs by direct hydrothermal or solvothermal and layer diffusion synthesis method and characterize them by different physico-chemical methods such as single-crystal X-ray diffraction, powder X-ray diffraction, FT-IR, elemental analysis (C, H, N), UV-Vis spectral analysis, TGA (Thermogravimetric analysis) etc.

► To perform gas sorption studies using activated MOFs (after elimination of guest solvent molecules); especially selective CO_2 trapping and theoretical interpretations of its behavior also attempted in this study. The separation of CO_2 from mixture of gases containing methane (CH_4) is very vital for the advancement and the treatment of biogas to improve purity of fuel.

► To examine photoluminescence behavior of MOFs in the solid state as well as in solvent dispersed medium. The π-conjugated organic linkers and coordination polymers with d^{10} metal centers (Cd, Zn etc.) have been used as luminescent materials with fascinating photoluminescent properties.

► To evaluate the catalytic activity of MOF in alcohol oxidation and tandem reaction (oxidation of styrene followed by Knoevenagel condensation) reactions. The effect of different reaction parameters such as temperature, solvent, base effect etc. on the catalytic reaction was also intended to study to optimize the reaction condition and finally to examine the recyclability and heterogeneity nature of the catalyst.

Consequently, it is convincing that research on MOFs continues to become more interdisciplinary, and the goal in the upcoming years will be to convert the acquired knowledge into technical applications.

1.7. Summary

The thesis contains of six (6) chapters as follows:

Chapter 1 introduces the general discussion on the multiple features of metal-organic frameworks (MOFs), numerous practices to design diverse functional MOFs, key role of the various carboxylate linkers in the adaptability of MOFs, involvement of transition metals to design carboxylate based and mixed-linker based MOFs while a variety of spacer has been used, application of MOFs in heterogeneous catalysis and the role of MOF solids in heterogeneous catalytic condensation reactions and epoxidation reactions; selective gas adsorption studies, luminescence properties etc. Scope of the current research and the summary of the research works have also been presented.

Chapter 2 illustrates the synthesis of a cadmium(II) containing mixed-linker 3D MOF *viz.* $\{[Cd(L_1)(L_2)](DMA)\}_n$ (**1**) (L$_1$ = 2-amino-1,4-benzenedicarboxylate, L$_2$ = 4,4′-azopyridine and DMA = N,N-dimethylacetamide) by solvothermal method. The compound exhibited a superior

sensing activity towards tri-positive metal ions (Fe^{3+}, Al^{3+}, Cr^{3+}) through "turn-on" process and selective nitro aromatic (TNP) sensing activity through "turn-off" mechanism. In addition, capability to accept water molecule into pores of MOF has been studied by vapor sorption measurements.

Chapter 3 discusses the selective adsorption capacity of pre synthesize cadmium(II) containing mixed-linker 3D MOF *viz.* $\{[Cd(L_1)(L_2)](DMA)\}_n$ (**1**) (L_1 = 2-amino-1,4-benzenedicarboxylate, L_2 = 4,4′-azopyridine and DMA = N,N-dimethylacetamide) towards CO_2 compared to other gas (H_2, N_2, CH_4) and evaluation of the heat of adsorption and selectivity parameter.

Chapter 4 accounts the synthesis of a one dimensional (1D) Cu(II) based mixed-linker polymer $\{Cu_2(L_3)_4(L_4)\}_n$ (**2**) (L_3 = 3-(2-thienyl)acrylic acid) L_4 = 4,4´- bipyridine) by layer diffusion method and characterized by single crystal X-ray diffraction. The compound coupled with TEMPO (2,2,6,6-tetramethylpiperidin-1-yl)oxyl or (2,2,6,6-tetramethylpiperidin-1-yl)oxidanyl) exhibited good catalytic activity for oxidation of primary alcohols in absence of any base with high selectivity and good yield, which is a very rare example.

Chapter 5 reports the solvothermal synthesis of a series of cobalt (II) based 2D MOF named as $\{[Co(L_5)(L_2)](H_2O)\}_n$ (**3**), $\{[Co(L_5)(L_6)]\}_n$ (**4**) and $\{[Co(L_5)(H_2O)](H_2O)_2\}_n$ (**5**) (L_5 = 5-amino-1,3-benzenedicarboxylic acid, L_2 = 4,4´-azopyridine and L_6 = 1,2-bis(4-pyridyl)ethane. The compounds have been characterized by single crystal XRD, powder XRD, IR and TGA and other spectroscopic and elemental analysis. The compounds contain redox active cobalt(II) centre and free amine functionality that played bi-functional catalytic role leading to catalyzing tandem reaction, styrene oxidation followed by Knoevenagel condensation, to produce corresponding benzylidenemalononitrile derivates.

Chapter 6 summarizes the noteworthy attainments of the effort embodied in the present thesis.

1.8. References

1. J. J. Perry IV, J. A. Perman, M. J. Zaworotko, Chem. Soc. Rev. 2009, **38**,1400.

2. W. Lu, Z. Wei, Z. Y. Gu, T. F. Liu, J. Park, J. Tian, M. Zhang, Q. Zhang, T. Gentle III, M. Bosch, H. C. Zhou, Chem. Soc. Rev. 2014, **43**, 5561.

3. Q. Qian, P. A. Asinger, M. J. Lee, G. Han, K. M. Rodriguez, S. Lin, F. M. Benedetti, A. X. Wu, W. S. Chi, Z. P. Smith, Chem. Rev. 2020, **120**, 8161.

4. S. S. Nagarkar, B. Joarder, A.K. Chaudhari, S. Mukherjee, S. K. Ghsoh, Angew. Chem. Int. Ed. 2013, **52**, 2881.

5. P. M. Stanley, J. Haimerl, N. B. Shustova, R. A. Fischer, J. Warnan, Nat. Chem. 2022, **14**, 1342.

6. R. Calmanti, M. Selva, A. Perosa, Green Chem**.** 2021, **23**, 1921.

7. Y. B. Huang, J. Liang, X-S. Yang, R. Cao, Chem. Soc. Rev. 2017.**46**. 126.

8. M. D. Allendorf, C. A. Bauer, R. K. Bhakta, R. J. T. Houk, Chem. Soc. Rev. 2009, **38,** 1330.

9. K. Sonowal, S. J. Kalita, S. K. Purkayastha, J. Goswami, P. Basyach, R. Das, A. Borborah, A. K. Guha, L. Saikia, ACS Omega 2024, **9**, 2504.

10. W. P. Lustig, S. Mukherjee, N. D. Rudd, A. V. Desai, J. Li, S. K. Ghosh, Chem. Soc. Rev. 2017, **46**, 3242.

11. M. Cametti, K. Rissanen, Chem. Commun. 2009, 2809.

12. M. R. Tchalala, P. M. Bhatt, K. N. Chappanda, S. R. Tavares, K. Adil, Y. Belmabkhout, A. Shkurenko, A. Cadiau, N. Heymans, G. De Weireld, G. Maurin, K. N. Salama, M. Eddaoudi, Nat. Commun. 2019, **10**, 1328.

13. H. Wang, W.P. Lustig, J. Li, Chem. Soc. Rev. 2018, **47,** 4729.

14. A. Kobayashi, H. Hara, S. Noro, M. Kato, Dalton Trans. 2010, **39**, 3400.

15. B. L. Chen, L. B. Wang, F. Zapata, G. D. Qian, E. B. Lobkovsky, J. Am. Chem. Soc. 2008, **130**, 6718.

16. Z. G. Xie, L. Q. Ma, K. E. de Krafft, A. Jin, W. B. Lin, J. Am. Chem. Soc. 2010, **132,** 922.

17. B. Gole, A. K. Bar, P. S. Mukherjee, Chem. Eur. J. 2014, **20**, 2276.

18. W. Zhang, R.-G. Xiong, Chem. Rev. 2012, **112**, 1163.

19. M. Kurmoo, Chem. Soc. Rev. 2009, **38**, 1353.

20. W. Zhuang, H. Sun, H. Xu, Z. Wang, S. Gao, L. Jin, Chem. Commun. 2010, **46**, 4339.

21. P. Horcajada, C. Serre, M. Vallet-Regí, M. Sebban, F. Taulelle, G. Férey, Angew. Chem. Int. Ed. 2006, **45**, 5974.

22. P. Horcajada, R. Gref, T. Baati, P. K. Allan, G. Maurin, P. Couvreur, G. Férey, R. E. Morris, C. Serre, Chem. Rev. 2012, **112**, 1232.

23. G. Li, H. Kobayashi, J. M. Taylor, R. Ikeda, Y. Kubota, K. Kato, M. Takata, T. Yamamoto, S. Toh, S. Matsumura, H. Kitagawa, Nat. Mater. 2014, **13,** 802.

24. J. -R. Li, J. Sculley, H. -C. Zhou, Chem. Rev. 2012, **112**, 869.

25. H. Sato, W. Kosaka, R. Matsuda, A. Hori, Y. Hijikata, R.V. Belosludov, S. Sakaki, M. Takata, S. Kitagawa, Science 2014, **343**, 167.

26. P. Nugent, Y. Belmabkhout, S. D. Burd, A. J. Cairns, R. Luebke, K. Forrest, T. Pham, S. Ma, B. Space, L. Wojtas, M. Eddaoudi, M. J. Zaworotko, Nature 2013, **495**, 80.

27. J. Liu, L. Chen, H. Cui, J. Zhang, L. Zhang, C.-Y. Su, Chem. Soc. Rev. 2014, **43**, 6011.

28. W.-Y. Gao, M. Chrzanowski, S. Ma, Chem. Soc. Rev. 2014, **43**, 5841.

29. M. Zhao, S. Ou, C.-D. Wu, Acc. Chem. Res. 2014, **47**, 1199.

30. J. Lee, O. K. Farha, J. Roberts, K. A. Scheidt, S. T. Nguyen, J. T. Hupp, Chem. Soc. Rev. 2009, **38,** 1450.

31. M. Yoon, R. Srirambalaji, K. Kim, Chem. Rev. 2012, **112,** 1196.

32. D. Saha, T. Maity, S. Koner, Dalton Trans. 2014, **43**, 13006.

33. R. Sen, D. Saha, S. Koner, P. Brandao, Z. Lin, ChemPlusChem, 2015, **80,** 591.

34. P. Ramaswamy, N. E. Wong, G. K. H. Shimizu, Chem. Soc. Rev. 2014, **43,** 5913.

35. T. Yamada, K. Otsubo, R. Makiura, H. Kitagawa, Chem. Soc. Rev. 2013, **42**, 6655.

36. D. Lim, H. Kitagawa, Chem. Rev. 2020, **120**, 8416.

37. Y. Shibata, Journal of the College of Science, Imperial University of Tokyo 1916, **37,** 1.

38. J. F. Keggin, F. D. Miles, Nature 1936, **137**, 577.

39. S. L. James, Chem. Soc. Rev. 2003, **32,** 276.

40. a) B. F. Hoskins, R. Robson, J. Am. Chem. Soc. 1989, **111,** 5962; b) B. F. Hoskins, R. Robson, J. Am. Chem. Soc. 1990, **112,** 1546; c) B. F. Abrahams, B. F. Hoskins, D. M. Michail, R. Robson, Nature 1994, **369,** 727.

41. a) D. Venkataraman, G. B. Gardner, S. Lee, J. S. Moore, J. Am. Chem. Soc.1995, **117**, 11600; b) G. B. Gardner, D. Venkataraman, J. S. Moore, S. Lee, Nature 1995, **374**, 792.

42. O. M. Yaghi, G. M. Li, H. L. Li, Nature 1995, **378**, 703.

43. S. Subramanian, M. J. Zaworotko, Angew. Chem. Int. Ed. 1995, **34**, 2127.

44. H. Li, M. Eddaoudi, M. O'Keeffe, O. M. Yaghi, Nature 1999, **402**, 276.

45. a) A. F. Wells, Acta Crystallogr. 1954, **7**, 535; b) A. F. Wells, Acta Crystallogr. 1954, **7**, 545; c) A. F. Wells, Three dimensional Nets and Polyhedra, Wiley, New York, 1977; d) A. F. Wells, Structural Inorganic Chemistry, Oxford University Press, London, 5th edn., 1984.

46. A. Y. Robin, K. M. Fromm, Coord. Chem. Rev. 2006, **250**, 2127.

47. S. I. Noro, S. Kitagawa, T. Akutagawa, T. Nakamura, Prog. Polym. Sci. 2009, **34**, 240.

48. M. J. Rosseinsky, Microporous Mesoporous Mater. 2004, **73**, 15.

49. J. A. Groves, S. R. Miller, S. J. Warrender, C. Mellot-Draznieks, P. Lightfoot, P. A. Wright, Chem. Commun. 2006, 3305.

50. M. T. Wharmby, J. P. S. Mowat, S. P. Thompson, P. A. Wright, J. Am. Chem. Soc. 2011, **133**, 1266.

51. S. L. James, Chem. Soc. Rev. 2003, **32**, 276.

52. J. L. C. Rowsell, O. M. Yaghi, Microporous Mesoporous Mater. 2004, **73**, 3.

53. M. Eddaoudi, D. B. Moler, H. Li, B. Chen, T. M. Reineke, M. O'Keeffe, O. M. Yaghi, Acc. Chem. Res. 2001, **34**, 319.

54. S. Kitagawa, R. Kitaura, S. Noro, Angew. Chem. Int. Ed. 2004, **43**, 2334.

55. B. Moulton, M. J. Zaworotko, Chem. Rev. 2001, **101**, 1629.

56. P. Pachfule, T. Panda, C. Dey, R. Banerjee, CrystEngComm. 2010, **12**, 2381.

57. J. J. Perry IV, J. A. Perman, M. J. Zaworotko, Chem. Soc. Rev. 2009, **38**, 1400.

58. a) J. Zhang, M. M. Matsushita, X. X. Kong, J. Abe, T. Iyoda, J. Am. Chem. Soc. 2001, **123**, 12105; b) G. J. E. Davidson, S. J. Loeb, Angew. Chem. Int. Ed. 2003, **42**, 74; c) E. S. Lee, J. S. Heo, K. Kim, Angew. Chem. Int. Ed. 2000, **39**, 2699.

59. M. Eddaoudi, J. Kim, N. Rosi, D. Vodak, J. Wachter, M. O'Keeffe, O. M. Yaghi, Science 2002, **295**, 469.

60. P. L. Llewellyn, S. Bourrelly, C. Serre, A. Vimont, M. Daturi, L. Hamon, G. De Weireld, J. S. Chang, D. Y. Hong, Y. K. Hwang, S. H. Jhung, G. Férey, Langmuir 2008, **24**, 7245.

61. M. M. Mohamed, F. I. Zidan, M. H. Fodail, J. Mater. Sci. 2007, **42**, 4066.

62. R. W. van den Brink, S. Booneveld, J. R. Pels, D. F. Bakker, M. Verhaak, App. Catal., B. 2001, **32**, 73.

63. K. Tanabe, W. F. Hölderich, Appl. Catal. A, 1999, **181**, 399.

64. S. R. Miller, P. A. Wright, C. Serre, T. Loiseau, J. Marrot, G. Férey, Chem. Commun. 2005, 3850.

65. D. T. de Lill, C. L. Cahill, Chem. Commun. 2006, 4946.

66. T. Chalati, P. Horcajada, R. Gref, P. Couvreur, C. Serre, J. Mater. Chem. 2011, **21**, 2220.

67. C. Janiak, J. K. Vieth, New. J. Chem. 2010, **34**, 2366.

68. U. Mueller, H. Puetter, M. Hesse, H. Wessel, US Patent. WO2005/049892.

69. Y. R. Lee, J. Kim, W. S. Ahn, Korean. J. Chem. Eng. 2013, **30**, 1667.

70. A. Rehman, S. Farrukh, A. Hussain, E. Pervaiz, Energy Environ. 2020. **31**. 367.

71. M. Safaei, M. M. Foroughi, N. Ebrahimpoor, S. Jahani, A. Omidi, M. Khatami, Trends Anal. Chem. 2019, **118**, 401.

72. N. Stock, S. Biswas, Chem. Rev. 2012, **112**, 933.

73. a) R. M. Barrer, J. Chem. Soc. 1948, 2158; b) D. W. Breck, W. G. Eversole, R. M. Milton, T. B. Reed, T. L. Thomas, J. Am. Chem. Soc. 1956, **78**, 5968; c) R. M. Barrer, L. Hinds, E. A. White, J. Chem. Soc. 1953, 1466.

74. Z. F. Bian, J. Zhu, F. L. Cao, Y. F. Lu, H. X. Li, Chem. Commun. 2009, 3789.

75. R. I. Walton, Chem. Soc. Rev. 2002, **31**, 230.

76. P. J. Hagrman, D. Hagrman, J. Zubieta, Angew. Chem. Int. Ed. 1999, **38**, 2639.

77. T. Jiang, A. Lough, G. A. Ozin, R. L. Bedard, J. Mater. Chem. 1998, **8**, 733.

78. G. J. Demazeau, Mater. Chem. 1999, **9**, 15.

79. X. X. Zhao, J. P. Ma, Y. B. Dong, R. Q. Huang, Cryst. Growth Des. 2007, **7**, 1058.

80. J. S. O. Evans, R. J. Francis, D. Ohare, S. J. Price, S. M. Clark, J. Flaherty, J. Gordon, A. Nield, C. C. Tang, Rev. Sci. Instrum. 1995, **66**, 2442.

81. V. V. Boldyrev, K. Tkakova, J. Mater. Synth. Process. 2000, **8**, 121.

82. A. Pichon, A. L. Garay, S. L. James, CrystEngComm. 2006, **8**, 211.

83. J. H. Bang, K. S. Suslick, Adv. Mater. 2010, **22**, 1039.

84. L. G. Qie, Z. Q. LI, Y. Wu, W. Wang, T. Xu, X. Jiang, Chem. Commun. 2008, **31**, 3642.

85. D. Xie, H. Xing, Z. Zhang, Q. Yang, Y. Yang, Q. Ren, Z. Bao, CIESC J. 2017, **68**, 154.

86. M. Du, C.-P. Li, X.-J. Zhao, Cryst. Growth Des. 2006, **6**, 335.

87. S.R. Halper, L. Do, J.R. Stork, S.M. Cohen, J. Am. Chem. Soc, 2006, **128**, 15255.

88. O.S. Bull, I. Bull, G.K. Amadi, C. O. Odu, E. Okpa, Orient. J. Chem. 2022, **38**, 490.

89. W. X. Zhang, Y. Y. Yang, S. B. Zai, W. N. Seik, X. M. Chen, Eur. J. Inorg. Chem. 2008, **2008**, 679.

90. S. Kaskel, Handbook of Porous Solids, Eds. F. Schüth, K. S. W. Sing, J. Weitkamp, Wiley, New York. 2002, **2**, 1190.

91. K. Barthelet, J. Marrot, D. Riou, G. Férey, Angew. Chem. Int. Ed. 2006, **41**, 281.

92. K. Barthelet, J. Marrot, G. Férey, D. Riou, Chem. Commun. 2004, 520.

93. G. Férey, C. Serre, C. Mellot-Draznieks, F. Millange, S. Surble, J. Dutour, I. Margiolaki, Angew. Chem. Int. Ed. 2004, **43**, 6296.

94. G. Férey, C. Mellot-Draznieks, C. Serre, F. Millange, J. Dutour, S. Surble, I. Margiolaki, Science 2005, **309**, 2040.

95. S. S. Y. Chui, S. M. F. Lo, J. P. H. Charmant, A. G. Orpen, I. D. Williams, Science 1999, **283**, 1148.

96. D. Wu, P. Zhang, G. Yang, L. Hou, W. Zhang, Y. Han, P. Liu, Y. Wang, Coord. Chem. Rev. 2021, **434**, 213709.

97. T. Yoskamtorn, P. Zhao, X. P. Wu, K. Purchase, F. Orlandi, P. Manuel, J. Taylor, Y. Li, S. Day, L. Ye, C. C. Tang, Y. Zhao, S. C. E. Tsang, J. Am. Chem. Soc. 2021, **143**, 3205.

98. A. M. Wright, C. Sun, M. Dinca, J. Am. Chem. Soc. 2021, **143**, 68.

99. J. Perego, C. X. Bezuidenhout, A. Pedrini, S. Bracco, M. Negroni, A. Comotti, P. Sozzani, J. Mater. Chem. A, 2020, **8**, 11406.

100. P. Brandt, A. Nuhnen, M. Lange, J. Mollmer, O. Weingart, C. Janiak, ACS Appl. Mater. Interfaces, 2019, **11**, 17350.

101. D. E. Jaramillo, H. Z. H. Jiang, H. A. Evans, R. Chakraborty, H. Furukawa, C. M. Brown, M. Head-Gordon, J. R. Long, J. Am. Chem. Soc. 2021, **143**, 6248.

102. X. Zhao, Y. Wang, D. S. Li, X. Bu, P. Feng, Adv. Mater. 2018, **30**, 1705189.

103. X. Y. Li, Z. J. Li, Y. Z. Li, L. Hou, Z. Zhu, Y. Y. Wang, Inorg. Chem. 2018, **57**, 12417.

104. X. Liu, W. Fan, M. Zhang, G. Li, H. Liu, D. Sun, L. Zhao, H. Zhu, W. Guo, Mater. Chem. Front. 2018, **2**, 1146.

105. E. Binaeian, Y. Li, D. Yuan, Chem. Eng. J. 2021, **421**, 129655.

106. H. Wang, D. Luo, E. Velasco, L. Yu and J. Li, J. Mater. Chem. A, 2021, **9**, 20874.

107. H. Li, M. Eddaoudi, T. L. Groy, O. M. Yaghi, J. Am. Chem. Soc. 1998, **120**, 8571.

108. O. M. Yaghi, H. Li, J. Am. Chem. Soc. 1996, **118,** 295.

109. O. M. Yaghi, C. E. Davis, G. Li, H. Li, J. Am. Chem. Soc. 1997, **119,** 2861.

110. H. Li, C. E. Davis, T. L. Groy, D. G. Kelley, O. M. Yaghi, J. Am. Chem. Soc. 1998, **120**, 2186.

111. O. M. Yaghi, M. J. Kalmutzki, C. S. Diercks, Angew. Chem. Int. Ed. 2019, **58**, 14024.

112. J. Jiang, Y. Zhao, O. M. Yaghi, J. Am. Chem. Soc. 2016, **138**, 3255.

113. D. N. Dybtsev, H. Chun, S. H. Yoon, D. Kim, K. Kim, J. Am. Chem. Soc. 2004, **126**, 3.

114. S. Q. Ma, X. S. Wang, D. Q. Yuan, H.C. Zho, Angew. Chem. Int. Ed. 2008, **47**, 4130.

115. L. Schlapbach, A. Züttel, Nature 2001, **414**, 353.

116. K. K. Gangu, S. Maddila, S. B. Mukkamala, S. B. Jonnalagadda, J. Energy Chem. 2019, **30**, 132.

117. M. P. Suh, H. J. Park, T. K. Prasad, D.-W. Lim, Chem. Rev. 2012, **112**, 782.

118. D. Saha, T. Maity, S. Das, S. Koner, Dalton Trans. 2013, **42**, 13912.

119. Y. W. Li, L. F. Wang, K. H. He, Q. Chen, X.-H. Bu, Dalton Trans. 2011, **40**, 10319.

120. M. R. Allen, D. J. Frame, C. Huntingford, C. D. Jones, J. A. Lowe, M. Meinshausen, N. Meinshausen, Nature 2009, **458**, 1163.

121. R. Banerjee, A. Phan, B. Wang, C. Knobler, H. Furukawa, M. O'Keeffe, O. M. Yaghi, Science 2008, **319**, 939.

122. R. Haldar, R. Matsuda, S. Kitagawa, S. J. George, T. K. Maji, Angew. Chem. Int. Ed. 2014, **53**, 11772.

123. I. Kochetygov, S. Bulut, M. Asgari, W. L. Queen, Dalton Trans. 2018, **47**, 10527.

124. V. A. Bolotov, K. A. Kovalenko, D. G. Samsonenko, X. Han, X. Zhang, G. L. Smith, L. J. McCormick, S. J. Teat, S. Yang, M. J. Lennox, A. Henley, E. Besley, V. P. Fedin, D. N. Dybtsev, M. Schröder, Inorg. Chem. 2018, **57,** 5074.

125. L.-W. Lee, T.-T. Luo, S.-H. Lo, G.-H. Lee, S.-M. Peng, Y.-H. Liu, S.-L. Lee, K.-L. Lu, Cryst. Eng. Comm. 2015, **17**, 6320.

126. A. Kondo, H. Noguchi, S. Ohnishi, H. Kajiro, A. Tohdoh, Y. Hattori, W.-C. Xu, H. Tanaka, H. Kanoh, K. Kaneko, Nano Lett. 2006, **6,** 2581.

127. T. Suzuki, R. Kotani, A. Kondo, K. Maeda, J. Phys. Chem. C. 2016, **120**, 21571.

128. M. Comotti, W.C. Li, B. Spliethoff, F. Schüth, J. Am. Chem. Soc. 2006, **128**, 917.

129. C. Zhu, Q. Mao, D. Li, C. Li, Y. Zhou, X. Wu, Y. Luo, Y. Li, Catal. Commun. 2018, **104**, 123.

130. G. Calleja, R. Sanz, G. Orcajo, D. Briones, P. Leo, F. Martínez, Catal. Today, 2014, **227**, 130.

131. N. Anbu, A. Dhakshinamoorthy, J. Colloid Interface Sci. 2017, **494**, 282.

132. N. T. S. Phan, K. K. A. Le, T. D. Phan, Appl. Catal. A Gen. 2010, **382**, 246.

133. L.T.L. Nguyen, C. V. Nguyen, G. H. Dang, K.K.A. Le, N.T.S. Phan, J. Mol. Catal. A Chem. 2011, **349**, 28.

134. D. Saha, T. Maity, R. Sen, S. Koner, Polyhedron 2012, **43**, 63.

135. N. B. Pathan, A. M. Rahatgaonkar, M. S. Chorghade, Catal. Commun. 2011, **12**, 1170.

136. O. Kikhtyanin, D. Kubicka, J. Cejk, Catal. Today, 2015, **243**, 158.

137. J. Gascon, U. Aktay, M. D. Hernandez-Alonso, G.P.M. van Klink, F. Kapteijn, J. Catal. 2009, **261**, 75.

138. M. Hartmann, M. Fischer, Microporous Mesoporous Mater. 2012, **164**, 38.

139. Y. Yang, H. Yao, F. Xi, E. Gao, J. Mol. Catal. A Chem. 2014, **390**, 198.

140. F. X. Llabrés i Xamena, F. G. Cirujano, A. Corma, Microporous Mesoporous Mater. 2012, **157**, 112.

141. F. Martínez, G. Orcajo, D. Briones, P. Leo, G. Calleja, Microporous Mesoporous Mater. 2017, **246**, 43.

142. N. Anbu, A. Dhakshinamoorthy, Appl. Catal. A Gen. 2017, **544**, 145.

143. O. A. Kholdeeva, I. Y. Skobelev, I. D. Ivanchikova, K. A. Kovalenkob, V. P. Fedin, A.R.B. Sorokin, Catal. Today. 2014, **238**, 54.

144. I. Y. Skobelev, A. B. Sorokin, K. A. Kovalenko, V. P. Fedin, O. A. Kholdeeva, J. Catal. 2013, **298**, 61.

145. V. V. Torbina, I. D. Ivanchikova, O. A. Kholdeeva, I. Y. Skobelev, O. V. Vodyankina, Catal. Today, 2016, **278**, 97.

146. Y. Li, L. Zhang, W. Ji, J. Mol. Struct. 2017, **1133**, 607.

147. S. Neogi, M. K. Sharma, P. K. Bharadwaj, J. Mol. Catal. A Chem. 2009, **299**, 1.

148. A. Bhunia, S. Dey, J. M. Moreno, U. Diaz, P. Concepcion, K. Van Hecke, C. Janiak, P. Van Der Voort, Chem. Commun. 2016, **52**, 1401.

149. N. T. S. Phan, T. T. Nguyen, C. V. Nguyen, T. T. Nguyen, Appl. Catal. A Gen. 2013, **457**, 69.

150. L. Chen, Z. Gao, Y. Li, Catal. Today, 2015, **245**, 122.

151. K. D. Nguyen, S. H. Doan, A. N. V. Ngo, T. T. Nguyen, N. T. S. Phan, J. Ind. Eng. Chem. 2016, **44**, 136.

152. N. Anbu, A. Dhakshinamoorthy, J. Colloid Interface Sci. 2017, **490**, 430.

153. J. W. Brown, N. N. Jarenwattananon, T. Otto, J. L. Wang, S. Glöggler, L. S. Bouchard, Catal. Commun. 2015, **65**, 105.

154. F. X. Luz, L. Xamena, A. Corma, J. Catal. 2012, **285**, 285.

155. G. H. Dang, H. Q. Lam, A. T. Nguyen, D. T. Le, T. Truong, N.T.S. Phan, J. Catal. 2016, **337**, 167.

156. L. Zhang, Z. Su, F. Jiang, Y. Zhou, W. Xu, M. Hong, Tetrahedron 2013, **69**, 9237.

157. R. Babu, R. Roshan, Y. Gim, Y. H. Jang, J. F. Kurisingal, D. W. Kim, D. Park, J. Mater. Chem. A 2017, **5**, 15961.

158. R. Babu, R. Roshan, A. C. Kathalikkattil, D. W. Kim, D.-W. Park, ACS Appl. Mater. Interfaces. 2016, **8,** 33723.

159. N. B. Pathan, A. M. Rahatgaonkar, M. S. Chorghade, Catal. Commun 2011, **12**, 1170.

160. Z. Miao, Y. Luan, C. Qi, D. Ramella, Dalton Trans. 2016, **45**, 13917.

161. J. Park, J.-R. Li, Y.-P. Chen, J. Yu, A. A. Yakovenko, Z. U. Wang, L.-B. Sun, P. B. Balbuena, H.-C. Zhou, Chem. Commun. 2012, **48**, 9995.

162. Z. Wu, Y. Li, C. Zhang, X. Huang, B. Peng, G. Wang, Chem. Catal. 2022, **2**, 1009.

163. T. Liu, X. Shen, X. Shen, C. He, J. Liu, J, -J, Liu, CrystEngComm. 2021, **23**, 4667.

164. P. Cancino, V. Paredes-García, J. Torres, S. Martínez, C. Kremer, E. Spodine, Catal. Sci. Technol. 2017, **7**, 4929.

165. (a) D. Shi, Y. Ren, H. Jiang, B. Cai. J. Lu, Inorg. Chem. 2012, **51**, 6498. (b) S. Parshamoni, J. Telangae, S. Sanda, S. Konar, Chem. Asian J. 2016, **11**, 540.

166. Y. Zhang, N. Wei, Z. Xing, Z.-B. Han, Appl. Catal. A Gen. 2020, **602**, 117668.

167. B. L. Ryland, S. S. Stahl, Angew. Chem. Int. 2014, **53**, 8824.

168. M. F. Semmelhack, C. R. Schmid, D. A. Cortes, C. S. Chou, J. Am. Chem. Soc. 1984, **106**, 3374.

169. A. Dhakshinamoorthy, M. Alvaro, H. Garcia, ACS Catal. 2010, **1**, 48.

170. X. Fang, B. Zong, S. Mao, Nano Micro Lett. 2018, **10**, 64.

171. Y.M. Wang, Z.R. Yang, L. Xiao, X.B. Yin, Anal. Chem. 2018, **90**, 5758.

172. S.A. Diamantis, A. Margariti, A.D. Pournara, G.S. Papaefstathiou, M.J. Manos, T. Lazarides, Inorg. Chem. Front. 2018, **5**, 1493.

173. J. J. Perry IV, P. L. Feng, S. T. Meek, K. Leong, F. P. Doty, M. D. Allendorf, J. Mater. Chem. 2012, **22**, 10235.

174. B. Wang, Q. Yang, C. Guo, Y. Sun, L. Xie, J. Li, ACS. Appl. Mater. Interfaces 2017, **9**, 10286.

175. Z. Hu, B. J. Deibert, J. Li, Chem. Soc. Rev. 2014, **43**, 5815.

176. W. P. Lustig, S. Mukherjee, N. D. Rudd, A. V. Desai, J. Li, S. K. Ghosh, Chem. Soc. Rev. 2017, **46**, 3242.

177. Y. Cui, Y. Yue, G. Qian, B. Chen, Chem. Rev. 2012. **112,** 1126.

178. Z. Afravi, V. Nobakht, N. Pourrza, M. Ghomi, D. Trzybinski, K. Wozniak, ACS Omega 2022, **7**, 22221.

179. J. Zhang, Y. Huang, D. Yue, Y. Cui, Y. Yang, G. Qian, J. Mater. Chem. B. 2018, **6**, 5174.

180. S. Sharma, S. K. Ghosh, ACS Omega 2018, **3**, 254.

181. M. Zhang, G. Feng, Z. Song, Y. P. Zhou, H. Y. Chao, D. Yuan, T. T. Y. Tan, Z. Guo, Z. Hu, B. Z. Tang, B. Liu, D. Zhao, J. Am. Chem. Soc. 2014, **136**, 7241.

182. K. Wang, T.-F. Zheng, J.-L. Chen, H.-R. Wen, S.-J. Liu, T.-L. Hu, Inorg. Chem. 2022, **61**, 16177.

183. S. L. Jackson, A. Rananaware, C. Rix, S. V. Bhosale, K. Latham, Cryst. Growth Des. 2016, **16**, 3067.

184. Z.-H. Xu, Z.-Q. Huang, X.-H. Liu, Y. Zhao, Y. Lu, W.-Y. Sun, Dalton Trans. 2021, **50**, 2183.

185. H.-R. Tian, C.-Y. Gao, Y. Yang, J. Ai, C. Liu, Z.-G. Xu, Z.-M. Sun, New J. Chem. 2017, **41**, 1137.

186. J. Zhao, Y. Wang, W. Dong, Y. Wu, D. Li, Q. Zhang, Inorg. Chem. 2016, **55**, 3265.

187. T. Zhou, S. Liu, X. Guo, Q. Wang, L. Fu, S. Mi, P. Gao, Q. Su, H. Guo, Cryst. Growth Des. 2021, **21**, 5108.

188. D.-G. Cai, C.-Q. Qiu, Z.-H. Zhu, T.-F. Zheng, W.-J. Wei, J.-L. Chen, S.-J. Liu, H.-R. Wen, Inorg. Chem. 2022, **61**, 14770.

189. X. Zhao, D. Tian, Q. Gao, H. Sun, J. Xu, X. Bu, Dalton Trans. 2016, **45**, 1040.

190. J. Zhang, S. Ren, H. Xia, W. Jia, C. Zhang, J. Mater. Chem. C, 2020, **8**, 1427.

191. Y. Salinas, R. M. Manez, M. D. Marcos, F, Sancenon, A. M. Costero, M. Parra, S. Gill, Chem. Soc. Rev. 2012, **41**, 1261.

192. J. Shen, J. Zhang, Y. Zuo, L. Wang, X. Sun, J. Li, W. Han, R. He, J. Hazard. Mater. 2009, **163**, 1199.

193. L. Yang, Y.-L. Liu, C.-G. Liu, F. Ye, Y. Fu, Inorg. Chem. Commun. 2020, **122.** 108272.

Chapter 2
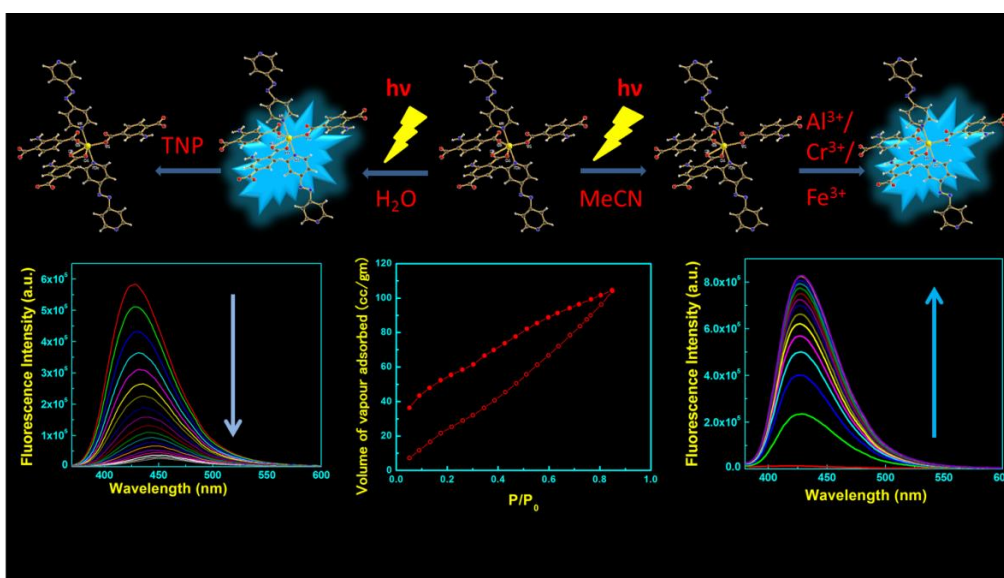
Selective luminescent sensing of metal ions and nitro aromatics over a porous mixed-linker cadmium(II) based metal–organic framework

2.1 Introduction

MOFs have been demonstrated to be fluorescent sensors for selective detection and identification of various cations, anions and metal ions based on their fluorescence response [1–4]. Besides, sensing of neutral molecule such as organic compounds, gases, vapors etc. also entails a large part of luminescence studies of MOF [5]. Neutral or charged species tends to engage in host–guest type interaction with MOF and in suitable cases that manifests in the change of emission profile of MOF. It is well known that sensing of various species with probes can be realized through two type of responses *viz.* ''turn-on'' and ''turn-off'' [6]. Presence of metal ions, especially heavy metal ions in water is a great concern of industrial water pollution. Metal ion pollutants make adverse effect on human health and as well as on the environment [7–12]. It is, however, well known that trace amount of metal ions is necessary for biological metabolism. Nevertheless, excess consumption is detrimental to human health and biological environment [13]. For example, iron being the most essential trace element present in living system plays significant roles for cellular metabolism, electron transfer process, DNA and RNA synthesis, oxygen uptake, hemoglobin formation and so on [48–50]. However, presence of excess of Fe^{3+} ions in living cell causes destruction of nucleic acids and proteins [14–16]. Likewise, Cr^{3+} is another essential trace element present in human body, but excessive amount of deposition cause deformity and also Cr^{3+} containing wastes create various environmental issues [17, 18]. Aluminum is the third most abundant element in earth and not essential trace element for human body. Hence its deposition in human body may cause direct influence on human health. Rampant use of aluminum foil, can and utensils in daily life, Al becomes the main source of poisoning in human body. Excess absorption of Al^{3+} causes of Parkinson's disease [19, 20]. It can even affect the function of central nervous system [21] and causes Alzheimer's diseases [22–26]. Apart from metal ion pollution, nitro explosives are also well known not only for their hazardous effect on environment but are also of great concern of homeland security, forensic investigation and mine field analysis [27–30]. Amongst the various explosives TNP (2,4,6-trinitrophenol) is most widely used in fireworks, dyes and leather industries [31]. This TNP containing wastes contaminate with water and soil. Mammalian metabolic process convert this TNP to picramic acid (2-amino-4,6-dinitrophenol), which has more mutagenic activity than TNP [32–34]. Concerning with the serious issues, development of techniques for detection of the poisonous contaminants with high accuracy and sensitivity is highly desirable. Compared to various traditional detection method today luminescence sensing

method is gaining the broader interest because of its high sensitivity and selectivity, simple sampling, quick response time and applicable both in solid and liquid phases. For this purpose, ligand based strategy has been involved to develop an MOF based photoluminescence sensor. Various functionalized π-conjugated organic ligand and their coordination with d^{10} metal ion produces MOF which are good candidate for luminescence sensing.

Thus, the effort has been made to synthesize a Cd(II) based mixed linker 3D MOF, $\{[Cd(L_1)(L_2)](DMA)\}_n$ (**1**) (L_1 = 2-aminobenzene-1,4-dicarboxylate; L_2 = 4,4′-azopyridine and DMA = N,N- dimethylacetamide) through solvothermal method. The framework compound featured interesting photoluminescence property in the solid state as well as in dispersed media. Interestingly, $\{[Cd(L_1)(L_2)](DMA)\}_n$ (**1**) exhibited turn-on/turn-off photoluminescence responses towards specific external stimuli. While the MOF displays a turn-on response towards tri-positive cations like Al^{3+}, Fe^{3+} and Cr^{3+}, luminescence quenching was observed in presence of nitro arenes with remarkable selectivity.

2.2 Experimental section

2.2.1 Materials

The chemicals, $Cd(NO_3)_2 \cdot 4H_2O$, 2-amino-1,4-benzenedicarboxylic acid, 4,4′-azopyridine were purchase from Sigma-Aldrich and used as received. The necessary chemicals for the sensing experiment of nitro-aromatics and metal salts were also purchased from Sigma-Aldrich. Solvents and all other chemicals were purchased from Merck, India. Solvents were distilled and dried before use.

2.2.2 Physical measurements

Powder X-ray diffraction analyses (PXRD) of well ground samples were performed on a Bruker D8 Advanced powder X-ray diffractometer at room temperature using CuKα (λ = 1.54056 Å) radiation generated at 40 kV and 40 mA. Diffraction lines were measured from 5–50° angle with scanning speed of 0.1° sec^{-1}. Fourier transformed IR spectra (4000–400 cm^{-1}) were recorded at 300 K on a Perkin Elmer RX1 FT-IR spectrometer using diamond plate. Elemental analysis was performed using a Vario-Micro V2.0.11 elemental (CHNSO) analyzer. Thermogravimetric analysis (TGA) was performed in the temperature range 30–800 ℃ (heating

rate = 10 ºC min^{-1}) using Perkin Elmer Pyris Diamond TG unit under nitrogen atmosphere (flow rate = 20 mLmin^{-1}). UV/VIS spectra were measured using Agilent 8453 diode array spectrophotometer and luminescence spectra were recorded using PTI (QM-40) spectrofluorimeter. The field emission scanning electron microscopic (FE-SEM) images were recorded on a JEOL, JSM-6700F machine. Dynamic light scattering measurements of **1** dispersed in various solvents under experimental conditions (*vide infra*) were performed on a Zetasizer Nano ZS (Malvern Instruments).

2.2.3 Synthesis of {[Cd(L$_1$)(L$_2$)](DMA)}$_n$ (1)

{[Cd(L$_1$)(L$_2$)](DMA)}$_n$ (**1**) was synthesized employing solvothermal method. Cd(NO$_3$)$_2$·4H$_2$O (77.1 mg, 0.25 mmol) dissolved in 5 mL water; 4,4´-azopyridine (46 mg, 0.25 mmol) and 2-amino-1,4-benzenedicarboxylic acid (76 mg, 0.25 mmol) were dissolved separately in 3 mL DMA (N, N-dimethylacetamide). The L$_1$ and L$_2$ solutions were added dropwise to the aqueous solution of metal salt with continuous stirring. The final mixture was then transferred to a Teflon lined (15 mL capacity) stainless steel Parr type autoclave and heated at 130 ºC for 72 h. After cooling to room temperature with a rate of about 10ºC min^{-1}, dark orange rod shaped single crystals were collected by filtration and washed with distilled water and dried at ambient temperature (yield 70% based on metal). Phase purity was verified through elemental analysis and X-ray powder diffraction analysis (*vide infra*). Anal. calcd. for C$_{22}$H$_{22}$CdN$_6$O$_5$ (FW 562.86), C, 46.95, H, 3.94, N, 14.93%; found C, 47.1, H, 3.8, N, 15.0%. FTIR peaks (cm^{-1}) (Figure 2.1): 3437, 3312 [ν (N–H stretching)], 1708 [ν$_{as}$ (COO$^-$)], 1584, 1547 [ν (N–H bending)], 1403 [ν$_s$ (COO$^-$)], 1367 [ν$_s$ (C–O)].

2.2.4 X-ray crystallography

A suitable single crystal of the {[Cd(L$_1$)(L$_2$)](DMA)}$_n$ (**1**) was used for data collection. Intensity data were collected using a Bruker D$_8$ QUEST area detector diffractometer equipped with graphite monochromated MoKα radiation (λ = 0.71073 Å). The molecular structure was solved by direct method and refined by full-matrix least squares on F^2 using the SHELXL-2018/3 package [35]. Non-hydrogen atoms were refined with anisotropic thermal parameters. All hydrogen atoms were placed in their geometrically idealized positions and constrained to ride on their parent atoms.

Table 2.1. Crystal data and refinement details of 1

Compound	**1**
Formula	$C_{18}H_{13}N_5O_4Cd$
Formula Weight	475.73
Crystal System	Orthorhombic
Space group	Cmca
a /Å	13.7449(17)
b /Å	20.8323(17)
c /Å	15.1571(15)
$\alpha\ /^o =\beta\ /^o =\gamma\ /^o$	90
V / (Å)^3	4340.1(8)
Z	8
Dc/g cm^{-3}	1.456
μ/mm^{-1}	1.037
R(int)	0.0286
Unique data	2512
Data with I >2σ(I)	2377
R1	0.0537
wR2	0.1748
GOF on F2	1.076

$R1 =\sum||F_o| - |F_c||/\sum|F_o|$, $wR2 = \{\sum[w(F_o^2-F_c^2)^2]/\sum w(F_o^2)^2\}^{1/2}$

Successful convergence was indicated by the maximum shift/error of 0.001 for the last cycle of the least squares refinement. In the azo group of 4, 4´-azopyridine, both the nitrogen atoms (N_1 and N_2) were disorder over two positions with 50% occupancy. Unable to assign any desirable disorder model for solvent molecule because of very high thermal parameter, the N,N-dimethylacetamide molecule was masked using solvent SQUEEZE instruction in Olex2 [36]. Absorption corrections were carried out using the SADABS program [37]. Data collection and structure refinement [38] parameters and crystallographic data of **1** are given in Table 2.1.

2.2.5 Vapor sorption measurements

Vapor sorption isotherms for H_2O (298K) in the pressure range 0-1 bar have been measured with an Autosorb iQ (Quantachrome Inc., USA) gas sorption system with an ultra-high pure (99.999% purity) gas source. In order to remove the solvent molecules from the crystal, sample is soaked in methanol for two days, filtered and evacuated (10^{-3} Torr) at 250 ºC for 12 h. Before the measurement sample was again evacuated under dynamic vacuum (10^{-3} Torr) at the desired temperature (150 ºC) for 10 h. For all isotherms, warm and cold free-space correction measurements were performed with ultrahigh pure He gas (99.999% purity). Water vapor sorption analysis was performed at 298 K.

2.2.6 Preparation of sample for UV-Vis and fluorescence measurements

For both UV-Vis and fluorescence titrations, stock of 1.0×10^{-3} M of **1** was prepared in CH_3CN under sonication. A 1.0×10^{-3} M stock solution of 2,4,6-trinitrophenol (TNP) in CH_3CN was prepared for fluorescence measurements. Other nitro explosives were prepared in CH_3CN. 2.5 mL MilliQ H_2O was pipetted out into a cuvette to which the required volume of probe was added to maintain a final concentration of 30 μM. TNP solution was added incrementally to get its concentration starting from 0 to 40 μM in a regular interval of volume and UV-Vis and fluorescence spectra were recorded for each solution. The 3 nm × 3 nm slit was used for fluorescence studies. Similarly, 1.0×10^{-3} M stock solutions of Cr^{3+}, Fe^{3+} and Al^{3+} were prepared dissolving corresponding nitrate salts in MilliQ water. 2.5 mL CH_3CN was pipetted out into a cuvette to which the required volume of probe was added to maintain a final concentration of 10 μM and Cr^{3+}, Fe^{3+} and Al^{3+} solutions were added incrementally starting from 0 to 11 μM, 0 to 4 μM and 0 to 2.5 μM, respectively, in a regular interval of volume and

fluorescence spectra were recorded for each solution. The 3 nm × 3 nm slit was used for fluorescence studies.

2.3 Results and discussion

2.3.1 X-ray structure

The single crystal X-ray analysis reveals that compound $\{[Cd(L_1)(L_2)](DMA)\}_n$ (**1**) has a three-dimensional polymeric networked structure and crystallized in orthorhombic crystal system with Cmca space group (Table 2.1). Perspective diagram of the coordination environment of Cd (II) in **1** is depicted in Figure. 2.2. Asymmetric unit of the compound consists of one cadmium ion, one L_1 ligand and half of L_2 ligand. **1** features a pillared layer mixed-linker structure, which is formed through induction of a second (L_2) linker to support the metal–carboxylate layer. Cadmium ions and L_1 ligands form a two-dimensional layer parallel to the crystallographic bc-plane (Figure 2.3a) and those layers are further connected by 4,4´-azopyridine (L_2) along a-axis to form a 3D network (Figure 2.3b). The Cd (II) ion is present as a hexa-coordinated distorted octahedral geometry where the equatorial plane is formed by the four oxygen atoms from three different L_1 ligands and two axial nitrogen atoms from two different L_2 ligands. The bond lengths and angles are collated in Table 2.2.

Table 2.2. Selected bond distances (Å) and angles (º) of 1

Atoms	Distance	Atoms	Distance
Cd1 - O1	2.241(5)	Cd1 - O4[a]	2.436(6)
Cd1 - O3[a]	2.325(6)	Cd1 - N3	2.367(6)
Atoms	**Angle**	**Atoms**	**Angle**
O1 - Cd1 - N3	90.6(1)	O2[d] - Cd1 - N3	86.7(1)
O1 - Cd1 - O3[a]	142.7(2)	N3 - Cd1 - N3[c]	172.3(2)
O1 - Cd1 - O4[a]	88.3(2)	O3[a] - Cd1 - O4[a]	54.5(2)

O1 - Cd1 - O2[b]	128.7(2)	O2[b] - Cd2 - O3[a]	88.6(2)
O3[a] - Cd1 - N3	91.9(1)	O2[b] - Cd2 - O4[a]	143.0(2)
O4[a] - Cd1 - N3	93.8(1)		

There are four Cd–O equatorial bonds involving O(1), O(2)[b], O(3)[a] and O(4)[a] with distances in the range 2.241(5)–2.437(6) Å, and two axial bonds Cd–N(3) and Cd–N(3)[c] with the distance 2.368(6) Å. The trans angles are (172.32(15)º, 143.01(15)º and 142.72(18)º) and the cis angles vary in a wide range, from 86.68(11)º to 128.73(18)º (Table 2.1). The highest value of trans angle 172.32(15)º corresponds to the angle N(3)–Cd(1)–N(3)[c]. The bond angles also show minor deviations from the ideal octahedral geometry. The four basal oxygen atoms and cadmium atom are positioned on a plane without any r.m.s. deviation. Upon removal of the DMA molecules the framework features a distorted rectangular type channels along a-axis with a dimension of approximately 11.6×8.4 Å, in which the –NH_2 groups exposed to the pores. $\{[Cd(L_1)(L_2)](DMA)\}_n$ (**1**) features a two-fold interpenetrated three-dimensional structure (Figure. 2.4). This may affect the accessible void space in framework material. Nevertheless, the PLATON analysis [39] shows that the solvent accessible void space is calculated to be 26.6%.
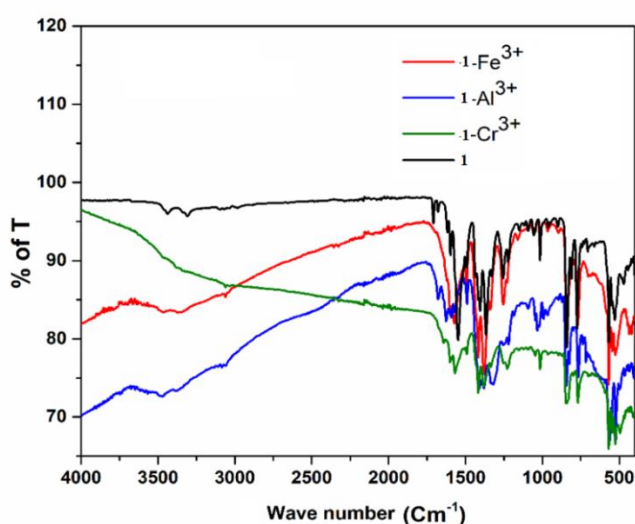
Figure 2.1. IR spectra of pristine 1 and after treatment with various metal salt solutions
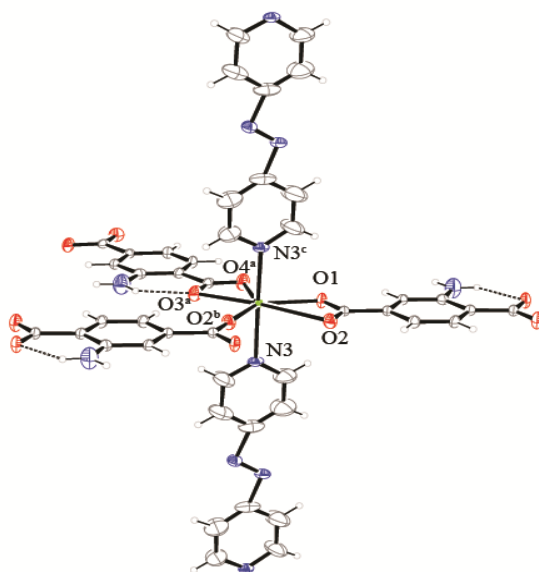
Figure 2.2. ORTEP view of {[Cd(L$_1$)(L$_2$)](DMA)}$_n$ (1) showing coordination environment around the metal center with ellipsoid at 30% probability
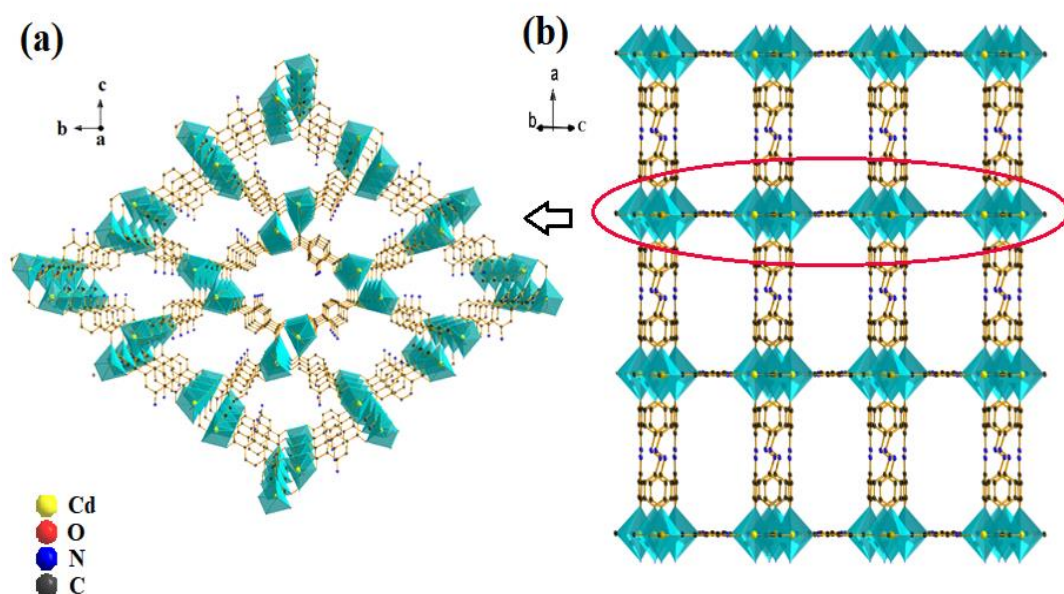
Figure 2.3. (a) 2D layer consists of Cd-L$_1$ network stacked parallel to crystallographic bc plane. (b) Pillared-layer 3D framework of 1 (single network of interpenetrated pillared-layer 3D framework is shown for clarity and Cd coordination environment is represented by the cyan colored polyhedron)
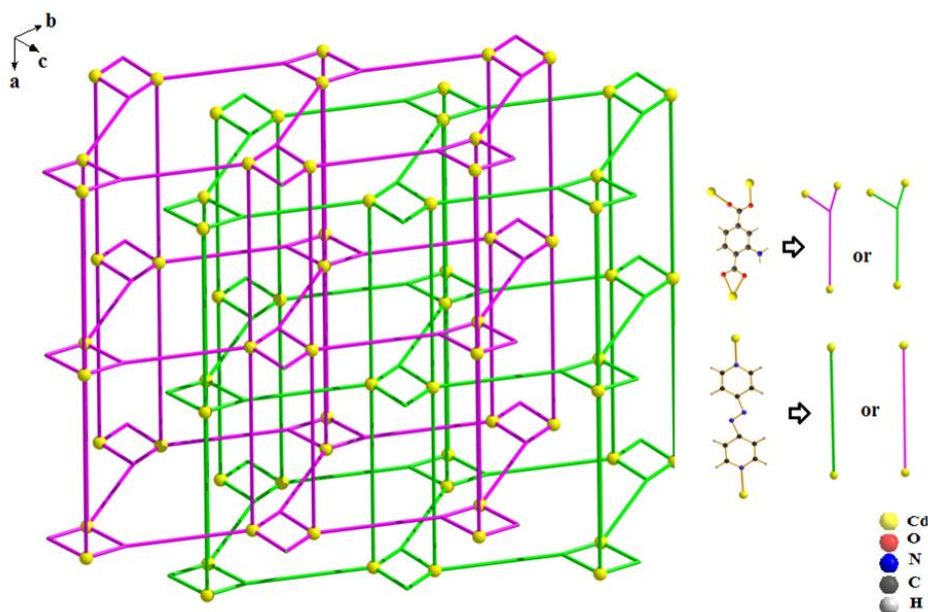
Figure 2.4 Simplified presentation of two-fold interpenetrated structure of 3D framework of 1

2.3.2 Thermogravimetric study

Thermogravimetric analysis was carried out to study the thermal stability of the framework in the solid state. Thermal analysis of **1** was performed using finely ground powder sample in the temperature range 30–800 ℃ under nitrogen atmosphere (Figure 2.5). Upon heating $\{[Cd(L_1)(L_2)](DMA)\}_n$ (**1**) displayed mass loss in two distinct steps. The first mass loss of ~15% in temperature range 150–260 ℃ may be attributable to removal of lattice DMA molecule (theoretical value 15.4%). On further heating the TG curve remains flat till 340 ℃ indicating desolvated MOF is thermally stable up to about 340 ℃. The second bout of mass loss of ~65% in the temperature range 360–630 ℃ attributed to decomposition of the framework compound to form the corresponding metal oxide. This matches well with the theoretical value of 64.9% mass loss corresponds to the decomposition of the remaining organic part of the desolvated MOF to form cadmium oxide. Notably, thermogravimetric analysis of the desolvated MOF shows no mass loss up to 340 ℃ (Figure 2.5).
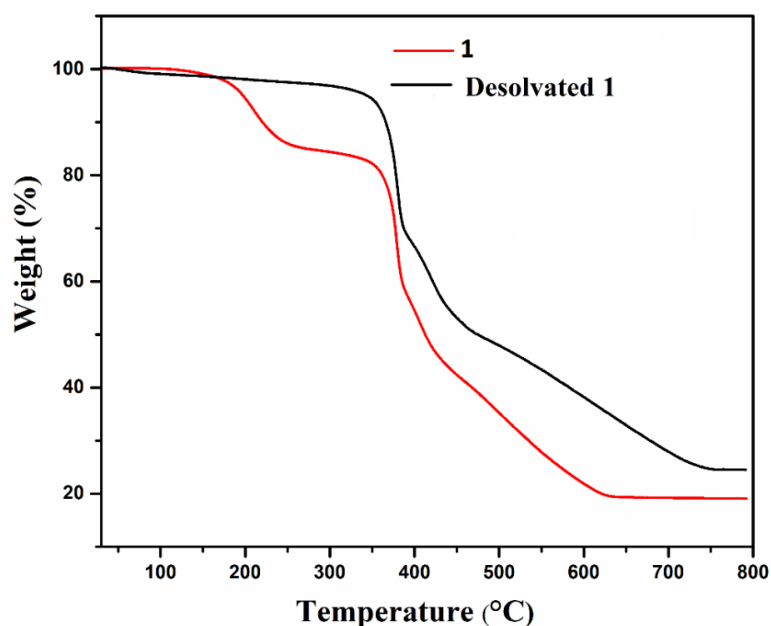
Figure 2.5 Thermogravimetric plots of $\{[Cd(L_1)(L_2)](DMA)\}_n$ (1) and its desolvated species

2.3.3 PXRD study

To confirm the phase purity of the bulk material of $\{[Cd(L_1)(L_2)](DMA)\}_n$ (**1**) powder X-ray diffraction (PXRD) measurements were carried out. PXRD patterns of the compound are shown in Figure 2.6. X-ray powder diffraction patterns of **1** were simulated using the single crystal data. Comparison of experimental and simulated PXRD patterns showed that all the major diffraction lines of experimental PXRD of **1** matched well with those of simulated ones, indicating reasonable crystalline phase purity of bulk materials. TG analysis indicates that upon heating **1** loses DMA molecule to produce a desolvated product which is stable up to 340 ºC. For PXRD measurement of desolvated species, required amount of desolvated product of **1** has been collected from the TG analyzer in several batches after heating up to 300 ºC. Desolvation can also be performed by following the same procedure used for activation in gas adsorption experiments. PXRD patterns of the calcined species matched well with original compound, $\{[Cd(L_1)(L_2)](DMA)\}_n$ (**1**) and position of diffraction lines are almost remained unaffected upon desolvation, suggesting the thermal robustness of the framework. Therefore, the structural integrity of **1** is retained even after desolvation. The framework structure also retained after gas adsorption study (Figure 2.7). Stability of the framework compound in various solvent media

was verified by PXRD measurements of **1** after exposure to solvents (Figure 2.7, 2.8). $\{[Cd(L_1)(L_2)](DMA)\}_n$ (**1**) was immersed in copious amount of solvents for 2–3 weeks at room temperature, separated by centrifugation and dried before PXRD patterns are measured.
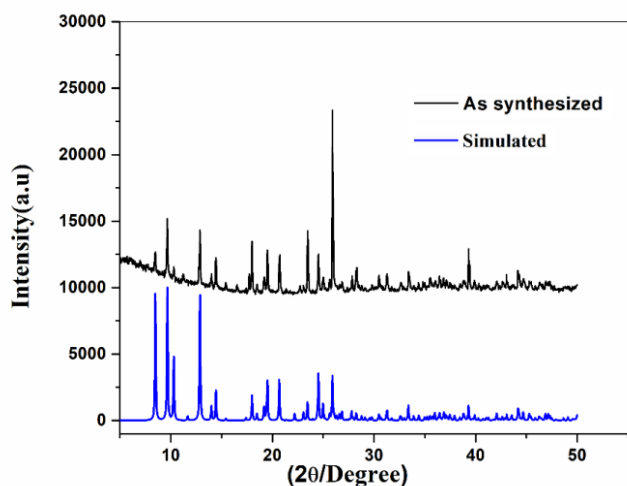
Figure 2.6. Powder X-ray diffraction pattern of 1 (simulated; blue) (as synthesize; black)
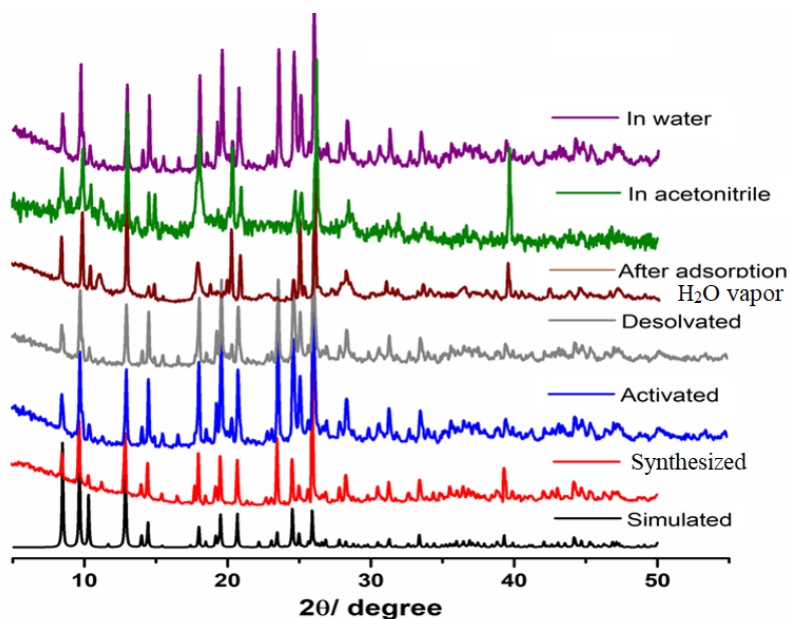
Figure 2.7. Powder X-ray diffraction pattern of 1 at different conditions
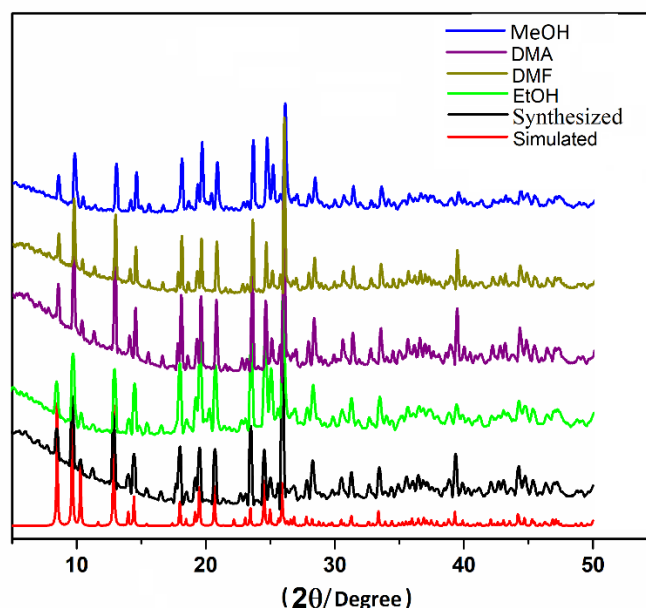
Figure 2.8. Powder X-ray diffraction pattern of 1 after immersing in various solvents

2.3.4 Water vapor sorption study

Metal–organic frameworks (MOFs) that possess suitable structure for water sorption are of potentially important in application of emerging technologies, such as adsorptive heat transformation, water harvesting from moist air, desalination etc. [40]. Presence of free $-NH_2$ functionality in the porous framework makes the study of water vapor sorption on **1**. Therefore, water vapor sorption measurements have been carried out using desolvated $\{[Cd(L_1)(L_2)](DMA)\}_n$ (**1**) after checking its stability upon exposure to water. The result showed the maximum amount of water vapor uptake is about 104.15 $cm^3 \cdot g^{-1}$ at 298 K and 1 bar pressure (Figure 2.9) (BET surface area 116.284 $cm^3 \cdot g^{-1}$ and Langmuir surface area is 5805.09 $cm^3 \cdot g^{-1}$) which corresponds to adsorption of ~ 2 water molecules per formula unit of MOF. The water vapor sorption study indicates that the framework compound contains permanent porosity through which water molecules can diffuse inside solid material.
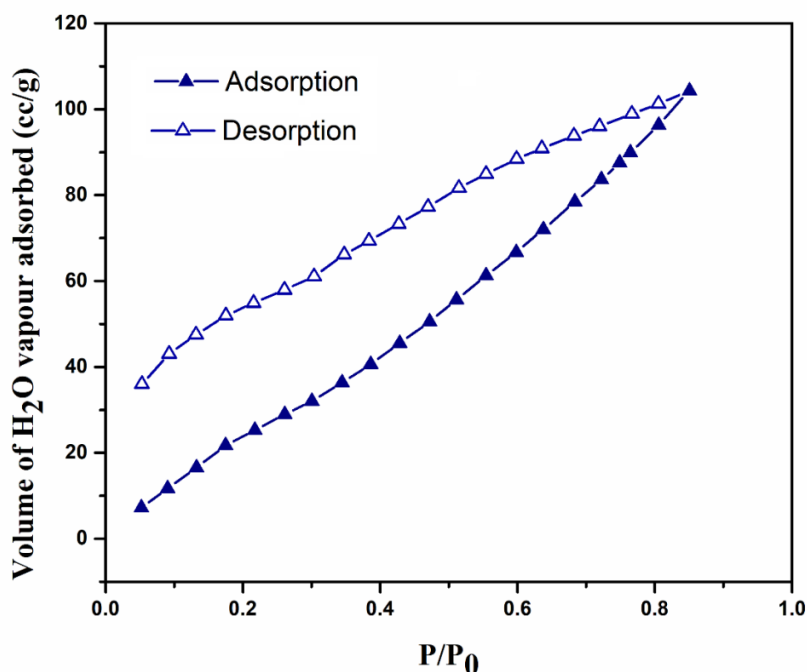
Figure 2.9. Water vapor adsorption isotherm measured at 298 K

2.3.5 Photoluminescence properties and sensing studies

The π-conjugated organic ligand containing metal–organic frameworks constructed from d^{10} metal centers (Cd, Zn etc.) have been employed as luminescent sensing materials [41–43]. Luminescence properties of such MOFs demonstrated their use in potential application of chemical sensing through host–guest chemistry. To examine the photoluminescence behavior of $\{[Cd(L_1)(L_2)](DMA)\}_n$ (**1**) and its desolvated species, emission spectral measurements have been carried out. There is no difference in photoluminescence behavior of $\{[Cd(L_1)(L_2)](DMA)\}_n$ (**1**) and its desolvated analogue. Emission spectra of **1** dispersed in various solvents (Figure 2.10) as well as in its pristine solid state (Figure 2.11), were measured at room temperature. Photoluminescence response for the **1** is found to depends on the solvent in which it is dispersed. The fluorescence response in CH_3CN is significantly weaker than the other solvents. Notably intensity of the excitation spectrum of **1** dispersed in water is higher than that of in acetonitrile (Figure 2.12).
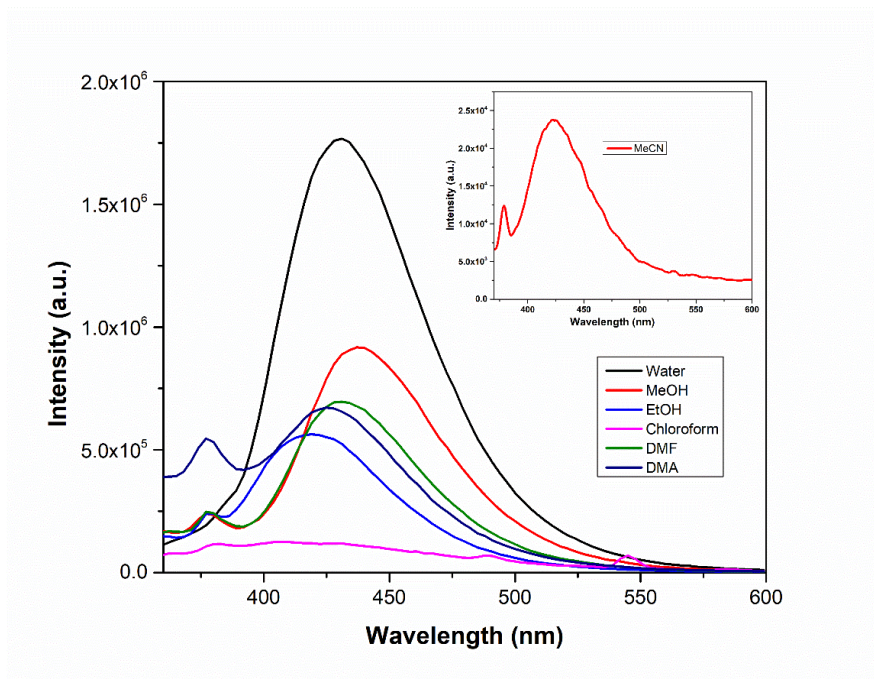
Figure 2.10. Comparison of fluorescence spectra of 1 dispersed in various solvent media (λ_{ex}= 370 nm). Fluorescence response of 1 dispersed in MeCN (inset) is weaker than other solvents.

$\{[Cd(L_1)(L_2)](DMA)\}_n$ (**1**) upon dispersion in various solvents showed red shift in its emission maxima in comparison with solid state spectrum. Selective responses (turn-on or turn-off) towards organic small molecules by luminescent MOF solids due to host–guest interaction are well documented in the literature [44]. Considering the intricacy of the framework structure possibility of similar kind of host–guest interaction in the **1** network is highly expected. It is noteworthy that while 2-amino-benzene-1,4-dicarboxylic acid is highly emissive in nature, 4, 4´- azopyridine remained non-emissive in the applied experimental conditions. Water dispersed fluorescence spectra of 2-amino-benzene-1,4-dicarboxylic acid exhibited an intense emission band centered at 428 nm upon excitation at 370 nm (Figure 2.13). This emission may be attributed to π^* - n or π^* - π transition.
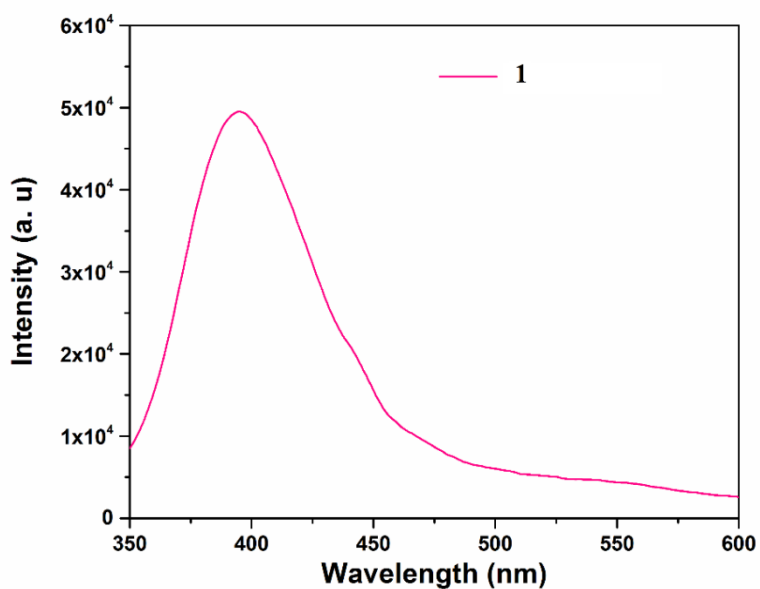
Figure 2.11. Solid state emission spectrum of 1 (λ_{ex}= 340 nm)
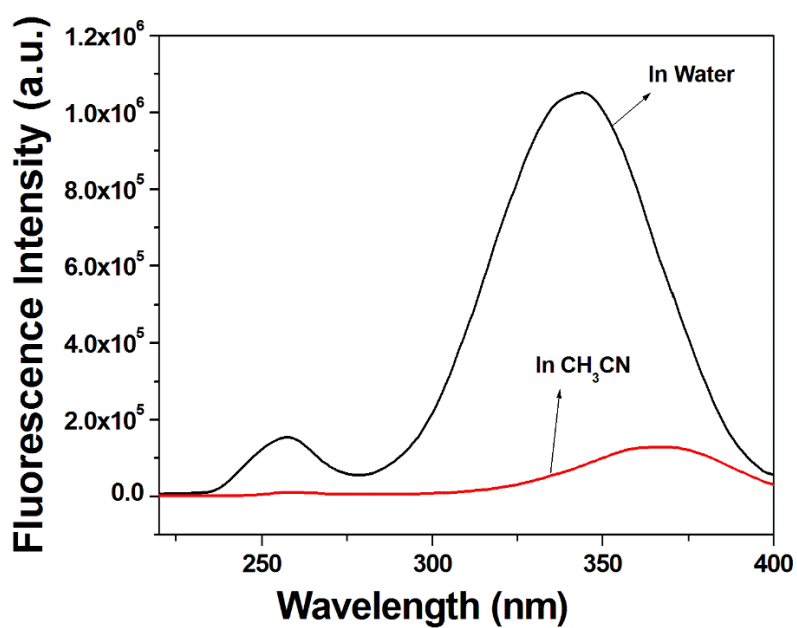
Figure 2.12. Comparison of excitation spectrum of 1 (10 μM) at λ_{em} = 428 nm in acetonitrile and water media
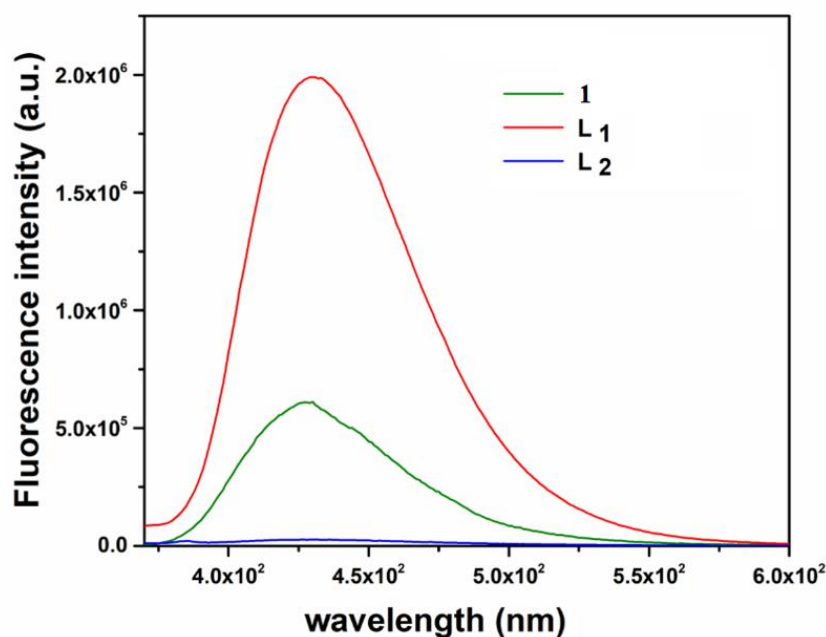
Figure 2.13. Emission spectra of L$_1$, L$_2$ and 1 (10 μM) measured in water dispersed medium (λ$_{ex}$ = 370 nm)

However, luminescence intensity markedly diminished for $\{[Cd(L_1)(L_2)](DMA)\}_n$ (**1**) compared to that of L$_1$ upon excitation at 370 nm (Figure 2.13). It is well known that for d^{10} metal compounds, no emission originates from the metal-to-ligand (MLCT) or ligand-to-metal charge transfer (LMCT) excited states, since the d^{10} metal ions are normally difficult to be oxidized or reduced [45–48]. Therefore, the fluorescent emission of **1** may be assigned primarily to the intra-ligand and inter-ligand charge transfer (ILCT) [49]. Emission spectral properties of $\{[Cd(L_1)(L_2)](DMA)\}_n$ (**1**) clearly demonstrate that the MOF is a potential candidate for luminescent sensor. In addition, two structural features of the framework are, particularly, of interest to undertake sensing studies: (i) the desolvated MOF being porous the organic molecules and metal ions dissolved in the solvent can be able to enter into interior of the MOF and (ii) after removal of DMA molecule from **1**, free –NH$_2$ groups of luminescent L$_1$ are poised to interact with organic molecules or metal ions that can modify its photoluminescence responses. Further, structural integrity of the desolvated MOF remained intact as no significant changes of the PXRD patterns of the as-synthesized and desolvated species are observed upon exposure to water (Figure. 2.7). It is pertinent to mention here that

water vapor sorption analysis clearly demonstrates water molecule can diffuse into interior of the solid MOF through pores.

To begin with luminescence sensing of nitro-aromatics, UV-Vis titration of the desolvated **1** against 2,4,6- trinitrophenol (TNP) was first recorded in water.
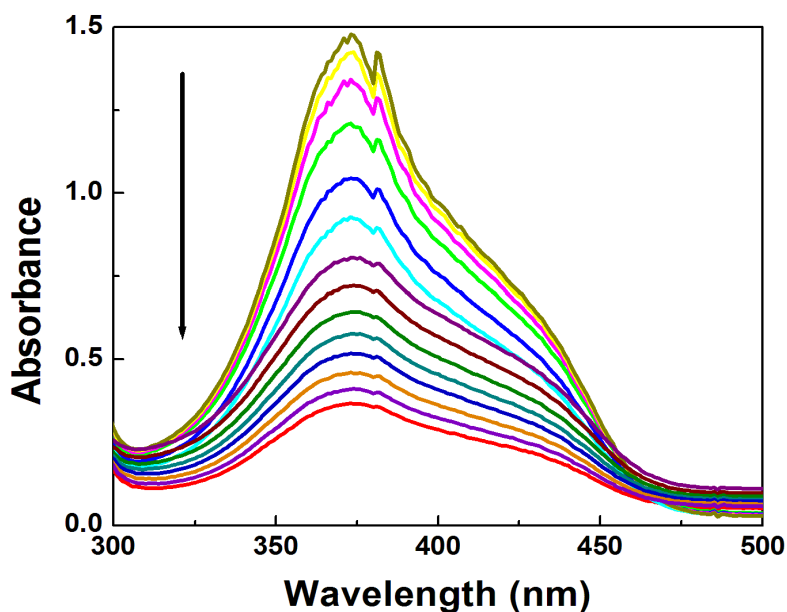
Figure 2.14 Absorption titration of 1 against TNP in water medium (change of intensity with TNP concentration directed by arrow)

$\{[Cd(L_1)(L_2)](DMA)\}_n$ (**1**) displayed well-defined absorption bands centered at 373 nm. On gradual addition of TNP there is a consistent decrease in absorbance at 373 nm (Figure 2.14). The fluorescence spectra of $\{[Cd(L_1)(L_2)](DMA)\}_n$ (**1**) exhibits a very strong emission band at 428 nm in the absence of TNP upon excitation at 370 nm. Notably, upon incremental addition of TNP there is a consistent decrease in emission and the emission shifted to 450 nm from 428 nm. The shift of emission λ_{max} may be attributable to interaction between framework and TNP through strong hydrogen bonds with free $-NH_2$ in presence of desolvated **1** (Figure 2.15). The emission spectra of the desolvated **1** and its fluorescence titrations against TNP (0–20 mM) were recorded. To ascertain the particle size of $\{[Cd(L_1)(L_2)](DMA)\}_n$ (**1**) during spectral measurements, dynamic light scattering study has been undertaken maintaining the experimental conditions. Particle size distributions remained almost unaffected upon gradual

increase of the concentration of TNP (Figure 2.16-2.18). After obtaining these encouraging luminescent emission results, the efficacy of **1** has been investigated for selective aqueous phase detection of nitroaromatics. To this end, emission spectral measurements of $\{[Cd(L_1)(L_2)](DMA)\}_n$ (**1**) were undertaken with addition of various nitroaromatics, such as, 2,4,6-trinitrophenol, 4-nitro benzoic acid, 2-nitrotoluene, 4-nitrotoluene, 1,2-dinitrobenzene and 2,4 dinitrophenol in water. The emission spectra showed variation of quenching efficiency towards the emission intensity of **1** for different nitro analytes. Remarkably, among all the nitro analytes, 2,4,6-trinitrophenol exhibits highest quenching of the emission intensity of **1** (Figure 2.19).
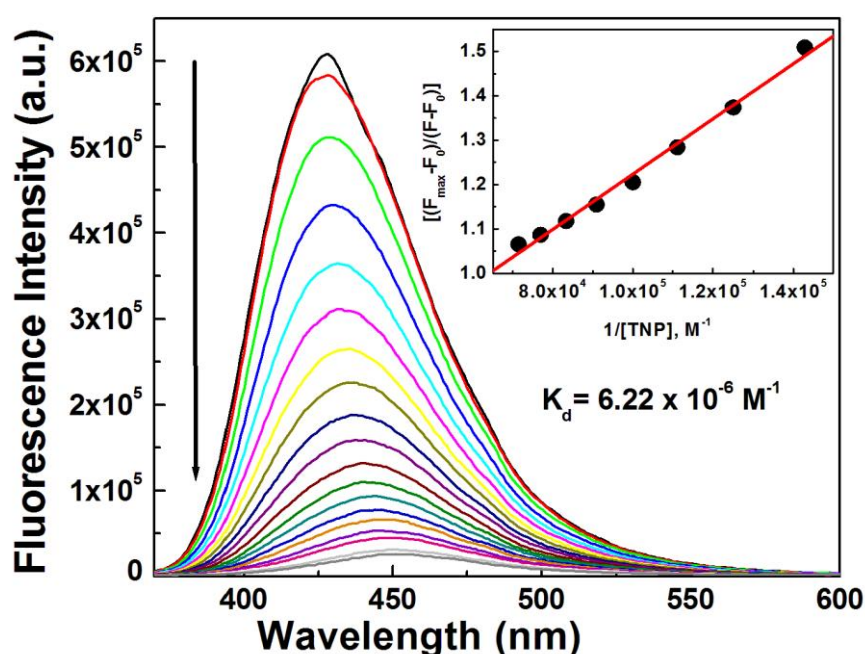
Figure 2.15. Fluorescence titration of desolvated 1 (10μM) against TNP (0-20μM) in water medium (λ_{ex}= 370 nm). Fluorescence maxima at 428 nm gradually shifted to 450 nm with increasing concentration of TNP during titration. Inset: Benesi-Hilderbrand fitting data

The Benesi-Hilderbrand equation (Eqn. No. 2.1) has been employed to determine the dissociation constant for $\{[Cd(L_1)(L_2)](DMA)\}_n$ (**1**)-TNP aggregate and to understand the quenching efficiency. The emission maxima (λ_{em}) at 428 nm display spectral overlap with the

absorption spectrum of TNP which lead to efficient quenching of this band by an energy transfer mechanism.

$$\frac{F_{max} - F_0}{F - F_0} = 1 + \frac{1}{K_d[M_n]} \ldots\ldots\ldots\ldots \textbf{Eqn. No. 2.1}$$

Where F_0 = initial fluorescence intensity, F_{max} = final fluorescence intensity, F = fluorescence intensity at a particular dispersed **1** medium while M = concentration of analytes. A linear least squares fit of $(F_{max} - F_0)/(F - F_0)$ against 1/[TNP] plot clearly reveals the dissociation constant (K_d) value 6.22×10^{-1} M^{-1} (Figure. 2.15) [50].

It is well established that when the absorption bands of the non-emissive analyte exhibit considerable overlap with the emission spectra of fluorophore, resonance energy transfer can occur efficiently [51]. Probability of resonance energy transfer greatly depends on the extent of spectral overlap between the analyte's absorption band and the emission band of the luminophore. A large extent of overlap between the absorption spectrum of TNP and the emission spectrum of **1** is observed in present case (Figure 2.18). It is pertinent to mention that free–NH$_2$ group is capable of forming strong H-bond through nitro group of nitroaromatics [34]. To understand the efficacy of the luminescence sensing procedure it is important to calculate limit of detection (LOD) of the analytes.
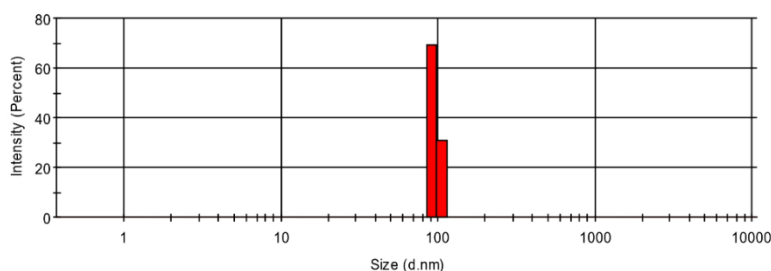
Figure 2.16. Dynamic light scattering plot showing particle size distribution of 1 (2 μM) in water medium
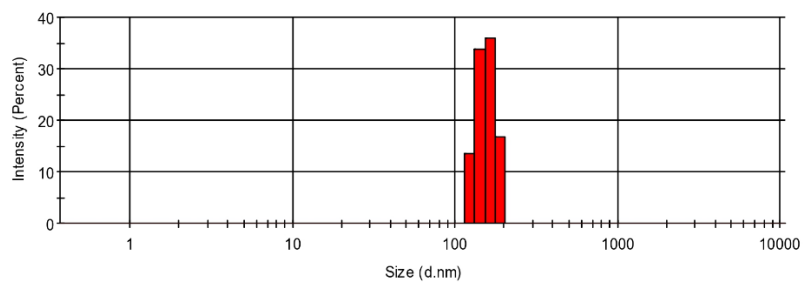
Figure 2.17. Dynamic light scattering plot showing particle size distribution of 1 (2 μM) in presence of TNP in water medium
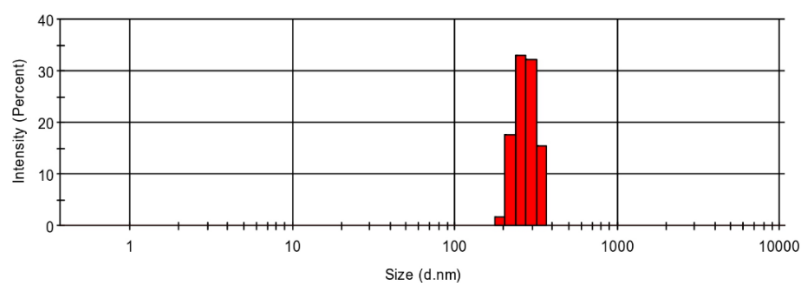
Figure 2.18. Dynamic light scattering plot showing particle size distribution of 1 (5 μM) in presence of TNP in water medium
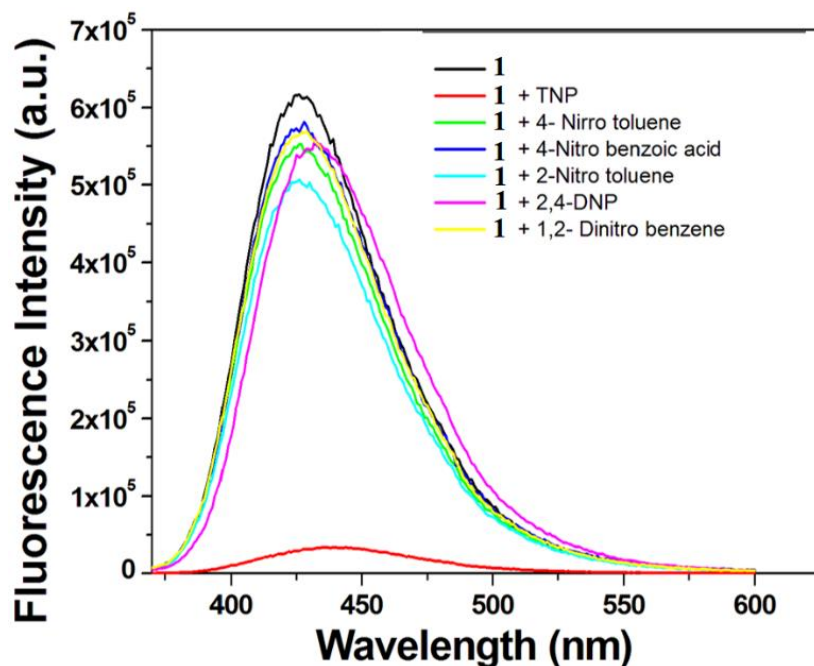
Figure 2.18. Fluorescence response of 1 towards various nitro explosives (vide Experimental section for sample preparation procedure)
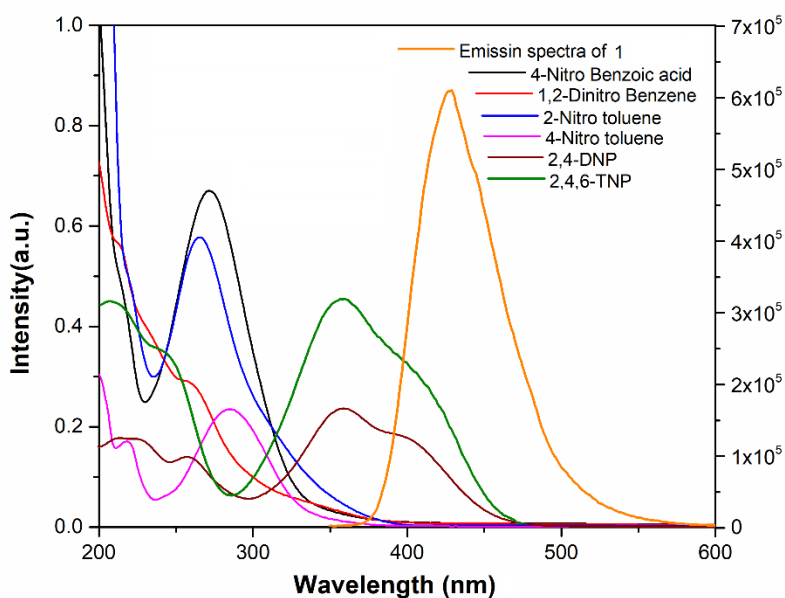
Figure 2.19. Plot showing the extent of spectral overlap between absorption band of nitroaromatics and emission band of the 1

In this study the detection limit for TNP has been determined. In order to calculate LOD (Limit of detection), fluorescence titration of **1** against TNP was carried out by adding aliquots of the micro molar concentration of TNP and LOD has been calculated by the 3σ method [52].

$$LOD = 3 \times \frac{\sigma}{S}$$

Where, σ is the standard deviation of the intercept of the blank (**1** only) obtained from a linear fitting of fluorescence intensity versus concentration of $\{[Cd(L_1)(L_2)](DMA)\}_n$ (**1**) plot, and S is the slope obtained from the linear part of the plot (Figure. 2.20). The 3σ method afforded the detection limit (LOD) of TNP equal to 7.03 μM.
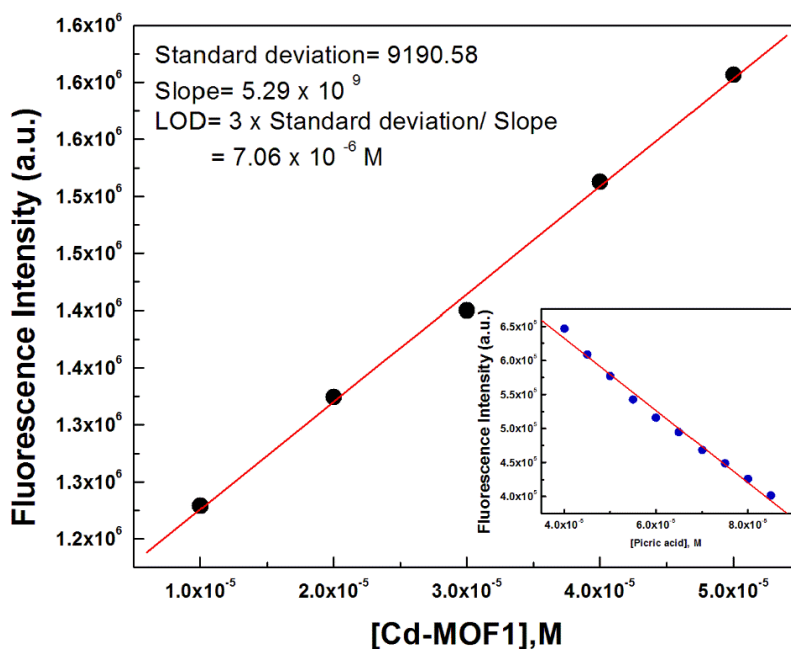
Figure 2.20. Determination of LOD of TNP by 3σ method
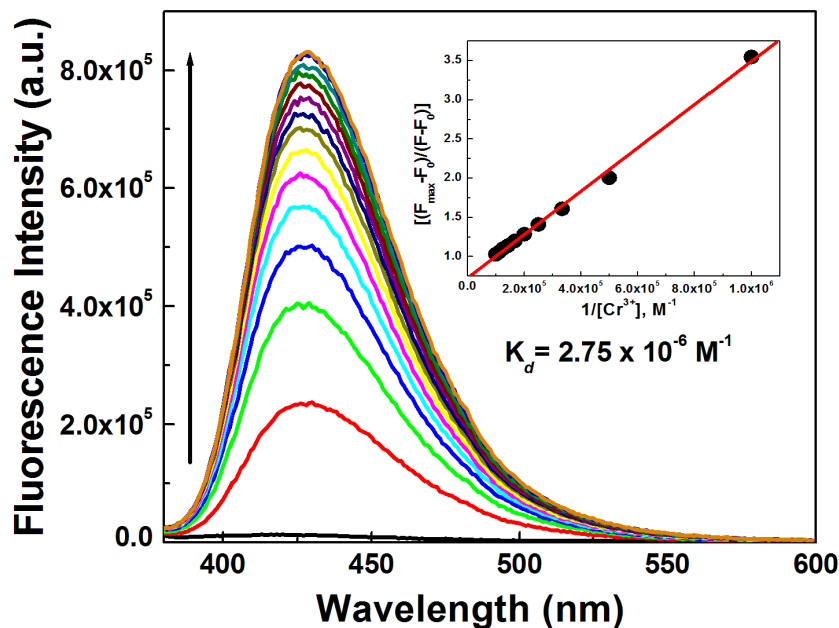
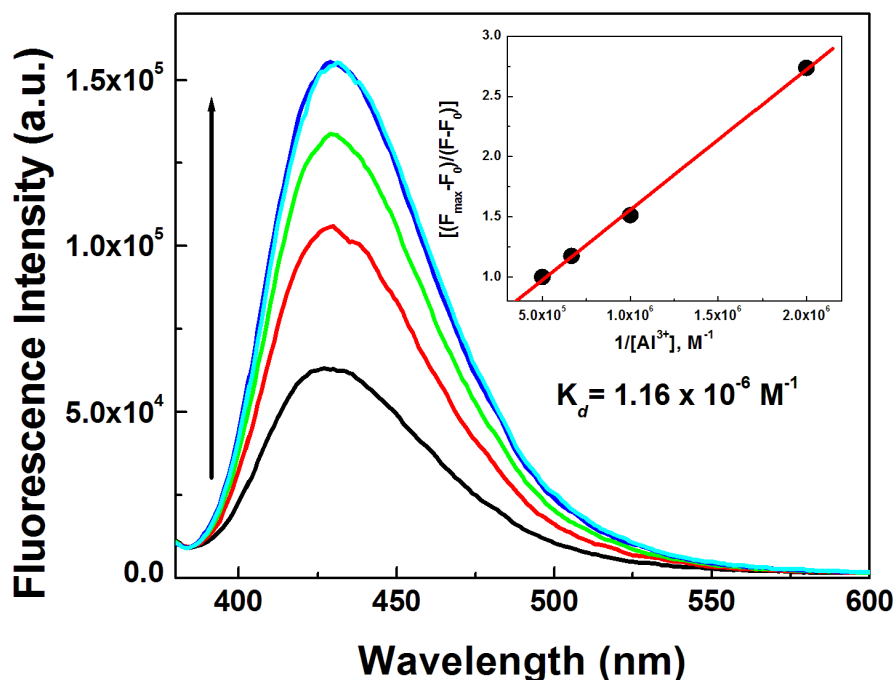**Figure 2.21. Fluorescence titration of 1 (10 mM) with increasing concentration of Cr^{3+}(0–11 mM) in CH_3CN medium (λ_{ex} = 370 nm and λ_{em} = 428 nm). Inset: Benesi–Hiderbrand fitting plot and red line denotes the least squares fit.**

After succeeded in luminescence sensing of TNP over **1** in aqueous medium attempted has been made to investigate sensing ability of **1** toward metal ions. In order to judge sensing ability fluorescence spectra of dispersed $\{[Cd(L_1)(L_2)](DMA)\}_n$ (**1**) were measured in presence of aqueous solution of the corresponding nitrate salt of the metal ions Ca^{2+}, Co^{2+}, Cu^{2+}, K^+, Mg^{2+}, Mn^{2+}, Na^+, Ni^{2+}, Sn^{2+}, Zn^{2+}, Cd^{2+}, Hg^{2+}, Cr^{3+}, Fe^{3+} and Al^{3+}. Interestingly, amongst all of them only trivalent metal ions, Cr^{3+}, Fe^{3+} and Al^{3+} gives turn-on response over **1**. The emission spectra of **1** and its titration with aqueous solution of trivalent metal ions (Cr^{3+}, Fe^{3+} and Al^{3+}) were recorded using a fixed concentration of **1** (Conc. = 10 µM) dispersed in CH_3CN medium (Figure 2.21-2.23). During the titration there was gradual increase of the fluorescence intensities with increasing concentration of metal ions.
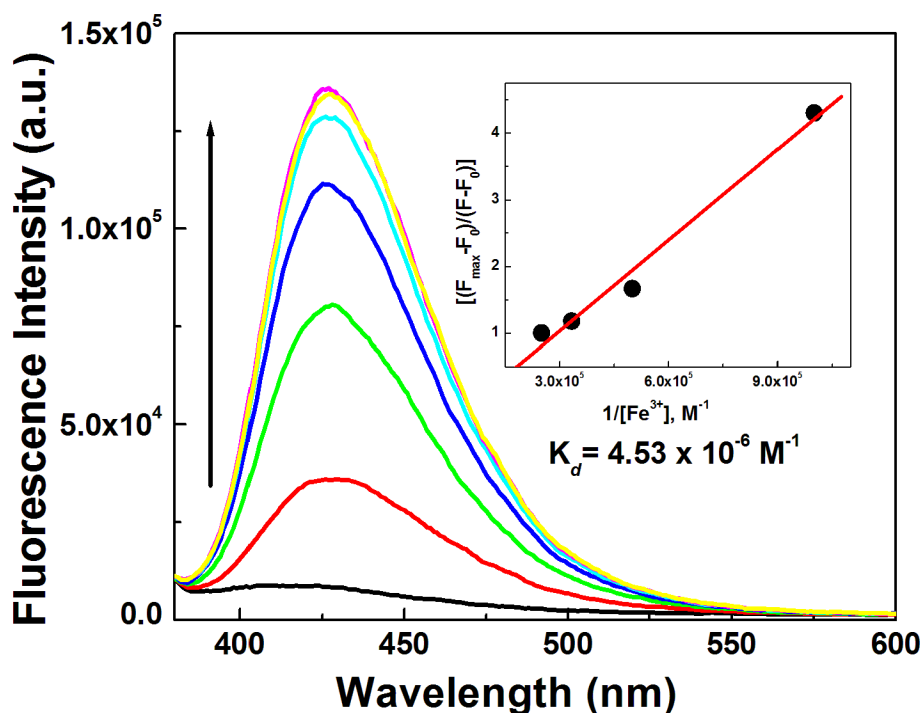
Figure 2.22. Fluorescence titration of 1 (10 mM) with increasing concentration of Fe^{3+}(0–11 mM) in CH_3CN medium (λ_{ex} = 370 nm and λ_{em} = 428 nm). Inset: Benesi–Hiderbrand plot and red line denotes the least squares fit.

There has been 80, 16 and 15 fold enhancement of fluorescence intensity for Cr^{3+}, Fe^{3+} and Al^{3+}, respectively, upon excitation at 370 nm (Figure. 2.24). The K_d values calculated using Benesi–Hilderbrand equation were 2.75×10^{-6} M^{-1}, 4.53×10^{-6} M^{-1} and 1.16×10^{-6} M^{-1} for Cr^{3+}, Fe^{3+} and Al^{3+}, respectively. The K_d value indicates good binding of Cr^{3+}, Fe^{3+} and Al^{3+} with $\{[Cd(L_1)(L_2)](DMA)\}_n$ (**1**) framework solid. The pendent $–NH_2$ group in the porous **1** (*vide supra*) which is poised to interact with incoming metal ions might giving the stability of $\{[Cd(L_1)(L_2)](DMA)\}_n$ (**1**)-metal ion binding through complex formation. The fluorescence intensity observed in the order Cr > Fe > Al.

Figure 2.23. Fluorescence titration of 1 (10 mM) with increasing concentration of Al^{3+} (0 mM–11 mM) in CH_3CN medium (λ_{ex} = 370 nm and λ_{em} = 428 nm). Inset: Benesi–Hiderbrand plot and red line denotes the least squares fit

The higher fluorescence intensity for Cr^{3+} probably due to the higher crystal field stabilization energy (CFSE) that leads stronger interaction between $-NH_2$ group of **1** and Cr^{3+} ions than that of Fe^{3+} or Al^{3+}. As Al^{3+} ion does not offer any CFSE, its fluorescence is being the least intense. The strong fluorescence emission in this case seems to be due to photoinduced energy transfer (PET) which is facilitated because of interaction between Lewis base site ($-NH_2$) and the trivalent metal ion. To get deeper insight into the interaction between $-NH_2$ group and Cr^{3+}, Fe^{3+} and Al^{3+} ions, IR spectra of $\{[Cd(L_1)(L_2)](DMA)\}_n$ (**1**) has been measured after treating with metal nitrate solutions. The N–H vibration bands (stretching and bending) of **1** were considerably affected after treatment with metal ion solutions. While shifting of N–H stretching vibration bands (appearing at ca. 3300 cm^{-1}) were, however, minimal, the shifting of N–H bending vibrations (appearing at ca.1550 cm^{-1}) towards lower wave-number region was remarkable after the treatment of metal ions (Figure 2.1). Besides, comparison of powder X-ray diffraction lines of pristine **1** and framework solid recovered after metal (Cr^{3+}, Fe^{3+}, Al^{3+}) sensing experiment is over, indicate integrity of the framework was remained intact (Figure

2.25). Minor change of intensity and slight shift of some diffraction lines of **1** after metal ions sensing (Cr^{3+}, Fe^{3+}, Al^{3+}) could be attributed to the lowering of local order due to interaction between the metal ions (Cr^{3+}, Fe^{3+}, Al^{3+}) and the framework.
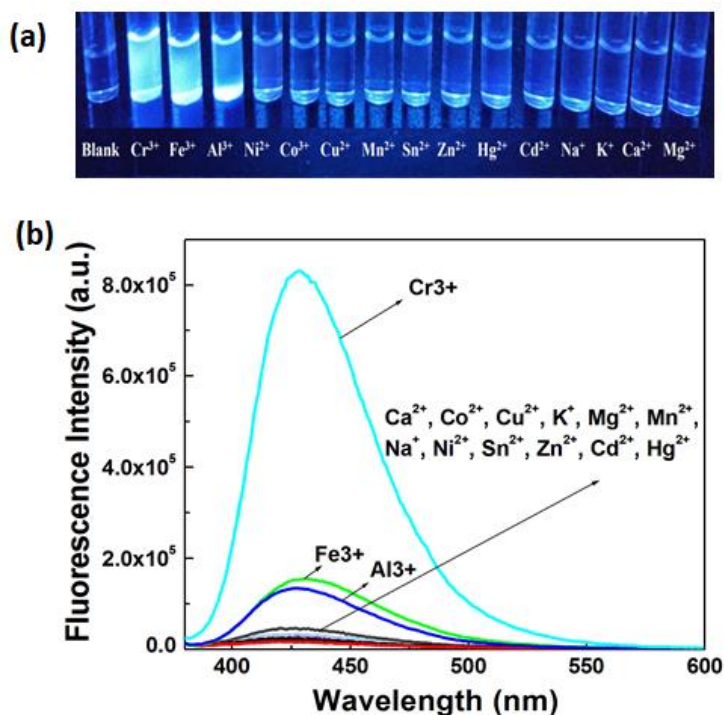
Figure 2.24. (a) Visual change of fluorescence intensity of 1 upon addition of metal ions (in water) under UV light; (b) Fluorescence response of 1 towards various metal ions
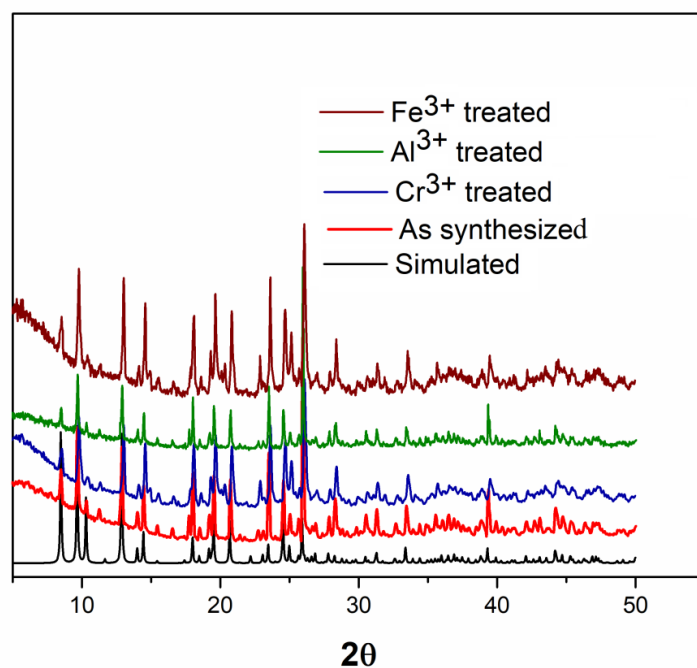
Figure 2.25. Powder X-ray diffraction patterns of 1 and solid recovered after metal ion (Fe^{3+}, Al^{3+} and Cr^{3+}) sensing experiment
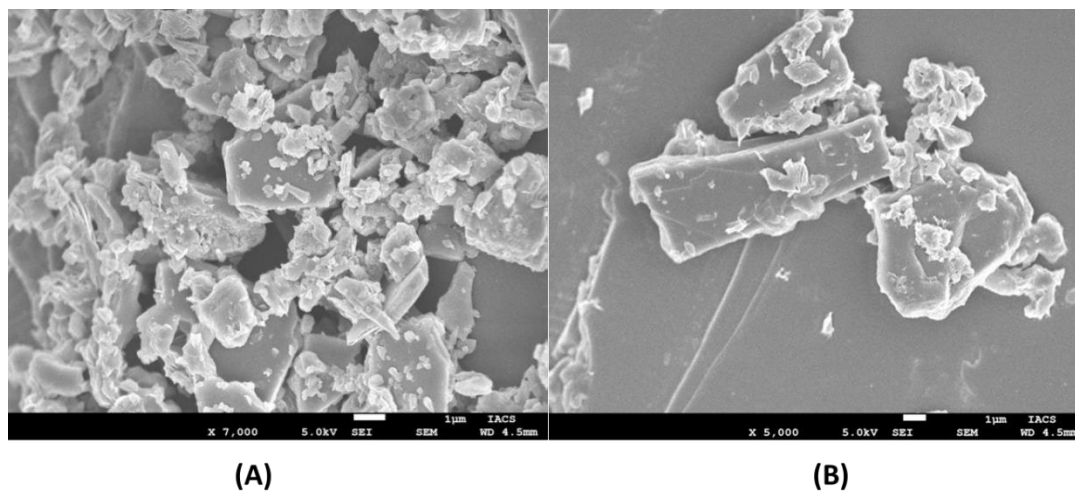
Figure 2.26. FE-SEM images of pure 1 (A) and metal treated 1 (B)

It is noteworthy that the field emission scanning electron microscopic (FE-SEM) images of pristine and metal treated {[Cd(L$_1$)(L$_2$)](DMA)}$_n$ (**1**) showed no noticeable difference in their crystallinity (Figure 2.26). The presence of metal ions in metal-salt treated **1** has been confirmed through EDS study (Figure 2.27).

Element	Weight %
C K	25.49
N K	16.89
O K	43.01
AlK	8.69
CdL	5.92

Element	Weight %
C K	7.16
N K	11.15
O K	39.99
CdL	4.68
FeK	37.02

Element	Weight %
C K	12.3528
N K	13.0594
O K	29.3898
CdL	14.3553
CrK	30.8427

Figure 2.27. EDS analysis of (a) Al^{3+} treated 1; (b) Fe^{3+} treated 1; (c) Cr^{3+} treated 1
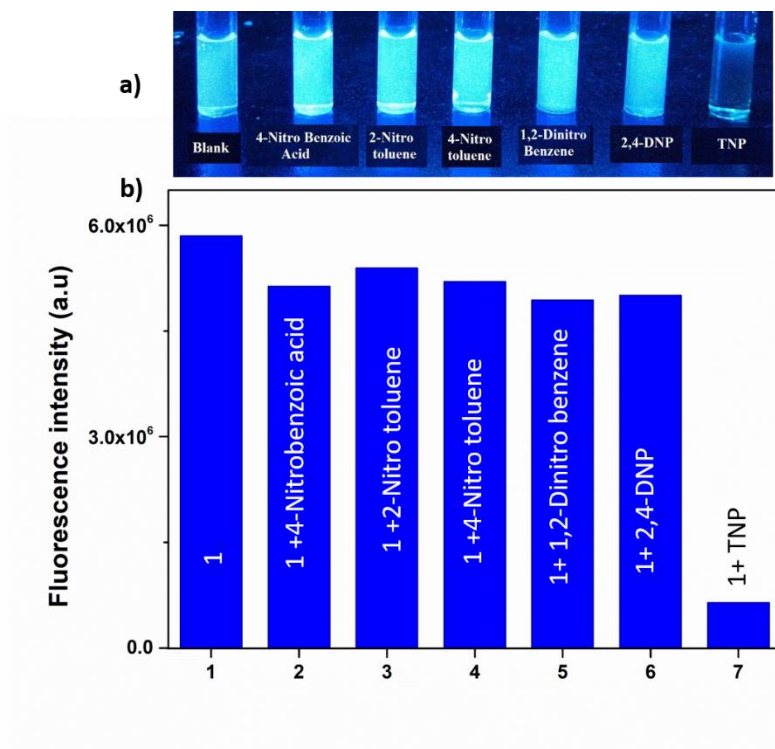
Figure 2.28. (a) Visual change of fluorescence intensity of 1 (in water) addition of nitro explosives under UV light; (b) Bar chart showing fluorescence response of 1 towards different nitro aromatics

Selectivity study is the essential requirement in search for an efficient fluorescent chemical sensor. This study reveals that amongst all nitro-explosives only TNP interact with $\{[Cd(L_1)(L_2)](DMA)\}_n$ (**1**) (Figure 2.28) and shows quenching, while amongst the all other metal ions it is only sensing the trivalent metal ions (Figure 2.27). It is interesting to mention that in the both the cases the luminescent color change could be observed by naked eye. No other metal ions such as Ca^{2+}, Co^{2+}, Cu^{2+}, K^+, Mg^{2+}, Mn^{2+}, Na^+, Ni^{2+}, Sn^{2+}, Zn^{2+}, Cd^{2+}, Hg^{2+} are interfering with trivalent metal ions. LOD values are also calculated for metal ions. LOD values for Cr^{3+}, Fe^{3+} and Al^{3+} are calculated to be 0.45 μM, 0.88 μM and 0.38 μM, respectively (Figure 2.21-2.23).

2.4 Conclusion

In summary, an interpenetrated 3D mixed-linker cadmium based porous metal–organic framework, $\{[Cd(L_1)(L_2)](DMA)\}_n$ (**1**) has been synthesized through solvothermal route and characterized. The desolvated porous **1** displayed good adsorption capacity towards water vapor. Photoluminescence properties of the framework solid have been thoroughly investigated. The MOF system displayed ''turn on'' and ''turn off'' type of photoluminescence responses selectively towards trivalent metal ions and nitro aromatics, respectively. The pendent $–NH_2$ group seems played important roles in fluorescent sensing. As **1** is capable of detecting aqueous phase analytes though luminescent sensing it has potential to allow preliminary in-field screening of industrial and environmental samples. Hence, $\{[Cd(L_1)(L_2)](DMA)\}_n$ (**1**) is a promising material for practical usage, particularly, in sensing applications.

2.5. Reference

1. B. L. Chen, S. C. Xiang, G. D. Qian, Acc. Chem. Res. 2010, **43**, 1115.

2. Y. Takashima, V. M. Martinez, S. Furukawa, M. Kondo, S. Shimomura, H. Uehara, M. Nakahama, K. Sugimoto, S. Kitagawa, Nat. Commun. 2011, **2**, 168.

3. L. E. Kreno, K. Leong, O. K. Farha, M. Allendorf, R. P. Van Duyne, J. T. Hupp, Chem. Rev. 2012, **112**, 1105.

4. S.-R. Zhang, D.-Y. Du, J.-S. Qin, S.-J. Bao, S.-L. Li, W.-W. He, Y.-Q. Lan, P. Shen, Z.-M. Su, Chem. – Eur. J. 2014, **20**, 3589.

5. M. R. Tchalala, P. M. Bhatt, K. N. Chappanda, S. R. Tavares, K. Adil, Y. Belmabkhout, A. Shkurenko, A. Cadiau, N. Heymans, G. De Weireld, G. Maurin, K. N. Salama, M. Eddaoudi, Nat. Commun. 2019, **10**, 1328.

6. J. R. Lakowicz, Principles of Fluorescence Spectroscopy, Springer. 3rd edn., 2006.

7. J. O. Nriagu, Science. 1996, **272**, 223.

8. C. Fu, X. Sun, G. Zhang, P. Shi, P. Cui, Inorg. Chem. 2021, **60**, 1116.

9. Y.-W. Li, J. Li, X.-Y. Wan, D.-F. Sheng, H. Yan, S.-S. Zhang, H.-Y. Ma, S.-N. Wang, D.-C. Li, Z.-Y. Gao, J.-M. Dou, D. Sun, Inorg. Chem. 2021, **60**, 671.

10. D. Zhao, X.-H. Liu, Y. Zhao, P. Wang, Y. Liu, M. Azam, S. I. Al-Resayes, Y. Lu, W.-Y. Sun, J. Mater. Chem. A, 2017, **5**, 15797.

11. H. Yu, Q. Liu, J. Li, Z.-M. Su, X. Li, X. Wang, J. Sun, C. Zhou, X. Hu, J. Mater. Chem. C, 2021, **9**, 562.

12. D. K. Singha, P. Mahata, Inorg. Chem. 2015, **54**, 6373.

13. Z.-F. Wu, L.-K. Gong, X.-Y. Huang, Inorg. Chem. 2017, **56**, 7397.

14. A. Borriello, I. Calderlli, M. C. Speranza, S. Scianguetta, A. Tramontano, D. Bencivenga, E. Stampone, A. Negri, B. Nobili, F. Locatelli, S. Perrotta, A. Oliva, F. D. Ragione, Biochim. Biophys. Acta, Gen. Subj. 2016, **1860**, 1211.

15. A. A. Mousa, M. Ghonem, E. M. Elhadidy, E. Azmy, M. Elbackry, A. A. Elbiomy, R. R. Elzehery, G. A. Shaker, O. Saleh, Endocr. Res. 2016, **41**, 81.

16. P. D. Pigatto, A. Ronchi, G. Guzzi, Int. J. Hematol. 2016, **103**, 724.

17. V. Rai, P. Vajpayee, S. N. Singh, S. L. Mehroto, Plant Sci. 2004, **167**, 1159.

18. Y.-S. Wang, Z.-Y. Pan, J.-M. Lang, J. M. Xu, Y.-G. Zheng, J. Hazard. Mater. 2007, **147**, 319.

19. P. Nayak, Environ. Res. 2002, **89**, 101.

20. S. Vallejos, A. Munoz, S. Ibeas, F. Serna, F. C. Garcia, J. M. Garcia, ACS Appl. Mater. Interfaces 2015, **7**, 921.

21. G. D. Fasman, Coord. Chem. Rev. 1996, **149**, 125.

22. K. P. Keep, Chem. Rev. 2012, **112**, 5193.

23. D. P. Perl, A. R. Brody, Science 1980, **208**, 297.

24. A. Shokrollahi, M. Ghaedi, M. S. Niband, H. R. Rajabi, J. Hazard. Mater. 2008, **151**, 642.

25. A. Salifoglou, Coord. Chem. Rev. 2002, **228**, 297.

26. S. Samanta, S. Goswami, M. N. Hoque, A. Ramesh, G. Das, Chem. Commun. 2014, **50**, 11833.

27. Y. Salinas, R. Martinez-Manez, M. D. Marcos, F. Sancenon, A. M. Castero, M. Parra, S. Gil, Chem. Soc. Rev. 2012, **41**, 1261.

28. S. W. Thomas, G. D. Jolly, T. M. Swager, Chem. Soc. Rev. 2007, **107**, 1339.

29. B. Chen, L. Wang, Y. Xiao, F. R. Fronczek, M. Xue, Y. Cui, G. Qian, Angew. Chem., Int. Eng. Ed. 2009, **48**, 500.

30. X. Zhou, H. Li, H. Xiao, L. Li, Q. Zhao, T. Yang, J. Zuo, W. Huang, Dalton Trans. 2013, **42**, 5718.

31. G. He, H. Peng, T. Liu, M. Yang, Y. Zhang, Y. Fang, J. Mater. Chem. 2009, 19, 7347.

32. P. G. Thorne, T. F. Jenkins, Field Anal. Chem. Technol. 1997, **1**, 165.

33. K. M. Wollin, H. H. Dieter, Arch. Environ. Contam. Toxicol. 2005, **49**, 18.

34. S. S. Nagarkar, B. Joarder, A. K. Chaudhari, S. Mukherjee, S. K. Ghosh, Angew. Chem., Int. Eng. Ed. 2013, **52**, 2881.

35. I. Usón, G. M. Sheldrick, Acta Crystallogr., Sect. D: Struct. Biol. 2018, **74**, 106.

36. O. V. Dolomanov, L. J. Bourhis, R. J. Gildea, J. A. K. Howard, H. Puschmann, J. Appl. Cryst. 2009, **42**, 339.

37. SAINT, version 6.02; SADABS, version 2.03, Bruker AXS, Inc.: Madison, WI. 2002.

38. G. M. Sheldrick, Acta Crystallogr. Sect. C: Struct. Chem. 2015, **71**, 3.

39. A. L. Spek, J. Appl. Crystallogr. 2003, **36**, 7.

40. X. Liu, X. Wang, F. Kapteijn, Chem. Rev. 2020, **120**, 8303.

41. B. Joarder, A. V. Desai, P. Samanta, S. Mukherjee, S. K. Ghosh, Chem. -Eur. J. 2015, **21**, 965.

42. V. Stavila, A. A. Talin, M. D. Allendorf, Chem. Soc. Rev. 2014, **43**, 5994.

43. J. Zhang, Y. Huang, D. Yue, Y. Cui, Y. Yang, G. Qian, J. Mater. Chem. B 2018, **6**, 5174.

44. W. P. Lustig, S. Mukherjee, N. D. Rudd, A. V. Desai, J. Li, S. K. Ghosh, Chem. Soc. Rev. 2017, **46**, 3242.

45. L.-P. Zhang, J.-F. Ma, J. Yang, Y.-Y. Pang, J.-C. Ma, Inorg. Chem. 2010, **49**, 1535.

46. B. Roy, S. Mukherjee, P. S. Mukherjee, CrystEngComm. 2013, **15**, 9596.

47. J. Zhang, J. Wu, G. Tang, J. Feng, F. Luo, B. Xu, C. Zhang, Sens. Actuators, B. 2018, **272**, 166.

48. J. Zhang, Y. Huang, D. Yue, Y. Cui, Y. Yang, G. Qian, J. Mater. Chem. B. 2018, **6**, 5174.

49. Z.-Q. Shi, Z.-J. Guo, H. G. Zheng, Chem. Commun. 2015, **51**, 8300.

50. R. Bhowmick, A. S. M. Islam, A. Giri, A. Katarkar, M. Ali, New J. Chem. 2017, **41**, 11661.

51. H. Wang, W. P. Lustig, J. Li, Chem. Soc. Rev. 2018, **47**, 4729.

52. R. Bhowmick, R. Alam, T. Mistri, D. Bhattacharya, P. Karmakar, M. Ali, ACS Appl. Mater. Interfaces. 2015, **7**, 7476.

Chapter - 3

N_2, H_2, CO_2

CO_2

N_2, H_2
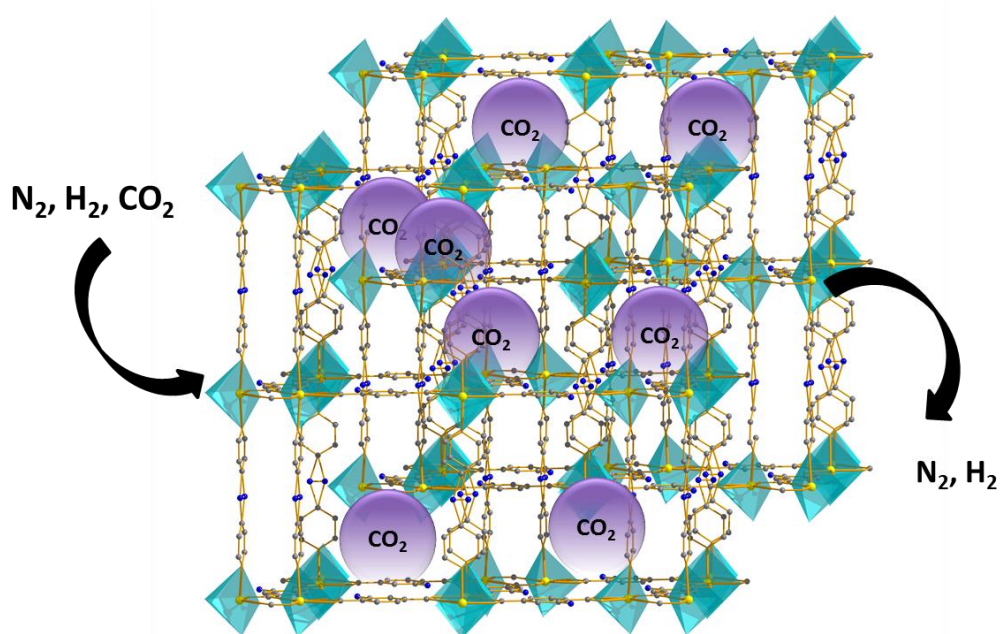
Preferential CO_2 Adsorption over Cadmium-based Porous Metal-organic Framework

3.1 Introduction

Carbon dioxide being primary source of greenhouse gas causing climate change and other environmental disorders, massive emission of anthropogenic CO_2 into the atmosphere has become a greatest environmental concern [1, 2]. Besides, separation of CO_2 from methane (CH_4) is also very crucial for upgradation and the treatment of biogas to improve purity [3]. In addition, pre-combustion CO_2 capture is essential to separate it from hydrogen (H_2), which is produced by the reaction of primary fuel with oxygen or air [4]. Hence, selective sorption of CO_2 is an important issue that needs deeper attention. Selective CO_2 adsorption by the MOFs can be achieved by: (a) control of pore aperture [5], (b) presence of open metal sites within the pore, (c) pore wall decoration by polar functional group [6, 7], or (d) by immobilization of alkali metal ions within the pore [8]. Nonetheless, it is difficult to achieve the selectivity of CO_2 over N_2 and CH_4 only by the fine control of the pore aperture as their kinetic diameters are very close to each other (CO_2 = 3.30 Å, N_2 = 3.65 Å, CH_4 = 3.76 Å). There are only few reports where selectivity is achieved by merely controlling the pore size. In most of the cases pore size as well as pore surface environment together helped in achieving selectivity. Creation of co-ordinately unsaturated metal centers or open metal sites in the cavity of MOF is one of the promising techniques for preparing the selective CO_2 adsorbing MOF. Because of having quadrupole moment, CO_2 can efficiently interact with the co-ordinately unsaturated metal sites present in any MOF. CO_2 uptake capacity of MOFs may be enhanced upon modifying the surface structure of framework by inducting local dipoles which can interact more strongly through weak forces. Hence, inclusion of electronegative atoms like N, O, or F in the pore structure is an effective means to increase adsorption energies for the molecules like H_2 and CO_2 [9-12]. The potential of fluorine or amine groups to interact with CO_2 has been reasonably exploited in the industry, as chemisorption of CO_2 over amines is being applied as an effective tool for removal of CO_2 from flue gases. It has been suggested that amending of pore surface by decorating Lewis base centers (-amino, -pyrimidine, -hydroxo) enhance low pressure CO_2 uptake and increase the isosteric heat of adsorption [10–12]. In order to facilitate CO_2 adsorption in MOFs, incorporation of electronegative atom containing ancillary ligand into the framework will be beneficial. However, it is, challenging to create open metal sites in the mixed-ligand-based MOFs.

Herein, attempt has been made to study the preferential adsorption of CO_2 on a pre-synthesized mixed-linker 3D metal carboxylate framework compound, $\{[Cd(L_1)(L_2)](DMA)\}_n$

(**1**) where L$_1$ is 2-amino-1,4-benzenedicarboxylate and L$_2$ is 4,4´-azopyridine. The linker 2-amino-1,4-benzenedicarboxylate is being used to strategically create polar centers in the pores of **1**. $\{[Cd(L_1)(L_2)](DMA)\}_n$ (**1**) shows very selective CO$_2$ adsorption with respect to small gas molecules like H$_2$, N$_2$, CH$_4$ at low partial pressure.

3.2. Experimental section

3.2.1 Materials

The chemicals required for synthesis of **1** is given in Chapter 2 (*vide* Section 2.2.1).

3.2.2 Physical Measurements

The detail of instruments used for physical measurement of **1** has been described in Chapter 2 (*vide* Section 2.2.2). Details of the gas adsorption methods have been discussed here. Gas sorption isotherms for N$_2$ (77 K), H$_2$ (77 K) and, for CO$_2$ and CH$_4$ (273 and 298 K) in the pressure range 0–1 bar have been measured with an Autosorb iQ (Quantachrome Inc., USA) gas sorption system with an ultra-high pure (99.999% purity) gas source. Before the measurement sample was evacuated under dynamic vacuum (10^{-3} Torr) at the desired temperature (150 °C) for 10 h. For all isotherms, warm and cold free-space correction measurements were performed with ultrahigh pure He gas (99.999% purity). For N$_2$ and H$_2$ sorption required temperature was maintain by using liquid nitrogen (77 K) bath. The CO$_2$ sorption experiment was performed at 273 and 298 K temperature using ice/water bath.

3.2.3 Synthesis $\{[Cd(L_1)(L_2)](DMA)\}_n$ (**1**)

Detailed synthesis procedure of **1** has been described in Chapter 2 (*vide* Section 2.2.3).
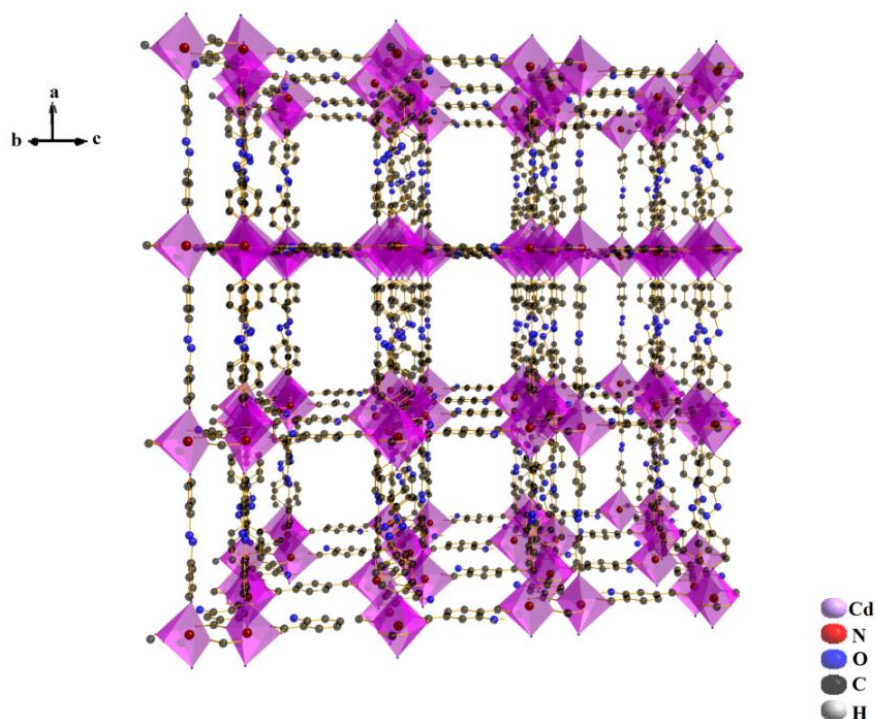
Figure 3.1. 3D network of 1

3.3 Results and discussion

3.3.1 PXRD studies and MOF structure

X-ray structure analysis of **1** has been describe in Chapter 2 (Section 2.2.4). The salient features of the three-dimensional structure which are relevant to adsorption will be discussed here. The networked structure of $\{[Cd(L_1)(L_2)](DMA)\}_n$ (**1**) is depicted in Figure 3.1. **1** possesses a typical pillared-layer mixed-linker system [13], in which metal–carboxylate network propagates as a two-dimensional layer parallel to the crystallographic bc-plane while 4,4´-azopyridine (L$_2$) connects the layers along a-axis to form a three-dimensional network. It is pertinent to mention here that three-dimensional stacking of **1** structure features a two-fold interpenetrated framework (Figure 3.2.). The DMA molecules are entrapped in the 3D cavity. Upon removal of the DMA molecules the network provides rectangular type channels parallel to a-axis with a dimension of ca. 11.6×8.4 Å, in which the -NH$_2$ groups exposed to the pores. The free amine group is poised to attract CO$_2$ through non-bonding interaction which is the key

interest. As a result, enhancement of sorption of CO_2 in comparison to other small gas molecules like H_2, N_2 etc. is expected. Removal of DMA from **1** creates the accessible void space in framework material. The PLATON analysis [14] indicates that the solvent accessible void space is ca. 26.6%.

Before the gas sorption measurements are performed, **1** is made desolvated. To remove DMA molecules $\{[Cd(L_1)(L_2)](DMA)\}_n$ (**1**) is kept immersed in methanol for two days, then the solid material is filtered and evacuated (10^{-3} Torr) at 150 °C for 12 h. To confirm the phase purity of the bulk material of **1**, powder X-ray diffraction (PXRD) measurements were carried out.
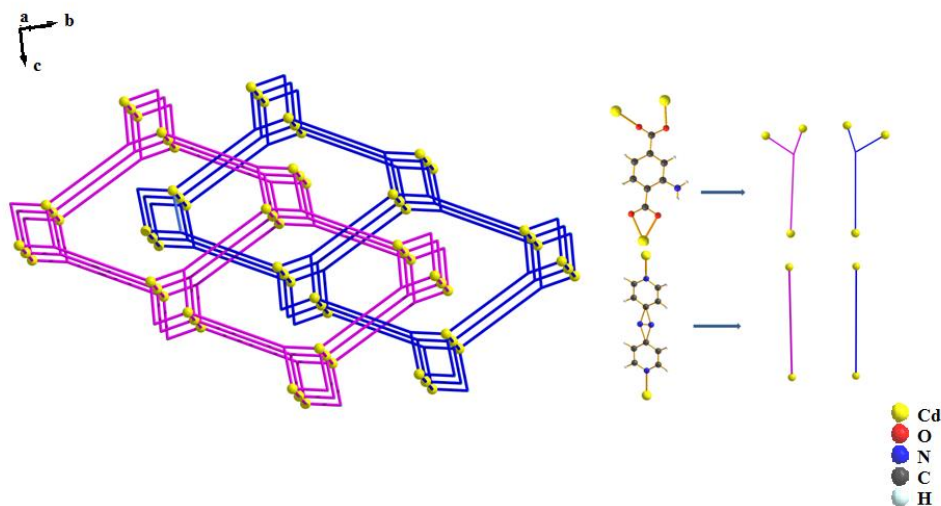
Figure 3.2. Picture showing two-fold interpenetrated structure of 3D framework of 1

The PXRD patterns of the **1** are shown in Figure 3.3. PXRD patterns of **1** were simulated using their single crystal data. Comparison of experimental and simulated PXRD patterns confirms that all the major peaks of experimental PXRD of $\{[Cd(L_1)(L_2)](DMA)\}_n$ (**1**) matched well with those of simulated ones, indicating its reasonable crystalline phase purity. PXRD patterns of the desolvated species are also measured. No noticeable change of diffraction lines is observed after desolvation of **1** suggesting the robustness of the framework (Figure 3.3). The framework structure also retains after gas adsorption study.
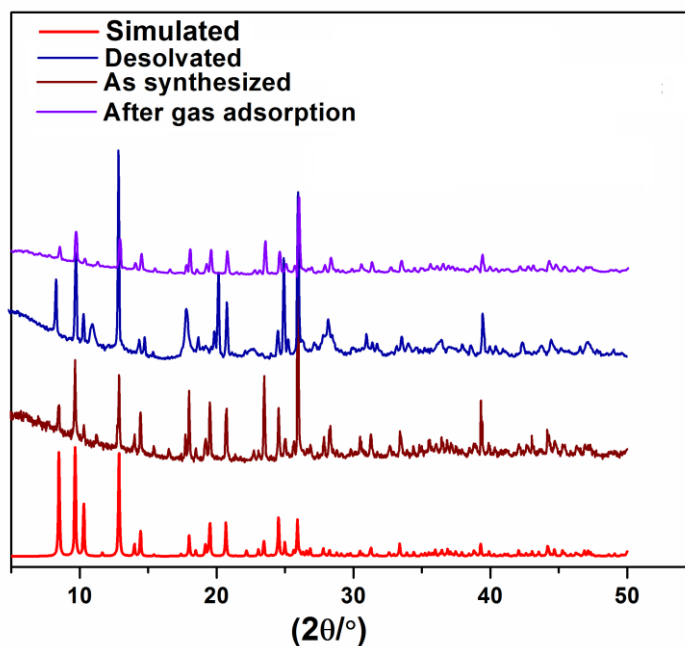
Figure 3.3. PXRD patterns of {[Cd(L$_1$)(L$_2$)](DMA)}$_n$ (1)

3.3.2 Gas sorption study

The desolvated species of {[Cd(L$_1$)(L$_2$)](DMA)}$_n$ (**1**) contains solvent accessible voids (*vide supra*) and pore sizes of the framework are seem to be bigger than the kinetic diameter of N$_2$, CH$_4$, CO$_2$ and H$_2$. Thus, to evaluate the porosity and adsorption capability of **1**, N$_2$, H$_2$, CH$_4$ and CO$_2$ adsorption measurements of the compound have been carried out. Before gas sorption analysis, the samples were activated as described in Experimental section (*vide supra*). Desolvated **1** exhibited preferential adsorption towards CO$_2$ in respect of N$_2$, CH$_4$ and H$_2$ especially in the low pressure region. This preferential CO$_2$ adsorption capacity of the activated **1** with respect to N$_2$ and H$_2$ is comparable with other reported 3D-porous MOFs [15-19]. Permanent microporosity of the framework has been verified through the N$_2$ adsorption measurement. The BET surface area of the MOF is 42.12 m^2/g. The H$_2$ uptake capacity of the desolavated MOF reached to 0.31 wt% or 34.87 cm^3/g at the adsorbate pressure of 1 bar at 77 K (Figure 3.4). It is noteworthy that {[Cd(L$_1$)(L$_2$)](DMA)}$_n$ (**1**) featured a 2-fold interpenetration in its structure (*vide supra*) which can compensate the void space created upon desolvation, leading to low N$_2$ sorption [20].

CO$_2$ adsorption isotherms for the desolvated **1**, was measured at 273 and 298 K up to 1 bar pressure. At 298 K, the desolvated MOF showed an uptake of carbon-dioxide of 8.33 wt% or 42.42 cc/g at 1 bar pressure which is being increased to ca. 12.17 wt% or 62 cc/g at 1 bar pressure, upon cooling to 273 K (Figure 3.5). Similarly, CH$_4$ adsorption isotherms for the desolvated **1** were also measured at 273 and 298 K up to 1 bar pressure. In contrast, CH$_4$ uptake capacities of the desolavated MOF were 0.127 wt% or 1.79 cm^3/g and 1.34 wt% or 18.74 cm^3/g at the adsorbate pressure of 1 bar at 298 K and 273 K, respectively (Figure. 3.6). For post-combustion CO$_2$ capture, the pressure of the flue gas (~1 bar) and the low partial pressure of CO$_2$ (0.15 bar) that leads to the lower pressure region of the CO$_2$ adsorption isotherm is particularly interesting [21]. CO$_2$ adsorption of $\{[Cd(L_1)(L_2)](DMA)\}_n$ (**1**) shows type I isotherms. Steepness of the slope in the low pressure part of the isotherms indicates strong adsorption. The presence of hysteresis in adsorption desorption isotherm also indicates the presence of strong interaction of CO$_2$ with the surface of the framework. The selective CO$_2$ adsorption capacity of some 3D-porous MOFs with respect to N$_2$, H$_2$ and CH$_4$ have been previously reported [15, 16, 18, 22-33]. The selective CO$_2$ uptake capacity of desolvated **1** is comparable with those MOFs [15, 16, 18, 22-27]. It is noteworthy that **1** is moderately selective towards CO$_2$ adsorption over all three small gas molecules (H$_2$, N$_2$, CH$_4$) at low partial pressure.

High selectivity of CO$_2$ by the PCPs over multiple gas molecules are scanty in literature [33, 34]. Preferential CO$_2$ adsorption by the 2D Cu(II) PCP have been achieved onto MOF having the pore wall surface decorated by the fluorinated anions due to the strong interaction with CO$_2$ [34].
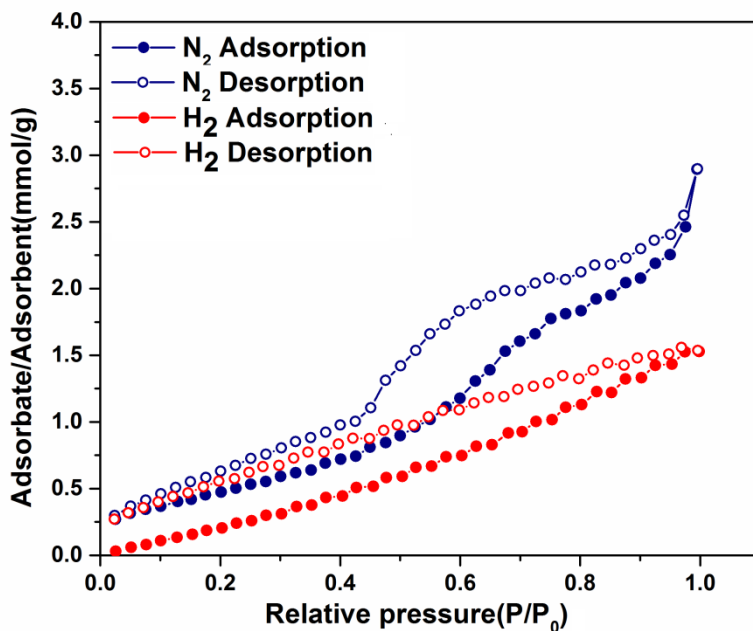
Figure 3.4. Gas adsorption isotherms of N$_2$ (blue), H$_2$ (red) measured at 77 K

CO$_2$ sorption selectivity of desolvated species of **1** was calculated using the ratio of the initial slopes in the Henry region of the CO$_2$ and CH$_4$ adsorption isotherms at 273 K. Selectivity of CO$_2$ with respect to CH$_4$ at 273 K is calculated to be 5.5 (Figure 3.7). Heat of adsorption calculated for **1** using DFT model with respect to the CO$_2$ isotherms of 298 K and 273 K was ~ 38 kJ mol^{-1} (Figure 3.8.). At higher loading of these values fall slightly as the highest affinity sites are filled.
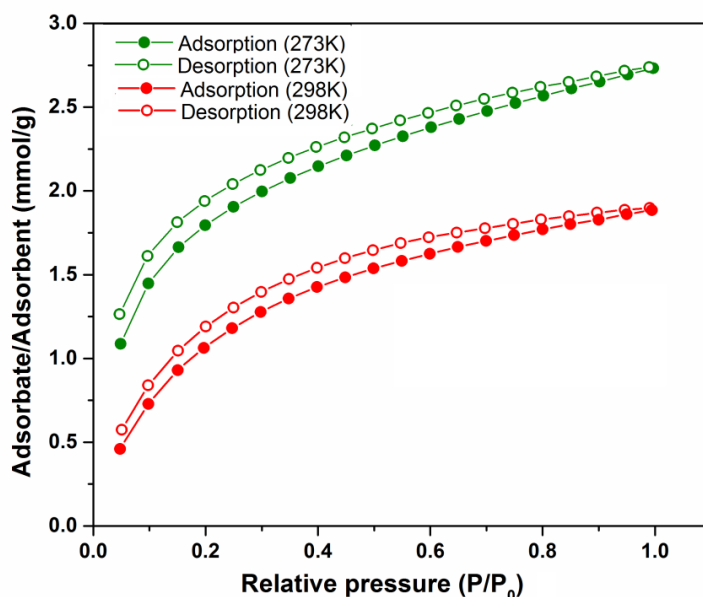
Figure 3.5. CO$_2$ adsorption isotherms measured at the temperature 273 K (green) and 298 K (red)

SIFSIX-2-Cu-i refer to $[Cu(dpa)_2(SiF_6)]_n.2.5\ CH_3OH$ is composed of doubly interpenetrated nets that are isostructural to the nets in SIFSIX-2-Cu where SIFSIX-2-Cu refer to $[Cu(dpa)_2(SiF_6)]_n$ (4,4′-dipyridylacetylene (dpa)). SIFSIX-3-Zn is a isoreticular MOF refer to $[Zn(pyr)_2(SiF_6)]_n$ (pyrazine (pyr)) The selective CO_2 adsorption over N_2 and H_2 may be because of strong interaction between CO_2 molecules and the pendant amine functionality which is poised towards vacant pores of the framework to attract gas molecules. In order to judge the CO_2 adsorption efficacy of $\{[Cd(L_1)(L_2)](DMA)\}_n$ (**1**) with other adsorbing systems heat of adsorption values are compared. Isosteric heat of adsorption is an important and relevant parameter which indicates the gas adsorption capacity of the adsorbents. Table 3.1 records the isosteric heat of adsorption for CO_2 of the adsorbent **1** compared to that of heat adsorption value of other relevant MOF based adsorbents reported in the literature [29–35].

Table 3.1. Comparison of isosteric heat of adsorption (Q_{st}) for CO_2 in different MOFs at low CO_2 loading

MOFs	Q_{st} (kJ/mol)	Ref.
1	38	this study
IISERP-MOF20, 2D Cu based ultramicroporous MOF	26	29
Mgdobdc	47	32
Nidobdc	41	32
Codobdc	37	32
SIFSIX-2-Cu	22	31
SIFSIX-2-Cu-i	31.9	31
SIFSIX-3-Zn	45	31
$\{[Mg_2(1,4\text{-bdc})_2(bpdo)]\cdot 2DMF\}_n$	34.9	33
$[Cu(PF_6)_2(4,4'\text{-bpy})_2]_n$	31	34
$[Cu_3(1,3,5\text{-btc})_2]_n$	35	35

H_4dobdc = 2,5-dihydroxyterephthalic acid; dpa = 4,4′-dipyridylacetylene; 1,4-H_2bdc = 1,4-benzenedicarboxylic acid; bpdo = 4,4′-bipyridine-N,N′-dioxide; 4,4′-bpy = 4,4′-bipyridine; 1,3,5-btc = 1,3,5-benzenetricarboxylate.
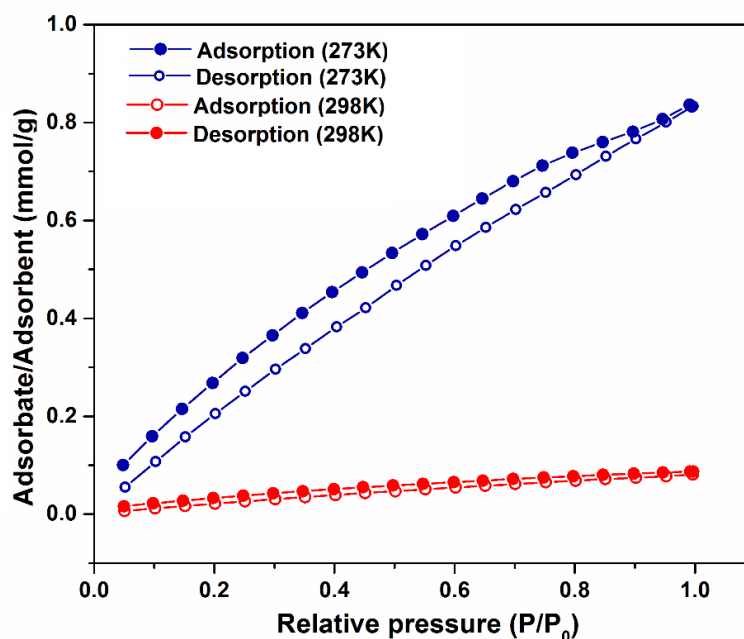
Figure 3.6. CH$_4$ adsorption isotherms measured at the temperature 273 K (blue) and 298 K (red)

Polymer based membranes have been commercially utilized in gas separations for gas pairs like O_2/N_2, CO_2/CH_4, H_2/N_2, He/N_2, H_2/CH_4, He/CH_4 etc. [36]. However, such membrane matrices need to be improved to achieve selectivity/permeability trade off, thermal stability, plasticization etc. for enhancement of carbon-dioxide sorption. To this end, zeolite has been used to cast mixed-membrane matrix to increase CO_2 sorption capacity of the hybrid membrane [37]. Polymer based mixed-membrane matrix consists of porous MOF, ZIF-8 has also been utilized for selective separations of CO_2/CH_4 mixed-gas feeds with higher efficiency [38]. Recently, a pure mixed-linker MOF membrane is found to be capable of separating nitrogen from CH_4/N_2 mixture [39].
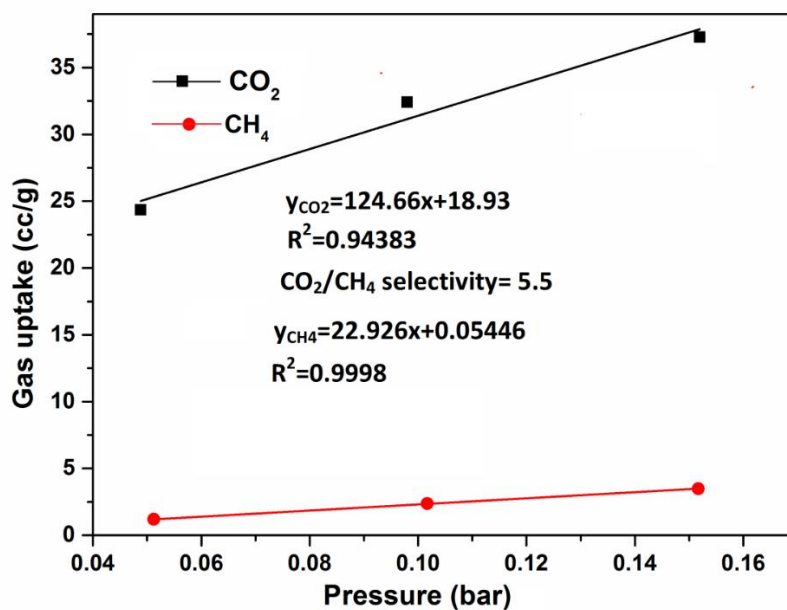
Figure 3.7. CO_2/CH_4 selectivity of desolvated 1 at 273 K
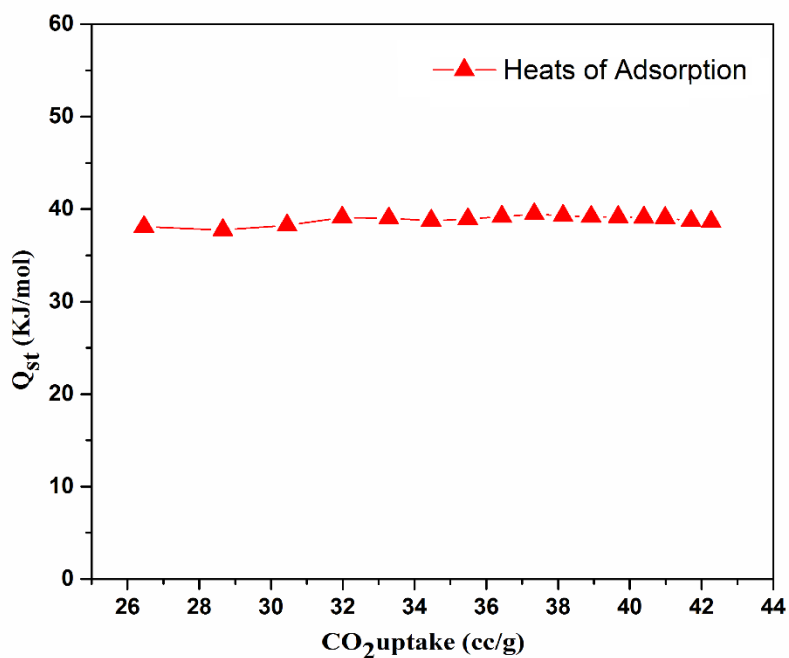
Figure 3.8. Isosteric heat of adsorption for CO_2 adsorption calculated using DFT model for 1

3.4. Conclusion

In essence, the porous 3D metal carboxylate framework compound, $\{[Cd(L_1)(L_2)](DMA)\}_n$ (**1**) exhibited a considerable solvent accessible void space (26.6%) upon removal of DMA molecules led to opening up of pendant Lewis basic -NH$_2$ groups directed towards the pores. At 298 K, the desolvated MOF showed an uptake of carbon-dioxide of 8.33 wt% or 42.42 cc/g at 1 bar pressure which is enhanced to ca. 12.17 wt% or 62 cc/g at 1 bar pressure, upon cooling to 273 K. The desolvated **1** product is highly selective towards CO$_2$ adsorption over all three small gas molecules *viz.* H$_2$, N$_2$ and CH$_4$. Preferential adsorption of CO$_2$ over other gases is presumably because of presence of pendant -NH$_2$ groups in the framework pores. This type porous MOF is highly promising for application in CCS technology in future.

3.5. Reference

1. M. Z. Jacobson, Energy Environ. Sci. 2009, **2**, 148.

2. K. S. Lackner, S. Brennan, J. M. Matter, A. -H. Alissa Park, A. Wright. B. Zwaan, Proc. Natl. Acad. Sci. U. S. A. 2012, **109**, 13156.

3. S. Chaemchuen, N. A. Kabir, K. Zhou, F. Verpoort, Chem. Soc. Rev. 2013, **42**, 9304.

4. J. -R. Li, Y. Ma, M. C. McCarthy, J. Sculley, J. Yu, H. -K. Jeong, P. B. Balbuena, H. -C. Zhou, Chem. Rev. 2011, **255**, 1791.

5. B. Chen, S. Ma, F. Zapata, F. R. Fronczek, E. B. Lobkovsky, H. -C. Zhou, Inorg. Chem. 2007, **46**, 1233.

6. R. Vaidhyanathan, S. S. Iremonger, K. W. Dawson, G. K. H. Shimizu, Chem. Commun. 2009, **35**, 5230.

7. S. A. Sapchenko, D. N. Dybtsev, D. G. Samsonenko, R. V. Belosludov, V. R. Belosludov, Y. Kawazoe, M. Schröder, V. P. Fedin, Chem. Commun. 2015, **51**, 13918.

8. C. F. Leong, T. B. Faust, P. Turner, P. M. Usov, C. J. Kepert, R. Babarao, A. W. Thornton, D. M. D'Alessandro, Dalton Trans. 2013, **42**, 9831.

9. Z. Hulvey, D. A. Sava, J. Eckert, A. K. Cheetham, Inorg. Chem. 2011, **50**, 403.

10. G. Feréy, M. Latroche, C. Serre, F. Millange, T. Loiseau, A. P. G. Gan, Chem. Commun. 2003, **24**, 2976.

11. R. Vaidhyanathan, S. S. Iremonger, G. K. H. Shimizu, P. G. Boyd, S. Alavi, T. K. Woo, Science 2010, **330**, 650.

12. S. Chen, J. Zhang, T. Wu, P. Feng, X. Bu. J. Am. Chem. Soc. 2009, **131**, 16027.

13. J. -R. Li, J. Sculley, H. -C. Zhou, Chem. Rev. 2012, **112**, 869.

14. A. L. Spek, J. Appl. Cryst. 2003, **36**, 7.

15. S. S. Dhankhar, N. Sharma, S. Kumar, T. J. Dhilip Kumar, C. M. Nagaraja, Chem. Eur. J. 2017, **23**, 16204.

16. W. M. Bloch, R. Babarao, M. R. Hill, C. J. Doonan, C. J. Sumby, J. Am. Chem. Soc. 2013, **135**, 10441.

17. J. Liu, G. -P. Yang, Y. Wu, Y. Deng, Q. Tan, W. -Y. Zhang, Y. -Y. Wang, Cryst. Growth Des. 2017, **17**, 2059.

18. Y. -L. Huang, Y. -N. Gong, L. Jiang, T. -B. Lu, Chem. Commun. 2013, **49**, 1753.

19. H. -C. Kim, S. Huh, S. -J. Kim, Y. Kim, Sci. Rep. 2017, **7**, 17185.

20. S. B. Choi, H. Furukawa, H. J. Nam, D. -Y. Jung, Y. H. Jhon, A. Walton, D. Book, M. O'Keeffe, O. M. Yaghi, J. Kim, Angew. Chem. Int. Ed. 2012, **51**, 8791.

21. K. Sumida, D. L. Rogow, J. A. Mason, T. M. McDonald, E. D. Bloch, Z. R. Herm, T. -H. Bae, J. R. Long, Chem. Rev. 2012, **112**, 724.

22. A. Hazra, S. Bonakala, S. K. Reddy, S. Balasubramanian, T. K. Maji, Inorg. Chem. 2013, **52**, 11358.

23. S. Parshamoni, J. Telangae, S. Konar, Dalton Trans. 2015, **44**, 20926.

24. B. Ugale, S. S. Dhankhar, C. M. Nagaraja, Cryst. Growth Des. 2017, **17**, 3295.

25. J. Liu, G. -P. Yang, Y. Wu, Y. Deng, Q. Tan, W. -Y. Zhang, Y. -Y. Wang, Cryst. Growth Des. 2017, **17**, 2059.

26. H. -C. Kim, S. Huh, S. -J. Kim, Y. Kim, Sci. Rep. 2017, **7**, 17185.

27. Z. -J. Wang, L. -J. Han, X. -J. Gao, H. -G. Zheng, Inorg. Chem. 2018, **57**, 5232.

28. W. -G. Jin, W. Chen, P. -H. Xu, X. -W. Lin, X. -C. Huang, G. -H. Chen, F. Lu, X. -M. Chen, Chem. Eur. J. 2017, **23**, 13058.

29. S. Nandi, R. Maity, D. Chakraborty, H. Ballav, R. Vaidhyanathan, Inorg. Chem. 2018, **57**, 5267.

30. V. A. Bolotov, K. A. Kovalenko, D. G. Samsonenko, X. Han, X. Zhang, G. L. Smith, L. J. McCormick, S. J. Teat, S. Yang, M. J. Lennox, A. Henley, E. Besley, V. P. Fedin, D.N. Dybtsev, M. Schroder, Inorg. Chem. 2018, **57**, 5074.

31. P. Nugent, Y. Belmabkhout, S. D. Burd, A. J. Cairns, R. Luebke, K. Forrest, T. Pham, S. Ma, B. Space, L. Wojtas, M. Eddaoudi, M. J. Zaworotko, Nature 2013, **495**, 80.

32. S. R. Caskey, A. G. Wong-Foy, A. J. Matzger, J. Am. Chem. Soc. 2008, **130**, 10870.

33. S. Noro, J. Mizutani, Y. Hijikata, R. Matsuda, H. Sato, S. Kitagawa, K. Sugimoto, Y. Inubushi, K. Kubo, T. Nakamura, Nat. Commun. 2015, **6**, 5851.

34. S. Noro, Y. Hijikata, M. Inukai, T. Fukushima, S. Horike, M. Higuchu, S. Kitagawa, T. Akutagawa, T. Nakamura, Inorg. Chem. 2013, **52**, 280.

35. Q. M. Wang, D. Shen, M. Bülow, M. L. Lau, S. Deng, F. R. Fitch, N. O. Lemcoff, J. Semanscin, Microporous Mesoporous Mater. 2002, **55**, 217.

36. L. M. Robeson, J. Membr. Sci. 2008, **320**, 390.

37. M. B. Mohamad, Y. Y. Fong, A. Shariff, Procedia Eng. 2016, **148**, 621.

38. A. Kertik, L. H. Wee, M. Pfannmöller, S. Bals, J. A. Martens, I. F. J. Vankelecom, Energy Environ. Sci. 2017. **10**, 2342.

39. S. Zhou, O. Shekhah, A. Ramírez, P. Lyu, E. Abou-Hamad, J. Jia, J. Li, P. M. Bhatt, Z. Huang, H. Jiang, T. Jin, G. Maurin, J. Gascon, M. Eddaoudi, Nature 2022, **606**, 706.

Chapter 4
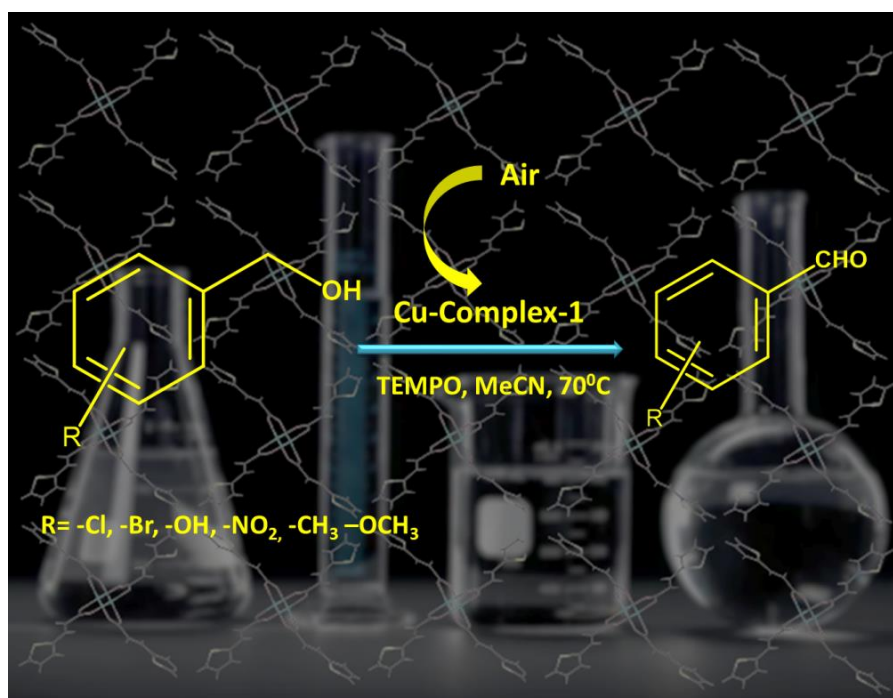
Aerobic oxidation of alcohol over copper(II) based metal-organic framework: Synthesis, X-ray structure and catalytic study

4.1 Introduction

Alcohol oxidation is a fundamental chemical transformation in organic chemistry that involves the conversion of alcohols into carbonyl compounds, such as aldehydes or ketones, through removal of the hydrogen from alcohol functional group. This reaction plays a crucial role in the synthesis of various organic compounds and is widely employed in the pharmaceutical, fine chemicals, and materials industries [1, 2]. Alcohols may be oxidized using a variety of ways, each with its own set of benefits depending on the targeted result and reaction circumstances. Metal-based reagents, organic peroxides, and molecular oxygen are all common oxidizing agents. Usually, oxidant is needed large excess than simply stoichiometric amount to run the reaction smoothly. Most of the oxidants are highly hazardous, corrosive and often expensive, such as DMSO-coupled reagents [3], hypervalent iodine [4,5], and heavy-metal reagents [6]. Hazardous nature of metal-based oxidant and production of large quantities of toxic bi-product make limited application of these oxidants in green process. In this context, selective oxidation of alcohols with molecular oxygen is an elegant method for its environmentally friendly nature and low cost [7]. Transition metal catalysts are widely used for alcohol oxidation due to easy accessibility, less hazardous nature and good catalytic efficacy [8]. There are quite a few examples available in the literature that showed Cu(II)/ TEMPO (TEMPO = 2,2,6,6-tetramethylpiperidine-*N*-oxyl) systems are catalytically active towards aerobic oxidation of primary alcohols in presence of base [9-11].

Mechanism of alcohol oxidation by molecular oxygen under Cu(I) or Cu(II)/ TEMPO based catalyst is well established [11]. However, such type of catalyst requires copious amount of base leading to formation of various bi-products, which makes separation procedure cumbersome [12]. Considering this fact, it is highly desirable to design catalysts which are active in catalytic oxidation of alcohol in base free condition. In this context, some recent studies concerning the catalytic oxidation of Cu/TEMPO in base free condition deserve to be mentioned. Cu/TEMPO can oxidize alcohol without added base in homogeneous medium [10]. Even though homogeneous catalytic systems are known to exhibit better reactivity than heterogeneous systems, for large-scale liquid-phase reactions, heterogeneous catalyst is highly desirable because of ease of handling, simple recovery/recycling of the catalyst and minimization of unnecessary toxic wastes.

Motivated by above facts and upon further exploration of metal carboxylate system a novel copper(II) containing mixed-linker one dimensional metal-organic framework compound, namely, $[Cu_2(L_3)_4(L_4)]_n$ (**2**) (L_3 = 3-(2-thienyl)acrylic acid, L_4 = 4,4´-bipyridine) has been isolated. $[Cu_2(L_3)_4(L_4)]_n$ (**2**) features a one-dimensional networked structure containing copper "paddle-wheel (PW)" as secondary building unit (SBU). Notably, $[Cu_2(L_3)_4(L_4)]_n$ (**2**) is capable of activating molecular oxygen under base free condition in catalytic oxidation of alcohols.

4.2 Experimental section

4.2.1 Materials

$Cu(NO_3)_2 \cdot 3H_2O$, 3-(2-thienyl)acrylic acid (L_3) and 4,4´-bipyridine (L_4), were purchase from Sigma-Aldrich and used as received. The necessary chemicals for catalytic experiment were also purchased from Sigma-Aldrich. Solvents and other chemicals were purchased from Merck India. Solvents were distilled and dried before use.

4.2.2 Physical measurements

The detail of instruments required for initial characterization is same as Chapter 2 (*vide* Section 2.2.2). The FE-SEM image and EDS spectroscopy were analyzed using a JEOL-JSM 7500F instruments and JED-2300 Analysis Station, respectively.

4.2.3 Synthesis of $[Cu_2(L_3)_4(L_4)]_n$ (2)

Framework compound **2** was synthesized employing slow diffusion of layers method. $Cu(NO_3)_2 \cdot 3H_2O$ (24.16 mg, 0.1 mmol) was dissolved in 3 mL water and taken in a glass reaction tube. 3-(2-thienly)acrylic acid (31 mg, 0.2mmol) and 4, 4´-bipyridine (15.6 mg, 0.1 mmol) were dissolved separately in 3 mL of DMA. Finally, the ligand solutions were transferred gently and cautiously over the aqueous solution of the metal salt to form layers and the tube was sealed properly with Teflon tape and kept in 80 ºC for five days without disturbance. Bluish-green colored crystals thus formed were collected and washed with distilled water and dried at ambient temperature (yield ~80% based on metal). Phase purity of **2** was determined form elemental analysis and PXRD analysis. Anal. Calcd. for $C_{19}H_{14}CuNO_4S_2$ (FW 442.21), C, 52.02, H, 3.19, N, 3.17% found C, 52.3, H, 3.0, N, 3.2%. FTIR peaks (cm^{-1}) (Figure. 4.1) 1678 [v_{as} (COO$^-$)], 1388 [v_s (COO$^-$)], 1345 [v_s (C-O)].

4.2.4 X-ray crystallography

An X-ray quality crystal of $[Cu_2(L_3)_4(L_4)]_n$ (**2**) was selected for data collection. Intensity data were collected at 273K using a Bruker D8 QUEST area detector diffractometer equipped with graphite monochromated MoKα radiation (λ = 0.71073 Å). The molecular structure was solved by direct method and refined by full-matrix least squares on F^2 using the SHELXL-2018/3 package [13]. An empirical absorption correction method (SADABS) [14] was applied. Non-hydrogen atoms were refined with anisotropic thermal parameters. All hydrogen atoms were placed at their geometrically idealized positions and ride on their parent atoms located in the Fourier map. Successful convergence was indicated by the maximum shift / error of 0.001 for the last cycle of the least-squares refinement. Due to the high thermal parameter, it was not possible to assign any desirable disorder model for guest molecule. SQUEEZE subroutine of the Olex2 [15] software suite was applied to remove the scattering from the highly disordered guest molecules. Data collection and structure refinement [16] parameters and crystallographic data of the **2** are given in Table 4.1.
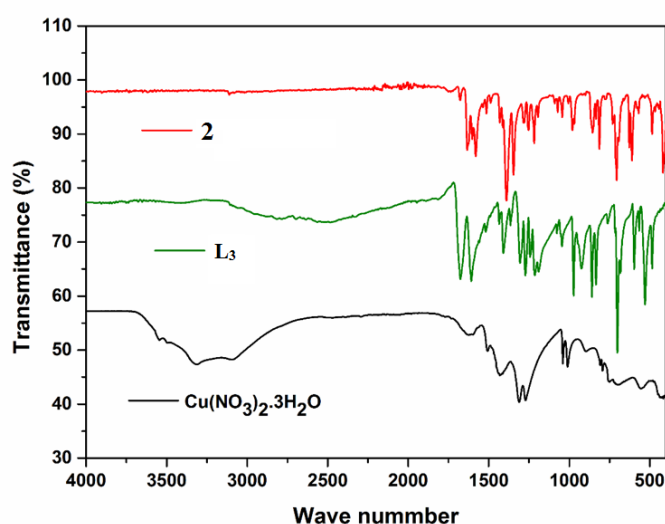
Figure 4.1. IR-spectra of 2 (red), L_3 (green) and metal salt used (black)

4.2.5 Theoretical studies

Gaussian 09 software was used to optimize the geometrical structure of the singlet ground state of the copper compound utilizing the DFT technique and the B3LYP functional approach [17, 18]. The geometry of the Cu-compound is fully optimized in solid state without any symmetry constrains and the theoretical model shows good agreement with the experimental structure. Gauss View 5.1 software was used to compose the figures showing MOs and the difference density plots. All the calculations were performed with the Gaussian 09W software package.[19]

4.2.6 Hirshfield surface study

To create the Hirshfeld surfaces and 2D fingerprint plots from crystal structure files (CIF) Crystal Explorer 3.1 was used [20, 21]. To further improve the analysis accuracy and precision, a normalized Hirshfeld surface, d_{norm}, was mapped over the Hirshfeld surface, enabling the derivation of shape indices and the decomposition of fingerprint plots by the function of d_e versus d_i. This approach ensures a thorough and meticulous study of the crystal structures. The d_{norm}, expressed as

$$d_{norm} = (d_i - r_i^{vdw})/r_i^{vdw} + (d_e - r_e^{vdw})/r_e^{vdw}$$

During the analysis of atoms, it is essential to consider their van der Waals radii, specifically r_i^{vdw} and r_e^{vdw}. These radii are essential for determining the regions in which intermolecular interactions are possible. In order to comprehend molecular structures better, exploring their three-dimensional shapes and the several forms of close interaction they exhibit is useful. The surface map was generated by Crystal Explorer and TONTO, using the parameters B3LYP/6-311G(d,p)±0.03 a.u.

4.2.7 Catalytic study

The catalytic oxidation of alcohol was carried out in a glass batch reactor in presence of aerial oxygen at atmospheric pressure absence of any external bases as per method given below. Alcohols (0.2 mmol), TEMPO (0.02 mmol) and catalyst (5 mol %, 5 mg) were mixed together in 4 mL acetonitrile. The mixture was equilibrated to the desired temperature (70 ℃) in an oil

bath with continuous stirring. The progress of the reaction was monitored by TLC. After 4 hours, the reaction mixtures were collected, cooled to room temperature and mixed with ice cold water then extracted with ethyl acetate. The obtained organic layer was collected and washed with brine solution, dried over anhydrous sodium sulphate and concentrated in vacuum. The collected residue was further purified by column chromatography on silica gel (60-120 mesh). The product was characterized by ^{1}H NMR spectroscopy and elemental analysis and compared with the literature value.

4.3 Results and discussion

4.3.1. Synthesis

Chemistry of incorporating multiple linkers in order to assemble metal centers leading to multivariate metal-organic frameworks is of recent interest. Mixed-linker systems consisting of a carboxylate linker and a neutral spacer could afford fascinating framework compounds. In this study an attempt has been made to design Cu(II) based mixed-linker MOF by involving a carboxylate linker, 3-(2-thienyl)acrylic acid (L_3) and a neutral spacer 4,4´-bipyridine (L_4). Simple mixing of an aqueous solution of $Cu(NO_3)_2$ and dimethylacetamide (DMA) solution of linkers led to form an intractable solid. Solvothermal treatment of a mixture of aqueous metal solution and DMA solution of L_3 and L_4 also did not produce any desirable product. Finally, crystalline product of the desired MOF has been successfully isolated by employing layer technique. In this method aqueous solution of $Cu(NO_3)_2 \cdot 3H_2O$ was taken in a 1.2 cm wide (inner diameter) and 35 cm long glass tube and over this the linkers dissolved in DMA was added cautiously without disturbing the first layer; in between two layers a buffer layer of pure DMA was made to arrest the fast mixing of metal and linker solutions. The tube was closed with a stopper and sealed properly with Teflon tape and kept at 80 ºC for five days without disturbance (*vide infra*). Upon slow diffusion of solutions present in two layers single crystals of $[Cu_2(L_3)_4(L_4)]_n$ (**2**) were formed in the glass tube. Crystal were collected from the solution, washed with distilled water, and dried in a desiccator.

4.3.2 X-ray structure

X-ray single crystal diffraction analysis reveals $[Cu_2(L_3)_4(L_4)]_n$ (**2**) crystallized in triclinic crystal system with space group P$\bar{1}$, Z= 2 (Table 4.1). Schematic diagram of the coordination environment of Cu(II) in **2** is depicted in Figure 4.5. Asymmetric unit consists of single Cu(II)

ion with two units of linker L_3 and half unit of L_4 (Figure 4.3). Cu(II) center features a square-pyramidal geometry and copper atom is coordinated by four oxygen atoms from four different L_3 ligands thereby forming the basal plane and axial position is occupied by one nitrogen atom of L_4 ligand. The trigonality index ($\tau = (\phi_1 - \phi_2)/60$, where ϕ_1 and ϕ_2 are the two largest L-M-L angles of the coordination sphere) [22] has been calculated for the pentagonal copper sites. $\tau = 0.001$ for Cu1, confirming the square pyramidal character of copper sites. ($\tau = 0$ infers a perfect square pyramid, and $\tau = 1$ infers a perfect trigonal bipyramid).

$[Cu_2(L_3)_4(L_4)]_n$ (**2**) features a one-dimensional chain structure. Two neighboring Cu centers are bridged by four carboxylato group of four different L_3 ligands led to formation of paddle wheel $[Cu_2(COO^-)_4]$ secondary building unit (SBU). The paddle wheel units are interconnected by bidentate 4,4′-bipyridine ligands to form one dimensional infinite chain network. Each L_3 ligands coordinated with Cu ions in a bidentate bridging fashion and L_4 ligands coordinated by pyridyl N atom in bidentate bridging mode. The bond lengths and bond angles are summarized in the Table 4.2. There are four Cu-O equatorial bonds to O_1, O_2, O_3 and O_4 within in the range 1.977 Å to 1.982 Å and one axial Cu-N bonds with the distance 2.186 Å. Trans angles are 167.62º, 167.55º and the cis angles are between 88.03º to 97.59º.

Table 4.1. Crystal data and refinement parameters

Compound	**2**
Formula	$C_{19}H_{14}CuNO_4S_2$
Formula weight	447.98
Crystal system	triclinic
Space group	$P\bar{1}$
A /Å	8.0814(7)
b /Å	10.1055(9)

c /Å	12.4307(11)
α (º)	109.005(2)
γ(º)	101.424(2)
β(º)	93.298(2)
V /Å^3	932.63(14)
Z	2
D_c/g cm^{-3}	1.575
μ/mm^{-1}	1.399
R(int)	0.271
Unique data	4115
Data with $I > 2\sigma(I)$	3835
R1	0.0676
*w*R2	0.1804
GOF on F^2	1.051

R1 $= \sum ||F_o| - |F_c||/\sum |F_o|$, wR2 $= \{\sum[w(F_o^2 - F_c^2)^2]/\sum w(F_o^2)^2\}^{1/2}$
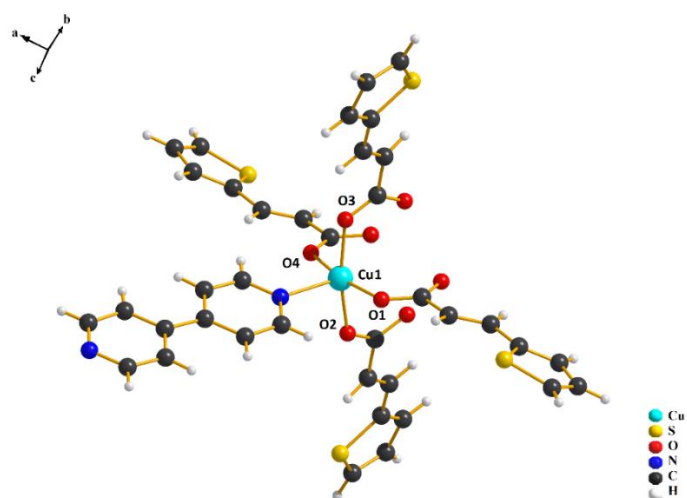
Figure 4.2. Coordination environment around the metal center of 2
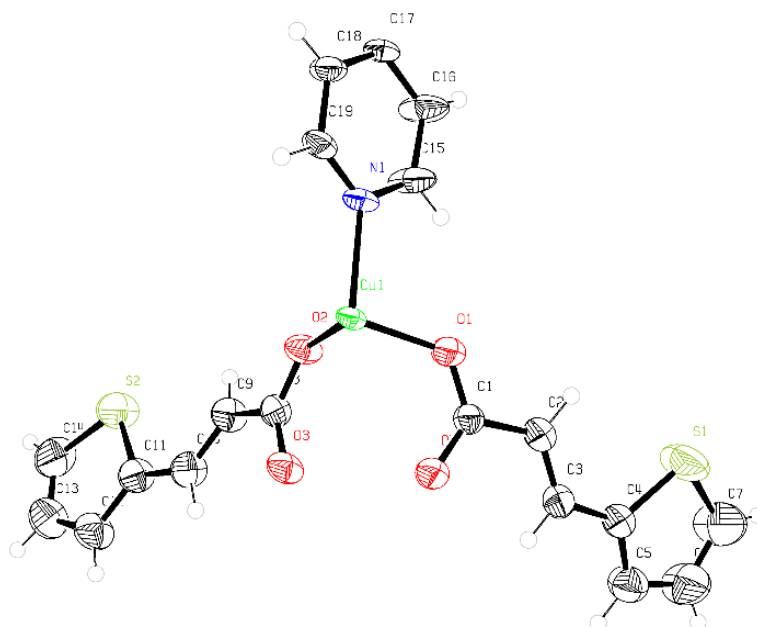
Figure 4.3. ORTEP diagram asymmetric unit of 2 (with 30% probability)
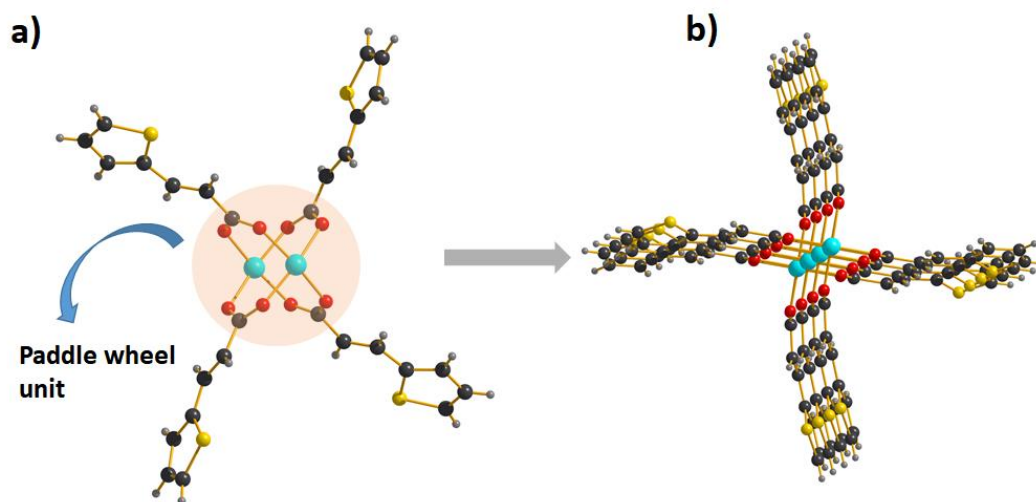
Figure 4.4. **Structural unit of 2; a) Paddle wheel unit (SBU) contains metal center with L$_3$ ligand; b) Propeller shape formed by staking of SBU**
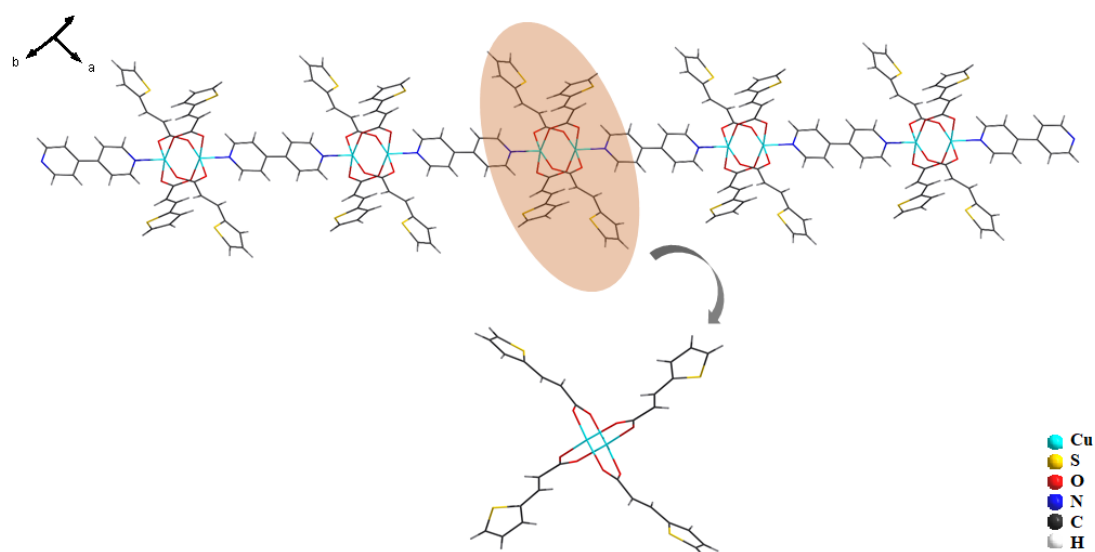
Figure 4.5. **One-dimensional chain structure of 2**
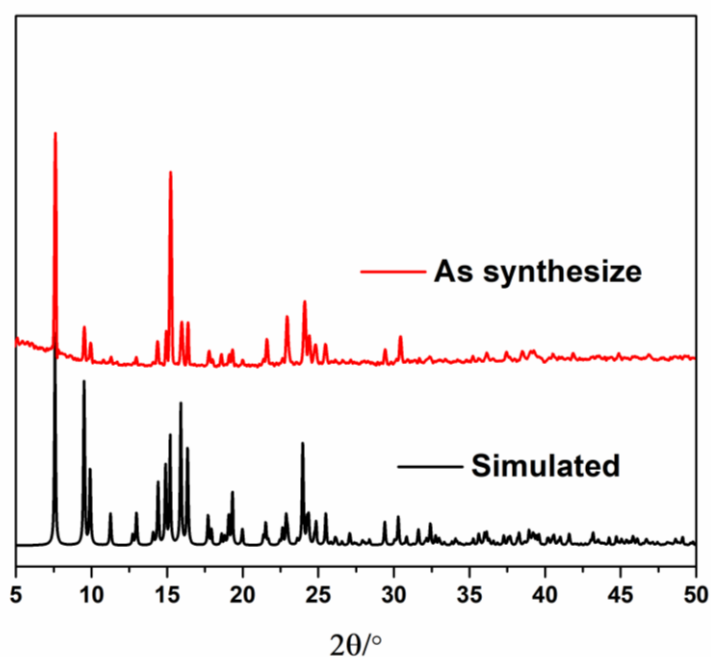
Figure 4.6. Powder X-ray diffraction pattern of 2

Table 4.2. Bond distances (Å) and angles (º) around the metal center of 2

Atoms	Distance	Atoms	Angle	Atoms	Angle
Cu1-O1	1.978(3)	O1 -Cu -O2	89.80(12)	O2-Cu1-O4^b	89.24(11)
Cu1-O2	1.978(3)	O1- Cu1-N1	97.59(12)	O2-Cu1-N1	95.63(12)
Cu1-O3^b	1.982(3)	O1-Cu1-O3^b	88.03(12)	O3^b-Cu1-N1	96.81(12)
Cu1-O4^b	1.977(3)	O1-Cu1-O4^b	167.62(12)	O4^b-Cu1-N1	94.79(12)
Cu1-N1	2.183(3)	O2-Cu1-O3^b	167.55(12)	O3^b-Cu1-O4^b	90.26(11)

4.3.3 Thermogravimetric analysis

To understand the thermal stability of the **2**, thermogravimetric analysis was performed using solid compounds. Thermal analysis was carried out with well ground powder sample in the temperature range 30-800 ℃ under contentious flow of nitrogen (Figure 4.7). Upon heating the $[Cu_2(L_3)_4(L_4)]_n$ (**2**) showed mass loss in two distinct steps. On heating a steep decrease of the TGA curve is observed measuring a weight loss of ~67.71%, in the temperature range 180℃ to 400℃. This weight loss is due to breakdown of framework corresponding to loss of two L_3 ligands with theoretical value 68.39%. The second weight loss of ~16.99% is observed at the temperature range 450℃ to 750℃ might be due to the removal of half of L_3 ligand that corresponds to a calculated value of 17.43%. Finally, after heating up to 800 ℃ sample converted to metal oxide.
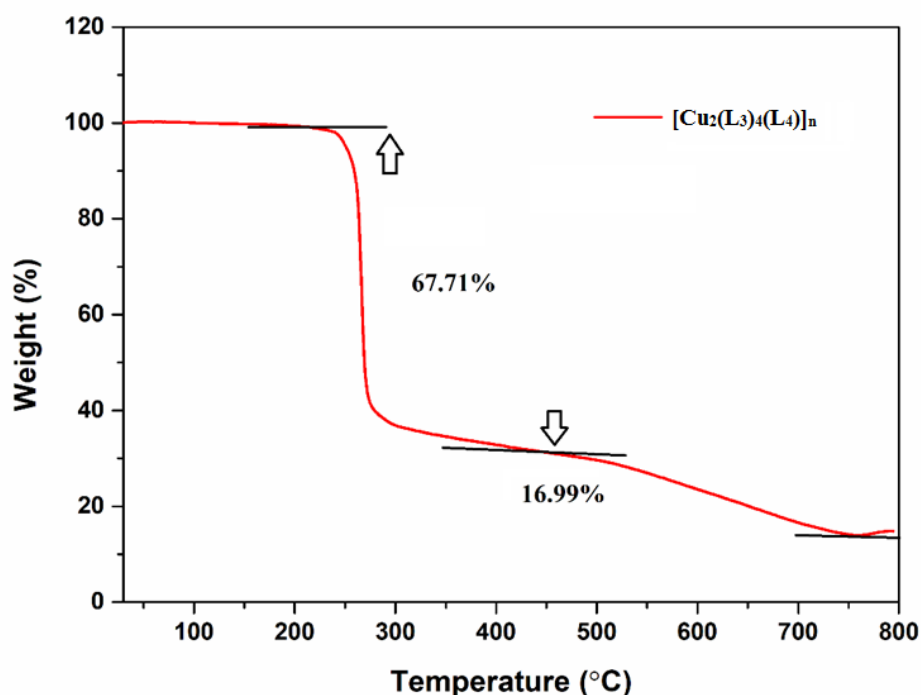
Figure 4.7. Thermogravimetric plot of 2

4.3.4 FMO explanation of 2

Amongst various theoretical studies, FMO energy calculation offers a vast application for explanation of numerous properties like stability and reactivity, spectroscopy etc. In this context, HOMO stands for highest occupied molecular orbital and the energy associate with this orbital (EHOMO) implies the tendency to donate electron. Where the LUMO is lowest unoccupied molecular orbital and energy related to this (ELUMO) associate with the tendency to get reduced. The large energy gap is related to the higher stability of the molecule. The energy gap of the orbitals is 1.82 eV as shown in the Figure 4.8. While Figure 4.9 represents the optimized structure of the reported molecule. The FMO study shows that the HOMO is mainly comprises of the L_3 moiety and the LUMO is mainly resides on the Cu(II) center, which satisfy the reported fact that the Cu(II) center of the complex is capable to accept electrons *i.e.* redox active and can efficiently catalyze the alcohol oxidation.
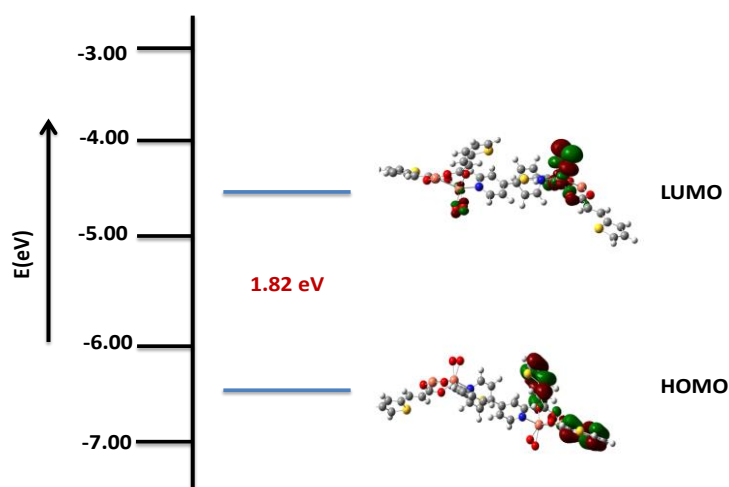
Figure 4.8. Partial MO diagram of 2
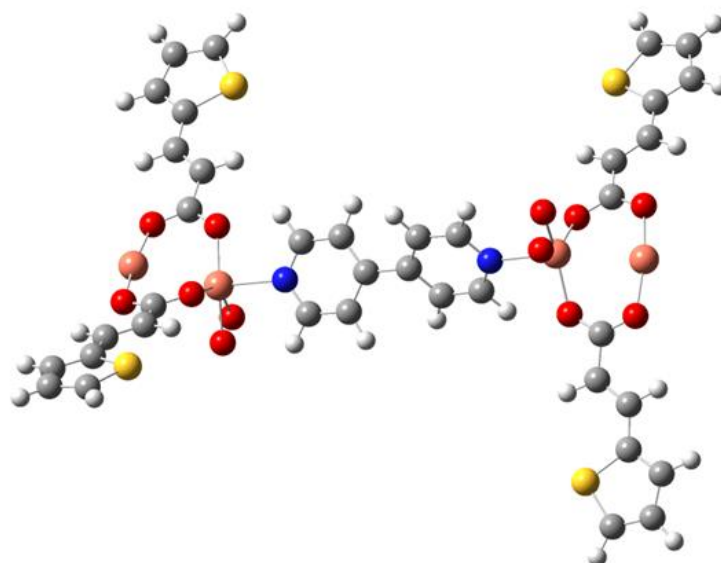
Figure 4.9. Optimized structure of 2

4.3.5 Hirshfeld surface analysis

One of the most effective ways to identify the molecular interactions is Hirshfeld analysis. Hirshfeld analysis of **2** is carried out using asymmetric unit present in the crystal structure, providing information about the interaction present in the molecule. To create the surface a standard resolution of high quality was employed within the scale -1.1 to 1.4 Å. The d_{norm} provides valuable information about the distance between the two atoms across the surface, with respect to the atomic radius. The d_e and d_i also provide the distance between the closest nuclei outside and inside the Hirshfeld. The bright red spot present in the d_{norm} surface map indicate the presence of short contact as shown in the Figure 4.10. Further analysis of the Hirshfeld surface indicate that the dark red spot is due to the presence of C-C, C-H, O-H and H-H contacts. 2D fingerprint plot of **2**, given in Figure 4.11, is generated using asymmetric unit that gives the quantitative explanation of the intermolecular attraction forces. After the analysis, it has been found that the N···H, O···H, H···H, C···H, and O···C contacts significantly contribute to the total Hirshfeld. However, the C–H and H–H interactions contribute highest to the total

Hirshfeld rather than other interactions (O–H, N–H, S–H etc.). Lower N···H, O···H interaction indicate that the less preference of hydrogen bonding interactions. Therefore, it is implying that the synthesize molecule get stability and interact with other molecule through van der Waals interaction preferably.
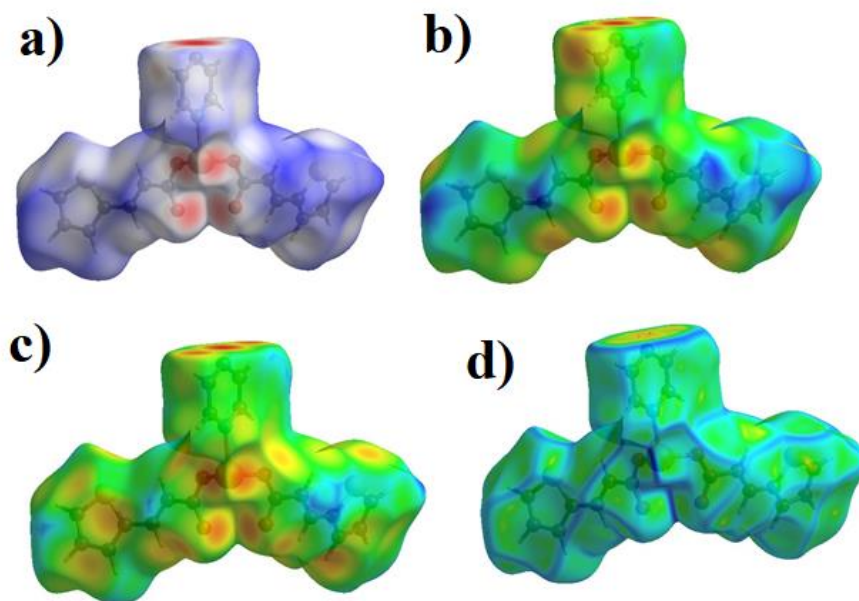
Figure 4.10. **The Hirshfeld surface of the 2 mapped with (a) d_{norm} ; (b) d_i ; (c) d_e and (d) curvedness**
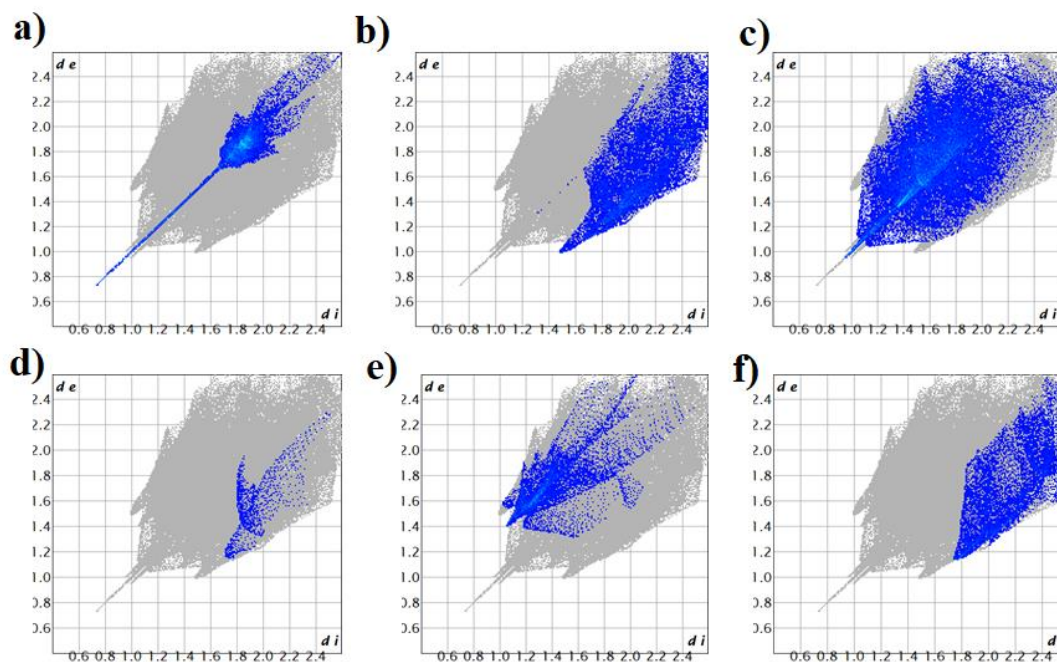
Figure 4.11. Two-dimensional fingerprint plots showing, (a) C ···C; (b) C···H; (c) H ···H; (d) N···H; (e) O···H; (f) S···H interactions

4.3.5 FE-SEM and EDS analysis

To study the surface morphology of $[Cu_2(L_3)_4(L_4)]_n$ (**2**) FE-SEM analysis of the freshly prepared compound has been under taken. A well-formed plate like crystalline solids has been clearly observed in the FE-SEM micrograph (Figure 4.12). EDS analysis on the selected area of the crystal surface (Figure 4.13) convincingly demonstrates the presence all the elements including copper which acts as the active center of catalytic oxidation of alcohols**.**
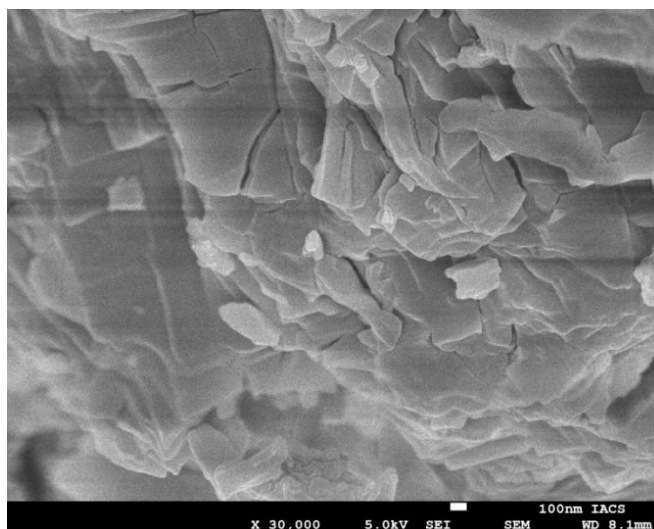
Figure 4.12. Picture showing surface morphology of 2
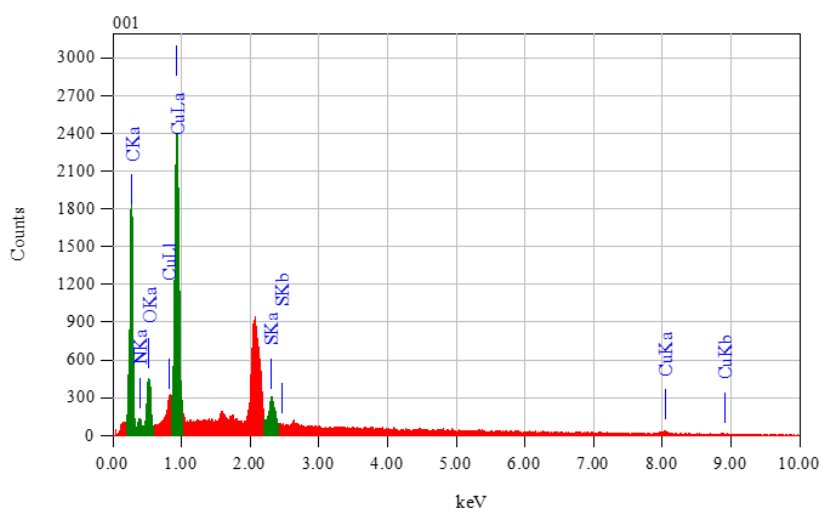
Figure 4.13. EDS spectrum of the selected area of crystalline surface of 2

4.3.6 Catalytic study

The catalytic activity of $[Cu_2(L_3)_4(L_4)]_n$ (**2**) towards oxidation of alcohol was investigated using various substituted benzyl alcohol. Initially the catalytic conditions were optimized using benzyl alcohol as a standard substrate. To determine the optimal condition, a series of controlled experiment were undertaken and the effect of different parameters such as solvents,

temperature, oxidant etc. has been verified. In fact, when no catalyst in controlled experiment was used, there were hardly any reactions, which confirm the role of catalyst in oxidation of alcohol. Results of the optimization experiments are collated in Table 4.3. Evidently the solvent plays a crucial role in catalytic oxidation process. With increase in polarity of the solvent, yield of the product is also increased. Amongst different solvents, highest yield is obtained in MeCN. Further increase of solvent polarity, selectivity towards corresponding aldehyde decreases, even though, conversion of the substrate increases. Therefore, MeCN is selected for other alcohol oxidation.

No product could be isolated when reaction happened in absence of oxygen. Catalytic activity was observed to be poor in presence of $CuCl_2$ salt. The probable reason for poor catalytic activity of $CuCl_2$ may be due to the absence of coordinated ligand [23] which contains a basic center. Above results showed that, under the specified conditions, the catalytic process of aerobic oxidation of benzyl alcohols was enhanced in conjunction with ligand and copper(II) centers present in the $[Cu_2(L_3)_4(L_4)]_n$ (**2**). The probable mechanism of such copper (II) TEMPO system is well established in the literature [24].

Table 4.3. Optimization for $[Cu_2(L_3)_4(L_4)]_n$ (2)/TEMPO catalyzed aerobic oxidation of benzyl alcohol[a].
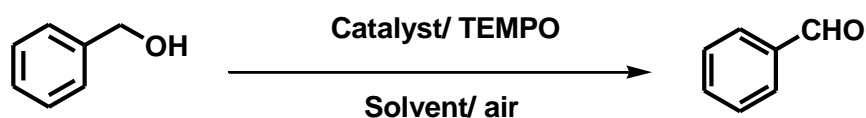
Entry	Catalyst	Oxidant	Solvent	Yield[b](%)
1	$[Cu_2(L_3)_4(L_4)]_n$	TEMPO	CH_3CN	84
2	$CuCl_2$	TEMPO	CH_3CN	30
3	None	TEMPO	CH_3CN	Trace
4	$Cu(CH_3COO)_2$	TEMPO	CH_3CN	37
5	$[Cu_2(L_3)_4(L_4)]_n$	None	CH_3CN	0
6	$[Cu_2(L_3)_4(L_4)]_n$	TEMPO	Toluene	26
7	$[Cu_2(L_3)_4(L_4)]_n$	TEMPO	H_2O	18
8	$[Cu_2(L_3)_4(L_4)]_n$	TEMPO	EtOH	30
9	$[Cu_2(L_3)_4(L_4)]_n$	TEMPO	$CHCl_3$	42
10[c]	$[Cu_2(L_3)_4(L_4)]_n$	TEMPO	CH_3CN	56
11[d]	$[Cu_2(L_3)_4(L_4)]_n$	TEMPO	CH_3CN	Not detected

[a]Reaction conditions: benzyl alcohol (0.2 mmol), TEMPO (0.02 mmol), CH_3CN (4 mL), catalyst (5 mol %), temperature 70°C, 4 h and air as an oxygen source. [b]Isolated yield. [c]Temperature 90 °C. [d]Reaction performed under argon atmosphere instead of oxygen.

Table 4.4. Optimization of amount of TEMPO for [Cu₂(L₃)₄(L₄)]ₙ (2)/TEMPO catalyzed aerobic oxidation of benzyl alcohol[a]
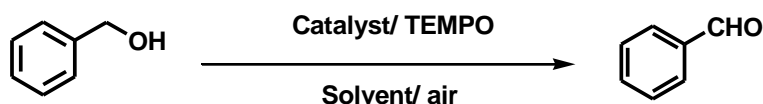
[a]Entry	Catalyst	TEMPO amount (mmol)	[b]Yield(%)
1	[Cu₂(L₃)₄(L₄)]ₙ	0	Trace
2	[Cu₂(L₃)₄(L₄)]ₙ	0.01	42
3	[Cu₂(L₃)₄(L₄)]ₙ	0.02	84
4	[Cu₂(L₃)₄(L₄)]ₙ	0.03	82
5	[Cu₂(L₃)₄(L₄)]ₙ	0.05	79

[a]Reaction conditions: Substrate (0.2 mmol), TEMPO (0.02 mmol), CH_3CN (4 mL), catalyst (5 mol %), temperature 70ºC, 4 h and air as an oxygen source. [b]Isolated yield.

      In order to investigate the scope of aerobic oxidation of alcohol by [Cu₂(L₃)₄(L₄)]ₙ (**2**) the oxidation of various aromatic alcohols was performed (Table 4.5). Under the base free condition all the alcohols, like benzyl alcohol give the respective products in high yield with 100% selectivity. The electronic nature of the substituent has a great impact on the yield of the product. The substrate contains the electron donating group (EDG) such as -CH₃, -OCH₃, -OH reacted to give the corresponding product noticeably higher than the substrate contains electron withdrawing group (EWG) such as -NO₂, -Cl etc. However, these findings showed that the compound effectively encouraged the aerobic oxidation of different types of alcohols using an EDG or EWG. The result demonstrated that the compounds exhibited a good catalytic efficiency towards different types of alcohols.

Table 4.5. Aerobic oxidation of substituted benzyl alcohol to corresponding aldehyde catalyzed by 2[a]

$[Cu_2(L_3)_4(L_4)]_n$, TEMPO

CH_3CN, 70^0C, 4h
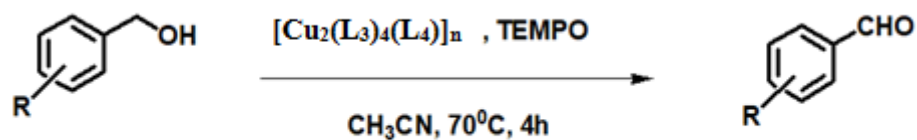
R= -Cl, -NO$_2$, -CH$_3$, -Br, -OH, -OCH$_3$

Entry	Substrate	Product	Yield[b](%)
1			84
2			75
3			80
4			82
5			90

6			72
7			89
8			86
9			82

[a]Reaction conditions: Substrate (0.2 mmol), TEMPO (0.02 mmol), CH$_3$CN (4 mL), catalyst (5 mol %), temperature 70ºC, 4 h and air as an oxygen source. [b]Isolated yield.

4.4 Stability, heterogeneity and reusability test of the catalyst

Hot filtration experiment was performed to assess the heterogeneity behavior of the catalyst, which could provide the evidence that metal was not leached out during the catalysis. The solid catalyst was filtered hot after 1 hour of reaction and the catalytic activity of the filtrate after separation of the catalyst has been studied. Filtrate was kept in reaction condition for another 3 h and the composition of the solution has been analyzed time to time. No progress of reaction was observed during this period, which excludes the presence of active species in the solution. This experiment clearly demonstrates that there was no dissolution of solid catalyst during reactions (Figure. 4.14).
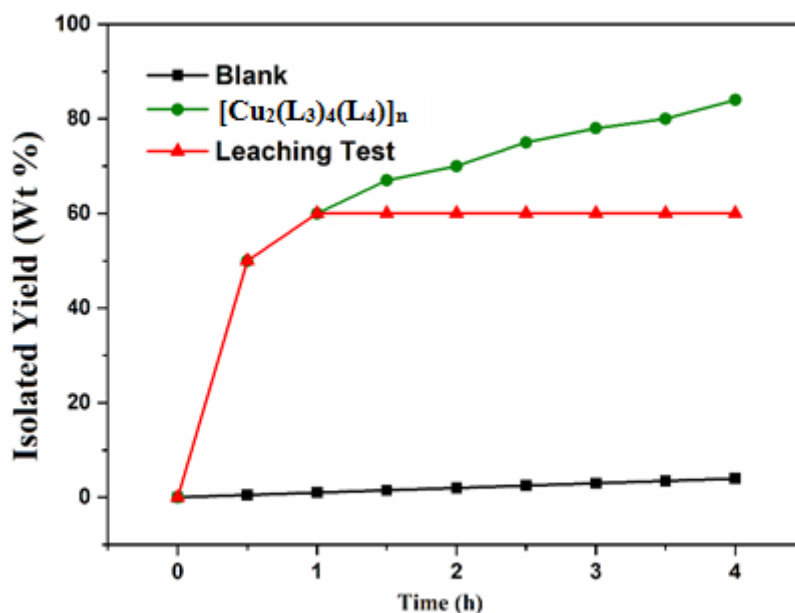
Figure 4.14. Leaching test of catalyst (reaction condition: benzyl alcohol (0.2 mmol), TEMPO (0.02 mmol), CH$_3$CN (4 mL), catalyst (5 mol %, 5mg), temperature 70ºC, 4h and air as an oxygen source).

After the reaction is over, the catalyst was separated by centrifugation and washed with water and dichloromethane mixture thoroughly and dried under vacuum. As the amount recovered catalyst was very small in a single batch, recovered catalyst collected up to five batches to get considerable amount of sample that is suitable for PXRD and IR studies. In order to check the stability of the catalyst after reaction, powder X-ray diffraction analysis (PXRD) was carried out. Comparison of PXRD patters of the recovered catalyst (Figure 4.15) with the pristine compound clearly indicates that the structural integrity of the MOF remained intact after the catalysis reaction. The recover catalyst shows almost the same catalytic activity after five successive runs convincingly demonstrates the recyclability of **2** (Figure 4.16).
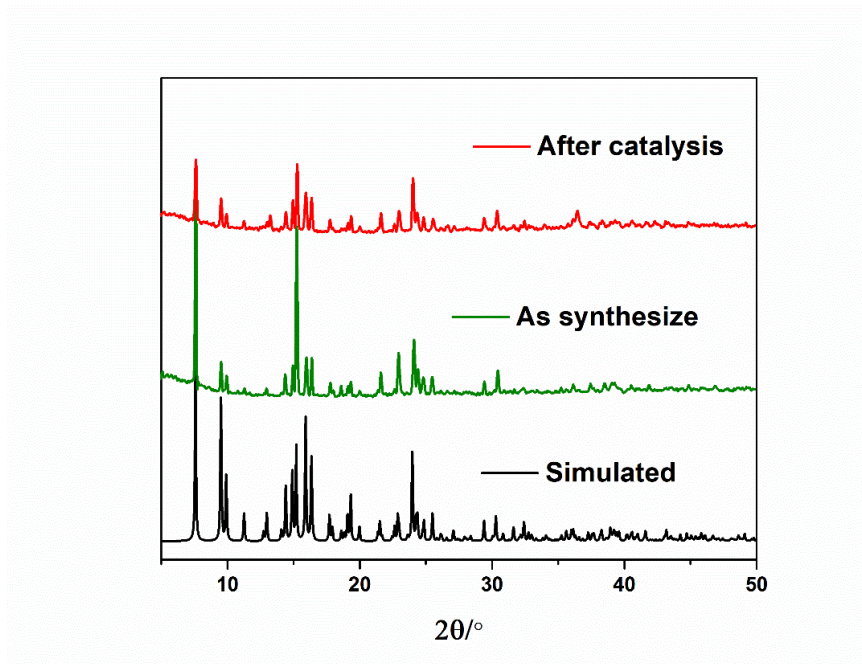
Figure 4.15. Powder X-ray diffraction pattern of 2 after catalysis
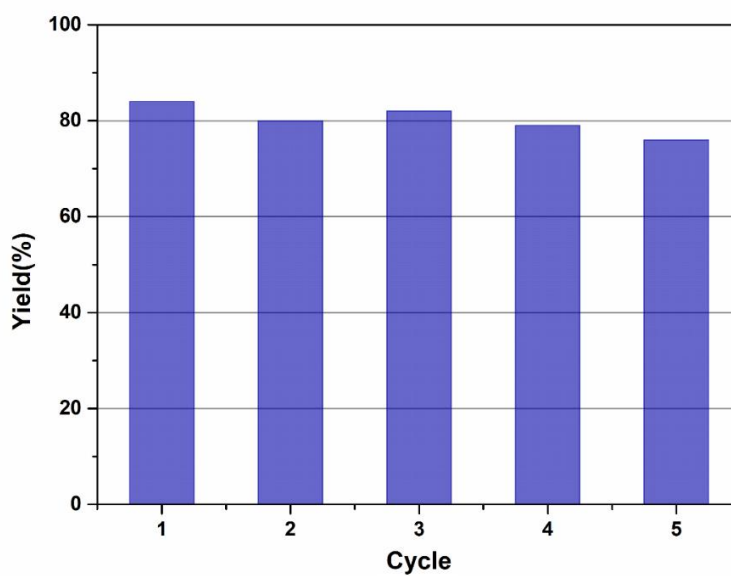
Figure 4.16. Catalytic activity of 2 towards benzyl alcohol oxidation up to five catalytic cycles

4.5 Conclusion

In summary, a copper based one-dimensional framework compound $[Cu_2(L_3)_4(L_4)]_n$ (**2**) has been synthesized by slow diffusion two layers at 80 ºC. $[Cu_2(L_3)_4(L_4)]_n$ (**2**) is capable to catalyze alcohols efficiently under environmentally benign condition by activating molecular oxygen. Notably, no base is required in the catalytic reactions. Molecular oxygen has rarely been utilized in oxidation of alcohols under base free condition.

4.6 References

1. M. Baumann, I. R. Baxendale, Beilstein J. Org. Chem. 2013, **9**, 2265.

2. R. A. Sheldon, J. K. Kochi, Adv. Catal. 1976, **25**, 272.

3. B. A. Steinhoff, S. R. Fix, S. S. Stahl, J. Am. Chem. Soc. 2002, **124**,766.

4. M. Uyanik, M. Akakura, K. Ishihara, J. Am. Chem. Soc. 2009, **131**, 251.

5. R. D. Richardson, T. Wirth, Angew. Chem. Int. Ed. 2006, **45**, 4402.

6. M. Hudlicky, Oxidations in Organic Chemistry, American Chemical Society, Washington, D.C. 1990.

7. P. Gamez, I. W. C. E. Arends, J. Reedijk, R. A. Sheldon, Chem. Commun. 2003, **19**, 2414.

8. G. An, X, Zhang, C. Zhang, H. Gao, S. Liu, G. Qin, H. Qi, J. Kasemchainan, J. Zhang and G. Wang, Chin J. Catal. 2023, **50**, 126.

9. B. L. Ryland, S. S. Stahl, Angew. Chem. Int. Ed. 2014, **53**, 8824.

10. M. F. Semmelhack, C. R. Schmid, D. A. Cortes, C. S. Chou, J. Am. Chem. Soc., 1984, **106**, 3374.

11. B. L. Ryland, S. D. McCann, T. C. Brunold, S. S. Stahl, J. Am. Chem. Soc. 2014, **136**, 12166.

12. A. Taher, D. W. Kim, I-M Lee, RSC Adv. 2017, **7**, 17806.

13. I. Usón, G.M. Sheldrick, Acta Cryst. Sect. D. 2018, **74**, 106.

14. SAINT, version 6.02; SADABS, version 2.03; Bruker AXS, Inc.: Madison, WI, (2002).

15. O. V. Dolomanov, L. J. Bourhis, R. J. Gildea, J. A. K. Howard, H. Puschmann, J. Appl. Crystallogr. 2009, **42**, 339.

16. G.M. Sheldrick, Acta Cryst. 2015, **71**, 3.

17. A. D. Becke, J. Chem. Phys. 1993, **98**, 5648.

18. C. Lee, W. Yang, R.G. Parr, Phys. Rev. 1988, **B37**, 785.

19. 2009 Gaussian 09, Revision D.01; Gaussian, Inc.: Wallingford, CT, 2009.

20. M.A. Spackman, D. Jayatilaka, Hirshfeld surface analysis, CrystEngComm. 2009, **11**, 19.

21. S.K. Seth, D. Sarkar, A. Roy, T. Kar, CrystEngComm. 2011, **13**, 6728.

22. A. W. Addison, T. N, Rao, J. Reedijk, J. van Rijn, G. C. Verchoor, J. Chem. Soc. Dalton Trans. 1984, 1349.

23. C. Bai, Q. Zhao, Y. Li, G. Zhang, F. Zhang, X. Fan, Catal. Lett. 2014, **144**, 1617.

24. B. D. Ryland, S. D. McCann, T. C. Brunold, S. Stahl, J. Am. Chem. Soc. 2014, **136**, 12166.

Chapter 5
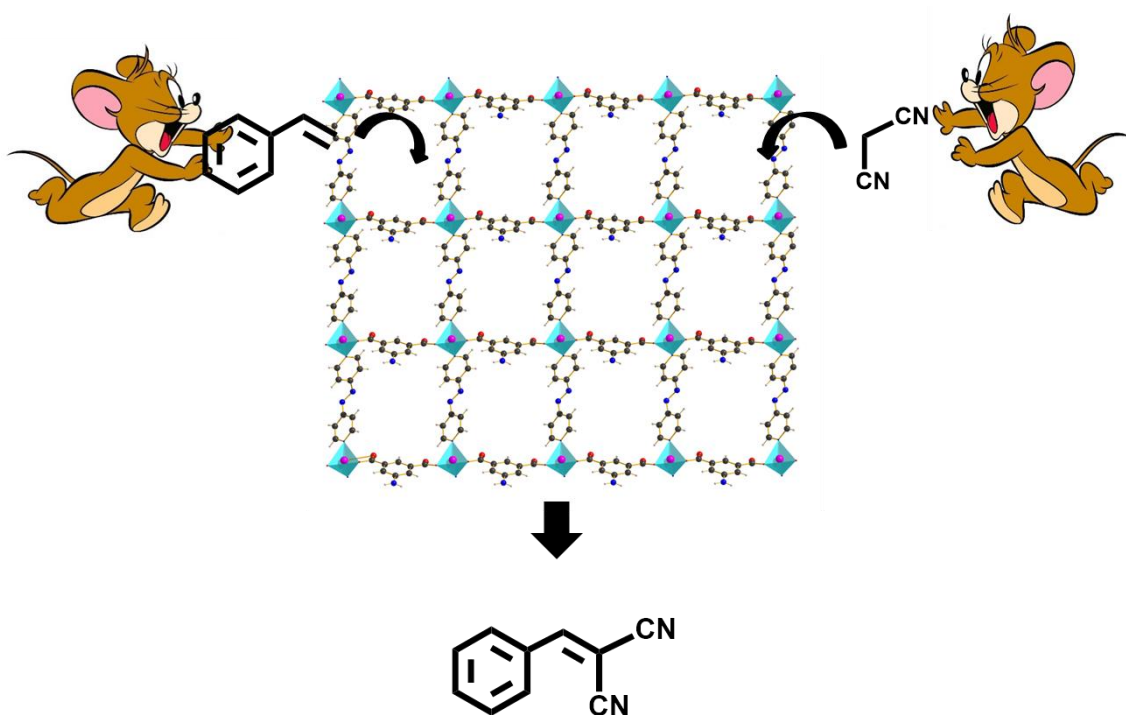
Cobalt(II) based bi-functional MOF as efficient tandem catalyst towards olefin oxidation followed by Knoevenagel condensation

5.1 Introduction

Framework solids are being investigated to use in a variety of organic reactions as heterogeneous catalyst for last few decades [1]. Amongst them tandem catalysis, in which two or more consecutive reactions can be achieved through one catalyst in a single reactor to obtain the desired product which attracted immense attention lately [2].The tandem reactions are characterized by their high level of atom, space, redox and pot economy [3].

Obviously, a simplified purification process can be availed through single pot tandem reaction, which not only reduces chemical waste but also minimizes reaction time and cost [4, 5]. Despite of its advantages, implementation of tandem reaction is difficult in a catalytic process that requires the existence of different catalysts in the same solution. To overcome this difficulty, a catalyst with multifunctional active site is utilized in the synergistic fashion in which one active site involves in producing intermediate of a two-step reaction and second active site interacts with intermediate to produce the targeted product [6]. To this end, multifunctional solids containing different types of active sites in one material have a lot of potential for tandem catalysis. After suitable functionalization, variety of solid materials like mesoporous silica [7, 8], porous organic frame works [9,10] and montmorillonite [11] etc. have been successfully employed as catalyst. With the advent of growing knowledge about multifunctional MOF, various approaches have been employed, to activate MOFs in tandem catalysis. Framework material that affords multiple catalytic centers can be designed and constructed by direct synthesis or post synthetic modification. MOFs that poised to create open metal sites, capable to host nanoparticle or polyoxometalate or simple metal complex guest are suitable choice for designing prospective catalyst. However, metal nanoparticles attached to the solid surface prone to migrate and aggregate into larger particles to minimize their surface energy while polyoxometalate moiety can easily be leached out from MOF during reaction. As a result, MOF materials often undergo deactivation during continuous reactions. Hence, it is desirable that MOF itself should carry catalytically active centers in the framework. It is well understood that removal of coordinated solvent molecules from MOF leads to creation of defects or coordinatively unsaturated metal centers that enables MOFs to act as Lewis acid catalyst and/or redox catalysts. Continued exploration into MOF based catalyst to activate various organic reaction like C-C, C-N, C-O coupling reactions, aldol condensation, hydrogenation, epoxidation etc., led to formulation various efficient catalytic systems[12-18].

Few years ago, a series of MOFs containing two different metal ions have been success fully isolated that catalyzed two different reactions sequentially [19]. The heterometallic MOFs that contains copper and alkaline earth metals like Mg, Ca, Sr and Ba are capable to catalyze first olefin epoxidation reaction using redox catalytic center copper to produce epoxides and subsequently epoxides undergo ring-opening reaction, which is catalyzed by alkaline earth metal Lewis acid centers leading to formation of diol. On further exploration in this line a MOF based tandem catalyst has beendesignedwhich willhave a redox catalytic center and a Lewis base center to catalyze oxidation olefin followed by Knoevenagel condensation of the oxidized product of olefin. The catalytic active sites may be the metal centre or an organic functionality located in the linker unit or both, which can be accommodated in MOF by employing suitable synthetic procedures [20,21]. In order to design the desired framework, carboxylate linker has been used, 5-amino-1,3-benzenedicarboxylic acid; with an intension to synthesize a metal-organic framework consist of cobalt carboxylate backbone of the network that contains free amine functionality. In the hybrid MOF-based catalyst, the redox cobalt (II) centers catalyze the oxidation of olefin followed by Knoevenagel condensation catalyze by the free $-NH_2$ Lewis base center through organo-catalysis.

This chapter reports solvothermal synthesis of a series of cobalt(II) containing 2D MOF *viz.* $\{[Co(L_5)(L_2)](H_2O)\}_n$ (**3**), $\{[Co(L_5)(L_6)]\}_n$ (**4**) and $\{[Co(L_5)(H_2O)](H_2O)_2\}_n$ (**5**) have been (L_5 = 5-amino-1,3-benzenedicarboxylic acid, L_2 = 4,4′-azopyridine and L_6 = 1,2-bis(4-pyridyl)ethane**.** Interestingly tandem catalytic reactions involving olefin oxidation followed by Knoevenagel condensation are efficiently catalyzed by the framework **3** and **4** promoted by the presence of redox active Co(II) and free amine functionality. Notably, **5** which has no free amine catalyzes only the olefin oxidation.

5.2 Experimental section

5.2.1 Materials

Cobalt(II) nitrate hexahydrate, 5-amino-1,3-benzenedicarboxylic acid (L_5), 4,4′azopyridine (L_2) and 1,2-di(4-pyridyl)ethane (L_6) were purchase from Sigma-Aldrich and used as received. All other chemicals were of AR grade and purchased from Sigma-Aldrich. Solvents were purchased from Merck (India) and those were distilled and dried before use.

5.2.2 Physical measurements

The detailsof the instruments used for physical measurement of **3, 4** and **5**has been described inChapter 2 (Section 2.2.2).

5.2.3 Syntheses

5.2.3.1 Synthesis of {[Co(L$_5$)(L$_2$)](H$_2$O)}$_n$ (3)

{[Co(L$_5$)(L$_2$)](H$_2$O)}$_n$ (**3**) was synthesized employing solvothermal method. Co(NO$_3$)$_2$·6H$_2$O (0.25 mmol, 77 mg) dissolved in 2 mL water, and 5-amino-benzene-1,3-dicarboxylic acid (L$_5$) (0.25 mmol, 45 mg) and 4,4´-azopyridine (L$_2$) (0.25 mmol, 46 mg) were separately dissolved in 2 mL DMF. All the solutions were mixed together and transfer to a Teflon lined (15 mL capacity) Parr type autoclave. After stirring well, the mixture was heated at 130 ºC for 72 hours. Upon cooling to room temperature with a rate 10 ºC/min deep blue block shape crystals **3** were collected by filtration and washed with water and dried open at ambient temperature (yield 75% based on metal). Phase purity was verified through elemental analysis and X-ray powder diffraction analysis (vide infra). Anal. Calcd. for C$_{18}$H$_{21}$CoN$_5$O$_8$ (FW 494.26), C, 43.70, H, 4.27, N, 14.16% found C, 42.92, H, 4.32, N, 13.97%. FTIR peaks (cm^{-1}) (Figure 5.1) 3447, 3359 [ν (N-H stretching)], 1667 [ν$_{as}$ (COO$^-$)], 1594, 1556 [ν (N-H bending)], 1403 [ν$_s$ (COO$^-$)], 1367 [ν$_s$ (C-O)].
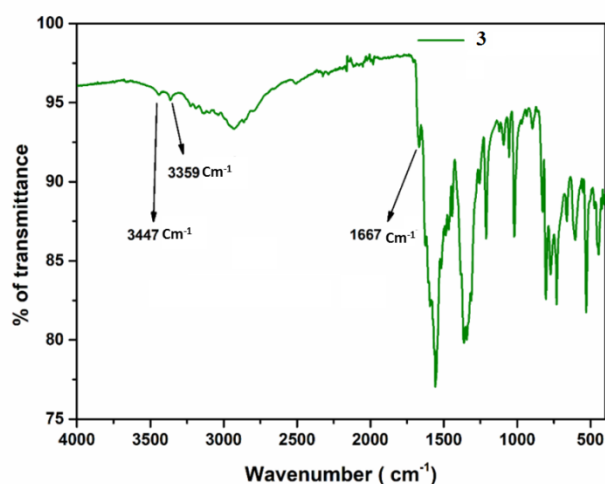
Figure 5.1. IR-spectra of 3

5.2.3.2 Synthesis of $\{[Co(L_5)(L_6)]\}_n$ (4)

Following the same synthesis procedure as in **3** addition of auxiliary ligand 1,2-bis(4-pyridyl)ethane (L_6) (0.25 mmol, 46 mg) in place of L_2 deep blue crystals of $\{[Co(L_5)(L_6)]\}_n$(**4**) were obtained (yield 70% based on metal). Anal. Calcd. for $C_{20}H_{17}CoN_3O_4$ (FW 422.30), C, 56.83, H, 4.05, N, 9.94% found C, 57.19, H, 3.98, N, 9.71%. FTIR peaks (cm^{-1}) (Figure 5.2) 3370, 3450 [ν (N-H stretching)], 1740 [ν_{as} (COO$^-$)], 1598, 1548 [ν (N-H bending)], 1615 [ν_s (COO$^-$)], 1367 [ν_s (C-O)].
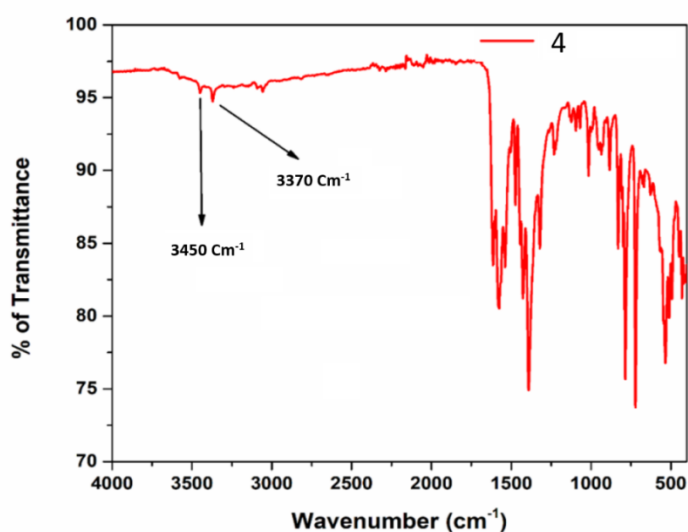
Figure 5.2 IR-spectra of 4

5.2.3.3 Synthesis of $\{[Co(L_5)(H_2O)](H_2O)_2\}_n$ (5)

$\{[Co(L_5)(H_2O)](H_2O)_2\}_n$ (**5**) was also synthesized employing solvothermal method. $Co(NO_3)_2 \cdot 6H_2O$ (0.25 mmol, 77 mg) dissolved in 2 mL water was mixed with 5-aminobenzene-1,3-dicarboxylic acid (0.25 mmol, 45 mg) dissolved in 2 mL DMF and the mixture was transferred to a Teflon lined (15 mL capacity) Parr type autoclave. After stirring well 1 mL ethanol was added to the mixture and heated at 130 ºC for 72 hours. Deep blue block shaped crystals of **5** were obtained upon cooling the mixture to room temperature with a rate 10 ºC/min.Crystals were collected by filtration and washed with water and dried open (yield 70% based on metal). Phase purity was verified through elemental analysis and X-ray powder

diffraction analysis (vide infra). Anal. Calcd. for $C_8H_{11}CoNO_7$ (FW 292.11), C, 32.86, H, 3.76, N, 4.79% found C, 33.05, H, 4.13, N, 4.75%. FTIR peaks (cm⁻¹) (Figure 5.3): 3266, 3150 [ν (N-H stretching)], 1655 [$ν_{as}$ (COO⁻)], 1565, 1540 [ν (N-H bending)], 1430 [$ν_s$ (COO⁻)], 1373 [$ν_s$ (C-O)].
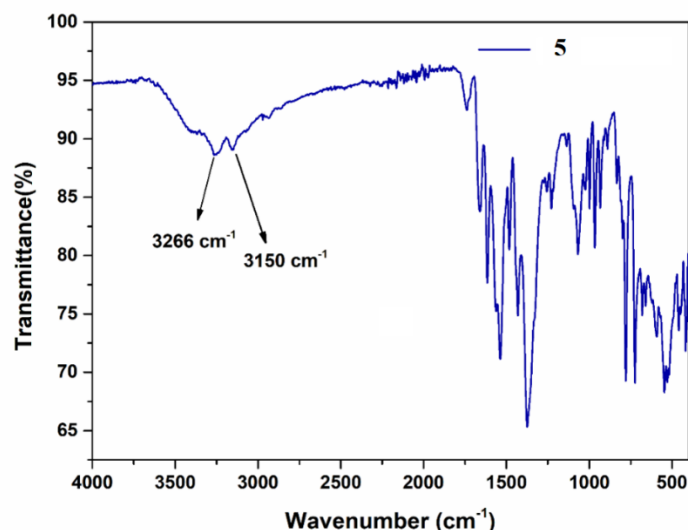
Figure 5.3 IR-spectra of 5

5.2.4 X-ray crystallography

For single crystal X-ray diffraction data collection good quality crystals of **3**, **4** and **5** were selected while bulk materials filtered after solvothermal process. X-ray diffraction data were collected at 273K using suitable single crystal on a Bruker D8 QUEST area detector diffractometer equipped with graphite monochromated MoKα radiation (λ = 0.71073 Å). The molecular structure was solved by direct method and refined by full-matrix least squares on F^2 using the SHELXL-2018/3 package [22]. An empirical absorption correction method (SADABS) [23] was applied. Non hydrogen atoms were refined with anisotropic thermal parameters. All hydrogen atoms were placed in their geometrically idealized positions using suitable riding models on their parent atoms located in the Fourier map. Successful convergence was indicated by the maximum shift / error of 0.001 for the last cycle of the least squares refinement. Due to the high thermal parameter unable to assign any desirable disorder model for

guest molecule, SQUEEZE subroutine of the PLATON software suite was applied to remove the scattering from the highly disordered guest molecules. Solvent molecules were masked for **3** using solvent SQUEEZE instruction in Olex2 [24]. Data collection and structure refinement [25]parameters and crystallographic data of the framework compounds are collated in Table 5.1.

Table 5.1.Crystal data and refinement parameters

Compound	3	4	5
Formula	$C_{18} H_{13} Co N_5 O_4$	$C_{20} H_{17} Co N_3 O_4$	$C_8 H_{11} Co N O_7$
Formula Weight	422.26	422.30	291.75
Crystal System	monoclinic	triclinic	triclinic
Space group	P 21/n	P $\bar{1}$	P $\bar{1}$
a /Å	10.1369(8)	10.005(3)	7.7345(7)
b /Å	11.2986(9)	10.069(3)	8.5639(8)
c /Å	18.9220(15)	10.521(3)	8.5741(8)
α (º)	90	78.366(7)	85.555(3)
γ(º)	90	68.154(7)	75.885(2)
β(º)	96.253(2)	83.134(8)	65.796(2)
V /Å^3	2154.3(3)	962.4(5)	502.20(8)
Z	4	2	2
D_c/g cm^{-3}	1.302	1.457	1.929
μ/mm^{-1}	0.827	0.923	1.734
R(int)	0.1103	0.0961	0.0640
Unique data	4765	4330	2120
Data with I>2σ(I)	3605	3480	2148
R1	0.0549	0.0545	0.0355
wR2	0.1198	0.1551	0.0936
GOF on F^2	1.029	1.036	1.090

$$R_1 = \sum ||F_o| - |F_c||/\sum |F_o|, wR_2 = \{\sum[w(F_o^2 - F_c^2)^2]/\sum w(F_o^2)^2\}^{1/2}$$

5.2.5 Catalytic reactions

One pot synthesis of benzylidene-malanonitrile derivatives from substituted styrene and active methyelene group containing substrate via tandem catalysis that involves oxidation and subsequent condensation reaction is studied here using framework compound as catalyst. The sequential catalytic reactions i.e. oxidative cross coupling was carried out in glass batch reactor according to the procedure given below. Substrate 1 (styrene or styrene derrivative, 1mmol) and substrate 2 (malononitrile or ethyl-cyanoacetate,1.2 mmol), acetonitrile (2 mL) and catalyst (10 mg) were first mixed. The mixture was equilibrated to the desire temperature (70 °C) in an oil bath. After addition of hydrogen peroxide (5 mmol) the mixture was stirred continuously in N_2 atmosphere. The progress of the reaction was monitored by thin layered chromatography. After 4 hours, the reaction mixtures were collected and allowed to cool down to room temperature, mixed with ice cold water and extracted with ethyl acetate. The obtained organic layer was collected and washed with brine solution, dried over anhydrous sodium sulphate and concentrated in vacuum. The collected residue was further purified by column chromatography on silica gel (60-120 mesh). The product was characterized by ^{1}H NMR spectroscopy and elemental analysis and compared with literature value.

5.3 Results and discussion

5.3.1 X-Ray structure

Solvothermal treatment of the mixture of aqueous solution of $Co(NO_3)_2\cdot 6H_2O$ and 5-amino-benzene-1,3-dicarboxylic acid (L_5), and DMF solution of 4,4´-azopyridine (L_2) in the specified condition yielded blue colored mixed-linker metal-organic framework $\{[Co(L_5)(L_2)](H_2O)\}_n$ (**3**) that consists of sole tetrahedral cobalt(II) center (Figure 5.4a). When the same synthesis procedure was employed with use of an auxiliary ligand 1,2-di(4-pyridyl)ethane (L_6) (ethanolic solution) in place of 4,4´-azopyridine (L_2) a pink colored hexa-coordinated cobalt containing MOF $\{[Co(L_5)(L_6)]\}_n$ (**4**) has been isolated. However, when no auxiliary ligand was used, solvothermal treatment of $Co(NO_3)\cdot 6H_2O$ and L_5 yielded an MOF $\{[Co(L_5)(H_2O)](H_2O)_2\}_n$ (**5**) (vide supra). Both **3** and **4** are mixed-linker metal-organic framework while **5** is not. Nevertheless, all three MOFs feature the two-dimensional networked structure, even though, cobalt (II) center has different coordination environment in each of

them. Coordination modes of the carboxylate ligand (L_5) in compounds **3-5** is depicted in Figure 5.5.
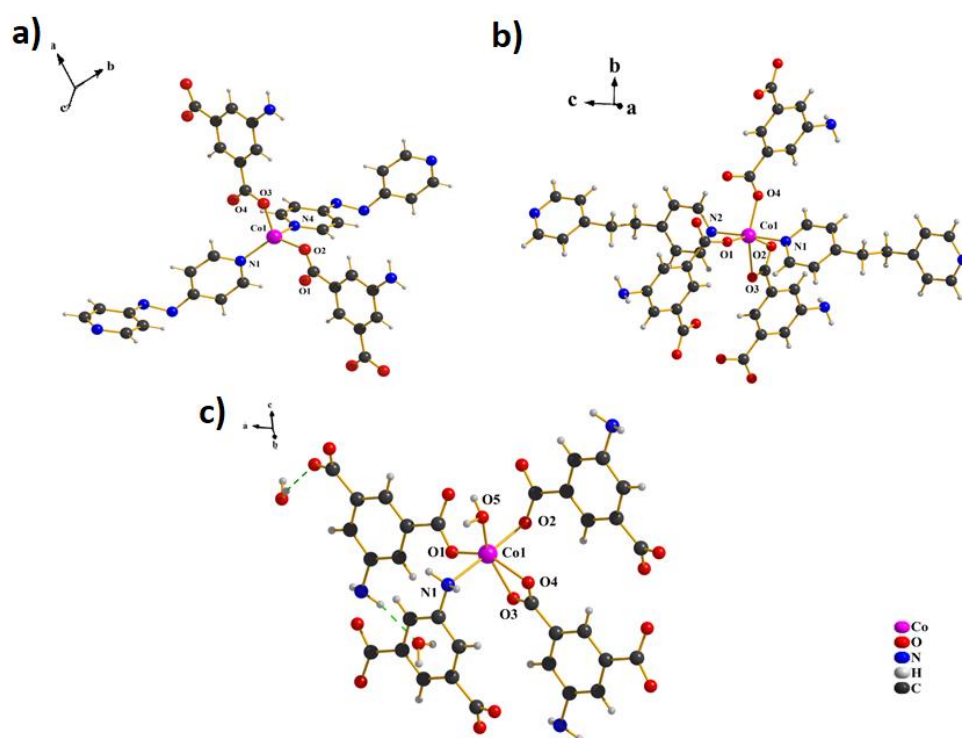
Figure 5.4. Coordination environment around cobalt(II) center in 3-5 given in (a-c)
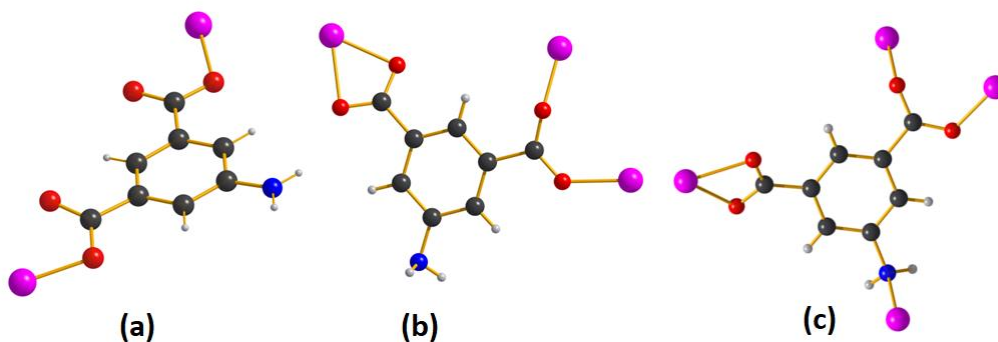

Figure 5.5. Coordination mode of carboxylato ligand (L_5) in 3-5 depicted in (a-c), respectively, Color scheme is the same as in Figure 5.4

5.3.1.1 X-Ray structure of {[Co(L₅)(L₂)](H₂O)}ₙ (3)

X-ray analysis of **3** reveals that it has a two-dimensional planer structure and crystalized in a monoclinic crystal system with P21/n space group and Z = 4 (Table 5.1). **3** has a 2D neutral framework structure arising out from interconnected zigzag chains. The asymmetric unit contains one crystallographically independent cobalt(II) center coordinated to one L_5 ligand and one L_2 ligand (Figure 5.6).The central Co(II) ions, which features a tetrahedral geometry, are coordinated by two pyridyl nitrogen atoms of two different 4,4´-azopyridine (L_2) molecules while other two coordination positions are occupied by two carboxylate oxygen atoms of 5-amino-benzene-1,3-dicarboxylic acid (L_5) (Figure 5.4a). Co(II) with tetrahedral geometry is rarely found in framework compounds. The nitrogen atom of pyridyl moiety present at other end of 4,4´-azopyridine molecule binds a different Co(II) ions to form a 1D chain. 4,4´-azopyridine itself possesses a cis geometry and acts as a bidentate ligand. Each 1D chain further connected by L_5 ligand though carboxylate oxygen atom to form the 2D layer (Figure 5.7). Co-ordination environment around the metal center is shown in Figure 5.4(a) and, bond lengths and angles are summarized in Table 5.2. In {[Co(L_5)(L_2)](H₂O)}ₙthe L_5 ligand coordinates Co center via carboxylato oxygen in bidentate bridging mode keeping amine group free (Figure 5.4a). The O-Co-O, O-Co-N and N-Co-N bond angles are in the range 98.17(9)º to 118.61(9)º indicating minor deviation from ideal tetrahedral coordination geometry around Co(II). Framework compound of tetrahedral cobalt (II) is scarcely been reported in the literature [26,27], MOF made of solely tetrahedral Co centers is even more rare [27].
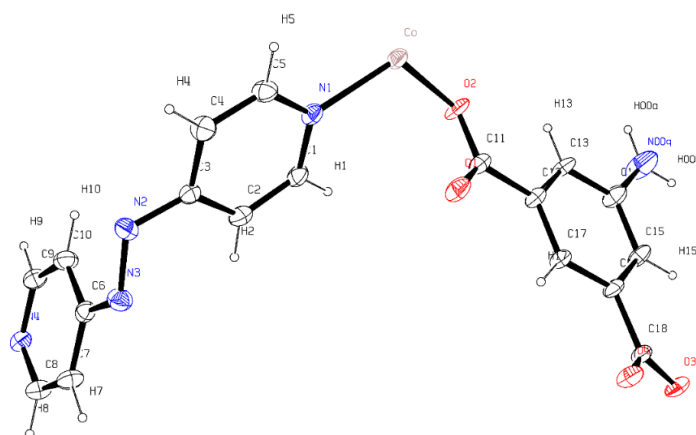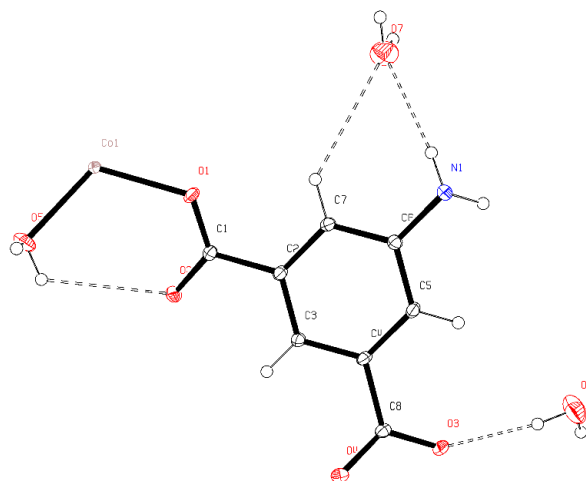

Figure 5.6. Asymmetric unit of 3 (ORTEP diagram with 30% probability)
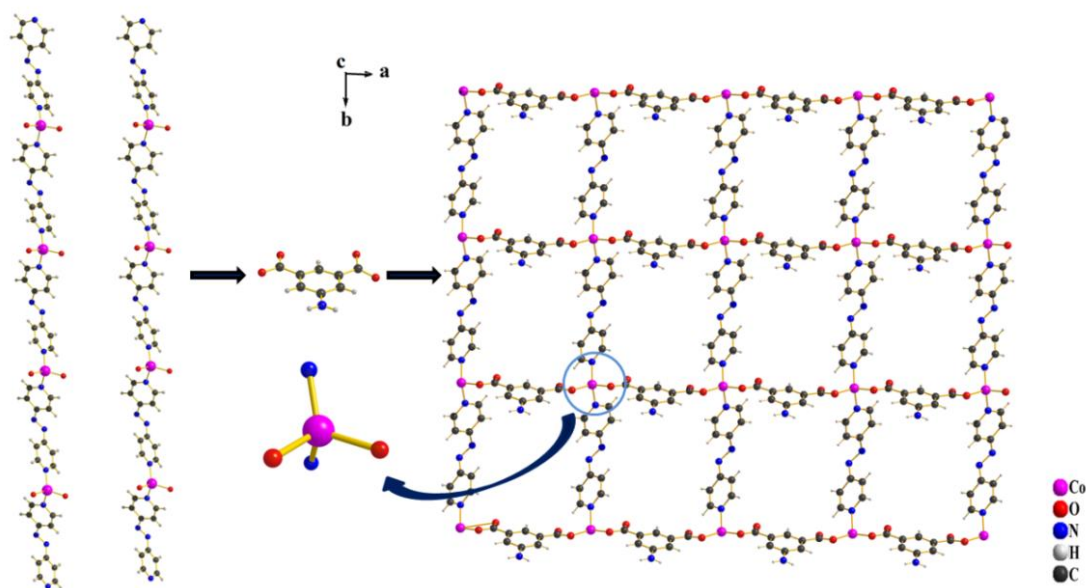
Figure 5.7. Two-dimensional network of 3

5.3.1.2 X-Ray structure of {[Co(L₅)(L₆)]}ₙ (4)

{[Co(L$_5$)(L$_6$)]}$_n$(**4**) crystalizes in triclinic crystal system with P$\overline{1}$ space group, Z = 2 (Table 5.1). The asymmetric unit consists of one crystallographically independent cobalt(II) center coordinated to one L$_5$ ligand and one L$_6$ ligand(Figure 5.8). The hexa-coordinated Co1 center surrounded by four oxygen atoms from three different L$_5$ ligands, which forms the basal plane and remaining two axial positions are occupied by two nitrogen atoms from two L$_6$ ligands to give rise to a distorted octahedral geometry (Figure 5.4b). Coordination environment around the central metal ion is given in the Figure 5.4b. Selected bond lengths and angles are summarized in Table 5.3. The 5-aminobenzene-1,3-dicarboxylato ligand utilizes four oxygen donor atoms of its two different -COOH groups to bind three cobalt centers acting as a tridentate ligand, while leaving one pendent amine functionality free making a double chain structure extended along the crystallographic b-axis. Two parallel double chains are further connected by L$_6$forming two-dimensional infinite network (Figure 5.9). The Co-O bonds, viz. Co1 to O(1)^d, O(2)^c, O(3)^c and O(4) distances are in the range 2.014(3) to 2.227(3) Å. L$_6$ binds two cobalt centre in a bridging bidentate fashion and showed a bond distance for Co1 – N1 and Co1 – N2^b equal to 2.176(3) and 2.182(3) Å, respectively. The trans angles are (158.09(8)º, 177.95(11)º and 154.34(9)º) and the cis angles vary in a wide range (from 59.86(9)° to 106.69(9)°(Table 5.3).
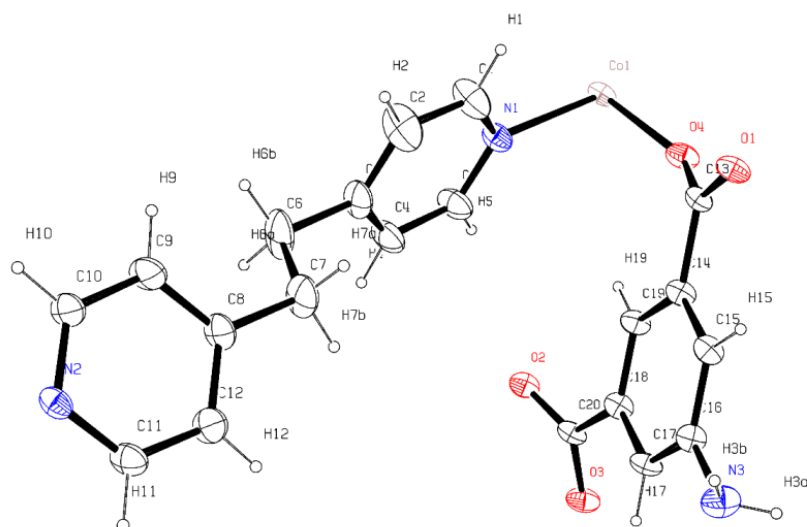
Figure 5.8. Asymmetric unit of 4 (ORTEP diagram with 30% probability)
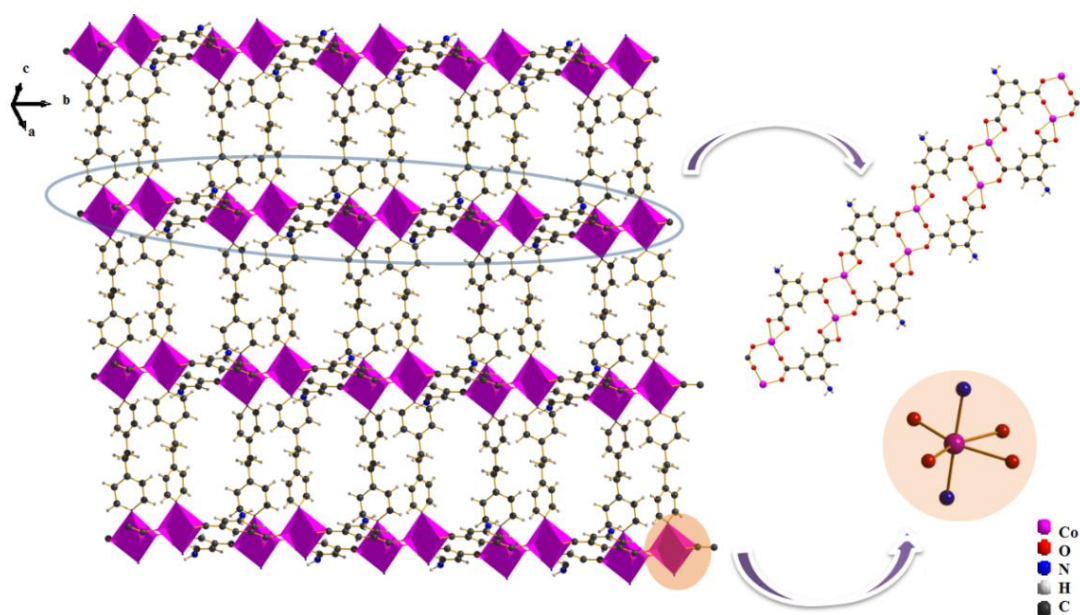
Figure 5.9. Two-dimensional network of 4

5.3.1.3 X-ray structure of {[Co(L$_5$)(H$_2$O)](H$_2$O)$_2$}$_n$(5)

The X-ray structure of {[Co(L$_5$)(H$_2$O)](H$_2$O)$_2$}$_n$(**5**) has been reported previously [28]. However, its structure has been re-determined and the results which are relevant in this discussion have been enumerated suitably below.
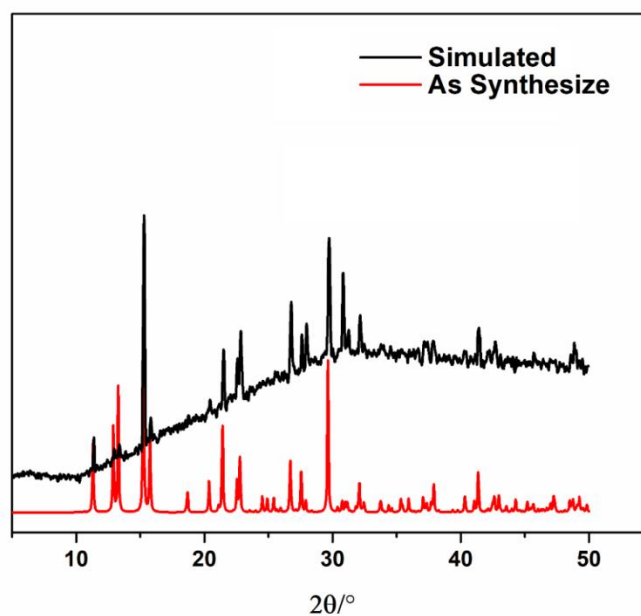

Figure 5.10. Asymmetric unit of 5 (ORTEP diagram with 30% probability)
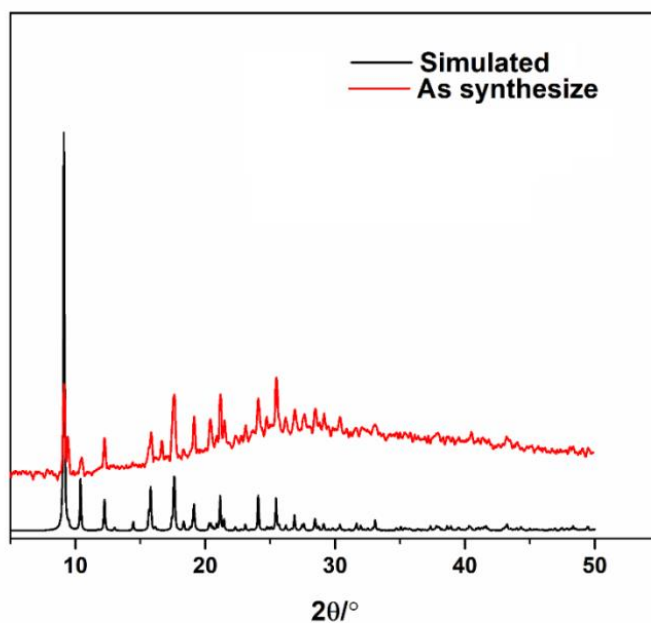
Figure 5.11. Powder X-ray diffraction pattern of 3
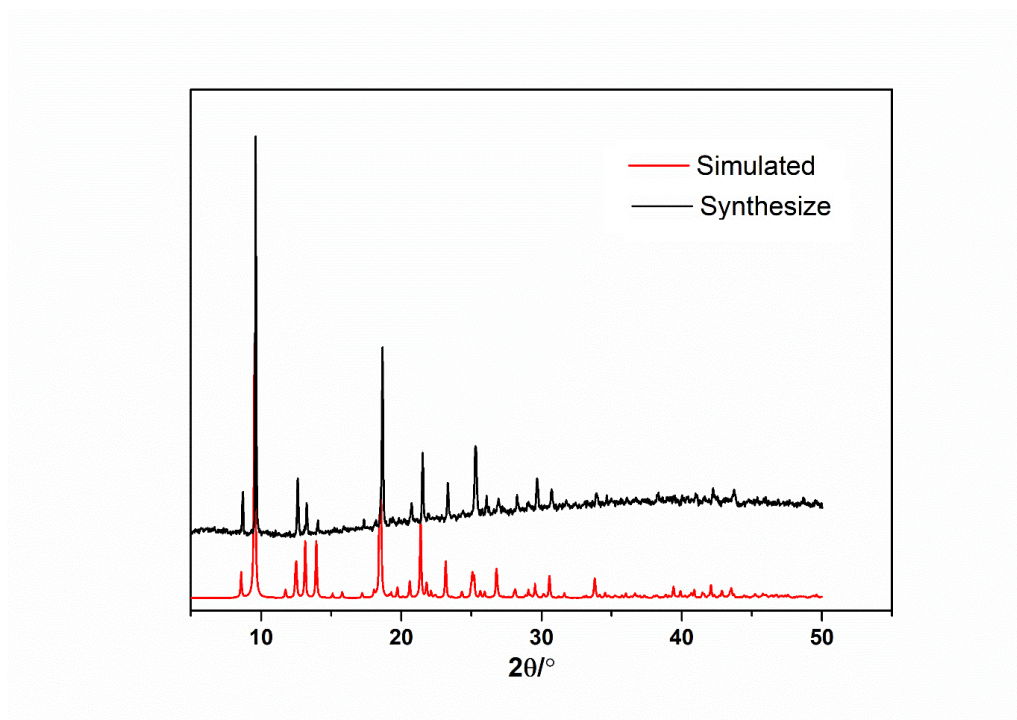
Figure 5.12.Powder X-ray diffraction pattern of 4

**Figure 5.13. Powder X-ray diffraction pattern of 5**

Table 5.2 Bond distances (Å) and angles (º) around the metal center in 3

Atoms	Distance	Atoms	Distance
Co - O2	1.986(2)	Co - N1	2.036(2)
Co - O3^a	2.004(2)	Co - N4^c	2.060(2)
Atoms	**Angle**	**Atoms**	**Angle**
O2 -Co - N1	114.38(9)	N1 – Co – N4^c	110.52(10)
O2 - Co - O3^a	98.17(9)	O3^a – Co – N1	118.61(9)
O2 – Co – N4^c	106.29(9)	O3^a – Co – N4^C	107.65(9)

Table. 5.3. Bond distances (Å) and angles (º) around the metal center in 4

Atoms	Distance	Atoms	Distance
Co1 – N1	2.176(3)	Co1 – O3^C	2.227(3)
Co1 – N2^b	2.182(3)	Co1 – O4	2.014(3)
Co1 – O2^c	2.145(2)	Co1 – O1^d	2.041(2)
Atoms	**Angle**	**Atoms**	**Angle**
O4 – Co1 – N1	91.42(11)	O1^d - Co1 - N1	94.92(11)
O4 – Co1 – N2^b	88.66(11)	O2^c – Co1 – N2^b	87.64(11)
O2 – Co1 – O4	98.26(9)	O3^c – Co1 – N2^b	89.25(11)
O3^c – Co1 – O4	158.09(8)	O1^d – Co1 – N2^b	87.02(11)
O1^d – Co1 – O4	106.69(9)	O2^c – Co1 – O3^c	59.86(9)
N1 - Co1 – N2^b	177.95(11)	O1^d – Co1 – O2^c	154.34(9)
O2^c – Co1 – N1	90.32(11)	O1^d – Co1 – O3^c	94.98(9)
O3^c- Co1 – N1	89.91(11)		

Table 5.4 Bond distances (Å) and angles (º) around the metal center in 5

Atoms	Distance	Atoms	Distance
Co1 – O1	2.016(2)	Co1 – O4[a]	2.216(3)
Co1 – O5	2.061(3)	Co1 – O2[c]	2.096(3)
Co1 – O3[a]	2.166(3)	Co1 – N1[d]	2.259(3)
Atoms	**Angle**	**Atoms**	**Angle**
O1 – Co1 – O5	115.24(11)	O5 – Co1 – N1[d]	85.54(11)
O1 – Co1 – O3[a]	92.45(10)	O3[a] – Co1 – O4[a]	59.82(9)
O1 – Co1 – O4[a]	150.48(9)	O2[c] – Co1 – O3[a]	87.21(10)
O1 – Co1 – O2[c]	97.27(10)	O3[c] – Co1 – N1[d]	96.13(10)
O1 – Co1 – N1[d]	85.58 (10)	O2[c] – Co1 – O4[a]	91.63(10)
O3[a] - Co1 – O5	152.29(10)	O4[a] – Co1 – N1[d]	87.51(10)
O2[c] - Co1 – O5	90.12(11)	O2[c] – Co1 – N1[d]	175.53(9)
O4[a] - Co1 – O5	92.73(10)		

5.3.2 Thermogravimetric analysis

To check the thermal stability of **3** and **4** thermogravimetric (TG) analysis (30-800ºC) has been performed on a powdered sample under nitrogen atmosphere. The TG curve indicates that **3**(Figure 5.14) starts to lose water molecules at ∼60 °C and dehydration completes around 230ºC. The mass loss of ∼12.4% shown in the range 60-230 °C corresponds to the loss of guest water molecules (theoretical value 12.6%). Thereafter the TG curve displays a plateau up till ∼350 °C, indicating no mass loss in this temperature range. On further heating, a subsequent sharp weight loss is observed in the temperature range 350-600ºC owing to the decomposition of organic skeletal of the compound to form the corresponding metal oxide (experimental wt. loss 15%; calculated 14.7%).
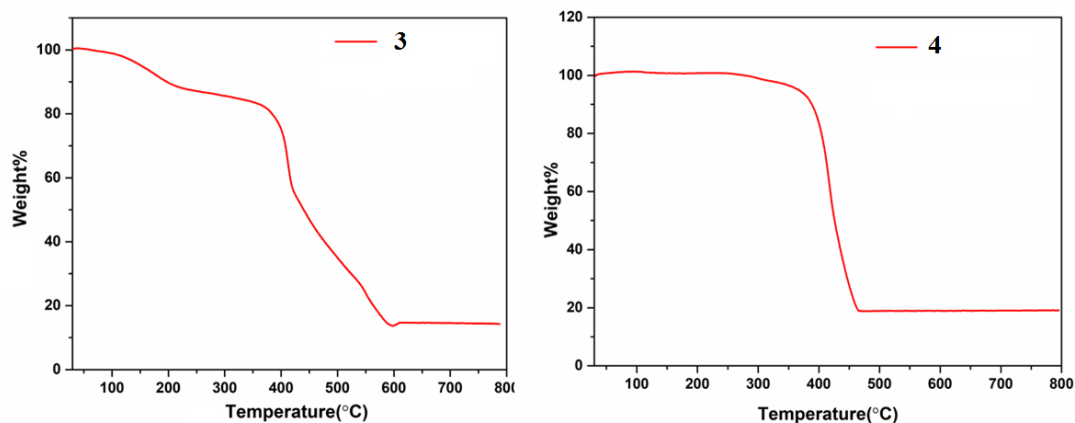
Figure 5.14. Thermogravimetric Plot of 3 and 4

Thermogravimetric analysis **4** reveals that there is no remarkable weight loss up to the temperature 340ºC indicating the compound is fairly thermally stable (Figure 5.14). A sharp weight loss is observed in the temperature range 350-470ºC due to the decomposition of organic framework and thereby transforms to corresponding metal oxide (experimental wt. loss 18%; calculated 18.6%).
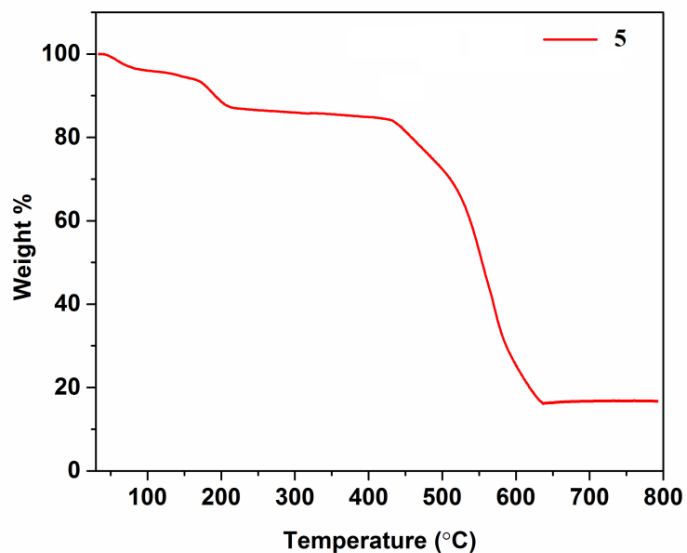
Figure 5.15. Thermogravimetric Plot of 5

The result of thermogravimetric analysis of **5** shows weight loss in three distinct steps (Figure 5.15). First weight loss of 11.5% from 40ºC up to 160ºC validate with the theoretical value 12.3% may be due to the removal of water molecules between the layers. The second weight loss about 6% (calculated 6.1%) is observed in the temperature range 170ºC to 250ºC corresponding to loss of water coordinated molecule per formula unit. The anhydrous compound is stable up to 450ºC without any weight loss. A sharp weight loss is observed within the temperature range 450ºC to 600ºC leads to the decomposition of organic framework to form corresponding metal oxide.

5.3.3 Catalytic study

Having synthesized and characterized the MOFs in hand, attempt has been made to employ these solid catalysts in the heterogeneous tandem catalytic reaction. Investigation was initiated by examining the optimized reaction conditions using styrene and malononitrile as model substrates. Catalytic oxidation of styrene followed by Knoevenagel condensation between aldehyde and malononitrile has been optimized employing **3** as catalyst. To determine the optimal condition for the reaction the effects of various parameters like temperature, solvents, catalysts and oxidants were tested (Table 5.5). Additionally, a blank experiment was conducted to further verify the activity of the catalyst. Optimization table shows that solvent plays a crucial role for this conversion. Catalytic activity of the compounds was tested in different solvents and found that toluene is not suitable as solvent for conversion of styrene. With increasing polarity of solvents catalytic performance increases and acetonitrile is selected as solvents for this reaction. Further increase in solvent polarity (methanol) selectivity of oxidation reaction is decreases. It can be seen from the Table 5.5 that among various oxidants like air oxygen, TBHP and H_2O_2, maximum product is obtain from H_2O_2.It is beneficial to use H_2O_2 in catalysis as its end product is water and product is easily removed from reaction mixture. Temperature also has influence to the catalytic activity of compounds. At high temperature (90ºC) the selectivity of styrene conversion to benzaldehyde decreases and yield of the desire product decreases. The catalytic oxidation of styrene by hydrogen peroxide were performed in glass batch reactor under mild conditions (2 mL MeCN, 70 ºC) with 0.025 mmol of catalyst and H_2O_2 (5 mmol) under vigorous stirring for 4 hours. The products obtained are collected and separated by column chromatography and characterized by NMR. Knoevenagel condensation reaction between benzaldehyde and malononitrile catalyzed by reported

compounds were performed in reaction tube under mild solvent free condition with continuous stirring for 4 hours. The products of each reaction were purified and characterized followingthe methods given above.

Catalytic oxidation of styrene and subsequent coupling reactions with activated methylene (malononitrile) using **3**-**5** were performed in an acetonitrile medium at 70ºC in the presence of hydrogen peroxide under heterogeneous condition. In every cases for **3** and **4** benzylidene-malononitrile was the obtainedas product, but in case of **5**only trace amount of benzylidene-malononitrile product was detected. The overall conversion from styrene to benzaldehyde decreases from **3**-**5**. In case of **3** and **4**, subsequently, benzaldehyde converts to the corresponding benzylidenemalononitrileafter reaction with malononitrile and the conversion was more than 70%. The catalytic activity of **3** and **4**forvarious styrene derivatives and activemethylenegroup containing substrates, malononitrile and ethyl-cyanoacetate are collated in the Table 5.6. Therefore, it is clear that for catalysts**3** and **4** styrene converts to the benzylidenemalononitrile via formation of the corresponding aldehyde. However, in case of **5**only trace amount of benzylidenemalononitrile product was detected, implying that the poor catalytic activity of **5** towards the 2nd step. Evidently, framework compounds **3** and 4 are act as bi-functional catalyst. The compounds contain the redox active Co(II) center along with free amino functionality, which behave as a Lewis base in nature. The cobalt center is highly active towards olefin oxidation in presence of H_2O_2 in acetonitrile medium.There are different examples of olefin oxidation by Co(II) catalyst [29]. The free amine group also catalyzes the Knoevenagel condensation [30]. As a result, the framework compounds play dual role and catalyze the two sequential reactions step by step to form the desire product with good yield. However, the catalytic efficiency of **3** and **4** is different towards oxidation reaction, which can be correlated to different structural feature of the active centers. In**4** the cobalt (II) centers are hexa-coordinated and more crowded, hence, less active, whereas in **3**, cobalt(II) features a tetrahedral geometry showing greater activity towards oxidation. Furthermore, in **3** the active Co (II) centers are in coordinatively unsaturated tetrahedral geometry accompanied with presence of polar azo group in azopyridine ligand may be cooperatively facilitate the good conversion of styrene to corresponding aldehyde. However, the 2nd step of the sequential reaction is not so much affected by these factors as both contains the free amine functionality. But in case of **5** trace amount of final product was detected though it also contains active Co (II) center. The main difference in catalytic activity is due to the fact that in catalyst **5**, amine
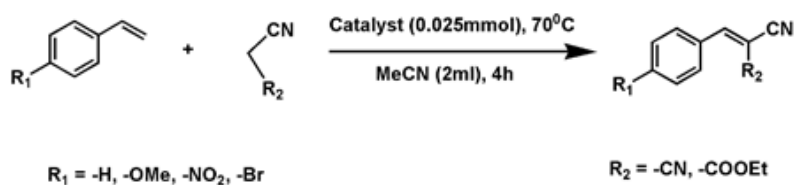
functionality is coordinated with metal center leading to reduced basicity and makes less available for catalyzing Knoevenagel condensation reaction. Therefore, the maximum yield is obtaining in case of **3**. To verify the bi-functional nature of catalysts **3** and **4** each step of sequential catalysis reactions were undertaken separately. In addition, same procedure has also been followed for framework compound **5**. For the styrene oxidation in every case benzaldehyde is the major product, i.e. each compound can oxidize styrene to benzaldehyde due to the presence of active cobalt center (Table 5.7). In case of 2nd step i.e. Knoevenagel reaction between benzaldehyde and malononitrile above 90% conversion for catalysts **3** and **4** is observed, but in case of **5** only ~10% final product is obtained (Table 5.8). This clearly showed the significant role of free amine functionality towards catalytic Knoevenagel condensation reaction. Presence of free amine functionality facilitates to catalyze both the reactions sequentially for **3** and **4**. But in case of **5**, amine functionality of L_5 ligand is coordinated to central cobalt atom, makes its unavailability as Lewis basic site for catalyzing Knoevenagel condensation. As a result, only trace amount of final product is obtained in oxidation followed by condensation reaction. Hence, it is clear that the framework compounds **3** and **4** contain two different active centers which can catalyze two different reactions in a single pot to afford the desire product.

Table 5.5. Optimization of reaction condition
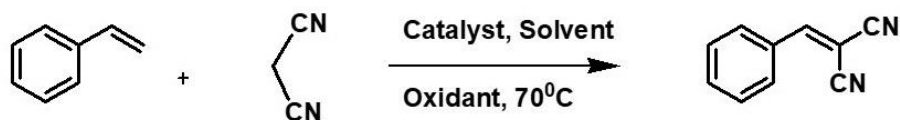
Entry[a]	Catalyst	Oxidant	Solvent	Yield[b](%)
1	$\{[Co(L_5)(L_2)](H_2O)\}_n$	H_2O_2	Toluene	6
2	$\{[Co(L_5)(L_2)](H_2O)\}_n$	H_2O_2	DCM	48
3	$\{[Co(L_5)(L_2)](H_2O)\}_n$	H_2O_2	THF	53
4	$\{[Co(L_5)(L_2)](H_2O)\}_n$	H_2O_2	CH_3OH	50
5	$\{[Co(L_5)(L_2)](H_2O)\}_n$	H_2O_2	CH_3CN	70
6	$\{[Co(L_5)(L_2)](H_2O)\}_n$	Air oxygen	CH_3CN	12
7	$\{[Co(L_5)(L_2)](H_2O)\}_n$	TBHP	CH_3CN	43
8[c]	$\{[Co(L_5)(L_2)](H_2O)\}_n$	H_2O_2	CH_3CN	54
9[d]	$\{[Co(L_5)(L_2)](H_2O)\}_n$	H_2O_2	CH_3CN	59
10	$\{[Co(L_5)(L_2)](H_2O)\}_n$	H_2O_2	CH_3CN	64
11	$\{[Co(L_5)(L_2)](H_2O)\}_n$	H_2O_2	CH_3CN	10
12	Blank	H_2O_2	CH_3CN	2
13	$Co(NO_3)_2 \cdot 6H_2O$	H_2O_2	CH_3CN	5

[a]Reaction condition: Styrene (1mmol), malononitrile (1.2mmol), oxidant (5 mmol), solvent (2mL), at 70ºC upto 4h. [b]Isolated yield; [c] at 50ºC; [d] at 90ºC. TBHP = tert-butylhydroperoxide.

Table 5.6. Styrene derivative to benzylidene-malononitrile conversion catalyzed by 3,4[a]

R_1 = -H, -OMe, -NO$_2$, -Br

R_2 = -CN, -COOEt

Entry[a]	Substrate-1	Substrate-2	Product	Yield[b] (%)
1		CN CN	CN CN	I) 70 II) 64
2		CN COOEt	CN COOEt	I) 69 II) 62
3	Br	CN CN	Br CN CN	I) 72 II) 66
4	Br	CN COOEt	Br CN COOEt	I) 70 II) 62
5	O$_2$N	CN CN	O$_2$N CN CN	I) 82 II) 75
6	O$_2$N	CN COOEt	O$_2$N CN COOEt	I) 79 II) 69
7	MeO	CN CN	MeO CN CN	I) 65 II) 60
8	MeO	CN COOEt	MeO CN COOEt	I) 61 II) 52

[a]Reaction conditions: Substrate (styrene or styrene derivative, 1mmol), substrate (malononitrile or ethyl-cyanoacetate, 1.2mmol) H$_2$O$_2$ (5mmol), catalyst (0.025mmol) and acetonitrile (2ml), temperature 70ºC, reaction time 4h, I- II denote the catalytic activity of **3** and **4**, respectively.[b]Isolated yield.

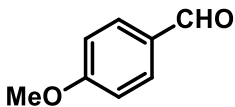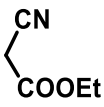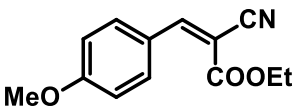**Table 5.7. Oxidation of substituted styrene to substituted benzaldehyde catalyzed by 3-5[a]**

Catalyst (0.025mmol), 70°C

H$_2$O$_2$, MeCN

R$_1$ = -H, -OMe, -NO$_2$, -Br
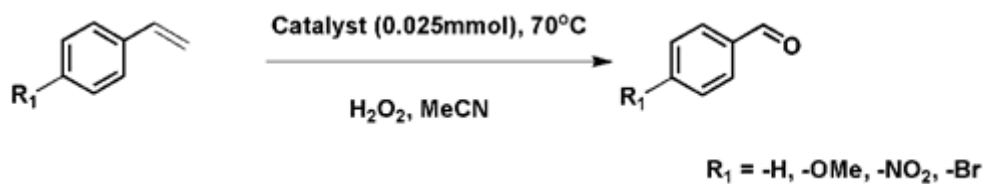
Entry[a]	Substrate	Product	Yield[b]
1	(styrene)	(benzaldehyde)	I) 72 II) 67 III) 63
2	(4-Br styrene)	(4-Br benzaldehyde)	I) 76 II) 69 III) 70
3	(4-NO$_2$ styrene)	(4-NO$_2$ benzaldehyde)	I) 81 II) 73 III) 70
4	(4-OMe styrene)	(4-OMe benzaldehyde)	I) 68 II) 65 III) 60

[a]Reaction conditions: Substrate (styrene or styrene derivative 1mmol), H$_2$O$_2$ (5mmol), catalyst (0.025mmol) and acetonitrile (2mL) temperature 70°C, reaction time (4h), I-III denoted the catalytic activity of **3** to **5**, [b] Isolated yield.

Table 5.8. Knoevenagel condensation catalyzed by 3, 4[a]

R_1 = -H, -Br, -OMe, -NO$_2$ R_2 = -CN, -COOEt
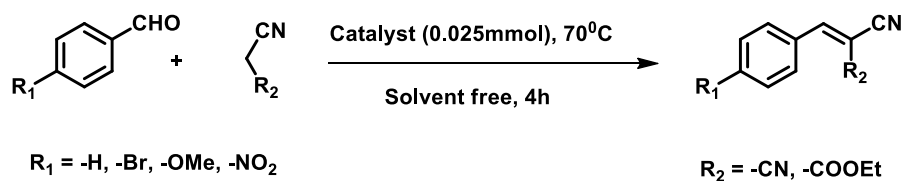
Entry[a]	Substrate-1	Substrate-2	Product	Yield[b]
1				I) 87 II) 85
2				I) 86 II) 82
3				I) 89 II) 90
4				I) 85 II) 83
5				I) 95 II) 92
6				I) 92 II) 90
7				I) 83 II) 80

8	MeO—⬡—CHO	NC–CH_2–$COOEt$	MeO—⬡—$CH{=}C(CN)(COOEt)$	I) 79 II) 74

[a]Reaction conditions: Substrate-1 (styrene or styrene derivative, 1mmol), Substrate-2 (malono nitrile or ethyl-cyanoacetate), 1.2mmol), Catalyst (0.025mmol), Solvent free conditions, Temperature 70°C. I-II denoted catalytic activity of **3** and **4**, [b] Isolated yield.

5.4 Stability, heterogeneity and reusability test of the catalyst

A hot filtration experiment was performed to check the heterogeneity behavior of catalyst that could be the proof of metal was not leached out during the catalysis. After completion of reaction the catalysts were easily recovered by simple centrifugation and washed thoroughly by acetonitrile and dried at ambient temperature. Structural integrity of the recovered catalyst was checked by powder X-ray diffraction analysis (Figures 5.16 and 5.17) and SEM analysis (Figure 5.18). The recovered catalyst almost shows the same catalytic activity upto five successive runs demonstrate their reuse ability (Figures 5.19 and 5.20).
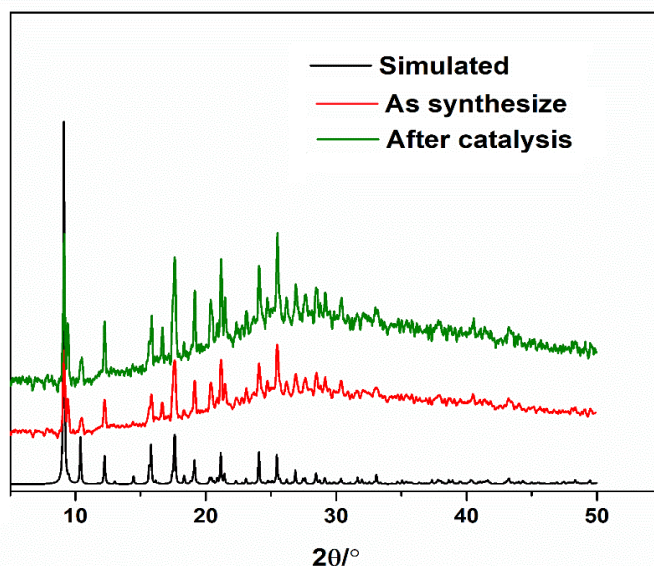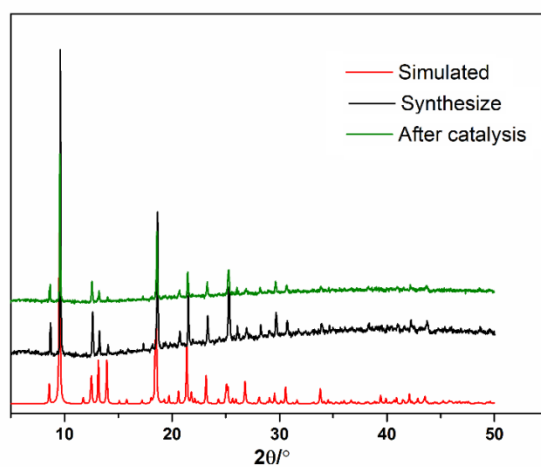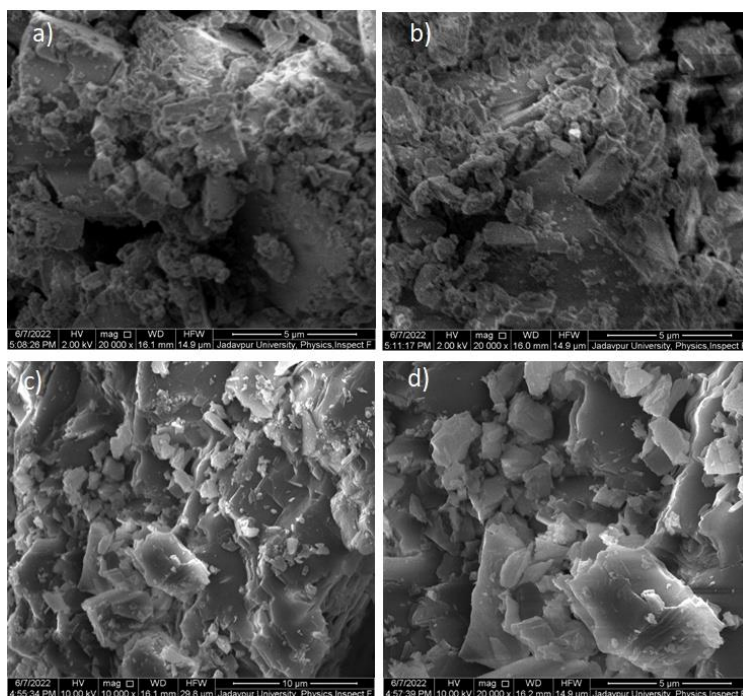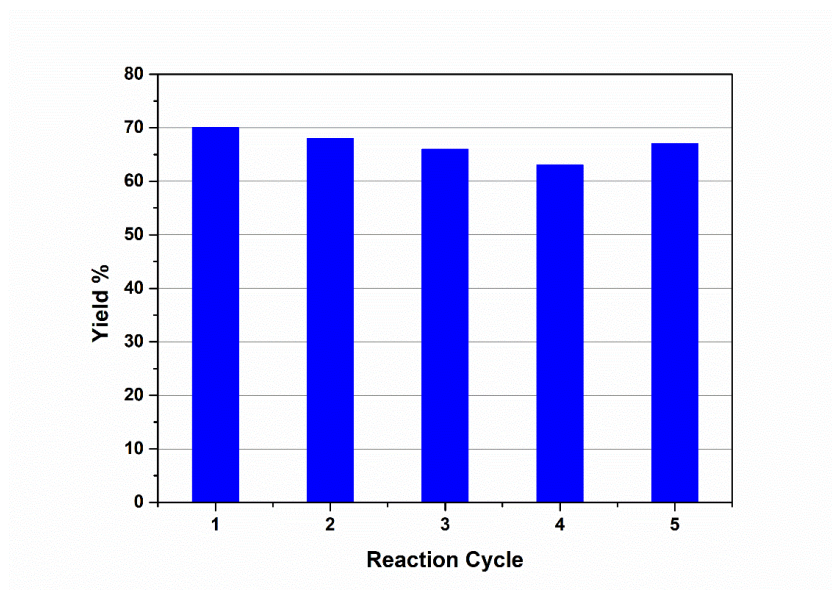

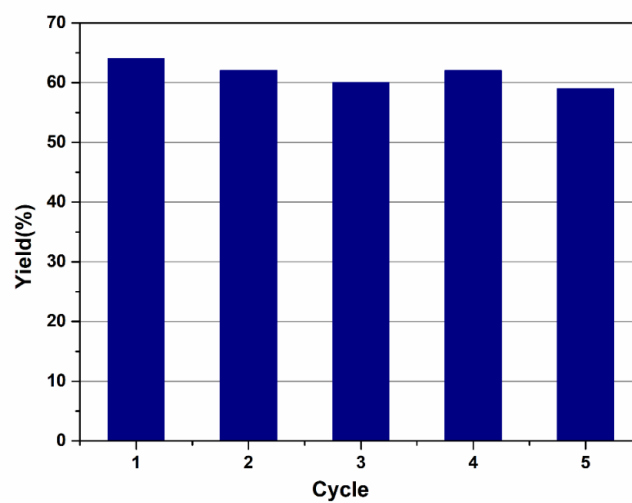**Figure 5.16. Powder X-ray diffraction pattern of 3**

Figure 5.17. Powder X-ray diffraction pattern of 4

Figure 5.18. SEM picture of the reported compounds recovered after catalysis (a and b for 3; c and d for 4)

Figure 5.19. Tandem reaction catalyzed by 3 in five successive runs

Figure 5.20. Tandem reaction catalyzed by 4 in five successive runs

5.5 Conclusion

In conclusion, cobalt based two-dimensional functionalized framework compounds$\{[Co(L_5)(L_2)](H_2O)\}_n$ (**3**),$\{[Co(L_5)(L_6)]\}_n$(**4**) and $\{[Co(L_5)(H_2O)](H_2O)_2\}_n$ (**5**) has been synthesized by solvothermal method. In case of framework compound **3** the central cobalt ion is adopting tetrahedral geometry, which is very rare. Both of the compounds **3** and **4** contain free amine functionality and plays bi-functional role, catalyzes oxidation of styrene followed by Knoevenagel condensation in tandem.However, in case of **5** as the amine functionality, which acts as catalytic center for Knoevenagel reaction, is coordinated with cobalt ion, as a result, lost its catalytic activity towards Knoevenagel condensation. This clearly indicates the role of free amino group towards catalyzing the Knoevenagel condensation. Therefore, among three compounds **3** and **4** are efficient catalyst for styrene oxidation followed by Knoevenagel condensation in tandem.

5.6 References:

1. F. Llabrés i Xamena, J. Gascon, Metal Organic Framework as Heterogeneous Catalyst, Chapter 1, RSC Publishing, Cambridge, 2013, pp.1.

2. Y. B. Huang, J. Liang, X. S. Wang, R. Cao, Chem. Soc. Rev. 2017, **46**, 126.

3. A. Grossmann, D. Enders, Angew. Chem. 2012, **51**, 314.

4. L. F. Tietze, Chem. Rev. 1996, **96**, 115.

5. L. F. Tietze, G. Brasche, K. M. Gericke, Wiley-VCH, Weinheim, 2006.

6. J.H. Kim, Y.O. Ko, J. Bouffard, S.-G. Lee, Chem. Soc. Rev. 2015, **44**, 2489.

7. S. Shylesh, A. Wagener, A. Seifert, S. Ernst, W. R. Thiel, Angew. Chem. 2010, **49**, 184.

8. Y. Yang, X. Liu, X.Li, J. Zhao, S. Bai, J. Liu, Q. Yang, Angew. Chem. 2012, **51**, 9164.

9. E. Merino, E.Verde-Sesto, E. M. Maya, M.Iglesias, F. Sánchez, A. Corma, Chem. Mater.2013, **25**, 981.

10. Y. Zhang, B. Li, S. Ma, Chem. Commun.2014, **50**, 8507.

11. G. B. B. Varadwaj, S. Rana, K. Parida, B. B. Nayak, J. Mater. Chem. A.2014, **2**, 7526.

12. D. Farrusseng, S. Aguado, C. Pinel, Angew. Chem. 2009, **48**, 7502.

13. L. Q. Ma, C. Abney, W. B. Lin, Chem. Soc. Rev. 2009, **38**, 1248.

14. O. Ohmori, M. Fujita, Chem. Commun. 2004, 1586.

15. F. Song, C. Wang, J. M. Falkowski, L. Ma, W. Lin, J. Am. Chem. Soc. 2010, **132**, 15390.

16. T. Maity, D. Saha, S. Koner, ChemCatChem, 2014, **6**, 2373.

17. D. Saha, T. Maity, S. Das, S. Koner, Dalton Trans, 2013, **42**, 13912.

18. P. Garcia-Garcia, J. M. Moreno, U. Diaz, M. Bruix, A. Corma, Nat. Commun. 2016, **7**, 10835.

19. D. Saha, D. K. Hazra, T. Maity, S. Koner, Inorg. Chem. 2016, **55**, 5729.

20. M. Y. Masoomi, A. Morsali, A. Dhakshinamoorthy, H. Garcia, Angew. Chem. 2019, **58**, 15188.

21. A. Bavykina, N. Kolobov, I. S. Khan, J.A. Bau, A. Ramirez, J. Gascon, Chem. Rev. 2020, **120**, 8468.

22. I. Usón and G.M. Sheldrick, ActaCrystallogr. Sect. D2018, **74**, 106.

23. O. V. Dolomanov, L. J. Bourhis, R. J. Gildea, J. A. K. Howard, H. Puschmann, J. Appl. Cryst. 2009,**42**, 339.

24. SAINT, version 6.02; SADABS, version 2.03; Bruker AXS, Inc.: Madison, WI, (2002).

25. G.M. Sheldrick, Acta. Cryst. C71, 2015, 3.

26. Somnath, M. Ahmad, K. A. Siddiqui, J. Mol. Struct. 2022,**1265**, 133399.

27. Y. Zorlu, D. Erbahar. A. Cetinkaya, A. Bulut, T. S. Erkal, A. O. Yazaydin, J. Beckmann, G. Yucesan, Chem. Commun. 2019, **55**, 3053.

28. Q. -J. Deng, M. -C. Wu, Z. -T. Liu, M. -H. Zeng, J. -Y. Huang, H. Liang, J. Mol. Struct. 2008, **875**, 162.

29. Y. Ma, H. Peng, J. Liu, Y. Wang, X. Hao, X. Feng, S. U. Khan, H. Tan, Y. Li. Inorg. Chem. 2018, **57**, 4109.

30. H. Liu, F.-G. Xi, W. Sun, N.-N. Yang, E.-Q. Gao. Inorg. Chem. 2016, **55**, 5753.

Chapter 6

Highlights

6.1 Highlights

The main findings of the present investigation are collated in this chapter. The thesis presents a glimpse of recent advances in the field of gas adsorption, heterogeneous catalysis and luminescence properties of metal-organic frameworks vis-à-vis their synthesis and structural diversity. The major emphasis given in on the synthesis, structural characterization, gas uptake capacity of small gas molecules like CO_2, H_2, CH_4, N_2 etc. especially selective CO_2 adsorption over N_2, CH_4 and theoretical interpretation and photoluminescence behaviors.

The importance of framework compounds in industrial and fundamental research led to develop various metal-based systems mostly d^{10} metals (Cd, Zn etc.) and transition metals (Cu, Co etc.) that have potential application in luminescence properties, heterogeneous catalysis and gas adsorption studies. To develop porous MOFs, various types of carboxylate linkers and spacers have been used in a variety of reaction conditions. Solvothermal and hydrothermal both techniques have been used for synthesis of MOFs. Depending on the nature of framework MOFs have been appropriately selected and employed in different studies.

A potential luminescence sensor based on porous metal organic framework (MOF) for the detection of metal ions (Al^{3+}, Fe^{3+} or Cr^{3+}) and nitro explosive, 2,4,6-tri-nitrophenol (TNP) has been identified. The cadmium(II) containing mixed-linker MOF viz. $\{[Cd(L_1)(L_2)](DMA)\}_n$ (**1**) (L_1 = 2-amino-1,4-benzenedicarboxylate, L_2 = 4,4´-azopyridine and DMA = N,N-dimethylacetamide) has been prepared through solvothermal method using L_1 and L_2 dissolved in DMA medium. Single crystal X-ray diffraction analysis revealed $\{[Cd(L_1)(L_2)](DMA)\}_n$ (**1**) features an interpenetrated 3D framework structure. Porosity of the compound has been investigated by N_2, H_2, CO_2 adsorption as well as water vapor adsorption. The compound exhibits selective turn on sensing towards tri positive metal ions (Al^{3+}, Fe^{3+} or Cr^{3+}) and turn off sensing towards TNP. The free $-NH_2$ group plays active roles in fluorescent sensing. Notably, **1** is capable of detecting aqueous phase analytes though luminescent sensing. Clearly, it has potential to allow preliminary in-field screening of industrial and environmental samples.

Preferential carbon-dioxide sorption was observed on the cadmium based mixed-linker metal-organic framework $\{[Cd(L_1)(L_2)](DMA)\}_n$ (**1**). The MOF features an interpenetrated 3D networked structure consist of pendant Lewis basic $-NH_2$ groups directed towards the pores. PLATON analysis shows that the solvent accessible void space of the MOF is ca. 26.6%. At

298 K, the desolvated **1** showed an uptake of carbon-dioxide of 8.33 wt% or 42.42cc/g at 1 bar. Preferential adsorption of CO_2 over other gases is presumably because of presence of pendant $-NH_2$ groups in the framework pores. This type porous MOF is highly promising for application in carbon capture and sequestration (CCS) technology in future.

Furthermore a new Cu based mixed linker 1D co-ordination polymer $[Cu_2(L_3)_4(L_4)]_n$ (**3**) (L_3 = 3-(2-thienyl)acrylic acid, L_4 = 4,4´-bipyridine) has been synthesis by slow diffusion of layer technique. Single crystal X-ray data revealed that the compound crystalizes in triclinic crystal system. Two neighboring copper centers linked via carboxylate bridge through L_3 ligand to form paddle wheel unit $[Cu_2(L_3)_4]$ (SBU) are further connected by L_4 unit forming infinite one dimensional network. Notably, $[Cu_2(L_3)_4(L_4)]_n$ is capable of activating molecular oxygen under base free condition in catalytic oxidation of alcohols. It is a rare example of activating molecular oxygen in alcohol oxidation without using the base.

A series of cobalt(II) based mixed linker bi-functional MOF catalysts $\{[Co(L_5)(L_2)](H_2O)\}_n$ (**3**), $\{[Co(L_5)(L_6)]\}_n$ (**4**) and $\{[Co(L_5)(H_2O)](H_2O)_2\}_n$ (**5**) functionalized catalyst (L_5 = 5-amino-1,3-benzenedicarboxylic acid, L_2 = 4,4´-azopyridine and L_6 = 1,2-bis(4-pyridyl)ethane) have been synthesized through hydrothermal route. Characterization was done by single crystal X-ray diffraction, PXRD, TGA and IR. Single crystal X-ray diffraction data revealed that the compounds are forming infinite two-dimensional framework. While MOFs **3** and **4** exhibited excellent catalytic activity towards tandem reaction involving styrene oxidation followed by Knoevenagel condensation between oxidized product and active methylene group containing substrates, malononitrile or ethyl-cyanoacetate MOF **4** could only catalyzed oxidation reaction. Evidently presence of free $-NH_2$ group in MOFs **3** and **4** facilitated the tandem reaction through organo-catalysis pathway. Nevertheless, in case of **5**, reaction stops at oxidation of styrene only; the reaction does not proceed further as the $-NH_2$ group is not free in $\{[Co(L_5)(H_2O)](H_2O)_2\}_n$ (**5**) rather it is coordinated to Co(II) ion.

Therefore, it can be concluded that MOFs are the potential candidate for uses in various applications, as have been discussed in preceding chapters. It is evident that these materials, particularly porous MOFs, will be subject for more multidisciplinary studies in the future due to their fundamental and useful applications in the fields of gas storage and separations, catalysis, sensing, and other areas. These applications could result in the development of better systems with potential use in industry or other settings.

Appendix I

1. **Rakesh Debnath**, Pameli Ghosh, subratanath Koner, Appl. Organomet. Chem. 2024. Aerobic oxidationn of alcohol over copper (II) –based metal organic frame work: synthesis, x-ray structure, and catalytic study.

2. **Rakesh Debnath**, Pameli Ghosh, Subratanath Koner. Journal of porous material. 2022. **30**. 1163. Preferential CO_2 adsorption over cadmium-based Porous Metal-organic Framework.

3. **Rakesh Debnath**, Rahul Bhowmik, Pameli Ghosh, Saptarshi Biswas, Subratanath Koner. New j. Chem. 2022. **46**. 8523. Selective luminescent sensing of metal ions and nitroaromatics over a porous mixed-linker cadmium(II) based metal–organic framework.

4. Pameli Ghosh, Tanmoy Maity , Nilufa Khatun, **Rakesh Debnath**, Subratanath Koner. Polyhedron. 2022. **219**. 115789. 2D paddle wheel lanthanide metal-organic framework: Synthesis, structure and exploration of catalytic *N*-arylation reaction**.**

5. Mrinmoy Ghosh, Parthapratim Chakrabarty, AtishDipankar Jana, DieterSchollmeyer, Hiroshi Sakiyama, Mashiro Mukuriya, **Rakesh Debnath**, Paula Brandao, Dasarath Mal, Sandip Saha. Inorganic Chimica Acta. 2022. **531**. 120713. Ligand mediated structural diversity of copper(II)-azido moiety: Synthesis, structure and magnetic study.

6. Saikat Gayen,Pameli Ghosh, Hishasi Honda, Debraj Saha, Saptarshi Biswas, **Rakesh Debnath**, subratanath koner. Polyhedron. 2021. **208**. 115444. Solvent mediated photoluminescence responses over mixed-linker cadmium (II) based metal–organic frameworks.

7. Birendra Nath Patra, Pameli Ghosh, Nayim Sepay, Saikat Gayen, Subratanath Koner, Paula Brandao, Zhi Lin, **Rakesh Debnath**, Jahar Lal Pratihar, Tanmay Maity, Dasarath Mal. Appl. Organomet. Chem. 2022. **36**. 1099**.** Aerobic epoxidation of olefins by carboxylate ligand-based cobalt (II) compound: synthesis, X-ray crystallography, and catalytic exploration.

8. Pameli Ghosh , Tanmoy Maity , Saptarshi Biswas , **Rakesh Debnath** , Subratanath Koner. Polyhedron 2021. **194**. 114934. Thermally stable and robust gadolinium-based

metal-organic framework: Synthesis, structure and heterogeneous catalytic O-arylation reaction.

9. Pameli Ghosh, **Rakesh Debnath**, Subratanath Koner, Polyhedron. 2024, **262**, 117177. O-arylation reaction over lanthanide metal–organic framework: Synthesis, structure and catalytic reaction.

10. Prithwiraj Sasmal**, Rakesh Debnath,** Prof. Subratanath Koner, Dr. Paula Brandao, Dr. Malay Dolai, Dr. Prasanta Kumar Bhaumik, Dr. Abhijit Banerjee, Dr. Pameli Ghosh, Dr. Debopam Sinha, Anupam Chowdhury, Dr. Asit kumar Das, Dr. Dasarath Mal. ChemistrySelect, 2024, **9**. Insight into the Structural Optimization and Electric conductivity of Ni(II)/Mn(II) bipyridine –dicyanamide complexes.

Appendix II

Selective ^{1}H NMR spectra

Table-4.5, Entry: 1; ^{1}H NMR (400 MHz, CDCl$_3$) δ 10.04 (s, 1H), 7.94 – 7.87 (m, 2H), 7.70 – 7.61 (m, 1H), 7.60 – 7.51 (m, 2H). Anal. Calcd. for C$_7$H$_6$O: C, 79.22%; H, 5.70%. Found C, 77.37; H, 5.83%.
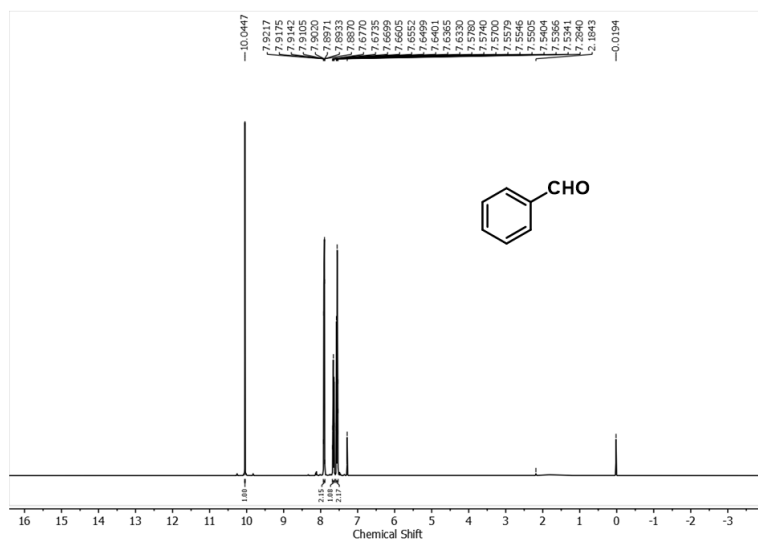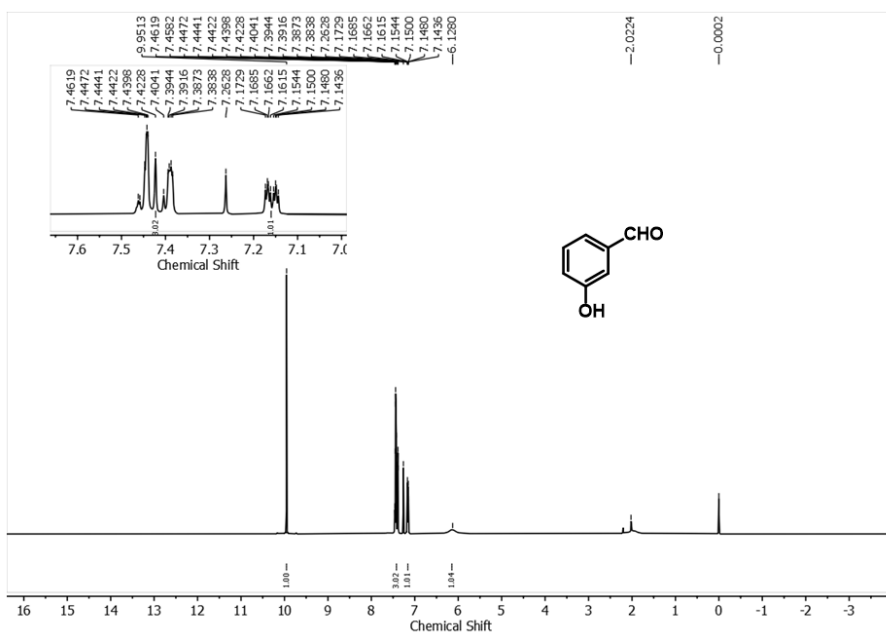

Table-4.5, Entry: 2; ^{1}H NMR (400 MHz, CDCl$_3$) δ 10.18 (s, 1H), 8.46 – 8.38 (m, 2H), 8.14 – 8.06 (m, 2H). Anal. Calcd. for C$_7$H$_5$NO$_3$: C, 55.63%; H, 3.33% ; N, 9.27 %; Found C, 55.48 %; H, 3.43%; N, 9.35%.
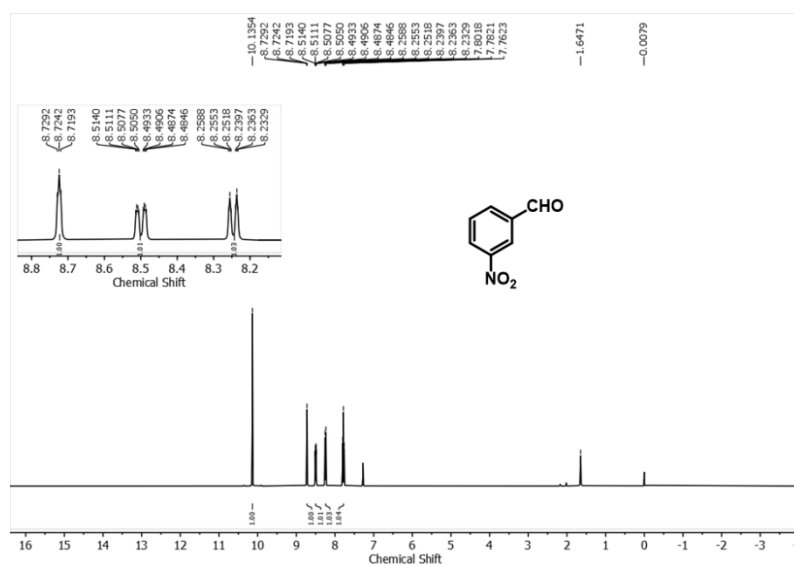
Table-4.5, Entry: 3; ^{1}H NMR (400 MHz, CDCl$_3$) δ 9.97 (d, J = 2.0 Hz, 2H), 7.84 (q, J = 2.2 Hz, 2H), 7.76 (dq, J = 7.6, 1.6 Hz, 2H), 7.59 (ddd, J = 7.0, 3.1, 1.7 Hz, 2H), 7.48 (td, J = 7.8, 2.0 Hz, 2H), Anal. Calcd. for C$_7$H$_5$ClO: C, 59.83% ; H, 3.59% . Found C, 59.78 % ; H, 3.48%.
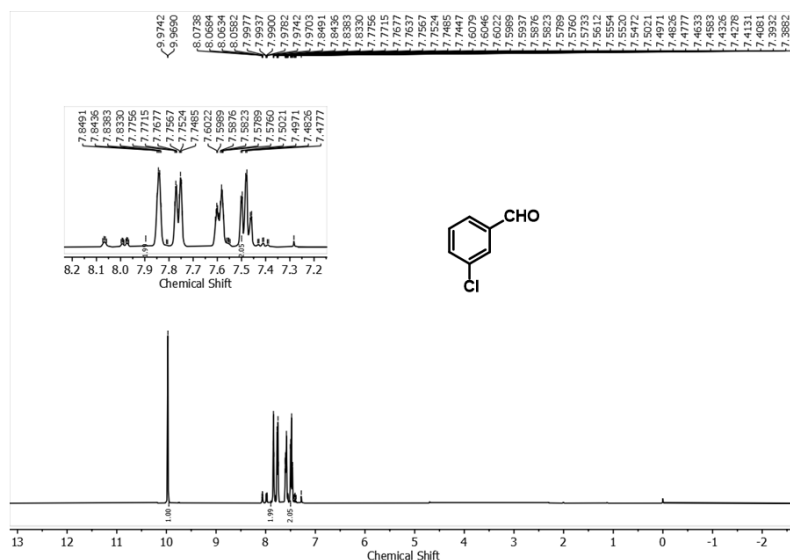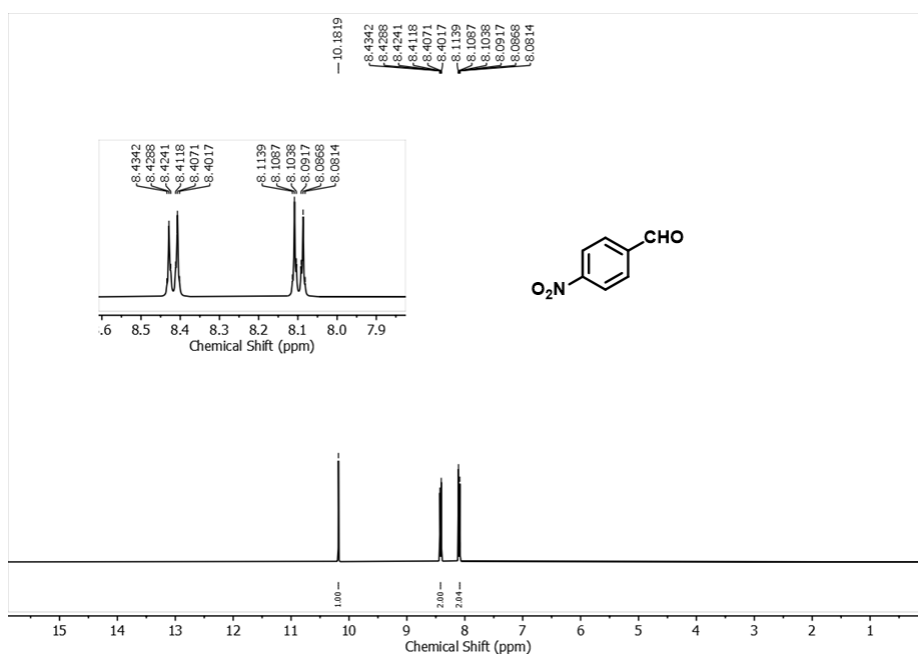

Table-4.5, Entry: 4; ^{1}H NMR (400 MHz, CDCl3) δ 9.95 (s, 1H), 7.48 – 7.42 (m, 1H), 7.46 – 7.38 (m, 1H), 7.42 – 7.36 (m, 1H), 7.16 (ddd, J = 7.2, 2.6, 1.8 Hz, 1H), 6.13 (s, 1H). Anal. Calcd. for C$_7$H$_6$O$_2$: C, 68.85% ; H, 4.95% . Found C, 69.05 % ; H, 4.68%.

**Table-4.5, Entry: 5;** ^{1}H NMR (400 MHz, CDCl3) δ 9.94 (s, 1H), 7.79 – 7.73 (m, 2H), 7.31 (d, J = 7.9 Hz, 2H), 2.42 (s, 3H). Anal. Calcd. for C_8H_8O: C, 79.97%; H, 6.71% . Found C, 80.23 %; H, 6.63%.
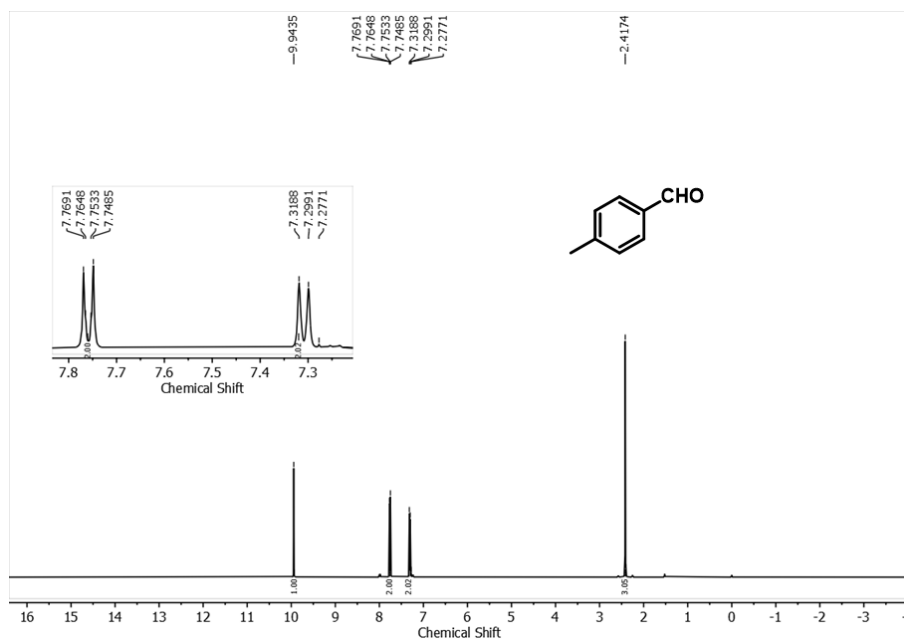
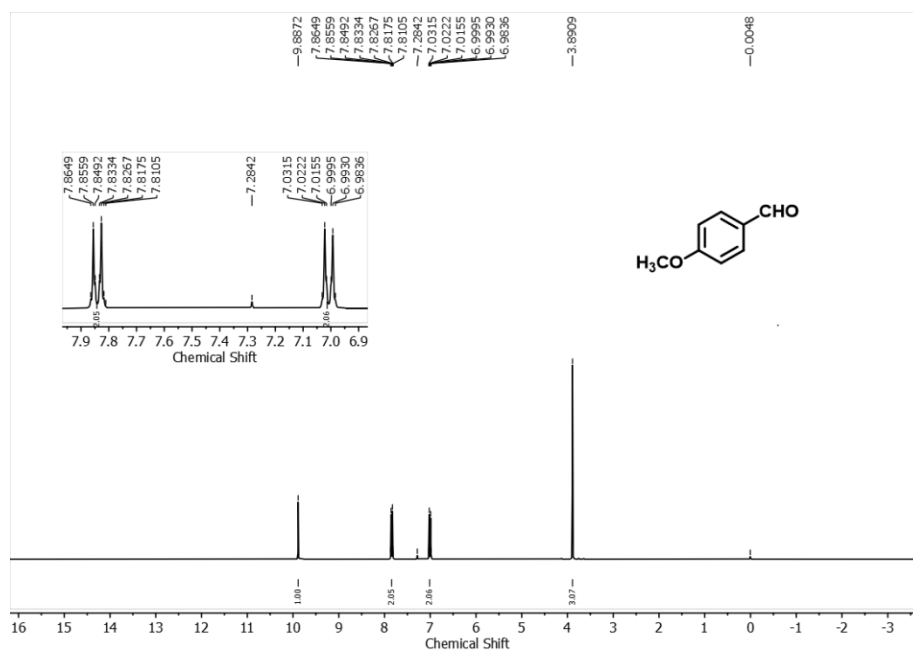**Table-4.5, Entry: 6;** ^{1}H NMR (400 MHz, CDCl3) δ 10.18 (s, 1H), 8.46 – 8.38 (m, 2H), 8.14 – 8.06 (m, 2H). Anal. Calcd. for $C_7H_5NO_3$: C, 55.63%; H, 3.33% ; N, 9.27 %; Found C, 55.79 %; H, 3.46%; N, 9.43%.

Table-4.5, Entry: 7; ^{1}H NMR (400 MHz, CDCl3) δ 9.89 (s, 1H), 7.87 – 7.79 (m, 2H), 7.02 – 6.94 (m, 2H). Anal. Calcd. for $C_7H_6O_2$: C, 68.85%; H, 4.95% . Found C, 69.15 %; H, 4.72%.
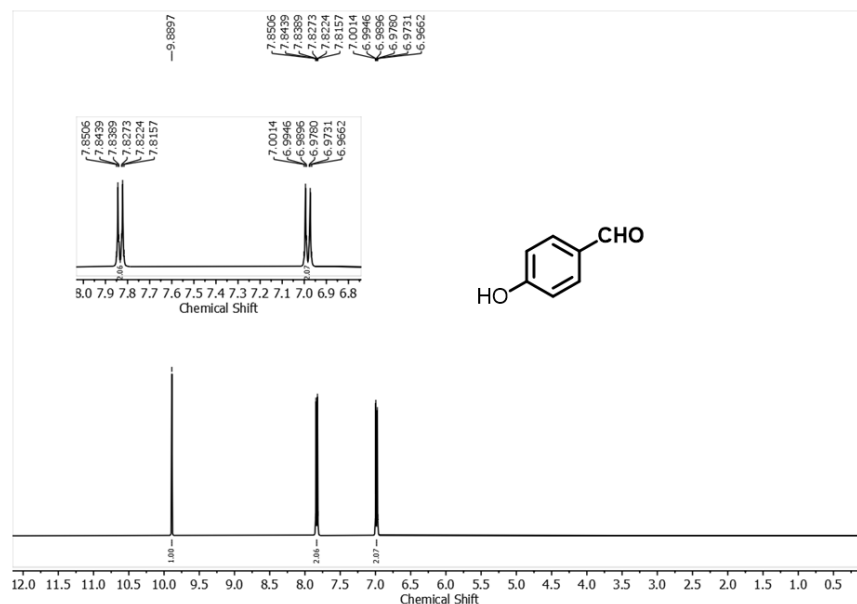

Table-4.5, Entry: 8; ^{1}H NMR (300 MHz, CDCl3) δ 9.89 (s, 1H), 7.89 – 7.79 (m, 2H), 7.06 – 6.92 (m, 2H), 3.89 (s, 3H). Anal. Calcd. for $C_8H_8O_2$: C, 70.57%; H, 5.92% . Found C, 69.78 %; H, 6.03%.

**Table-4.5, Entry: 9;** ^{1}H NMR (400 MHz, CDCl$_3$) δ 10.00 (s, 1H), 7.81 – 7.64 (m, 4H). Anal. Calcd. for C$_7$H$_5$BrO$_2$: C, 45.44%; H, 2.72% . Found C, 45.61 %; H, 2.68%.

Table-5.6 and 5.8, entry 1: White solid, ^{1}H NMR (300 MHz, CDCl$_3$) δ 7.99 – 7.89 (m, 1H), 7.81 (s, 0H), 7.72 – 7.62 (m, 0H), 7.62 – 7.51 (m, 1H). Anal. Calcd. for C$_{10}$H$_6$N$_2$: C, 77.91%; H, 3.92%; N, 18.17%. Found C, 77.97; H, 3.96%; N, 18.15%.

Table-5.6 and 5.8, entry 2: White solid, ^{1}H NMR (300 MHz, CDCl$_3$) δ 8.28 (s, 1H), 8.08 –
7.97 (m, 2H), 7.65 – 7.45 (m, 3H), 4.42 (q, *J* = 7.1 Hz, 2H), 1.43 (t, *J* = 7.1 Hz, 3H). Anal.
Calcd. for C$_{12}$H$_{11}$NO$_2$: C, 71.63%; H, 5.51%; N, 6.96%. Found : C, 71.69%; H, 5.56%; N,
6.93%.
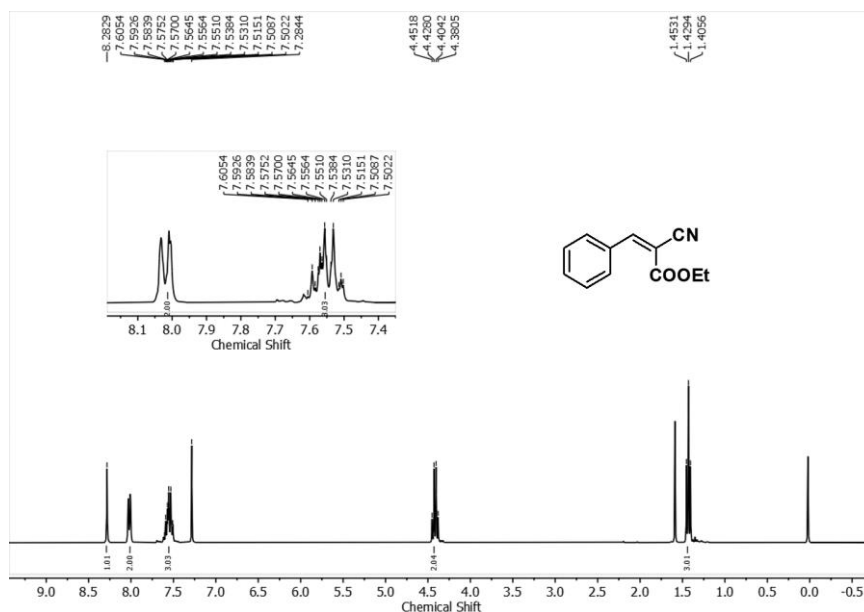
Table-5.6 and 5.8, entry 3: Yellow solid ^{1}H NMR (300 MHz, CDCl3) δ 7.82 – 7.77
(m, 2H), 7.74 (s, 1H), 7.73 – 7.69 (m, 2H). Anal. Calcd. for C$_{10}$H$_5$BrN$_2$: C, 51.53%; H,
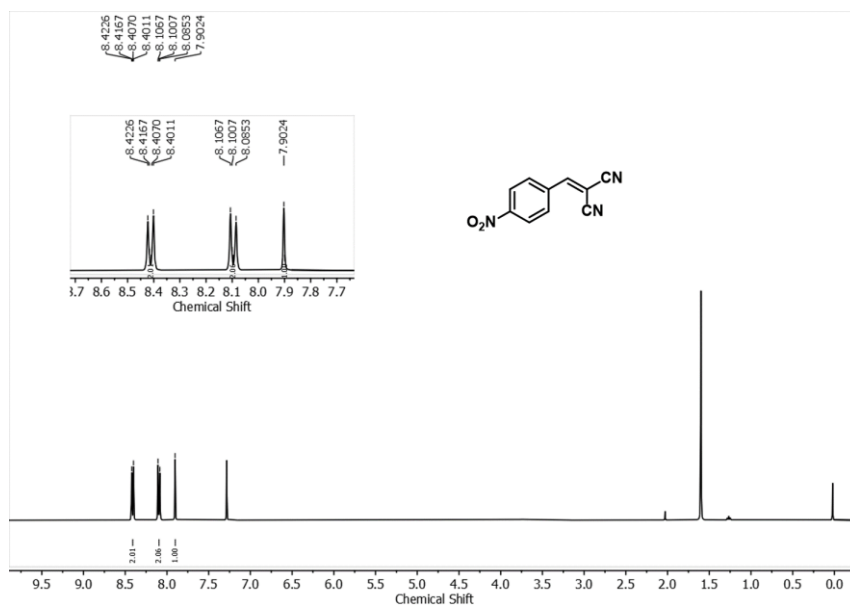2.16%; N, 12.02%. Found : C, 51.51%; H, 2.20%; N, 12.18%.
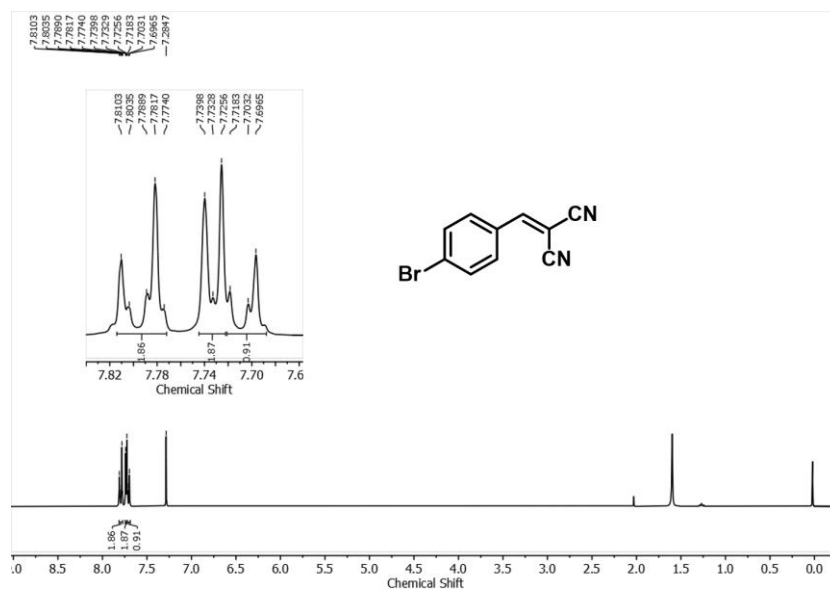
Table- 5.6 and 5.8, entry 4 : White solid, ^{1}H NMR (300 MHz, CDCl3) δ 8.20 (s, 1H), 7.93 – 7.82 (m, 2H), 7.72 – 7.61 (m, 2H), 4.41 (q, J = 7.1 Hz, 2H), 1.62 (s, 2H), 1.42 (t, J = 7.1 Hz, 3H). Anal. Calcd. For $C_{12}H_{10}BrNO_2$: C, 51.45%; H, 3.60%; N, 5.00%. Found C, 51.52%; H, 3.63%; N, 5.09%.
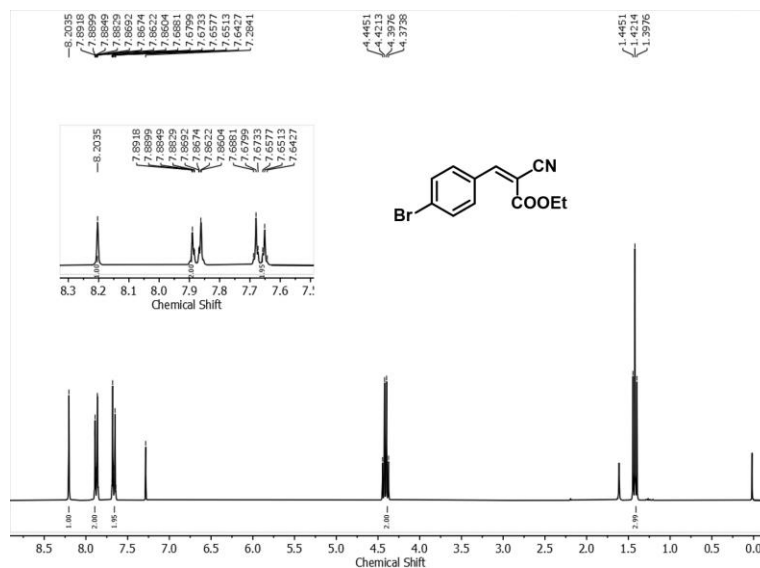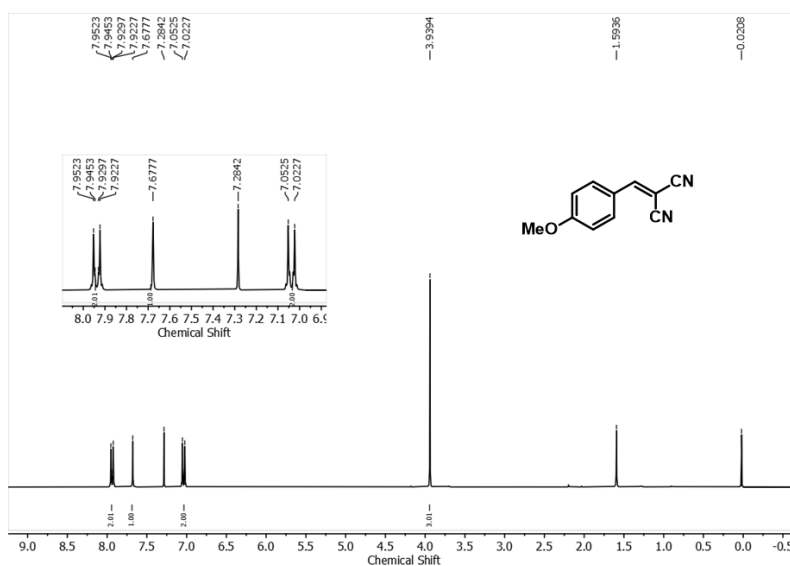

Table- 5.6 and 5.8, entry 5: ^{1}H NMR (400 MHz, CDCl$_3$) δ 8.44 – 8.37 (m, 2H), 8.12 – 8.07 (m, 2H), 7.90 (s, 1H). Anal. Calc. For $C_{10}H_5N_3O_2$: C, 60.31%; H, 2.53%; N, 21.10%. Found C, 60.30%; H, 2.51%; N, 21.09%.

Table- 5.6 and 5.8, entry 6: Yellow solid ^{1}H NMR (400 MHz, CDCl$_3$) δ 8.20 (s, 1H), 7.90 – 7.85 (m, 2H), 7.69 – 7.65 (m, 2H), 4.41 (q, *J* = 7.1 Hz, 2H), 1.42 (t, *J* = 7.1 Hz, 3H).). Anal. Calc. For C$_{12}$H$_{10}$N$_2$O$_4$ C, 58.54%; H, 4.09%; N, 11.38%. Found C, 58.64%; H, 4.16%; N, 11.42%.
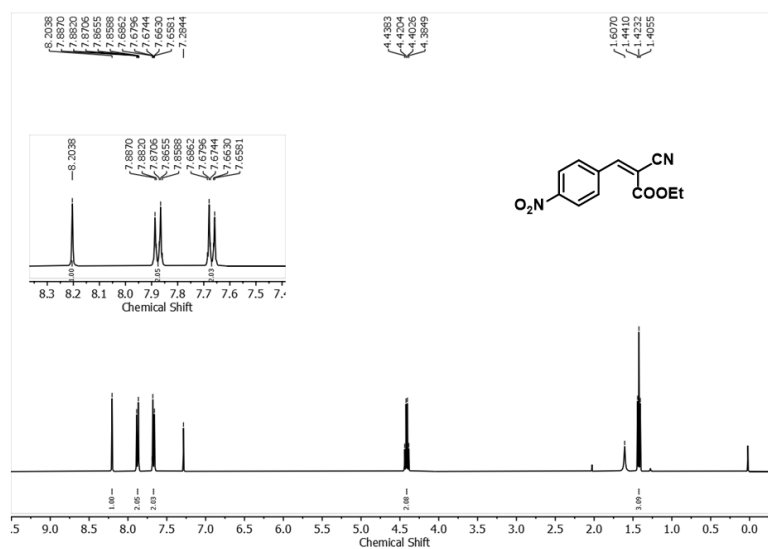
Table- 5.6 and 5.8, entry 7: White solid, ^{1}H NMR (300 MHz, CDCl$_3$) δ 7.99 – 7.88 (m, 2H), 7.68 (s, 1H), 7.09 – 6.98 (m, 2H), 3.94 (s, 3H). Anal. Calcd. for C$_{11}$H$_8$N$_2$O: C, 71.73%; H, 4.38%; N, 15.21%.. Found C, 71.71%; H, 4.37%; N, 15.19%.

Table-5.6 and 5.8, entry 8: White solid, ^{1}H NMR (400 MHz, CDCl$_3$) δ 8.22 – 8.17 (m, 1H), 8.06 – 7.98 (m, 2H), 7.05 – 6.98 (m, 2H), 4.39 (qt, *J* = 7.2, 1.3 Hz, 2H), 3.94 – 3.89 (m, 3H), 1.45 – 1.37 (m, 3H). Anal. Calc. for C$_{13}$H$_{13}$NO$_3$: C, 67.52%; H, 5.67%; N, 6.06%. Found C, 67.52%; H, 5.63%; N, 6.02%.